

Understanding the behavior of the Sun's large scale magnetic field and its relation with the meridional flow

A THESIS

SUBMITTED FOR THE DEGREE OF

Doctor of Philosophy

IN THE FACULTY OF SCIENCE

by

Gopal Hazra



Joint Astronomy Programme
Department of Physics
Indian Institute of Science
Bangalore – 560 012, INDIA

JULY 2017

© Gopal Hazra
July 2017
All rights reserved

Declaration

I hereby declare that the work reported in this doctoral thesis titled “Understanding the behavior of the Sun’s large scale magnetic field and its relation with the meridional flow” is entirely original and is the result of investigations carried out by me in the Department of Physics, Indian Institute of Science, Bangalore, under the supervision of Prof. Arnab Rai Choudhuri and Prof. Dipankar Banerjee.

I further declare that this work has not formed the basis for the award of any degree, diploma, fellowship, associateship or similar title of any University or Institution.

Date:
Bangalore, India

Gopal Hazra
Department of Physics
Indian Institute of Science

To My Parents

Acknowledgements

The memorable journey to the final stage of Ph.D. and completion of the thesis have only been possible with the support and encouragement of numerous people including my friends, my well-wishers, and colleagues. First and foremost, I thank my supervisors Arnab Rai Choudhuri and Dipankar Banerjee for their continued support, their patience, and their wise advice. They have provided me with opportunities beyond compare. All of the stimulating discussions with them throughout the years have always nurtured my fascination for solar physics. I must mention that the books ‘The Physics of Fluids and Plasmas’ and ‘Astrophysics for Physicists’ written by Arnab Rai Choudhuri have been always with me from the very first day of my Ph.D. and I have learned a lot from these books. I hope to write one day as well as he does regularly.

I wish to thank Mark Miesch for giving me the opportunity to work with him. He has always treated me as one of his own student. His deep insights and positive outlook have contributed greatly to my own improvement. I thank Mausumi Dikpati, Kinfe Teweldebirhan, Hideyuki Hotta, Kyle Augustson, Junfeng Wang and Lokesh Bharti for those memorable days during my stay in HAO, Boulder. My thanks also go to my senior Bidya Binay Karak, who walked these steps before me and helped me a lot to find my own way. I also thank the past and present members of Dipu da’s group, Tanmoy, Vaibhav, Sudip, Subhamoy, Rakesh, Girju da, Krishna da, Chandru da, Vemareddy and Manjunath in Indian Institute of Astrophysics for various discussions and help.

I would take this opportunity to thank all of the faculty members, postdocs and students of our Astrophysics group for their constant supports and discussions. Special thanks to Prateek Sharma and Chanda J. Jog who taught us Numerical Methods and Galaxy & ISM respectively during our graduate coursework. Thanks to Prateek again for answering various queries regarding numerical methods during my research. I also thank all of the JAP instructors who taught us in our coursework.

I also thank my seniors Sujit Kumar Nath, Upasana Das, Indrani Banerjee, Nazma Islam, Arpita Roy, Samyaday Choudhury and Susmitha Anthony for the discussion and help during my Ph.D. days.

Special thanks to my batchmates- Kartick, Abir, Sreehari, Soumavo, Deovrat, and Mohan. I cherish many evenings and late nights which we have spent together at Gymkhana and Faculty club. Those days were really memorable.

Thanks to Soumavo and Prasun for being fantastic friends and supporting me as and when required. Thanks to Debasish da, Siddhartha, Prakriti, Ajay and Tirthankar for their help and discussion in many aspects.

A big thank you to all the nice people of IISc. IISc is enjoyable and wonderful because of you. I need to finish my thesis, so I would name only a few: Rahool, Krishna Prasad, Sukanya, Kingshuk, Malay, Hemanta, Sumanta, Phani, Gopi, Kaji, Subham, Sudipta, Debasmita, Soumi, Arijit, Rudra, Sourav, Rupak, Pradip, Monojit, Somnath & whole math group, Debabrata, Soumen, Adhip, Amit, Pushpender, Koushik, Arpan (UG) & Co., Swarup da, Sudip da, Somnath da, Amiya da, Apurba da, Nafiza di, Bidisha di, Indra da and members of Bandooz group.

Finally, I would like to thank my parents and my loving sister for their constant patience and support through the years. They have supported me with love on every step of this adventure. I appreciate the freedom my parents have given me to pursue my studies in physics. I also thank my elder brother Subrata for encouraging me to pursue study in physics.

The simulations were performed in SahasraT (SERC, IISc), Yellowstone (NCAR) and Pleiades (NASA). I thank two referees of my thesis, Prof. Paul Charbonneau and Prof. Prasad Subramanian for their helpful suggestions which helped a lot to improve the thesis. Financial supports from Council of Scientific and Industrial Research (India) as well as the J. C. Bose (DST, India) Fellowship awarded to Arnab Rai Choudhuri are also acknowledged.

Preface

Our Sun is a variable star. The magnetic fields in the Sun play an important role for the existence of a wide variety of phenomena on the Sun. Among those, sunspots are the slowly evolving features of the Sun but solar flares and coronal mass ejections are highly dynamic phenomena. Hence, the solar magnetic fields could affect the Earth directly or indirectly through the Sun's open magnetic flux, solar wind, solar flare, coronal mass ejections and total solar irradiance variations. These large scale magnetic fields originate due to Magnetohydrodynamic dynamo process inside the solar convection zone converting the kinetic energy of the plasma motions into the magnetic energy. Currently, the most promising model to understand the large scale magnetic fields of the Sun is the Flux Transport Dynamo model. In this thesis, various studies leading to better understanding of the large scale magnetic fields of the Sun are performed using the Flux Transport Dynamo (FTD) models.

FTD models are mostly axisymmetric models, though the non-axisymmetric 3D FTD models are also started to develop recently. Just like other physical models, FTD models have various assumptions and approximations for different processes which are responsible for the generation of large scale magnetic fields. Some of the assumptions are observationally verified and some of them are not till date. Considering the availability of resources, many approximations have been made in these models on the theoretical basis. Magnetic buoyancy is one of the important processes in these models. We discuss in details about how magnetic buoyancy has been treated in axisymmetric FTD models and the advantages and disadvantages of the different treatments. We finally realize that a proper treatment of the magnetic buoyancy needs a 3D treatment which motivates us to build a more realistic 3D Dynamo model.

The irregular solar cycles show some interesting properties in their ascending and descending phases. The properties of the solar cycle in the rising phase (e.g., Waldmeier effect) of the cycle have been already well recognized and well explained, but the properties in the decaying phase remain less noticed. We touch upon these properties in the decaying phase in great details. We find some interesting correlations in the decaying phase from Greenwich data and

as well as Kodaikanal observatory data. We provide an explanation of this observed correlation from FTD models.

Recent developments of the helioseismology challenge one of the very important assumptions of the FTD models. FTD models assume a single cell meridional circulation encompassing the whole convection zone of the Sun having a poleward flow on the surface and an equatorward return flow near the bottom of the convection zone. After helioseismology discovers that the meridional circulation might have a different spatial structure in the convection zone, we investigate this issue and justify that FTD models work perfectly fine as long as there is an equatorward propagation of the meridional flow at the bottom of the convection zone. Although the observations about the spatial structure of the meridional flow are found recently, temporal variation of meridional flow with the solar cycle has been found almost a decade ago. Since FTD models operate in the kinematic regime, we are not able to take into account the Lorentz Force feedback. But if we take this Lorentz force feedback into our model, we believe that the observed variation of the meridional circulation would be reproduced. We find that this is indeed the case! We just consider the effect of the Lorentz force feedback on the velocity equation as a perturbation over the steady flow and solve the perturbed equation coupled with the dynamo equations. By doing so, We are able to reproduce the observed variation of the meridional flow with the solar cycle.

Finally, we present some results with a 3D FTD model. Development of 3D dynamo model is necessary for plenty of reasons. Various processes in the solar dynamo are inherently 3D. The magnetic buoyancy, because of which the magnetic flux tube rises through the solar convection zone and creates sunspots is a 3D process. The decay of sunspots, and corresponding dispersion and migration of the sunspots fields by different convective flows and build up of polar field i.e. altogether the Babcock-Leighton process is also a 3D process. Modeling these 3D processes with an axisymmetric 2D FTD model is difficult. In 2D model, they are treated in a very clever but simplistic way which sometimes is not enough to capture whole physics of the problem. We explain these issues and their modeling procedures in 3D FTD models. We get results which are distinguishable from the results obtained by axisymmetric FTD models. The 3D FTD models open up plenty of windows to understand large scale solar magnetic fields and solar cycle much more realistically. For the first time, we incorporate observed surface convective flows data in 3D FTD model with the highest fidelity. We describe an initial implementation of the data feeding in these models which is very important for realistic treatment of Babcock-Leighton process.

List of Publications

1. **Hazra, G.**, Karak, B. B., & Choudhuri, A. R., 2014, *Is a Deep One-cell Meridional Circulation Essential for the Flux Transport Solar Dynamo?* **ApJ**, **782**, 93
2. **Hazra, G.**, Karak, B. B., Banerjee, D. & Choudhuri, A. R. 2015, *Correlation Between Decay Rate and Amplitude of Solar Cycles as Revealed from Observations and Dynamo Theory*, **Sol. Phys.** **290**, 6
3. Choudhuri, A. R. & **Hazra, G.**, 2016, *The treatment of magnetic buoyancy in flux transport dynamo models*, **Advances in Space Research**, **58**, 8
4. **Hazra, G.**, & Choudhuri, A. R., & Miesch, M. S., 2017, *A Theoretical Study of the Build-up of the Sun's Polar Magnetic Field by using a 3D Kinematic Dynamo Model*, **ApJ**, **835**, 39
5. Mandal, S., Hegde, M., Samanta, T., **Hazra, G.**, Banerjee, D. & Ravindra, B. 2017, *Kodaikanal digitized white-light data archive (1921-2011): Analysis of various solar cycle features*, **Astronomy & Astrophysics**, **601**, 106
6. **Hazra, G.** & Choudhuri, A. R., 2017, *A theoretical model of the variation of the meridional circulation with the solar cycle*, **MNRAS**, **472**, 2728
7. **Hazra, G.** & Miesch, M. S., 2017, *Incorporating Surface Convection into a 3D Babcock-Leighton Solar Dynamo Model*, **ApJ**, Under review, arXiv:1804.03100

Table of contents

List of figures	xvii
List of tables	xxi
1 Introduction	1
1.1 History of sunspot observations	4
1.2 Magnetic properties of Sunspots and Solar Cycle	6
1.3 Theoretical Background	10
1.3.1 Basic equations of Magnetohydrodynamics	10
1.3.2 Magnetoconvection	11
1.3.3 Flux tube dynamics and field amplification	13
1.3.4 Helioseismology	16
1.4 Dynamo Theory	20
1.5 Flux Transport Dynamo Model	25
1.5.1 Mean Flows	27
1.5.2 Turbulent Diffusion	29
1.5.3 Magnetic Buoyancy	30
1.5.4 Babcock-Leighton Mechanism	31
2 The Treatment of Magnetic Buoyancy in Flux Transport Dynamo Models	35
2.1 Introduction	35
2.2 The basic equations	37
2.3 Non-local and local treatment of magnetic buoyancy	38
2.3.1 Non-local magnetic buoyancy	39
2.3.2 Local magnetic buoyancy	40
2.3.3 Comparison between the non-local and local methods	42
2.4 Modeling irregularities of the solar cycle	43

2.5	The latitudinal distribution problem	47
2.6	Conclusion	49
3	Explaining various Irregular Properties of the Solar Cycle	51
3.1	Introduction	51
3.2	Observational Studies	54
3.2.1	Correlation between the Decay Rate and the Cycle Amplitude	55
3.2.2	Correlation between the Decay Rate and the Next Cycle Amplitude	56
3.2.3	Correlation between the Cycle Period and the Next Cycle Amplitude	59
3.2.4	Some irregular features of solar cycle from century long sunspot area data of Kodaikanal Observatory	60
3.2.4.1	Waldmeier Effect: The correlations in ascending phase of the solar cycle	60
3.2.4.2	The correlations in descending phase of the solar cycle	63
3.3	Theoretical Framework of the Dynamo Model	64
3.4	Results of Theoretical Modeling	65
3.4.1	Fluctuations in the Poloidal Field Generation	65
3.4.2	Fluctuations in the Meridional Circulation	67
3.4.3	Fluctuations in the Poloidal Field Generation and the Meridional Circulation	71
3.4.4	Robustness of the Results on Changing the Meridional Circulation and Differential Rotation Profiles	73
3.5	Conclusion	77
4	Multi-cell Meridional Circulation in Flux Transport Dynamo Models	79
4.1	Introduction	80
4.2	Mathematical formulation	84
4.3	Results with radially stacked cells	88
4.4	Results with more complicated cells	93
4.5	Results for low diffusivity versus high diffusivity	95
4.6	The effect of turbulent pumping	100
4.7	Conclusion	104
5	Why does Meridional Circulation Vary with the Solar Cycle?	109
5.1	Introduction	110
5.2	Mathematical Formulation	113
5.3	Results	122

5.3.1	Results with $P_m = 1$	123
5.3.2	Results with low Prandtl number ($P_m < 1$)	129
5.3.3	Dependence of the results on lower radial boundary condition	131
5.4	Conclusion	131
5.5	Appendix A: Calculation of the Viscosity Term	135
5.6	Appendix B: Importance of various advective terms	137
6	3D Flux Transport Dynamo Model and Build up of Solar Polar Field	139
6.1	Introduction	140
6.2	Mathematical Formulation	143
6.3	Our reference model	149
6.4	The build-up of the polar field	153
6.4.1	Polar field from one sunspot pair	154
6.4.2	Polar fields from two sunspot pairs in two hemispheres	160
6.5	The contribution of bipolar sunspots not obeying Hale's law	163
6.6	Conclusion	167
7	Incorporating Surface Convection into a 3D Flux Transport Dynamo Model	171
7.1	Introduction	172
7.2	The Numerical Model	176
7.3	Incorporating Non-Axisymmetric Convective Flows into STABLE	181
7.3.1	Empirical Model for Surface Convection	181
7.3.2	Subsurface Extrapolation of the Convective Flow	186
7.4	Axisymmetric Flows	187
7.5	Convective Flows	193
7.5.1	Amplification of fields by convective flows	193
7.5.2	Results with convective flows	195
7.6	Discussion: Does Convection Operate as a Turbulent Diffusion?	200
7.6.1	The turbulent electromotive force (emf)	200
7.6.2	Poleward Migration	202
7.6.3	Dynamo Efficiency	205
7.7	Summary and Conclusion	206
8	Concluding Remarks	209
	References	215

List of figures

1.1	Aurora visible on 6th March, 2017 from Iceland	3
1.2	Time series of Sunspot Numbers	5
1.3	Solar Magnetogram	7
1.4	Observed butterfly diagram	9
1.5	Image of sunspot in G band and in calcium H line	12
1.6	Isolated Flux tube	13
1.7	Buoyant rising of flux tube	14
1.8	Schematic diagram for amplification of magnetic field	15
1.9	Meridional flow deep interior of sun using HMI data	19
1.10	Toroidal field generation by differential rotation	21
1.11	Babcock-Leighton mechanism and Cartoon diagram of Flux Transport Dynamo model	25
1.12	Meanflows used in FTD models	28
1.13	Different diffusivity profiles used in FTD	29
2.1	Poloidal field lines in Durney's double ring	42
2.2	Poloidal and Toroidal magnetic fields for different treatment of magnetic buoyancy	44
2.3	Reproduction of Waldmeier effect using different treatment of magnetic buoyancy	46
3.1	Observed decay rate correlation with cycle amplitude from different sunspots data	55
3.2	Correlation of decay rate with next cycle amplitude	57
3.3	Correlation plot of n th cycle amplitude and the amplitude of the next $n + 1$ cycle from sunspot number data	58
3.4	correlation plot between the cycle amplitude and the period of the previous cycle	59
3.5	Panel (a) shows the yearly averaged solar cycle from kodaikanal sunspot area data. (b) 2 year averaged solar cycle from kodaikanal sunspot area data	61

3.6	Waldmeier effects from century long Kodaikanal sunspot area data	62
3.7	The correlation of decay rate with same cycle and next cycle amplitude from Kodaikanal sunspot area data	63
3.8	Results from stochastically forced dynamo model with B-L α fluctuations . .	66
3.9	Same as Figure 3.8 but with meridional circulation fluctuations.	69
3.10	Memory of meridional circulation explains the correlation between decay rate and next cycle amplitude	70
3.11	Same as Figure 3.8 but with both B-L α and meridional circulation fluctuations.	74
3.12	(a) Scatter plot of the amplitude of cycle n with the amplitude of cycle $n + 1$ with 75% fluctuation in B-L α . (b) Same as (a) but with 100% fluctuation in B-L α	75
3.13	Same as Figure 3.11 but in this model, the large-scale flow has three cells radially stacked in the solar convection zone and the differential rotation includes near surface shear layer.	76
4.1	Results with shallow meridional circulation	89
4.2	Results with radially stacked two cells	90
4.3	Results with two radially stacked cells but opposite sense	91
4.4	Results with radially stacked three cells	92
4.5	Cycle period vs velocity amplitudes of three different cells	93
4.6	Streamlines for two complicated meridional circulation patterns	94
4.7	Butterfly diagrams with complicated cells (Fig 4.6(a))	95
4.8	Same as Figure 4.7, for the meridional circulation given in Figure 4.6(b). . . .	96
4.9	Different Turbulent diffusivity used in our model	97
4.10	Results with low diffusivity for radially three stacked cells	97
4.11	Poloidal and Toroidal field lines for different diffusivity	99
4.12	Correlaton plot of polar flux with next cycle amplitude for different diffusivity	101
4.13	Results with radial pumping added in low diffusivity case with radially stacked three cells	102
4.14	Results with latitudinal pumping and shallow meridional circulation	103
5.1	Comparison between unperturbed meridional flow and reproduced flow . . .	116
5.2	Diffusivity profiles	121
5.3	Time evolution of the perturbed vorticity	122
5.4	Toroidal field, ϕ component of the curl of the Lorentz force, perturbed vorticity and perturbed velocity are shown in the meridional plane at different times of a cycle	124

5.5	Time latitude plot of the perturbed velocities at different radius	125
5.6	Variation of the meridional circulation with the solar cycle	126
5.7	Same as Fig. 5.4 but with low Prandtl number P_m	130
5.8	Same as Fig. 5.5 but with low Prandtl number P_m	130
5.9	On changing the bottom boundary condition to $\omega_1 = 0$ at $r = 0.55R_\odot$, the third row of Fig. 5.4 would get changed to this.	132
5.10	Behavior of various viscous terms	135
5.11	Behavior of various advective terms	137
6.1	Differential rotation and meridional circulation used in 3D dynamo model . .	144
6.2	V_θ component of meridional circulation	145
6.3	High diffusivity profile used in our simulation	147
6.4	Butterfly diagram from our 3D model	149
6.5	Mean toroidal and poloidal field lines	150
6.6	Azimuthal averaged toroidal fields for different turbulent diffusivity	152
6.7	Time evolution of radial fields for single pair sunspots	155
6.8	Toroidal and poloidal field lines for single pair sunspots at different times . .	156
6.9	Behavior of radial field at different times and at different latitudes	157
6.10	Radial field evolution for two pair of sunspots on both the hemispheres	157
6.11	Toroidal and poloidal field lines are shown for two sunspots pairs	159
6.12	Same as Figure 6.9 but with two pairs in two hemispheres	159
6.13	Polar field and Polar flux evolution for two sunspot pairs	162
6.14	Same as Figure 6.10 but sunspot pairs are placed at different longitudes	162
6.15	Radial Magnetic field structures with an “anti-Hale” sunspot pair	164
6.16	Butterfly diagram with an “anti-Hale” sunspot pair at different latitudes and at different phases of the solar cycle	165
6.17	Polar field evolution with time for one complete solar cycle with “anti-Hale” sunspot pair at different location and different time	166
7.1	Diffusivity profiles used for different cases	180
7.2	Observed convective flows	180
7.3	Radial extrapolation function	183
7.4	Visualization of the imposed convective flow field	185
7.5	Isosurfaces of the convective radial velocity V_r for a zoomed-in patch spanning 20° in latitude and longitude.	186
7.6	Time-latitude plot of the mean radial magnetic field on the solar surface, $\langle B_r \rangle$, for Case A1	189

7.7	Surface transport of sunspots with diffusivity $300 \text{ km}^2\text{s}^{-1}$	190
7.8	Surface transport of sunspots with diffusivity $80 \text{ km}^2\text{s}^{-1}$	190
7.9	Mean magnetic field lines with diffusion	192
7.10	Similar to Figures 7.7 and 7.8 but for the convective Case	196
7.11	Similar to Fig. 7.9 but for convective case	197
7.12	As in Fig. 7.6 but for convective case	198
7.13	butterfly diagram for different important cases	199
7.14	Correlation coefficient versus migration speed for different cases	203

List of tables

3.1	Correlation coefficients between different quantities of the solar cycle.	56
3.2	Correlation coefficients at different phase of solar cycle	64
3.3	Correlation coefficients at different levels of fluctuations and coherence time of meridional circulation.	72
7.1	Simulation Summary	188

"It is not too much to hope that in a not too distant future we shall be competent to understand so simple a thing as a star."

–Sir Arthur Stanley Eddington, 1926

1

Introduction

The importance of the Sun in human life and human civilization is well recognized from the ancient time. The Indians, the Greeks, the Romans, the Egyptians, and other ancient civilizations always worshiped the Sun, because they believed that the Sun is the source of our lives on earth. The Sun has always been an important wonder for mankind from the early days of civilization. Even in the 21st century, where it would not have been possible to step ahead without the use of technology, the study of the Sun is much more relevant and important. With the advancement of technology, the realization about importance of studying the Sun has also increased.

A great step towards understanding the effect of the Sun on earthly phenomena like Aurora, the geomagnetic storm was started after the observations of magnetic fluctuations by Anders Celsius and his assistant Olof Hiorter from Uppsala, Sweden, in 1741, who found that the magnetic fluctuations occurred at the same local time, as aurorae were sighted. Celsius also found that these magnetic disturbances associated with the aurora in Sweden were simultaneously observed in England by George Graham, who was a pioneering observer in geomagnetic variations. With this discovery, it became very clear that the magnetic disturbances associated with Aurora were global rather than regional character. It was around 1806, Alexander Von Humboldt also spent many tedious hours to record the variability of the magnetic fields, and

in the first-half of the 1800s, it was well appreciated that magnetic disturbances associated with aurorae were global in scale and nearly simultaneous everywhere. By 1837, Dennison Olmstead argued that the cause for the aurorae must exist outside of the Earth due to the global scope of the auroral-magnetic phenomenon (Schrijver & Siscoe, 2010). Historically, in 1843, Heinrich Schwabe discovered the solar cycle, and in 1852 Sabine showed a detailed correlation between the sunspot cycle and the frequency of auroral displays (Sabine, 1852). This was a remarkable discovery for the Sun and Earth connection, and a space influence outside of the Earth was established as the cause of Aurora. Around the same time, on 1st September 1859 the amateur English astronomer Richard C. Carrington while monitoring the sunspots noticed two rapidly brightening patches of light near the middle of a sunspot group. This is the first record of solar flare which was observed by human and presently known as the two-ribbon flare. The double Great Aurora of August 28 to September 2 1859 was believed to occur because of a pair of Coronal Mass Ejections (CMEs) was ejected from the Sun on or about August 27 and September 1. The first CME impacted Earth one day later on 28th August and the second faster CME is the Carrington's flare, observed on September 1. The observed Carrington's flare and corresponding occurrence of the Aurora made it clear that the Sun is influencing the Earth in many ways, and the sunspots which are the main drivers for violent flare and CME are mostly responsible for it.

While Scientists were busy to study the interrelation between solar activity with aurora and magnetic storms, some other things also kept on affecting people's daily life. During eighteenth and nineteenth centuries, magnetic compasses were the main high-tech frontier which was used for navigation. But in many places, disturbances of several degrees from 2° to 8° in compass measurement was reported for several hours (Lovering, 1857) making navigation unworkable. During great auroral display of September 2, 1859, the disturbances of the magnetic needle were almost 4° in half an hour. The worst scenario reported for this disturbance in navigation due to magnetic storms was on Sept. 24, 1946. The Los Angeles Times reported that "Brussels, Sept 23 (AP), Budget Minister Joseph Merlot today said: abnormal weather condition and the aurora borealis might have put the instruments out of order on the Sabena airlines plane that crashed near Gander, Newfoundland killing 26 persons". Not only the navigation systems but also the electric telegraphy systems got affected badly due to solar activity at that time. During an Aurora on Nov 17, 1848, Carlo Matteucci, the Director of Telegraphs in Pisa observed an anomalous behavior in telegraph connecting Pisa and Florence. He also noticed that electromagnets remained powered even without the battery attached, and ceased once the aurora dimmed. Solar activity has another impact on humans by disturbing radio communications. To communicate from one part with the other part of the Earth, a radio wave must be reflected from the ionosphere. During the solar flare, radio



Fig. 1.1 Aurora visible on 6th March, 2017 from Iceland. Picture Courtesy: Sigurdur William Brynjarsson

transmissions are disrupted by changes in the ionosphere layers due to x ray emissions from the flare. Other impacts on radio communications happen due to high energy protons coming from the Sun. It causes ionization of ionosphere layers, and signals ranging from approximately 3MHz through 40 MHz get attenuated by the absorption process creating blackouts of High Frequency (HF) and Very High Frequency (VHF) radio communications. Another direct effect of violent behavior of the Sun is on electrical power grids. The most famous outage occurred in Quebec on March 13, 1989, where a complete electrical blackout happened affecting 3 million people. Satellites are also getting affected by the solar X-ray and flare heating. There is a clear correlation between the sunspot cycle and the number of de-orbited satellites in Low-Earth orbit (Odenwald et al., 2005). Satellite anomalies were also reported when violent solar flare occurred in the Sun (e.g, Telstar-1, Anik E1 and E2, GOES-7, TDRS-1). Apart from affecting the man-made technologies, solar activity affects the Earth's climate as well. The total ultraviolet radiation coming from the Sun varies with the solar cycle which changes the Earth's temperature (Shindell et al., 1999) and during 1645-1725, there were no sunspots in the Sun, which is assumed to be responsible for the little ice age in Europe and North America (Eddy, 1976). Although, there are studies showing that other factors (e.g., volcanic eruptions,

internal climate variability) are also responsible for the little ice age along with the solar activity (Owens et al., 2017).

Therefore, the Sun has a profound impact on human life and their activity on the Earth. As time goes on, we are becoming more and more dependent on technology. Hence more vulnerable to solar activity. So to control technological damages, electrical blackouts, satellite anomalies and long term effect on the Earth's climate, we need to understand the violent explosions of the Sun. Solar flares, Coronal mass ejections, solar wind and high energy particles coming from the Sun are mostly responsible for affecting our Earth, and it is found that these phenomena are happening above the sunspot regions. When the Sun has lots of sunspots on its surface, it becomes more violent and becomes quiet, when there are fewer sunspots. That's why, we see a strong correlation between the sunspots number with the aurora frequency, magnetic storms, no. of satellites de-orbited and satellites anomalies. In order to understand thoroughly, how the Sun is going to affect our Earth, a study is necessary to understand when why and how sunspots are forming on the Sun's surface and how do they evolve.

Sunspots are the regions of highly concentrated magnetic fields of the Sun. After Heinrich Schwabe discovered that sunspot numbers wax and wane with a period of roughly 10 years, researchers started thinking the reason behind it. In 1908, George Ellery Hale first discovered the magnetic field in the sunspots (Hale, 1909) and it became very clear that the sunspots cycles are nothing but the magnetic cycle of the Sun. Just like our Sun, other stars also have starspots activity cycle (Noyes et al., 1984). After 100 years of discovery of magnetic fields in sunspots, we are able to understand many things about the sunspots and its cycle, but still many things about the Sun and sunspots remain unknown and we keep on wondering about them.

1.1 History of sunspot observations

As we already mentioned in the previous section that sunspots are the regions of strong concentrated magnetic fields in the photosphere of the Sun, they appear as very tiny dark blemishes in the solar disc. The size of the sunspots are also very small, and it is difficult to observe by the naked eye. But some of the sunspots are large enough or many sunspots can appear in a group, allowing them to be observed in the naked eye with suitable viewing conditions, where the Sun can be partially obscured by cloud or fog or thick mist or during sunrise and sunset time. The first naked eye observations of sunspots were made by Chinese in 800 BC. During that time, astronomers at the court of the Chinese and Korean emperors made regular notes of sunspots because of their possible astrological significance (Stephenson, 1990). After that in the pre-telescopic era, sunspots observations were recorded by many

others starting with Theophrastus (374–287 B.C.). But first sunspot drawing was found in the Chronicles of John of Worcester from a sighting on Saturday, 8 December 1128. Before the discovery of the telescope, there was confusion whether these sunspots are part of the Sun or some planets which are blocking the light to reach the Earth. In 1610, Galileo first observed the sunspots using his newly discovered telescope and it was found that the sunspots were associated with the Sun itself. 230 years after the telescopic discovery of the sunspots, it was Heinrich Schwabe, an amateur astronomer who recorded the sunspots for the period 1826 to 1843 and pointed out that sunspots follow a period of roughly 10 years between maxima in their number. In between telescopic discovery of sunspots and discovery of its cycle, the Sun has gone through a prolonged minimum where no sunspots were seen from 1645 to 1715. In 1887 and 1889, German astronomer Gustav Spörer published two papers showing a remarkable 70 years interruption in the ordinary course of the solar cycle. While studying the latitudinal distribution of sunspots, Spörer had found evidence that the numbers of spots in the northern and southern hemisphere of the Sun were not always balanced, and to check this observation he consulted historical records of sunspots from 17th and early 18th century, and discovered 70 years of interruption in sunspots number. After Spörer died, E. W. Maunder took the responsibility to investigate more about Spörer findings. In 1894, he pointed out in his article entitled “Prolonged Sunspot Minimum” providing more details and acknowledging Spörer findings that the sunspots were really not seen in that period (1645-1715) and it may happen in the Sun again (Eddy, 1976).

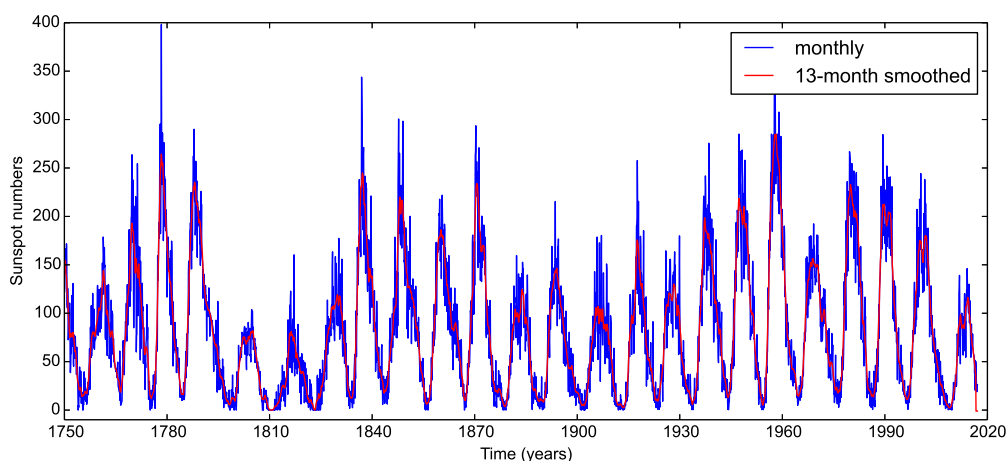


Fig. 1.2 Monthly sunspot numbers are plotted in blue lines with time from SIDC database. Yearly smoothed monthly sunspots numbers are over plotted with red line

After Schwabe’s discovery of solar cycle, Rudolf Wolf, director of the Observatory at Bern and later at Zurich, organized a number of European observatories to record sunspots on regular

basis and by a standard scheme. Wolf defined the relative sunspot number as

$$r = k(f + 10g) \quad (1.1)$$

where f is the number of individual spots including those distinguishable within groups on the Sun, g is the number of sunspots group and k is a correction factor which varies from one observer to another. Of course for Wolf's own observation k is used as 1. This procedure is still used for sunspot number calculations and this relative sunspot number is known as Wolf's sunspot number. After defining the Wolf's sunspot number and inaugurating an international effort which still continues today, Wolf started reconstructing the sunspot number from historical data and successfully reconstructed the data of sunspot number as far as the the 1755–1766 cycle, which conventionally known as cycle 1. According to this convention, we are in the declining phase of cycle 24 today (7th March, 2017). Rudolf Wolf's novel effort and initiative to make a universal method of sunspot monitoring helped a lot to better understand the behavior of sunspots with time. In Fig 1.2, the entirely revised historical sunspot number series is shown from SIDC (Clette et al., 2014). Recently a century long sunspot area data acquired from persistent observation at the Kodaikanal observatory in India are also available (Mandal et al., 2017a). Apart from the sunspot numbers and sunspot area, a number of other indices are now available to measure solar activity. They include various plage indices and the 10.7 cm solar radio flux (Hathaway, 2010). The latter have advantage particularly because they can be recorded for any type of weather conditions, but they are only available for last 5 cycles from 1946 (see chapter 3).

1.2 Magnetic properties of Sunspots and Solar Cycle

In 1908, George Ellery Hale observed a splitting in sunspot spectral line and by measuring Zeeman splitting in the observed spectral line, he estimated the value of magnetic field in the sunspots is approximately 3000 G (Hale, 1909). This discovery accelerated the understanding of the sunspots and solar cycle. It was understood then that the solar cycle is nothing but the magnetic cycle of the Sun and the magnetic field is continuously generated inside the Sun by some mechanism to maintain its activity cycle. About a decade after this ground breaking discovery, George Ellery Hale and his collaborators made another extremely important discovery. They found that sunspots are often seen side by side with opposite polarity i.e. the sunspots are bipolar in nature. The magnetic polarity of sunspots are also completely opposite in the two hemispheres (Hale et al., 1919) and these polarities in the two hemispheres also change with the solar cycle giving magnetic cycle period twice of the period of sunspot cycle.

This is known as the Hale's polarity law. In the very same paper (Hale et al., 1919), it was shown that the line joining of the two poles of bipolar sunspots always had an inclination with the East-West line of the Sun with the leading polarity sunspots are closer to the equator and following polarity sunspots are away from the equator. This inclination angle also known as tilt angle is found to vary linearly with latitudes. As latitudes increase, the tilt angles also increase from 3° near equator to 11° at 30° latitude. This latitudinal dependence of tilt angle is known as Joy's law, and as we will see in latter chapters, it has a huge implication in solar dynamo theory. There is also an interesting fact about the latitudinal distribution of sunspots. In the beginning of the cycle, they mostly come in higher latitudes (30° to 40°) and as cycle progresses, they are drifted more and more towards lower latitudes. This latitudinal drift of sunspots was first noticed by Richard Carrington during 1853-1861 which was known as Spörer's law and Edward Maunder in 1904, published the time latitude plot of sunspots for two cycles starting from 1877 to 1902 which is now known as the butterfly diagram.

Hale's pioneering work about the measurement of magnetic field in sunspots galvanized interest about the measurement of the weak diffuse general magnetic fields on the surface of the Sun. The spectroheliograph designed by George Ellery Hale was able to measure the magnetic field about 2-3 kilo Gauss value i.e. mainly the magnetic field in the sunspots. But to measure the very weak diffuse magnetic field, a more-precise instrument was necessary which could

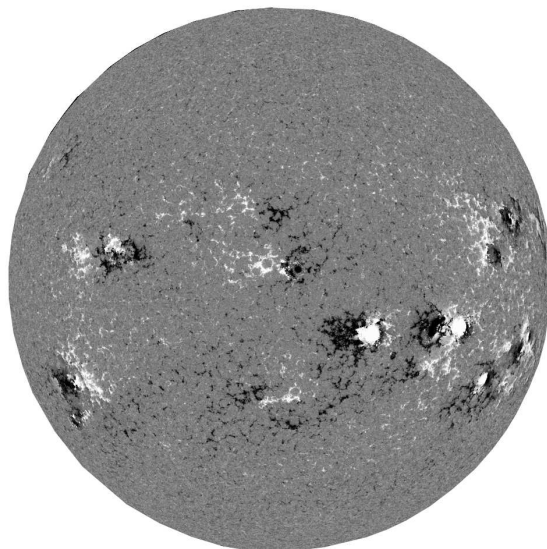


Fig. 1.3 Solar Magnetogram was taken on 7th July, 2014 by HMI on board SDO during solar maxima. The black color represents the magnetic fields which are directed towards us and white color represent the magnetic field away from us. Grey color is used for diffuse field in the solar photosphere

detect very tiny line shift in the Fraunhofer line. For example, a typical sunspot field (2-3 kG) would give the line displacement about is 0.1\AA which is easily detectable but for magnetic field of 1 Gauss, line displacement for Fraunhofer line is approximately $8 \times 10^{-5} \text{\AA}$ which was extremely difficult to detect (Babcock, 1953). However, in the early 1950s, H.D Babcock and H. W Babcock, a father son collaboration successfully designed a magnetogram which could readily measure very tiny line shift corresponding the weak general fields of the Sun having a value of 1-20 Gauss. This was also a remarkable invention. With this magnetogram, they were able to measure definite poloidal field on the surface of the Sun. They found a weak positive field in the north polar cap ($\theta > 55^\circ$) and a weak negative field in the southern polar cap (Babcock & Babcock, 1955) giving an antisymmetric dipolar structure of the Sun's magnetic fields. The reversal of polar fields also found during the sunspot maxima suggesting a strong correlation between poloidal field and the sunspots cycle.

In Fig. 1.3, a magnetogram is shown from HMI of onboard SDO during solar maxima on 7th of July 2014. In both of the hemispheres near low latitude, sunspots fields are shown in white and black colors. Black represents the positive polarity sunspots and white represents the negative polarity sunspots. If we make a time-latitude plot by taking an azimuthal average of magnetic fields as shown in magnetogram, it gives us the butterfly diagram as shown in Fig. 1.4. A careful scrutiny of full solar disc magnetogram shows us some very small fibril type of structures throughout the solar disc apart from the large black and white spots near the equator. These small structures come due to small scale magnetic fields which mostly lie in the granular and supergranular boundaries. The large scale structures or the large scale magnetic fields are believed to be generated by a hydromagnetic dynamo inside the solar convection zone, whereas the small scale magnetic fields are generated due to the interaction of convection with the turbulent motion in the photosphere (Cattaneo, 1999). The equatorward migration of sunspot fields are very clear from the Figure 1.4 along with the fields from the following polarity migrating towards the pole. These poleward migrating fields are very important because while migrating towards the pole, they reverse the existing polar field from the previous cycle. These photospheric features are the only key to understand what is happening inside the solar convection zone. A successful theoretical model should be able to explain all the characteristic of the butterfly diagram. In the next section (Section 1.3), we describe theoretical background to understand the generation mechanism of magnetic field in the Sun.

Let's discuss some properties of the solar cycle now. The average period of the solar cycle is 11 years but a solar cycle period can vary from minimum 9 years to maximum 14 years. The amplitude of the solar cycle is also not same for each cycle (see Fig 1.2). The peak amplitudes of sunspot numbers vary from cycle to cycle. The weak cycle has less number of sunspots and the strong cycle has more number of sunspots. This irregular behavior of the solar cycle makes

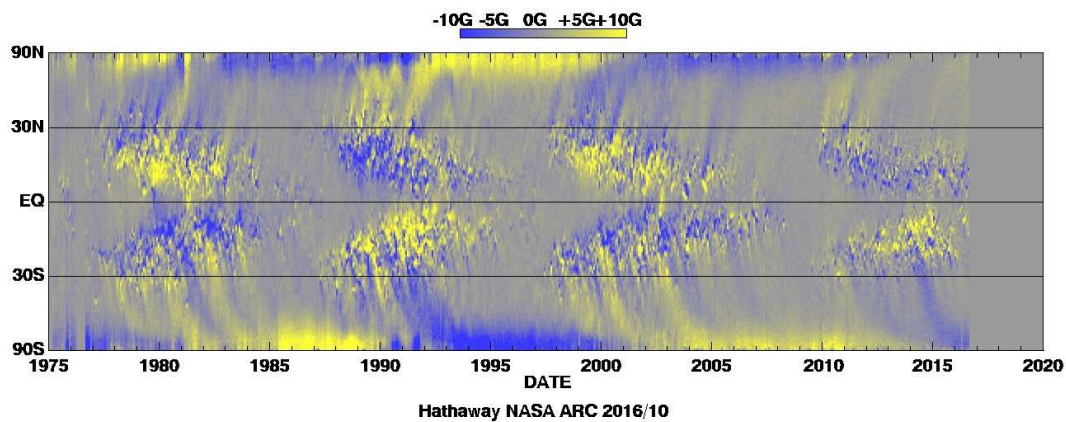


Fig. 1.4 Time latitude plot of radial fields as observed on the surface of the Sun. Courtesy: David Hathaway

it very difficult and interesting to predict the next cycle maximum. There are mainly two widely used methods to predict the amplitude of the next cycle. First, the precursor method, where the information about some of the cycle characteristics is studied in a cycle to predict the amplitude of the following cycle (Petrovay, 2010). Another method relies on the more physical ground. They are mostly based on the observationally data driven theoretical predictions (Choudhuri et al., 2007). Among some of the characteristics of the solar cycle, Waldmeier effect is very famous and important one (Wolf & Brunner, 1935). As we see in Fig 1.2 that the solar cycles are mostly asymmetric in nature. They take 3-4 years to reach its maxima after minimum and take 7-8 years to decay from maxima to its next minimum. In 1935, Waldmeier first noticed an anticorrelation between rise time of the cycle and its maxima. The stronger cycle takes less time to reach its maxima after the minimum and vice versa. While this correlation (rise time vs cycle maxima) is not robust in all of the solar activity indices (e.g., sunspot area), though see Mandal et al. (2017a), the rise rate, and cycle maxima has a very good strong correlation. The theoretical explanation for these correlations is given in Karak & Choudhuri (2011) based on flux transport dynamo theory. Although the rise time of the cycle shows a good correlation with its maxima, decay time shows exactly no correlation with its maxima or even with the next cycle maxima, rather decay rate of the cycle has a good correlation with its maxima and with next cycle maxima (Hazra et al., 2015). The detail description of correlations of the decay rate with the maxima of the same cycle and next cycle and their theoretical explanation are given in chapter 3.

1.3 Theoretical Background

While various facts about sunspots and solar cycle were being dug out by the observations, some theoretical models were necessary to understand them. Two very important discipline of physics ‘Magnetohydrodynamics’ and ‘Magnetoconvection’ were concurrently being developed which explained many of these observational features of magnetic fields of the Sun.

1.3.1 Basic equations of Magnetohydrodynamics

Magnetohydrodynamics is a discipline of physics which studies the motion of plasma in presence of magnetic field. As we know that the systems where the length scale is larger than the Debye length and time scale much larger than the inverse of plasma frequency, the charge separation can be neglected and we can apply MHD approximation there, provided the plasma velocities are non-relativistic. It is basically one fluid approximation of plasma in presence of magnetic fields. The plasma motions in the Sun are non-relativistic and slowly varying under the mechanical and magnetic forces making a perfect place to apply MHD approximations. The velocity fields and magnetic fields are governed by the following coupled equations:

$$\frac{\partial \mathbf{v}}{\partial t} + (\mathbf{v} \cdot \nabla) \mathbf{v} = \mathbf{F} - \frac{1}{\rho} \nabla p + \frac{1}{\rho c} \mathbf{j} \times \mathbf{B} + \nu \nabla^2 \mathbf{v} \quad (1.2)$$

$$\frac{\partial \mathbf{B}}{\partial t} = \nabla \times (\mathbf{v} \times \mathbf{B}) + \eta \nabla^2 \mathbf{B} \quad (1.3)$$

The Equation 1.2 is the magnetic Navier-Stokes equation similar to what we get in hydrodynamic case but only differs by the presence of magnetic force. The equation 1.3 is a whole new equation known as induction equation which determines the behavior of the magnetic field in presence of velocity fields and in arriving this equation, the scalar form of Ohm’s law is used. All the transport coefficients (e.g., viscosity and magnetic diffusivity) in the equations 1.2 and 1.3, are assumed to be scalar and constant in space. But in the complex realistic astrophysical scenario those are mostly tensor with spatial dependence, and easy to include those complex terms in equations 1.2 and 1.3. The RHS of the equation 1.2 includes the body force (\mathbf{F}), the pressure force, the magnetic force and the viscous force. For non-relativistic plasma, we can write $\nabla \times \mathbf{B} = \frac{4\pi}{c} \mathbf{j}$ and magnetic force term becomes $\frac{1}{4\pi\rho} (\nabla \times \mathbf{B}) \times \mathbf{B}$. After rearranging the magnetic force term, the new velocity equation can be written as:

$$\frac{\partial \mathbf{v}}{\partial t} + (\mathbf{v} \cdot \nabla) \mathbf{v} = \mathbf{F} - \frac{1}{\rho} \nabla \left(p + \frac{B^2}{8\pi} \right) + \frac{(\mathbf{B} \cdot \nabla) \mathbf{B}}{4\pi\rho} + \nu \nabla^2 \mathbf{v} \quad (1.4)$$

It is very clear from equation 1.4 that the magnetic force gives rise of magnetic pressure $\frac{B^2}{8\pi}$, and a magnetic tension $(\mathbf{B} \cdot \nabla)\mathbf{B}$ along the magnetic field lines. The magnetic pressure has a huge importance in the dynamics of flux tube as we see in the next subsection 1.3.2.

The generation and evolution of magnetic field are carried out by the induction equation (Equation 1.3) due to electrically conducting fluid motions. The RHS of induction equation has two terms and both of them have very important significance. First term, $\nabla \times (\mathbf{v} \times \mathbf{B})$ is mainly responsible for generation of the magnetic field (source term) and the second term $\eta \nabla^2 \mathbf{B}$ helps to decay the field (decay term). It is similar to an electrical system where varying current gives rise to the magnetic field and magnetic field decays due ohmic dissipation of current. But instead of the current, the plasma motions are doing the job here. The ratio of these two terms (1st term to 2nd term) is known as magnetic Reynolds number $R_m = \frac{LV}{\eta}$, where L and V represents the typical length scale and velocity, and η is magnetic diffusivity of the system. The value of R_m determines the relative importance of these two terms. For astrophysical systems, the R_m is very high and the first term dominates over the second term. Hence, For $R_m \gg 1$ the induction equation can be written as:

$$\frac{\partial \mathbf{B}}{\partial t} = \nabla \times (\mathbf{v} \times \mathbf{B}) \quad (1.5)$$

This equation has very important consequences for the astrophysical dynamo. It was Hannes Olof Gösta Alfvén, a pioneer in the study of the astrophysical magnetic fields who first pointed out that for astrophysical systems with high R_m value, magnetic field is almost frozen in the plasma and moves with the plasma flows. Mathematically,

$$\frac{d}{dt} \int_S \mathbf{B} \cdot d\mathbf{S} = 0.$$

This theorem is known as Alfvén's theorem of flux freezing and has a huge implication in the study of the astrophysical dynamo as well as in solar dynamo. For this contribution in the MHD, he was awarded Nobel prize in 1970. Therefore to study a system, more specifically to study the magnetic field generation process self consistently in a system due to plasma motion inside it, we need to solve the MHD Equations 1.2 and 1.3 along with an appropriate equation of state, energy equation and the equation of continuity.

1.3.2 Magnetoconvection

Magnetoconvection studies interaction of magnetic field with the thermal convection. The study of magnetoconvection was started after the discovery of strong magnetic field in the sunspots and realizing that the sunspots are relatively cooler than its surroundings. The study

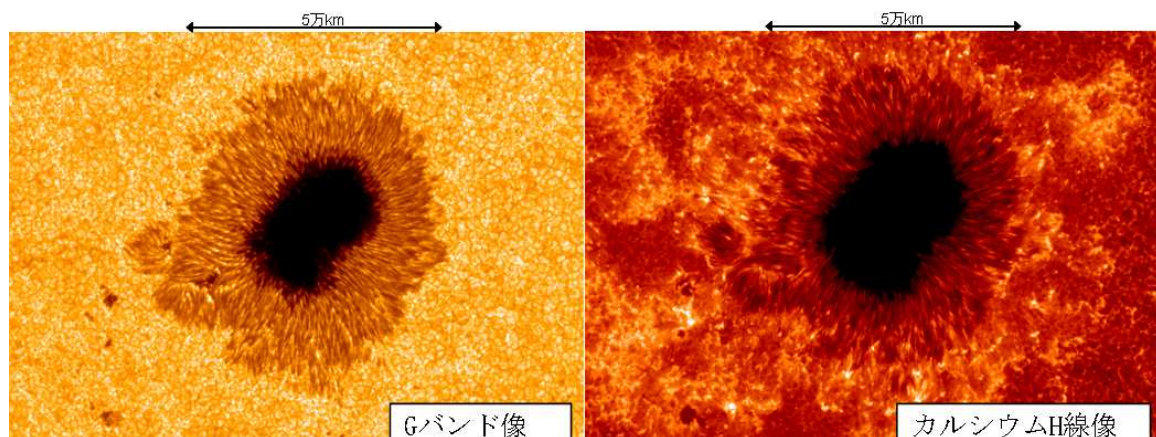


Fig. 1.5 Sunspot images are shown from Solar Optical Telescope, Hinode. The left panel is the photospheric image of the sunspot taken in the wavelength of the G band (430 nm). The chromospheric images in calcium H (396 nm) line is shown in right panel. The scales are shown with a black arrow have a length of 50000 km. Courtesy: Hinode website

of Magnetoconvection is almost on the same footing as the thermal convection. But the MHD equations are perturbed here instead of perturbing hydrodynamic equations (as done in Rayleigh-Benard convection) in order to find the conditions for which the magnetofluid becomes unstable for convection. No doubt, this stability analysis is much more complicated than the case without magnetic fields. The calculations of Rayleigh-Benard convection in presence of magnetic field was first carried out by [Thompson \(1951\)](#) and [Chandrasekhar \(1952\)](#). From their analysis, it was confirmed that the presence of magnetic field suppresses the convection or in other words, strong magnetic fields make magnetofluid more stable against convection. The physical reason behind this is the magnetic tension. As convection starts distorting the magnetic field lines, convective motions are opposed by the magnetic tension. Therefore, a steeper temperature gradient is necessary to drive the convection in presence of strong magnetic field.

The perturbative analysis can give us the condition for convection to start. But detail understanding about the nature of magnetoconvection needs rigorous simulation using all nonlinear equations with the parameters above the critical parameters for the onset of convection. The sunspots structure and surroundings granular structure as shown in Figure 1.5 provide a very good environment to study magnetoconvection. Also, it is found from the solar magnetogram study ([Solanki, 2002](#)) that the magnetic field is vertical at the center of the spot and becomes increasingly inclined towards the periphery of it. The convective flows are inhibited by the magnetic tension and make it cooler than its surroundings. The small scale structures i.e., the cellular patterns surrounding the sunspots are known as the supergranular and granular structure (left panel of Fig 1.5). These small scale structures are confined in the photosphere and not

visible in the chromospheric image (right panel of Fig 1.5). As magnetic tension opposes the convection, in supergranules and granules also, there is a partitioning of space in between magnetic field and convection. The dark lines in around the cells are the small inter-granular size magnetic field elements, where the convection is suppressed. For detail simulation of sunspots using magnetoconvection, see [Rempel & Schlichenmaier \(2011\)](#).

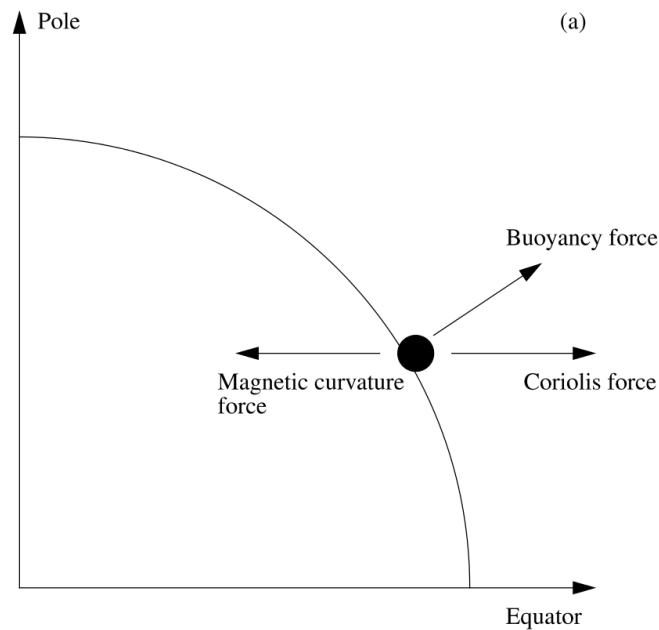


Fig. 1.6 Schematic diagram based on [Schüssler & Rempel \(2002\)](#) from [Fan \(2009\)](#) showing various forces acting on an isolated toroidal flux ring at the base of solar convection zone

1.3.3 Flux tube dynamics and field amplification

Probing the magnetic field inside the solar convection zone is an extremely difficult task and still, it is not possible with available modern resources. The observed east west orientation of the sunspots and Hale's polarity law of sunspots (Section 1.2), make it very clear that the subsurface fields are well organized, coherent and in the azimuthal direction. This well-organized nature of solar active regions also confirms that the magnetic fields are not disrupted by the abrupt convective motions inside the solar convection zone, so they must be very strong at least same order of magnitude or more than the equipartition value (10^4 G) of the convective motions. Another very important behavior of magnetic flux is they appear as intense intermittent elements in the flux-free, or nearly flux-free plasma. As the plasma inside solar convection zone is very highly conducting, magnetic fields are almost frozen in plasma which helps to develop this flux

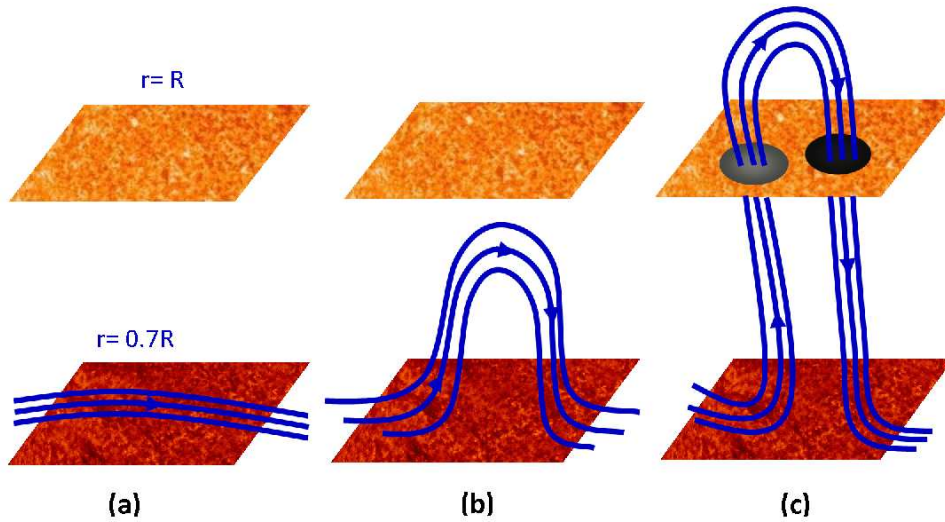


Fig. 1.7 Buoyant rise of a flux tube from the bottom of the convection zone to the surface. (a) Nearly horizontal flux tube under the solar surface near base of the convection zone. (b) Flux tube after its upper part rises through the convection zone and (c) The flux tube emerges above the solar surface and creates Bipolar sunspots.

tube like structure (Cattaneo et al., 2006). Let us consider an isolated flux tube in the solar convection zone as shown in Figure 1.6. Different forces acting on it have also been shown. As we see from the Figure 1.6 that the magnetic curvature force is balancing the Coriolis force, and the buoyancy force is the only deciding factor whether the flux tube is in equilibrium or going to rise. If the pressure inside the flux tube is p_i and the pressure in the outside ambient medium is p_e , then we can write,

$$p_e = p_i + \frac{B^2}{8\pi} \quad (1.6)$$

where $\frac{B^2}{8\pi}$ is the magnetic pressure exerted by the magnetic fields inside the flux tube. It is evident from Equation 1.6 that $p_i \leq p_e$, which often but not always implies that the density ρ_i inside the flux tube is less than the density ρ_e outside the flux tube. When this happens to a part of a flux tube, it becomes buoyant and rises up against gravitational field. A buoyant flux tube near the bottom of the solar convection zone is shown in the figure 1.7(a). As we see in figure 1.7(a), the whole flux tube may not be magnetically buoyant but some part of it becomes very light compared to its surroundings (For details see Choudhuri (1998); Fan (2009)) and rises up to the surface against the gravity (figure 1.7(b)) and creates bipolar sunspots as shown in Figure 1.7(c).

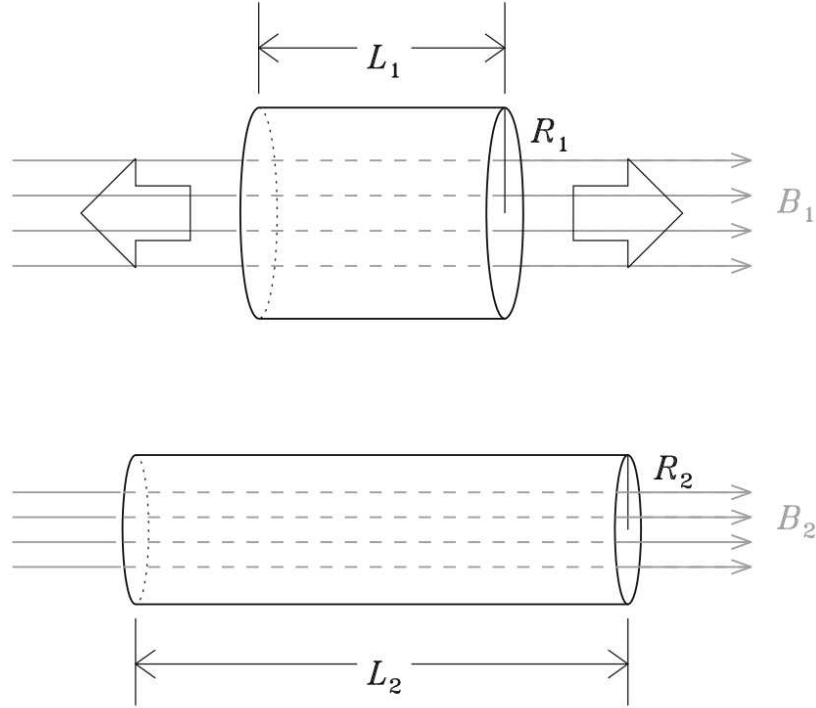


Fig. 1.8 Schematic diagram for amplification of magnetic field. Upper panel shows the magnetic field B_1 is frozen inside a cylindrical plasma motion of radius R_1 and length L_1 . The lower panel shows the configuration after the plasma motion are compressed in the perpendicular direction of the plasma motions. L_2 , R_2 and B_2 are the length, radius, and magnetic field strength after the stretching.

Direct implication of Alfvén's flux freezing theorem is found in flux amplification i.e. the growth of the magnetic field because of inductive effect of plasma flow \mathbf{v} . The induction equation (Eq. 1.5) with high R_m for incompressible flow ($\nabla \cdot \mathbf{v} = 0$) can be rewritten as

$$\left(\frac{\partial}{\partial t} + \mathbf{v} \cdot \nabla \right) \mathbf{B} = \mathbf{B} \cdot \nabla \mathbf{v} \quad (1.7)$$

The LHS is the Lagrangian time variation of magnetic field where the field is moving with the flow and RHS represents the field amplification due to local shear of the flow ($\mathbf{B} \cdot \nabla \mathbf{v}$).

Let us consider a very simplistic scenario to understand the field amplification as shown in Fig. 1.8 (Charbonneau, 2013). An uniform magnetic field (B_1) is frozen in cylindrical incompressible plasma flow of length L_1 . Now if plasma flow undergoes some stretching motion along its central axis such that length of the cylindrical plasma flow increases to L_2 ,

then from mass conservation we have,

$$\frac{R_2}{R_1} = \sqrt{\frac{L_1}{L_2}} \quad (1.8)$$

Now as the flux ($\pi R^2 B$) is also conserved inside the system, so that leads to,

$$\frac{B_2}{B_1} = \left(\frac{R_1}{R_2}\right)^2 = \frac{L_2}{L_1} \quad (1.9)$$

Here B_2 is the magnetic field after the cylindrical flow is stretched. As the flow is stretched, it also amplifies the magnetic field, and the amplification of field strength is directly proportional to the level of stretching (Equation 1.9). In this case, two things are very crucial to amplify the fields. One, the magnetic fields must be frozen in the plasma (high R_m regime), and second, the stretching motion along the tube axis must be accompanied by a squeezing fluid motion perpendicular to the axis in order to satisfy the mass conservation. Since the horizontal fluid motions are in same direction as the magnetic field, so it can not induct any magnetic field in the system according Equation 1.7. It is the perpendicular compressing fluid motion which is actually responsible for amplification of the field.

As mentioned above, stretching of a flux tube can amplify the magnetic field but it has to fulfill certain conditions and can be done with proper flows. Also, the magnetic flux remains constant in field amplification by stretching. But there is another kind of flow motion which can amplify the magnetic field and magnetic flux both. It is the shearing of the flow. The field amplification by sheared flow is very robust and it does not require any proper direction of flow motion for the field to amplify like stretching case. This field amplification by sheared flow is very common in astrophysical objects and we will describe it in details, in Section 1.4.

1.3.4 Helioseismology

In standard Astrophysics, the structure of the stars can be understood by the models of stellar structures and evolutions. These models are computed based on the assumed physical conditions in stellar interiors, including thermodynamical properties, the interaction between radiation and matter and the nuclear reaction that powers the stars. Whereas these models and observations relevant to the stellar interiors provide limited constraints on the detailed properties of the stars, Helioseismology and Asteroseismology provide a greater window to study the solar and stellar interiors by detecting waves on the surface of the Sun and stars. Helioseismology is a relatively new field, and it studies the oscillations of acoustic modes for the entire Sun which are trapped just below the photosphere.

In the 1960s, [Leighton et al. \(1962\)](#) discovered the oscillation on the surface of the Sun by analyzing series of dopplergram obtained at the Mount Wilson Observatory. They found two type of oscillation in the velocity field: large-scale horizontal cellular motion which is known as supergranulation and vertical quasi-periodic oscillations with a period of 5 min. In that time, these 5-minute oscillations were interpreted as local phenomena in the solar atmosphere but later, it was realized that these are the modes of acoustic oscillation in the Sun ([Christensen-Dalsgaard, 2002](#); [Kosovichev, 2011](#)). In presence of rotation and magnetic field, the frequencies of the mode of oscillations can be written as:

$$\nu_{n,l,m} = \nu_{n,l} + \sum_j c_j^{n,l} P_j^{n,l}(m) \quad (1.10)$$

Here $\nu_{l,m}$ is the mean frequency, $c_j^{n,l}$ are the splitting coefficients and $P_j^{n,l}(m)$ are the orthogonal polynomials set of degree j in m . In case, the Sun is spherically symmetric the frequency of the mode of oscillation would be equal to mean frequency which is determined by the horizontally averaged structure of the Sun. But the presence of rotation and magnetic field put the Sun away from spherical symmetry and lift up the degeneracy of frequencies in m . Since forces due to rotation and magnetic field are much smaller than pressure and gravity forces, they can be treated as small perturbation over the spherically symmetric structure and can be determined by the splitting coefficients $c_j^{n,l}$ as the departure from the spherical symmetry ([Antia, 2005](#)). From various ground based (GONG, BiSON) and space based (MDI, HMI) instruments, the mean frequency has been determined with high accuracy. Depending upon the frequency and degree, the acoustic modes are classified. The $n = 0$ modes are referred as the fundamental or f-mode (for large value of l , they are mainly surface gravity waves), $n > 0$ modes are p-modes or pressure modes (pressure gradients are the main restoring force) and $n < 0$ are the gravity modes of g-modes (reliable observation of this mode is still not found). The p modes are trapped in the different region of the solar interior depending upon the frequency and degree, and they are the very good probe for the internal structure of the Sun. As temperature inside the Sun increases, the speed of the sound wave traveling towards the center also increases and its path is successively bent, such that it is refracted back to the Sun's surface. The acoustic wave encounters a steep drop in density at the surface and reflect back inwards. The point from where they refracted back to the Sun's surface defines the critical layer and above it, the wave mode is trapped. Critical layer depends on the angle of inclination, and the angle of inclination of the surface with the radial direction is decided by the horizontal wavelength or the degree l . The modes with smaller l can penetrate deeper layers before they reflected outwards, whereas modes with larger l are trapped mostly nearly below the surface layers. $l = 0$ modes can penetrate to the center of the Sun. Hence, the p-mode analysis is a good tracer for studying

the internal structure of the Sun. Though the analysis of global mode frequencies of the Sun provides an unprecedented opportunity to study the interior of the Sun, this has some limitation. Especially it studies the longitudinal average of internal structures. So, to study more localized inferences, we need to have various local helioseismic analysis. It includes ring analysis and time-distance helioseismology (Thompson, 2004).

Helioseismological findings of solar rotation and meridional flow helped a lot to understand and model the solar magnetic field generation process and the solar cycle. Measuring the splitting of acoustic eigen modes of same n & l but m values of opposite sign as mentioned in Equation 1.10, the differential rotation profile of the Sun is estimated (Schou et al., 1998; Thompson et al., 1996). Furthermore, beside the existence of differential rotation throughout the solar convection zone, helioseismology finds that the rotation rate does not depend on the latitudes below the convection zone and hence it rotates almost like a solid body there. This transition region where differential rotation changes to solid body rotation is known as the tachocline (Spiegel & Zahn, 1992). This tachocline has huge importance in the solar dynamo and the toroidal field is mainly generated in this transition region due to differential rotation (Choudhuri et al., 1995). Since we have helioseismic data for almost two decades, the temporal variation of solar rotation rate is also studied by the helioseismology. It is found that the frequency splitting of acoustic eigenmodes (same n, l but m values of opposite sign) varies with time, and interestingly correlated with solar activity cycle. This is known as the solar torsional oscillation which has significant importance for the study of solar dynamo theory (Antia & Basu, 2000; Chakraborty et al., 2009; Zhao & Kosovichev, 2004).

The helioseismic measurements for the meridional flow are also available. The properties of the meridional flow near the surface are well established which is poleward and has speed around 20.0 m s^{-1} (Basu & Antia, 2000; Zhao & Kosovichev, 2004). Going deeper inside solar convection zone introduces lots of systematic noise in helioseismic data and it is extremely difficult to measure amplitude and direction of meridional flow there. Efforts have been made to measure the meridional flow in deeper interior by several groups and they have reported different results (Jackiewicz et al., 2015a; Rajaguru & Antia, 2015; Schad et al., 2013; Zhao et al., 2013). Please note that in most of the dynamo models, a single cell profile of meridional flow is assumed which has a poleward flow as observed and an equatorward return flow near the bottom of the convection zone. This equatorward propagation of meridional flow lacks observational support. Figure 1.9 is taken from Zhao et al. (2013) and Rajaguru & Antia (2015). Figure 1.9(a) and (b) show the meridional flow as inferred from analysis of HMI data by Zhao et al. (2013). It shows that meridional flow has an equatorward return flow at the depth $0.82R_{\odot} - 0.91R_{\odot}$ and then followed by a poleward flow up to depth $0.77R_{\odot}$. With the same data set and using time-distance helioseismology, Rajaguru & Antia (2015)

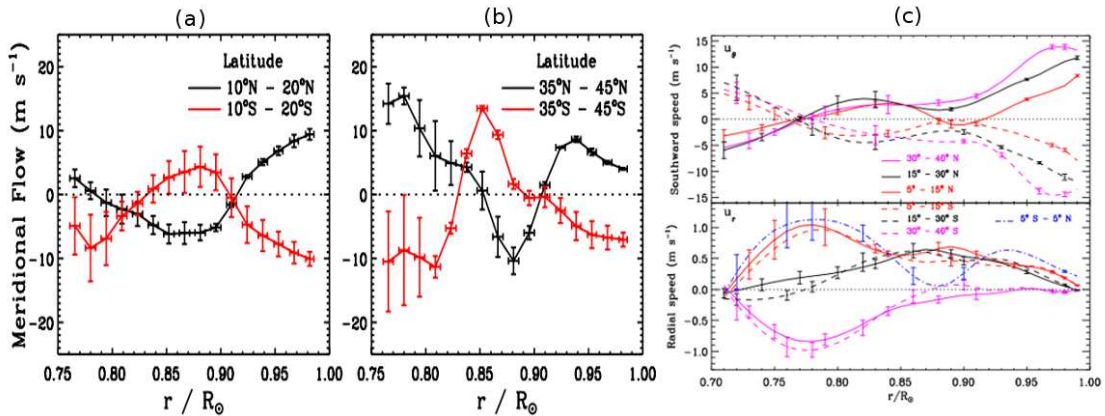


Fig. 1.9 Helioseismological measurement of meridional flow in deep interior of the Sun. (a) and (b) are taken from [Zhao et al. \(2013\)](#) and show the meridional flow variation with radius of the sun at different latitudes. (c) Meridional flow are shown inside the solar convection zone, as found by [Rajaguru & Antia \(2015\)](#). [Rajaguru & Antia \(2015\)](#) uses same techniques and same HMI data as [Zhao et al. \(2013\)](#) but constraints by mass conservations.

showed that an equatorward flow must exist below $0.77R_{\odot}$. Though latter have considered the mass conservations. Interestingly [Jackiewicz et al. \(2015a\)](#); [Schad et al. \(2013\)](#) have reported different results about meridional flow than [Rajaguru & Antia \(2015\)](#); [Zhao et al. \(2013\)](#). [Schad et al. \(2013\)](#) from their global helioseismic inversion got multi cell meridional circulation in solar convection zone whereas, [Jackiewicz et al. \(2015a\)](#) found a shallow meridional circulation. Numerical simulation of solar convection, whether hydrodynamical or magnetohydrodynamical, all predict multicell meridional flow profiles at Rossby numbers comparable to the Sun ([Miesch & Toomre, 2009](#)). In respect to the above scenario, it is extremely difficult to say what is the exact profile of meridional circulation our Sun has in its convection zone. Since meridional flow is very important for solar dynamo to operate, we have considered different profile of meridional circulation in order to see its effect on dynamo (see Chapter 4) and we find that the equatorward propagation is very important for dynamo to work (Though see Section 4.6 in Chapter 4). The time variation of meridional flow is also found from the Helioseismology ([Chou & Dai, 2001](#)). It is found that the meridional flow slows down during the solar maxima and becomes faster during the solar minima. A theoretical explanation for this variation of meridional circulation with the solar cycle is given in Chapter 5.

1.4 Dynamo Theory

The goal of dynamo theory is to understand, how do astronomical objects sustain their magnetic field against resistive decay or ohmic dissipation. For most of the astrophysical objects, the timescale for ohmic decay is very large, and once a field is generated inside the system that remains there for a longer time even if there is no mechanism to sustain it. For example, typical time scale for decay of magnetic field in Earth, Sun and a typical galaxy in presence of no plasma motions in the interior of them are 3×10^5 , 10^{11} and 3×10^{23} years respectively (Choudhuri, 1998). Certainly, the Earth's magnetic field still exists longer than its decay time and for galaxies, in spite of being larger decay than age of the universe, various effects like differential rotation can wind up and displace the magnetic field, unless some mechanism is there to prevent it. But for the Sun the story is different. The Sun has a magnetic cycle with 11 years periodicity representing oscillatory nature of magnetic field (Section 1.2). Hence to sustain oscillatory nature of solar magnetic field, some mechanism is needed irrespective of its large decay time scale. Therefore, all astrophysical magnetic fields have to be continuously generated by the dynamo process, and in this thesis, we are interested in understanding the ongoing dynamo mechanism inside the Sun much more realistically, which regulates its 11 years periodic solar cycle.

As pointed out in the Section 1.3.1 that our Sun follows the MHD approximations of plasma, and how the plasma flow and magnetic field would behave in the Sun can be understood by solving the MHD Equations (1.2 and 1.3) along with proper transport coefficients and equations of state. There are two approaches to understand the solar dynamo problem. First, the kinematic approach and Second, fully dynamical calculations. In kinematic approach, the velocity field is considered to be given and can be incorporated without any understanding about underlying dynamics. This approach has significant practical advantages. The dynamo equations becomes linear in \mathbf{B} and easy to solve. In fully dynamical calculations, the velocity fields are calculated by solving full set of MHD equations (Eqs. 1.2 and 1.3) with energy equation and a proper equation of state which includes back reaction of magnetic fields on the flows via Lorentz force. But these nonlinear MHD equations (1.2 and 1.3) are extremely difficult to solve self-consistently in the solar context, and need huge computation power. Unlike direct numerical simulations where large scale flows like differential rotation and meridional circulation have to come from the basic MHD equations self consistently, in kinematic approach we can invoke these large scale flows in the induction equation directly from helioseismology. That is why it is relatively easy to make a realistic solar dynamo model based on kinematic approach.

In a seminal paper, Parker (1955a) gave a qualitative idea of turbulent dynamo theory. The solar magnetic field can be decomposed into two components, the toroidal component or the azimuthal component of the magnetic field, B_ϕ and the poloidal component of the field (B_p).

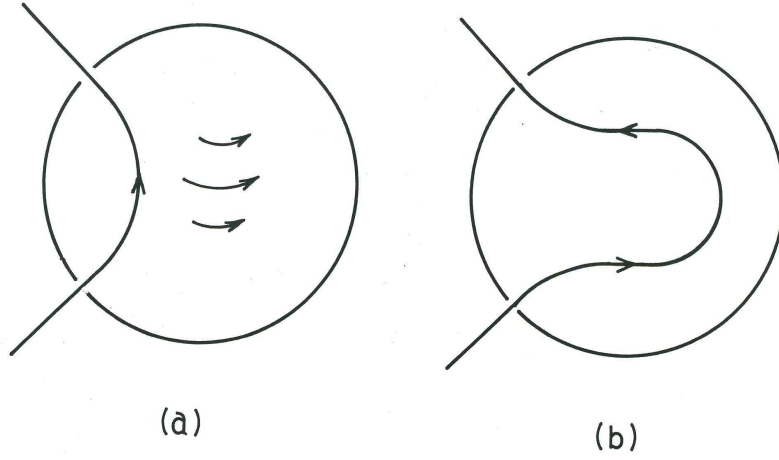


Fig. 1.10 Generation of toroidal field from the poloidal field by differential rotation, Image credit: [Choudhuri \(1998\)](#)

Hence total magnetic field can be written as

$$\mathbf{B} = B_\phi(r, \theta, t)\mathbf{e}_\phi + \mathbf{B}_p(r, \theta, t) = B_\phi(r, \theta, t)\mathbf{e}_\phi + \nabla \times [A(r, \theta, t)\mathbf{e}_\phi] \quad (1.11)$$

Where, A is the magnetic vector potential. Parker suggested that there is continuous exchange of energy between toroidal component and poloidal component of magnetic field which makes solar magnetic field oscillatory. This exchange of energy between toroidal part and poloidal part is possible by the following mechanisms:

Ω effect:

The Sun rotates differentially. Its equator rotates faster than its pole. If we have a field line in the meridional ($r - \theta$) plane of the Sun, i.e. the poloidal field line, then because of shearing by differential rotation, the poloidal field line will be twisted in the equator region as shown in Figure 1.10. Assuming the poloidal field line and differential rotation follow the same rotation axis, the flow profile can be taken as $\mathbf{v}(r, \theta) = r \sin \theta \Omega \mathbf{e}_\phi$. Invoking the magnetic field \mathbf{B} , the divergenceless flow \mathbf{v} and neglecting the magnetic diffusion, the induction Equation 1.7 can be written as:

$$\frac{\partial A}{\partial t} = 0 \quad (1.12)$$

$$\frac{\partial B}{\partial t} = r \sin \theta [\nabla \times A \mathbf{e}_\phi] \cdot \nabla \Omega \quad (1.13)$$

Now as A is constant over time (in reality this is not the case because of magnetic diffusion), integrating Equation 1.13 gives us

$$B(r, \theta, t) = B(r, \theta, 0) + (r \sin \theta [\nabla \times A \hat{\mathbf{e}}_\phi] \cdot \nabla \Omega) t \quad (1.14)$$

So, the toroidal component of magnetic field grows linearly in time and is proportional to the net local shear and the strength of the poloidal field. In the case of magnetic diffusion plays a role, the poloidal field will decay and toroidal field generation eventually stops unless there is a supply of poloidal field by some other means. Here, another important thing to note is, if the rotation profile is constant across the poloidal surface, the toroidal field generation stops (Ferraro's theorem). In the case of the Sun, the profile of the differential rotation is well mapped from helioseismology and the fact that toroidal field is generated by the Ω -effect is well established. Thus, if we have dipolar magnetic field like our Sun with a poloidal component as shown in Fig 1.10(a), then toroidal field generated via Ω -effect would have opposite sense of polarity in the two hemispheres which eventually leads to the opposite bipolar sunspots in the two hemispheres.

Turbulent α effect:

The generation of the toroidal field by differential rotation depends on the strength of the poloidal field, but due to finite magnetic diffusivity of the Sun, the poloidal field decays and eventually, the generation of toroidal field would stop. To sustain the toroidal magnetic field, we need to have some mechanism which will generate the poloidal magnetic field in the Sun. Parker (1955a) gave the crucial idea of how poloidal magnetic field can be generated in the Sun. Solar convection zone is highly turbulent. While toroidal field rises through the solar convection zone due to magnetic buoyancy, Coriolis force introduces a helical twist to the rising plasma blobs. As magnetic field is frozen in the plasma, toroidal field lines are twisted because of helical turbulence. This twisting of plasma blobs are happening in the rotating frame of reference, so the vorticity in the two hemispheres will be in opposite sense and the helical twist will be opposite sense. But the toroidal field in the two hemispheres is in opposite sense which makes the magnetic loops have the same sense in two hemispheres. Since there is turbulent diffusion in the solar convection zone, it smooths out the small loops and generated a large scale poloidal field. In this way, poloidal field can be generated from the toroidal field via helical turbulence. This procedure is known as classical α effect of helical turbulence. So, the stretching of the poloidal field by differential rotation generates the toroidal field and helical turbulence twists the toroidal field to generate poloidal field. Hence the poloidal and toroidal field can sustain each other through a cyclic feedback process and sustain the solar dynamo.

After a decade later, [Steenbeck et al. \(1966\)](#) first formulated a rigorous and systematic mathematical approach of Parker's turbulent dynamo theory. Since turbulence plays an important role in the turbulent dynamo, they have developed a scheme to handle turbulence which is known as mean field magnetohydrodynamics. They have used the ensemble approach to deal with the statistical properties of turbulence of the system. The velocity and magnetic field in a turbulent system can be written as summation of mean component and fluctuating component.

$$\mathbf{B} = \bar{\mathbf{B}} + \mathbf{B}', \mathbf{v} = \bar{\mathbf{v}} + \mathbf{v}' \quad (1.15)$$

Where the bar and the prime represent mean and fluctuating quantities respectively. Invoking Equation 1.15 in the induction equation 1.3 and taking an ensemble average, we can write:

$$\frac{\partial \bar{\mathbf{B}}}{\partial t} = \nabla \times (\bar{\mathbf{v}} \times \bar{\mathbf{B}}) + \nabla \times \boldsymbol{\varepsilon} + \eta \nabla^2 \bar{\mathbf{B}} \quad (1.16)$$

Here, η is the molecular diffusivity constant in space and $\boldsymbol{\varepsilon}$ is the mean field emf which is defined as

$$\boldsymbol{\varepsilon} = \overline{\mathbf{v}' \times \mathbf{B}'} \quad (1.17)$$

The beauty of the mean field theory is the build up of the mean emf ($\boldsymbol{\varepsilon}$) from the fluctuating part of the turbulent flows and magnetic fields which sustains the the dynamo against the Cowling's Anti-dynamo theorem ([Cowling, 1933](#)). Cowling Anti-dynamo theorem says that the axisymmetric magnetic field can not be sustained by axisymmetric flows. But Cowling's theorem does not hold for the mean field theory because of this extra mean emf in ensemble average equation 1.16. Hence we are able to get axisymmetric dynamo solution by solving mean field equation. For isotropic and homogeneous turbulence, the mean emf can be calculated in terms of mean quantity using the first order smoothing approximation (see [Choudhuri \(1998\)](#) for details) as given below

$$\boldsymbol{\varepsilon} = \alpha \bar{\mathbf{B}} - \eta_t \nabla \times \bar{\mathbf{B}} \quad (1.18)$$

Where $\alpha = -\frac{1}{3} \overline{\mathbf{v}' \cdot (\nabla \times \mathbf{v}')}$, and $\eta_t = \frac{1}{3} \overline{\mathbf{v}' \cdot \mathbf{v}'}$ and τ being the correlation time of the turbulence. Putting 1.18 in Equation 1.16 finally we get,

$$\frac{\partial \bar{\mathbf{B}}}{\partial t} = \nabla \times (\bar{\mathbf{v}} \times \bar{\mathbf{B}}) + \nabla \times (\alpha \bar{\mathbf{B}}) + (\eta + \eta_t) \nabla^2 \bar{\mathbf{B}} \quad (1.19)$$

Since the turbulent diffusivity is much larger than molecular diffusivity, we usually neglect the molecular diffusivity in solving mean field equation. Here the turbulent diffusivity is assumed to be constant in space also but for the solar convection zone, it has strong radial dependencies which simply allow some more terms to enter in Eq. 1.19. It is also found that the α parameter

correctly depicts the role of helical turbulence of plasma which generates the poloidal field from the toroidal field. Please note that, in case of inhomogeneous flow field, there will be other terms in the emf ε (Eq. 1.18) and Yokoi et al. (2016) showed that they might be important for dynamo in some of the systems like red dwarf stars.

After developing the mathematical formalism of mean field dynamo theory, Steenbeck & Krause (1969) solved the mean field Equation 1.19 for the Sun. They solved it in spherical geometry with realistic boundary conditions assuming the angular rotation of the Sun as a given quantity $\mathbf{v}(r, \theta) = \Omega r \sin \theta \hat{\mathbf{e}}_\phi$ and were able to get solar like butterfly diagram. This was the first reproduction of observed butterfly diagram from theoretical and numerical analysis (Steenbeck & Krause, 1969). While solving the mean field equation, it is found that the propagation of dynamo wave depends on the combination of helical turbulence and differential rotation $\alpha \frac{\partial \Omega}{\partial r}$. In northern hemisphere, if $\alpha \frac{\partial \Omega}{\partial r} < 0$ then dynamo wave propagates towards equator and if $\alpha \frac{\partial \Omega}{\partial r} > 0$ dynamo wave propagates towards pole. This is known as the Parker-Yoshimura sign rule (Parker, 1975; Yoshimura, 1975).

In the 1990s, thin flux tube simulations of flux emergence showed that the strength of magnetic field in the solar convection zone should be around $\sim 10^5$ G in order to match with the observed tilt angle variation of sunspots on the surface (Caligari et al., 1995; Choudhuri & Gilman, 1987; D'Silva & Choudhuri, 1993; Fan et al., 1993). This high strength of magnetic field in the convection zone is one order of magnitude higher than the equipartition value of convection (Parker, 1979), and it is difficult for helical turbulence to impart a sufficient twist on this strong rising toroidal flux tube and generate the poloidal field. Eventually, another school of thought which was developed in the 1960s by Babcock (1961) and Leighton (1969) was invoked as a possible candidate for the poloidal field generation from the toroidal field which is known as Babcock-Leighton Mechanism (see next section for details). In spite of being a potential mechanism for poloidal field generation, invoking this method in dynamo was having some issues. Based on the observed tilt angle variation, it is found that the Babcock-Leighton α is positive in the northern hemisphere and negative in the southern hemisphere. Also the radial shear $\frac{\partial \Omega}{\partial r}$ is positive at low latitude and negative at high latitude in both the hemispheres, as found by helioseismology (Schou et al., 1998). So, According to Parker-Yoshimura sign rule, we would expect a poleward propagating branch of dynamo wave at low latitudes and an equatorward branch at high latitudes which contradict the observations. On the other hand, the toroidal field is generated throughout the convection zone by differential rotation, but the magnetic buoyancy destabilizes the storage of magnetic field inside convection zone and it is understood that the shear layer between radiative zone and convection zone i.e. tachocline is the place where toroidal field can be amplified and stored (Moreno-Insertis et al., 1992). Hence dynamo is confined in two spatially segregated region of the solar convection zone coupled by

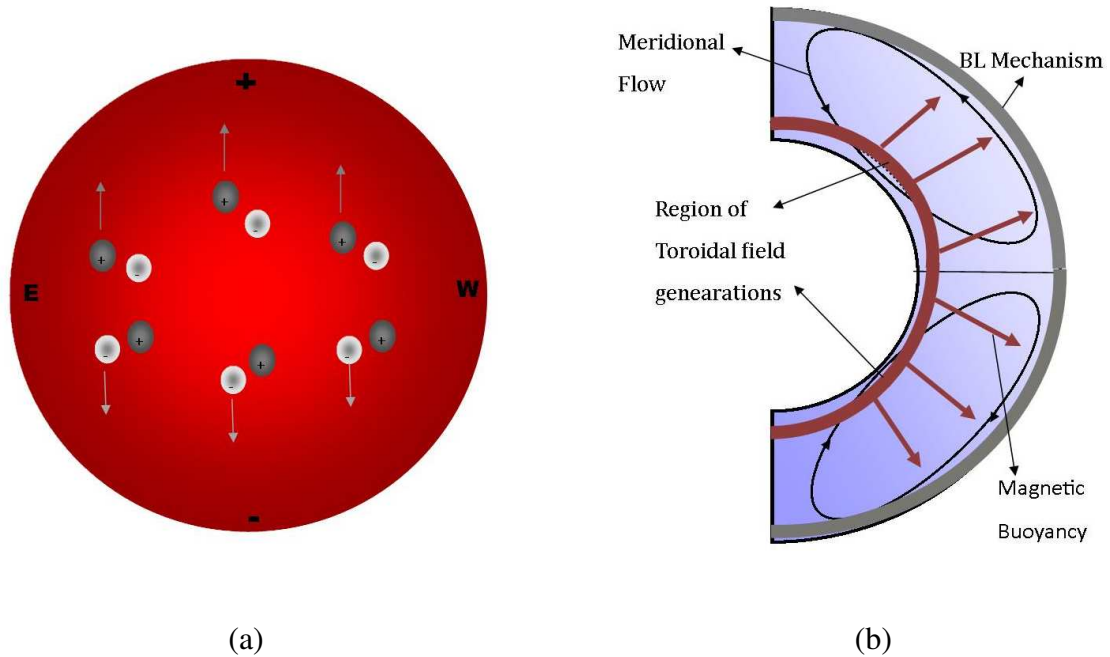


Fig. 1.11 (a) A schematic diagram of Babcock-Leighton mechanism on the surface of the Sun. The leading polarity sunspots closed to equator are shown in white (black) in the northern (southern) hemisphere and trailing polarity sunspots are shown in black (white) in northern (southern) hemisphere. (b) A cartoon diagram explaining flux transport dynamo model

diffusion. Wang et al. (1991) were the first to include a meridional circulation having a poleward flow on the surface and an equatorward return flow in the dynamo model which connects these two spatially separated region of the Sun and explained the equatorward migration of sunspots. Choudhuri et al. (1995) and Durney (1995) have further developed the idea of Wang et al. (1991) and made a numerical model with the single cell meridional circulation. With these calculations, it is found that the equatorward flow of meridional circulation near the base of the convection zone indeed helps dynamo wave to overcome poleward propagation (Parker-Yoshimura sign rule) and migrate sunspots eruptions towards equator. The dynamo model which includes Babcock-Leighton mechanism for poloidal field generation and where meridional circulation plays a key role is known as Flux Transport Dynamo model. In the next section, we discuss this model in detail.

1.5 Flux Transport Dynamo Model

In the rest of the chapters of this thesis, we will be dealing with the different aspects of the Flux Transport Dynamo model to understand solar magnetic field generation process, and properties

of the solar cycle more carefully with much more details. As we already mentioned, this type of models are basically successor of the axisymmetric mean field dynamo models, kinematic, and include Babcock-Leighton Mechanism as a poloidal field generation mechanism instead of helical turbulence. Apart from the differential rotation of the Sun and turbulent diffusion, a plasma flow in the meridional plane ($r - \theta$ plane) known as meridional circulation plays an important role in these models. The main ideas of these models are as follows. The poloidal field is stretched by the differential rotation and generates the toroidal magnetic field. The toroidal field is then amplified and stored near the base of the convection zone at tachocline (reddish brown region of the Figure 1.11(b)). When the toroidal field becomes buoyant, it rises through the solar convection zone (as shown by the reddish brown arrow in the Figure 1.11(b)) and creates the bipolar sunspots on the surface. While traveling through the convection zone, Coriolis force acts on the rising flux tube and produces a tilt between the bipolar sunspots with respect to the east west direction of the Sun. As these sunspots are the regions of strong magnetic field, they diffuse away and leading polarity sunspots (white in northern and black in southern hemisphere) move towards the equator from both the hemisphere and cancel each other as shown in Figure 1.11(a). Whereas the trailing polarity sunspots (black in northern and white in southern) are advected towards pole by meridional circulation and generate a large scale poloidal field. This is known as Babcock-Leighton (BL) process. The poloidal field then can be advected to the base of the convection zone by meridional circulation where differential rotation can again act on it to generate toroidal field. Hence the cycle goes on and solar magnetic field sustains its oscillatory behavior. This main idea of flux transport dynamo model is depicted in the cartoon diagram 1.11(b) where the reddish brown colors show the toroidal field generation region and reddish brown arrows show the magnetic buoyancy. The BL mechanism is shown in grey region on the surface and meridional circulation connecting two spatially segregated region is shown in black streamline. The basic equations of these models are

$$\frac{\partial A}{\partial t} + \frac{1}{s}(\mathbf{v} \cdot \nabla)(sA) = \eta_p \left(\nabla^2 - \frac{1}{s^2} \right) A + S(r, \theta, t), \quad (1.20)$$

$$\frac{\partial B}{\partial t} + \frac{1}{r} \left[\frac{\partial}{\partial r}(rv_r B) + \frac{\partial}{\partial \theta}(v_\theta B) \right] = \eta_t \left(\nabla^2 - \frac{1}{s^2} \right) B + s(\mathbf{B}_p \cdot \nabla)\Omega + \frac{1}{r} \frac{d\eta_t}{dr} \frac{\partial(rB)}{\partial r} \quad (1.21)$$

where \mathbf{A} is the magnetic vector potential corresponding to the poloidal field, B is the toroidal component of magnetic field (Equation 1.11) and $s = r \sin \theta$. η_t and η_p are the diffusion coefficients corresponding to poloidal and toroidal magnetic field respectively. Ω is the differential rotation, and v_r and v_θ are the components of meridional circulation. $S(r, \theta)$ is the source term which takes care for the magnetic buoyancy and Babcock-Leighton mechanism.

We solve Eq. 1.20 and 1.21 in a meridional plane in the range of $0.55R_{\odot} < r < R_{\odot}$ in radius and $0 < \theta < \pi$ in co-latitudes with the following boundary conditions.

At the poles ($\theta = 0, \pi$) we use, $A = 0$, and $B = 0$. In the bottom ($r = R_b$), we assumed a perfectly conducting solar core and for that we use $A = 0$, $B = 0$. At the surface ($r = R_{\odot}$), the toroidal field is assumed to be zero ($B = 0$), and poloidal field has to match with potential fields smoothly satisfying the free space equation.

$$\left(\nabla^2 - \frac{1}{r^2 \sin^2 \theta} \right) A = 0 \quad (1.22)$$

Since we have taken the bottom boundary much below the penetration depth of meridional circulation, the solutions do not depend on the bottom boundary conditions too much as shown by Chatterjee et al. (2004). From last two decades, these models are successful in explaining various observational properties of solar cycle which include equatorward migration of sunspots, 11 years period, irregular properties of solar cycle (Maunder minima, Waldmeier effect) and much more. It turns out that these models can also predict the future solar cycle by assimilating the polar field data during each minima of the cycle (Choudhuri et al., 2007). In spite of its success, sometime doubts have been expressed whether these models are realistic or all the explanation are merely accidental. To answer this question, we need to check whether all the assumptions and approximations which are made in these models are correct.

1.5.1 Mean Flows

Mean flows i.e. the differential rotation and meridional circulation are the basic building blocks of the flux transport dynamo model. Differential rotation is mainly responsible for toroidal field generation and meridional circulation helps to migrate sunspots towards equator overcoming the Parker-Yoshimura sign rule and advects field from the surface to the bottom for low diffusion case. The helioseismology probes the differential rotation inside solar convection zone nicely (Schou et al., 1998; Thompson et al., 1996) keeping no space to doubt on this. The surface meridional circulation is well observed and measured by various techniques but the equatorward return flow still lacks observational supports. Recently, there are observational evidences that the return flow can exist in the middle of the convection zone giving double cell meridional circulation or even multi-cell meridional circulation in the solar convection zone. In Chapter 4, we explain it in details and show that our dynamo model works perfectly fine provided there is an equatorward return flow near the bottom of the convection zone.

An analytical profile has been used in our model to incorporate the differential rotation which fit nicely with the helioseismology results (Dikpati & Charbonneau, 1999). The near surface shear layer (Corbard & Thompson, 2002) has not been considered in our model because

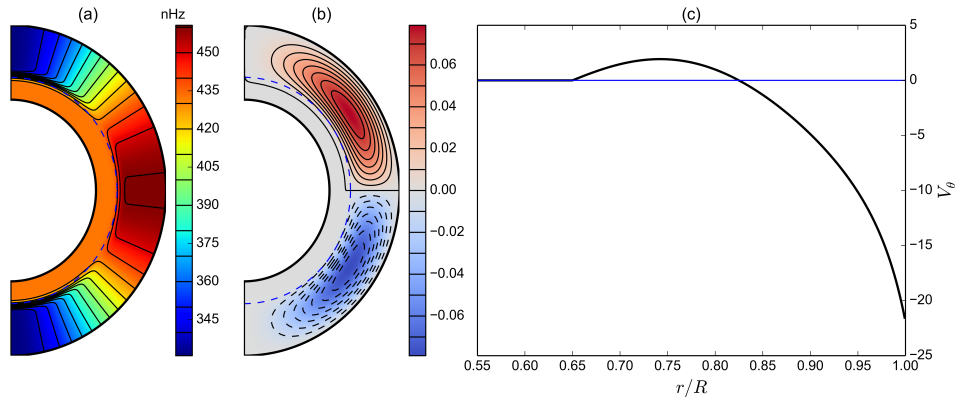


Fig. 1.12 (a) Differential Rotation, (b) Streamlines of the meridional Circulation. Solid contours with red filled colors show an anti-clockwise flow. Dashed contours with blue colors show clock-wise flow, and (c) θ component of Meridional flow at 45° latitude is plotted with radius of the Sun.

as studied by [Dikpati et al. \(2002\)](#), it does not have any effect on the flux transport dynamo. Magnetic field can be generated near the surface shear layer but can not be stored due to disruption by magnetic buoyancy. In Figure 1.12(a) we have shown the differential rotation profile used in our model. The streamlines for single cell meridional circulation is shown in Figure 1.12(b). Motivated by observations, we have assumed a poleward flow near the surface and an equatorward flow at the bottom of the convection zone. Though latter one has no observational evidence, we take it because of mass conservations. In Figure 1.12(c), we have plotted the meridional circulation with radius at mid-latitude $45^\circ N$. The detail parameterization how we can get the meridional profile as shown in Fig 1.12(b) is given in Chapter 4.

Our dynamo models are kinematic in nature and we do not consider the effect of back reaction due to Lorentz force on the large scale flows. But there are observational evidences that the zonal flows and meridional flows do vary with the solar cycle ([Basu & Antia, 2000](#); [Chou & Dai, 2001](#); [Hathaway & Rightmire, 2010](#); [Komm et al., 2015](#)). Whereas there is theoretical explanation considering the back reaction due to Lorentz force for the variation of zonal flows with the solar cycle known as torsional oscillation ([Chakraborty et al., 2009](#); [Durney, 2000](#)), the theoretical explanation why meridional flow varies with the solar cycle is still very primitive. [Rempel \(2006\)](#) considered a full mean-field model of both the dynamo and the large scale flows, and explain both the torsional oscillation and variation of meridional flow with the solar cycle. But they lack details explanation for the latter. In Chapter 5 we have developed a theoretical model to explain the variation of meridional flow with the solar cycle in detail considering the back-reaction due to Lorentz force.

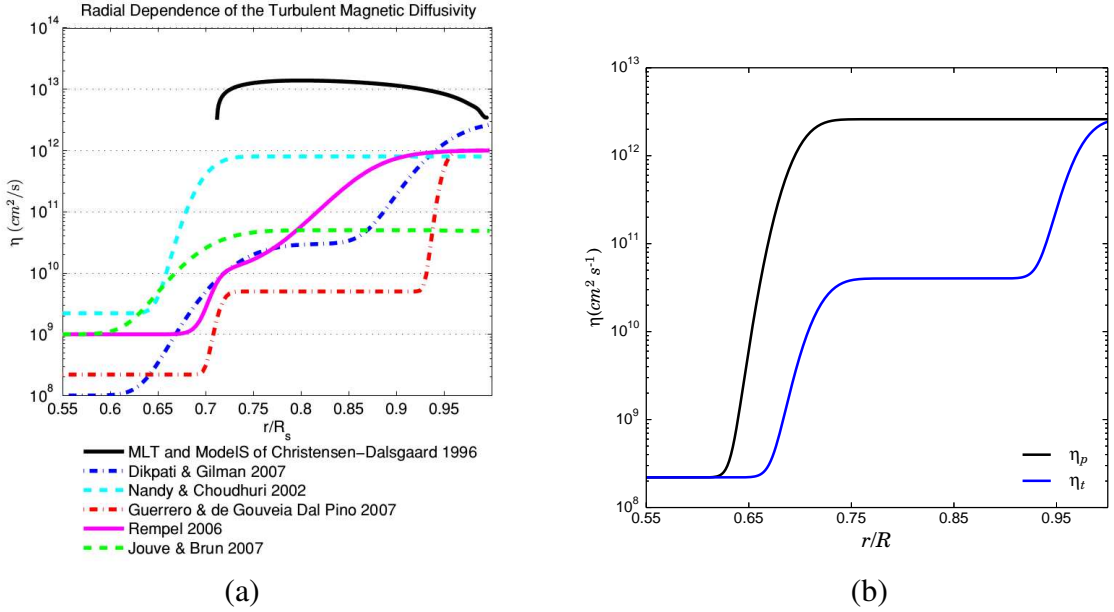


Fig. 1.13 (a) Different radial dependency of diffusivity profile used in various flux transport dynamo models (b) The diffusivity profile which we use in our flux transport model

1.5.2 Turbulent Diffusion

Turbulent diffusivity is a very important parameter in the flux transport dynamo model, and it is one of the important ingredients to transport magnetic field in between two spatially segregated regions where dynamo works. But, it is poorly constrained inside the solar convection zone. From the mean field theory, assuming first order smoothing approximation, the diffusivity can be written as (Moffatt, 1978)

$$\eta = \frac{\tau}{3} \langle v^2 \rangle \quad (1.23)$$

Where τ is the eddy correlation time and v is the turbulent velocity field. Using Mixing Length Theory (MLT) of turbulent convection and the standard SolarModelS (Christensen-Dalsgaard et al., 1996) we can estimate the order of magnitude of the turbulent diffusivity. According to these models, the turbulent diffusivity can be expressed in terms of mixing-length parameter α_p , the convective velocity v for different radii, and the pressure scale height H_p , and η becomes

$$\eta = \frac{1}{3} \alpha_p H_p v \quad (1.24)$$

The estimated turbulent diffusivity from Mixing Length Theory is shown by solid black lines in Fig 1.13(a). The diffusivity profile used by the different group of flux transport dynamo models are also shown in Fig 1.13(a) by different colors. As it is clear from the figure that, flux transport models use almost two orders of magnitude lesser value of turbulent diffusivity and

almost different radial profiles. This deviation leads to the fact that the dynamo model can not operate under the high diffusivity as suggested by the MLT. One possible solution for this is that these dynamo models are kinematic, and can not take into account the strong back reaction due to Lorentz force on the velocity fields which results in the suppression of turbulence, and hence quenches the turbulent diffusivity (Muñoz-Jaramillo et al., 2011). Though various diffusivity profiles are used in flux transport dynamo models, they qualitatively give solar like solutions. But of course, the different values of diffusivity in the bulk of the convection zone lead to different memory which leads to the different prediction of solar cycle (Yeates et al., 2008) and different results in explaining irregular properties of the solar cycle (e.g, Waldmeier Effect) (Karak & Choudhuri, 2011). In order to explain various observational results including dipolar parity (Chatterjee et al., 2004; Hotta & Yokoyama, 2010), lack of hemispheric asymmetry (Chatterjee & Choudhuri, 2006; Goel & Choudhuri, 2009), the correlation between the polar field at cycle minimum with the strength of next cycle (Jiang et al., 2007), and the Waldmeier effect (Karak & Choudhuri, 2011), a higher value of diffusivity is required, and we use higher value of diffusivity in most of our calculations using flux transport dynamo model as shown in Fig 1.13(b). Choosing higher diffusivity profile makes our model so called diffusion dominated model (Yeates et al., 2008). Since the toroidal field is much stronger than the poloidal field, we expect the quenching would be different for both of the components and use different diffusivity profile for both of them. Though for our 3D flux transport dynamo model, we use a two-step diffusivity profile (see Chapter 6 for details). Hence it is evident that, although the theory of turbulent diffusion is not well understood but different profiles used in flux transport dynamo do not invalidate the model and give qualitatively good results in agreement with observations.

1.5.3 Magnetic Buoyancy

Magnetic buoyancy is an important physical process in flux transport dynamo which governs the rise of toroidal flux tube from the bottom of the convection zone to the surface (see section 1.3.2). It is inherently a 3D process but in 2D axisymmetric dynamo model, we can treat them rather using some very crude approximations. Magnetic buoyancy has been treated using various method in the flux transport dynamo. The various methods about treatment of magnetic buoyancy are given in Chapter 2 in detail. We have explained that the proper treatment of magnetic buoyancy is an important issue in order to understand the irregular features (e.g., Waldmeier effect) of the solar cycle but the properties of solar cycle are qualitatively same in most of the magnetic buoyancy treatment. A proper realistic treatment of magnetic buoyancy needs a 3D model. Yeates & Muñoz-Jaramillo (2013) first developed this kind of 3D model where the buoyant rise of flux tube has been treated by simultaneously applying a radially outward velocity and a vortical velocity to a localized part of an azimuthal flux tube at the

bottom of the convection zone. We have also developed a 3D dynamo model where the magnetic buoyancy has been treated using a SpotMaker algorithm (Chapter 6). Whereas Yeates & Muñoz-Jaramillo (2013) have captured the physics of the early rise of the flux tube, Our 3D model captures the later phase of rising flux tubes more realistically.

1.5.4 Babcock-Leighton Mechanism

Although poloidal field generation from the decay of sunspots is proposed in the 1960s (Babcock, 1961; Leighton, 1969) and invoked as a poloidal field generation process to complete dynamo loop in the 1990s (after realizing that turbulent α effect is not able to generate poloidal field from the strong toroidal field at the convection zone due to helical turbulence), the observational supports is established rather recently (Dasi-Espuig et al., 2010a; Kitchatinov & Olemskoy, 2011a). Dasi-Espuig et al. (2010a) use sunspot data and tilt angle data from Mound Wilson Observatory and Kodaikanal Observatory for the cycle 15 – 21 and have found a strong correlation ($r = 0.65$ and $r = 0.70$ for Mount Wilson and Kodaikanal data set respectively) between the product of the strength of a cycle with its average tilt angle, and the strength of the next cycle. Basically the product of strength of the cycle with its average tilt angle represents the measure of the poloidal field due to Babcock-Leighton mechanism. If this product is strong, it would give us strong next cycle. Kitchatinov & Olemskoy (2011a) have also calculated the poloidal field from the decay of sunspots considering the tilt angle and sunspot area from Pulkovo Astronomical Observatory, and found a direct correlation between estimated poloidal field, and the A-index of the large-scale field (Makarov & Tlatov, 2000) for the solar minima of the following cycles. These correlations directly support the operation of Babcock-Leighton Mechanism in the Sun.

The Babcock-Leighton mechanism is an inherently 3D process and real depiction of this process in 2D axisymmetric flux transport dynamo model is only possible by very simple and crude approximations. We treat the Babcock-Leighton process using a parameter α in our 2D axisymmetric models.

$$\alpha = \frac{\alpha_0 \cos \theta}{4} \left[1 + \operatorname{erf} \left(\frac{r - r_1}{d_1} \right) \right] \left[1 - \operatorname{erf} \left(\frac{r - r_2}{d_2} \right) \right] \quad (1.25)$$

The parameters which we use are $r_1 = 0.95R_\odot$, $r_2 = R_\odot$, $d_1 = d_2 = 0.025R_\odot$ making sure that the Babcock-Leighton process is confined in the surface layer ($0.95R_\odot < r < R_\odot$). Since Babcock-mechanism is very much dependent on the tilt angle of the sunspots, and the cause of the tilt angle is Coriolis force which has a $\cos \theta$ dependency, we have taken a $\cos \theta$ dependency in our α parameter. In literature, some of the groups use $\cos \theta \sin \theta$ or even $\cos \theta \sin^2 \theta$ in α parameter to suppress the high latitude emergence of the sunspots. Here we should also

mention that we use a α quenching for dynamo saturation. Since the strong toroidal flux tube is less affected by Coriolis force while traveling through the convection zone, it would have a smaller tilt angle than the weaker ones. To incorporate these changes in tilt angle, we use a factor $\left[1 + \left(\frac{B}{B_0}\right)^2\right]^{-1}$ for α quenching. In 3D model, we have used a more sophisticated algorithm to deal with B-L mechanism. To capture B-L process more realistically in 3D, we first calculate the suitable places at the bottom of the convection zone in both longitudes and latitudes where the toroidal flux becomes magnetically buoyant, and put bipolar sunspots at those regions but on the surface, and let them evolve under the diffusion and mean flows, which eventually generate the poloidal field (see chapter 6 for details). The 3D treatment of BL process makes Flux Transport dynamo model much more realistic and in principle, it can capture the build up of polar fields and other observed phenomena in much greater details than before.

One of the advantages of treating B-L process in 3D is given in Chap 7. The original idea of Babcock-Leighton process involved the dispersal and migration of Bipolar sunspots by the supergranular convection motions on the surface which leads to the transport of magnetic field towards the pole and reverse the existing dipole moment. Leighton (1964) suggested that this process can be considered as a simple random walk on the solar surface and approximated it as a diffusion process. The diffusion coefficient calculated by Leighton (1964) considering the correct time of polar field reversal is $770 - 1540 \text{ km}^2 \text{ s}^{-1}$. After that various observational measurements have been done to estimate the value of the diffusion coefficient (for details see Chae et al. (2008); Jiang et al. (2014a); Schrijver et al. (1996a)). Jiang et al. (2014a) summarize the current measured values of diffusion coefficient on the surface (See Section 4.1 of their paper) which ranges from $100 - 600 \text{ km}^2 \text{ s}^{-1}$. Since solar photosphere consists of convective motions spanning different length scale (e.g., granular scale to supergranular scale), the diffusion coefficient has different value for different length scale in accordance with turbulence cascading (Chae et al., 2008). Till now, no Surface Flux Transport model or Flux Transport model has taken into account this spatial dependence of the diffusion coefficient. One of the possible approach to consider a realistic depiction of the surface diffusion would be direct incorporation of the random convective cellular flows in the model. Upton & Hathaway (2014a) have already implemented this in their 2D Surface Flux Transport model. Since incorporating the convective flows granulation and supergranulation in Flux Transport Dynamo models need extreme higher resolution and a 3D treatment, it has not been implemented in 2D axisymmetric Flux Transport dynamo models. We are the first to implement the direct observed convective velocity fields from SOHO MDI data in our 3D model to see how does it affect the overall features of solar magnetic fields. In Chap 7, we show the initial implementation procedure of this observed velocity fields in our model. The results obtained are generally in good agreement

with the observed surface flux evolution and with non-convective models that have a turbulent diffusivity on the order of $3 \times 10^{12} \text{ cm}^2 \text{ s}^{-1}$ ($300 \text{ km}^2 \text{ s}^{-1}$). However, we find that the use of a turbulent diffusivity underestimates the dynamo efficiency, producing weaker mean fields than in the convective models.

“No one ever accepts criticism so cheerfully. Neither the man who utters it nor the man who invites it really means it.”

–R.K. Narayan, *Malgudi Days*

2

The Treatment of Magnetic Buoyancy in Flux Transport Dynamo Models

One important ingredient of flux transport dynamo models is the rise of the toroidal magnetic field through the convection zone due to magnetic buoyancy to produce bipolar sunspots and then the generation of the poloidal magnetic field from these bipolar sunspots due to the Babcock–Leighton mechanism. Over the years, two methods of treating magnetic buoyancy—a local method and a non-local method—have been used widely by different groups in constructing 2D kinematic models of the flux transport dynamo. We review both these methods and conclude that neither of them is fully satisfactory—presumably because magnetic buoyancy is an inherently 3D process. We also point out so far we do not have proper understanding of why sunspot emergence is restricted to rather low latitudes.

2.1 Introduction

From 1990s a type of model has been developed for the solar dynamo known as the flux transport dynamo model ([Choudhuri et al., 1995](#); [Durney, 1995](#); [Wang et al., 1991](#)). At the present time, this model seems to be the most promising and satisfactory model for explaining

different aspects of the solar cycle (Charbonneau, 2014; Choudhuri, 2011b, 2015), although still doubts are sometimes expressed about its validity—especially because of the uncertainty in our knowledge of the meridional circulation which plays a crucial role in this model (see, for example, the Introduction of Hazra et al. (2014)). The flux transport dynamo model basically involves the following three processes. (i) The strong toroidal field is produced by the stretching of the poloidal field by differential rotation in the tachocline. (ii) The toroidal field generated in the tachocline gives rise to active regions due to magnetic buoyancy, and the decay of tilted bipolar active regions produces the poloidal field by the Babcock–Leighton mechanism. (iii) The poloidal field produced by the Babcock–Leighton mechanism is advected by the meridional circulation first to high latitudes and then down to the tachocline, while also diffusing down to the tachocline due to turbulent diffusion.

Most of the calculations of the flux transport dynamo model have been based on axisymmetric 2D kinematic mean field equations. It is completely straightforward to include the process (i) within such a formalism—especially because helioseismology gives us the profile of differential rotation. As far as process (iii) is concerned, there are some uncertainties in the nature of the meridional circulation (Hathaway, 2012b; Rajaguru & Antia, 2015; Schad et al., 2013; Zhao et al., 2013) as well as in the value of turbulent diffusion (Jiang et al., 2007; Yeates et al., 2008). Although early models assumed a simple one-cell form of meridional circulation, there have been some recent calculations with more complicated meridional circulation (Hazra et al., 2014; Jouve & Brun, 2007). However, once we specify the form of the meridional circulation and the turbulent diffusion within the framework of the kinematic model, there is absolutely no uncertainty in the mathematical forms of the terms involved in process (iii). Only in the case of process (ii) involving magnetic buoyancy and the Babcock–Leighton mechanism, there is considerable uncertainty at a fundamental level as to how this process should be included in a 2D kinematic model. Magnetic buoyancy involves the rise of a tilted flux loop through the convection zone and is an inherently 3D process, which can be included in a 2D dynamo model only through rather crude approximation procedures. Over the years, different groups have proposed different procedures for handling the process (ii). While carrying on calculations with the flux transport dynamo model, we have become aware that these different procedures often give significantly different results and we have tried to understand the physical reasons behind these differences. The obvious question is: which one is the most realistic procedure for treating the process (ii)? This is not an easy question to settle. Different procedures have their own strengths and own weaknesses. We have found that the subtleties involved in modeling the process (ii) are not sufficiently appreciated by the scientific community. Probably a fully satisfactory treatment of process (ii) is not possible within the 2D kinematic framework and one has to go beyond 2D. We discuss the different procedures which had been proposed by

different groups and critically examine the aspects of physics which are covered and which are not covered in these different procedures. We do not discuss the physics of magnetic buoyancy and, in that sense, this is not a comprehensive study of the whole topic of magnetic buoyancy, which is a vast subject. We restrict ourselves only to a discussion of how magnetic buoyancy can be included in kinematic dynamo models.

2.2 The basic equations

We assume both the mean magnetic field and the mean velocity field to be axisymmetric in 2D kinematic models. The magnetic field is written as

$$\mathbf{B} = B(r, \theta, t)\mathbf{e}_\phi + \nabla \times [A(r, \theta, t)\mathbf{e}_\phi], \quad (2.1)$$

where $B(r, \theta)$ is the toroidal component and $\mathbf{B}_p = \nabla \times A(r, \theta, t)$ is the poloidal component. We can write the velocity field as $\mathbf{v} + r \sin \theta \Omega(r, \theta)\mathbf{e}_\phi$, where $\Omega(r, \theta)$ is the angular velocity in the interior of the Sun and \mathbf{v} is the velocity of meridional circulation having components in r and θ directions. Then the main equations telling us how the poloidal and the toroidal fields evolve with time are

$$\frac{\partial A}{\partial t} + \frac{1}{s}(\mathbf{v} \cdot \nabla)(sA) = \lambda_T \left(\nabla^2 - \frac{1}{s^2} \right) A + S(r, \theta, t), \quad (2.2)$$

$$\frac{\partial B}{\partial t} + \frac{1}{r} \left[\frac{\partial}{\partial r}(rv_r B) + \frac{\partial}{\partial \theta}(v_\theta B) \right] = \lambda_T \left(\nabla^2 - \frac{1}{s^2} \right) B + s(\mathbf{B}_p \cdot \nabla)\Omega + \frac{1}{r} \frac{d\lambda_T}{dr} \frac{\partial}{\partial r}(rB), \quad (2.3)$$

where $s = r \sin \theta$, λ_T is the turbulent diffusivity and $S(r, \theta, t)$ is the dynamo source term.

The term $s(\mathbf{B}_p \cdot \nabla)\Omega$ in Equation 2.3 corresponds to process (i) involving the generation of the toroidal field from the poloidal field involving differential rotation. On the other hand, the terms $s^{-1}(\mathbf{v} \cdot \nabla)(sA)$ and $\lambda_T (\nabla^2 - 1/s^2)A$ in Equation 2.2 correspond to process (iii) involving the advection of the poloidal field due to the meridional circulation and the turbulent diffusion together. It is the source term $S(r, \theta, t)$ which incorporates the process (ii). Sometimes we have to do some extra things to Eq. 2.2 as well (as described below) in order to include the magnetic buoyancy of the toroidal field B .

In the early $\alpha\Omega$ dynamo model postulated by Parker (1955b) and Steenbeck et al. (1966), the source term is $S = \alpha B$ (see, for example, Choudhuri (1998), Chapter 16). Here α is a measure of helical turbulence and is usually referred as the α -effect. Although the Babcock–Leighton mechanism also can be encapsulated by a superficially similar α -coefficient, its physical interpretation is completely different from that of the α -effect, which implies the twisting of

the toroidal field. When it was realized that the toroidal field at the bottom of the convection zone is much stronger than what was assumed earlier (Caligari et al., 1995; Choudhuri, 1989; Choudhuri & Gilman, 1987; D’Silva & Choudhuri, 1993; Fan et al., 1993) and the traditional α -effect would be suppressed, the Babcock–Leighton mechanism was invoked to take its place, with a similar-looking α -coefficient having a different interpretation (Durney, 1997). Since the Babcock–Leighton mechanism primarily takes place near the surface, the α -coefficient corresponding to it is usually assumed to be confined near the solar surface. Choudhuri et al. (1995) simply took $S = \alpha B$, with α concentrated at the surface as expected. Even with such a source function which did not include magnetic buoyancy explicitly, they were able to get a periodic solution because of the term

$$\frac{1}{r} \left[\frac{\partial}{\partial r}(rv_r B) + \frac{\partial}{\partial \theta}(v_\theta B) \right]$$

in Eq. 2.3, which implied that the toroidal field generated at the tachocline was advected by the meridional circulation to the surface where the Babcock–Leighton mechanism operated on it. Küker et al. (2001) also followed this approach.

Although it is possible to construct a Babcock–Leighton dynamo model in this way without explicitly including magnetic buoyancy, this is certainly not very physical or satisfactory. When the toroidal field becomes sufficiently strong, its rise time due to magnetic buoyancy is expected to be much shorter than the advection time by the meridional circulation. So magnetic buoyancy is expected to dominate over such advection and has to be included in the model to make it more realistic. In the next Section, we discuss two popular procedures for incorporating magnetic buoyancy—a non-local procedure and a local procedure. We first discuss how these procedures are used in order to obtain regular dynamo solutions. Then we shall point out in Section 2.4 that we get into added complications when we want to study irregularities of the solar cycle

2.3 Non-local and local treatment of magnetic buoyancy

The methods of specifying magnetic buoyancy in 2D kinematic models of the flux transport dynamo can be broadly classified into two categories: non-local and local. Since the non-local treatment of magnetic buoyancy is somewhat simpler, we discuss that first.

2.3.1 Non-local magnetic buoyancy

The Babcock–Leighton mechanism essentially involves the generation of the poloidal field near the surface from the strong toroidal field at the bottom of the convection zone, which has risen due to magnetic buoyancy. A simple way of incorporating it is to take the source term $S(r, \theta, t)$ in Eq. 2.2 to have the form

$$S(r, \theta, t) = \alpha(r, \theta)B(r = r_{\text{bot}}, \theta, t), \quad (2.4)$$

in which we usually take $\alpha(r, \theta)$ to be significantly non-zero only near the surface, to ensure that $S(r, \theta, t)$ makes a contribution only near the surface. Also, to get $S(r, \theta, t)$ near the surface, we multiply $\alpha(r, \theta)$ not by the toroidal field B there, but by the toroidal field $B(r = r_{\text{bot}}, \theta, t)$ at the bottom of the convection zone. Since the rise time due to magnetic buoyancy is small compared to the period of the dynamo, we normally use the same t in S and B without introducing any time delay.

To the best of our knowledge, the method of treating magnetic buoyancy in this way was first proposed by Choudhuri & Dikpati (1999) in their study of the evolution of the solar poloidal field. Afterwards, Dikpati & Charbonneau (1999) adopted it for their flux transport dynamo model. Some other authors have followed this procedure in their dynamo calculations since that time (Charbonneau & Dikpati, 2000; Charbonneau et al., 2005; Guerrero & Muñoz, 2004; Hotta & Yokoyama, 2010).

This method of treating magnetic buoyancy is a simple, robust and stable method. It is found that dynamo models based on this method of treating magnetic buoyancy remain stable on changing the values of basic parameters over wide ranges. However, in spite of its simplicity and attractiveness, this method has the following unphysical features.

(1) We expect the toroidal field to be unstable to magnetic buoyancy only after it has become sufficiently strong. However, in the non-local method of treating buoyancy, even a very weak toroidal field at the bottom of the convection zone starts contributing to the source term in Eq. 2.2. It is, in principle, possible to put a threshold on the strength of the magnetic field even in the non-local treatment, although very few authors following this approach have done this (Charbonneau et al., 2005).

(2) As a result of buoyant rise from the bottom of the convection zone, the toroidal field at the bottom of the convection keeps getting weaker. The simple method of treating magnetic buoyancy described above does not incorporate this effect and most of the authors who treated magnetic buoyancy in this way did not allow the weakening of the toroidal field due to magnetic buoyancy. As we shall see in the next Section, not doing this has serious consequences when we study irregularities of the solar cycle such as the Waldmeier effect.

It should be pointed out that the physics of how magnetic flux depletion takes place in the convection zone is still rather poorly understood. The toroidal field of one cycle has to be removed from the convection zone by the time the toroidal field of the next cycle starts building up. If the toroidal field has a strength of 10^5 G as suggested by the flux tube rise simulations, then certainly it cannot be destroyed by turbulent diffusion, which will be completely suppressed in the presence of such a strong magnetic field. Then magnetic buoyancy remains the only viable mechanism for removing the magnetic field, although how this happens is unclear. If the toroidal field exists in the form of a flux ring going around the rotation axis and a part of it rises to form active regions, then other portions of the flux ring remain anchored at the bottom of the convection zone and there is certainly not an overall reduction of flux there. In fact, [Rempel & Schüssler \(2001\)](#) have pointed out that some processes can actually amplify the magnetic field in the anchored part next to the rising portion of the flux tube. A scenario proposed by [Choudhuri \(2003\)](#) is that only some parts of the toroidal field become concentrated to 10^5 G and rise to form active regions, whereas the magnetic field remains more diffuse and much weaker in other regions. If these weaker fields diffuse by turbulent diffusion, then the buoyant rise of concentrated magnetic fields may reduce the flux. Although we do not understand many aspects of the physics of magnetic fields at the bottom of the convection zone, the assumption that the magnetic flux is depleted due to magnetic buoyancy seems reasonable and is essential to explain certain aspects of observational data, as we shall discuss in Section 2.4.

2.3.2 Local magnetic buoyancy

In this approach, some toroidal magnetic field is transferred from the bottom of the convection zone to the solar surface and then this toroidal field at the surface is expected to produce the poloidal field locally. Magnetic buoyancy is known to be particularly destabilizing within the convection zone ([Moreno-Insertis, 1983](#); [Parker, 1975](#)). So, as the toroidal field evolves according to Eq. 2.3, we check at periodic intervals if the toroidal field at any point within the convection zone becomes stronger than a critical value B_c and, if so, then some toroidal field from such region is transferred to the surface. It may be noted that this procedure introduces a limit to the growth of the dynamo by not allowing B to grow much beyond B_c . As a result, the dynamo can exhibit non-growing oscillatory solutions even without introducing any kind of quenching. On the other hand, in the non-local procedure described in Section 2.3.1, it is absolutely essential to include some kind of quenching (a quenching of the α -coefficient being the most common) to stop the runaway growth of the magnetic field. After the toroidal field is shifted to the top of the convection zone, we have to prescribe some way of generating the poloidal field from it. Two ways of doing this are described in the next two paragraphs.

Local α parameterization. One way is to prescribe the source term $S(r, \theta, t)$ in Eq. 2.2 simply as a product of $\alpha(r, \theta)$ confined around the surface and the toroidal field $B(r, \theta, t)$ there, which has been shifted there from those regions at the bottom of the convection zone where B exceeded B_c in a way that ensured the conservation of the toroidal flux (i.e. the amount of toroidal flux deposited near the surface has to equal the amount of toroidal flux removed from the bottom of the convection zone). This method has been followed in several publications from our group (Chatterjee & Choudhuri, 2006; Chatterjee et al., 2004; Choudhuri & Karak, 2009; Choudhuri et al., 2004, 2005, 2007; Goel & Choudhuri, 2009; Hazra et al., 2015; Karak & Choudhuri, 2011, 2012, 2013; Nandy & Choudhuri, 2001, 2002).

Durney's double ring method. The ideas of Babcock (1961) and Leighton (1969) were followed more closely by Durney (1995, 1997). Due to the action of the Coriolis force, the rising flux tube gets tilted (D'Silva & Choudhuri, 1993) and produces two sunspots of opposite polarity at slightly different latitudes. In an axisymmetric 2D formulation, we have to average over longitude, which gives us two flux rings of opposite sign at two slightly different latitudes. The generation of the poloidal field is prescribed in the following way. Whenever B in some region within the convection exceeds a critical value B_c , we assume that a part of this B gives rise to the flux ring above the region and we put A appropriate for this flux ring in Eq. 2.2. Here we do not discuss the details of how we find A appropriate for a flux ring, except to mention that some assumption has to be made about the magnetic field structure below and above the flux ring. Presumably the bipolar sunspot pair eventually gets disconnected from the toroidal flux ring at the bottom of the convection zone from which it formed, though it is not clear at the present time how and when this disconnection takes place (Longcope & Choudhuri, 2002). Figure 2.1 from Muñoz-Jaramillo et al. (2010) shows the typical poloidal field structure assumed by them in their dynamo model with Durney's double ring algorithm.

It is found that the above two methods—local α parameterization and Durney's double ring method—give qualitatively similar results (Nandy & Choudhuri, 2001). However, Muñoz-Jaramillo et al. (2010) have argued that the double ring method is a superior method from the conceptual point of view.

It may be pointed out that the local treatment of magnetic buoyancy also has an element of non-locality in it. Whenever we put some toroidal flux just below the surface or a double ring at the surface, non-local considerations (the value of the toroidal field near the bottom of the convection zone) determine when and where this should be done. However, once the toroidal flux or the double ring has been put near the surface, its subsequent evolution is governed by local physics. On the other hand, in the non-local treatment, the source term explicitly has a dependence on the magnetic field in a different location, as seen in Eq. 2.4. Whether 'local' and 'non-local' are the best terminology to describe these approaches can be questioned. However,

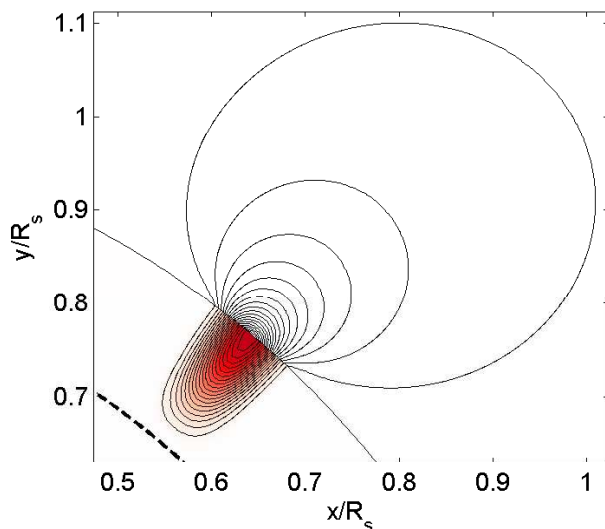


Fig. 2.1 The poloidal field lines of a double ring formed near the surface due to magnetic buoyancy. Taken from [Muñoz-Jaramillo et al. \(2010\)](#).

it is important to distinguish between these two approaches and we have merely followed the terminology used by many authors.

2.3.3 Comparison between the non-local and local methods

It would have been wonderful if the non-local and local methods of treating magnetic buoyancy gave qualitatively similar results. Unfortunately, that is not the case! When this was first discovered by [Choudhuri et al. \(2005\)](#), it came as a surprise to most of the researchers in the field, though now from hindsight we feel that this should have been an expected result. Figures 2.2(a) and 2.2(b) show the poloidal field configurations in two dynamo models in which magnetic buoyancy is treated by non-local and local (α parameterization) methods, but which are identical dynamo models in all other respects. The time-latitude plots of the toroidal field at the bottom of the convection zone are shown in Figures 2.2(c) and 2.2(d). When we use non-local buoyancy, even the weak toroidal fields produced at the high latitude start giving rise to the poloidal field. This causes a multi-lobe structure of the poloidal field in this case, shortening the period of the dynamo. While the model with the local α parameterization gives a period of 14 years, we get a period of barely 6.1 years on using the non-local treatment of magnetic buoyancy. It is possible to obtain solar-like solutions with the non-local treatment of magnetic buoyancy with a completely different set of parameters, as seen in the results of [Dikpati & Charbonneau \(1999\)](#) and other authors. However, for the set of parameters which

give solar-like solutions with the local treatment of magnetic buoyancy, we get a totally different kind of result on changing to a non-local treatment of magnetic buoyancy (while keeping all the other things same).

Because of these big differences, we cannot avoid the question as to which of these two methods is better. We first note that both the methods are gross over-simplifications of a complicated 3D process. In this sense, neither of these two methods can be taken as a realistic depiction of magnetic buoyancy. We believe that the local treatment is a more physical and realistic depiction of what actually happens in the Sun—a conclusion that will be further reinforced from the discussion of the next Section. We have used this method of local treatment in most of the calculations done in our group. Unfortunately, this method is less robust and less stable than the non-local method and seems to give results only within a narrow range of various important dynamo parameters. So, when we want to vary our dynamo parameters over a wide range or when we use unusual parameter specifications (such as a multi-cell meridional circulation in Chapter 4), we are often unable to obtain results with the local α parameterization procedure and are forced to use the more robust non-local procedure described in Section 2.3.1 (Hazra et al., 2014; Karak et al., 2014b).

2.4 Modeling irregularities of the solar cycle

The previous section outlined the various ways of treating magnetic buoyancy and pointed out the differences in the periodic dynamo solutions we get with them. Within the last few years, one of the goals of solar dynamo theory has been to model the irregularities of the solar cycle. Only very recently we realized that different formulations of magnetic buoyancy may give radically different results in this important field of study—especially when we consider irregularities of the solar cycle caused by the variations in the meridional circulation.

The duration of the solar cycle becomes longer when the meridional circulation slows down (Dikpati & Charbonneau, 1999; Yeates et al., 2008). So it is expected that variations in the meridional circulation will introduce irregularities in the cycle. When this problem is studied with the help of local α parameterization, the theoretical results are broadly in agreement with observational data (Choudhuri & Karak, 2012; Hazra et al., 2015; Karak, 2010; Karak & Choudhuri, 2011, 2013). Before explaining how things change on changing the method of treating magnetic buoyancy, let us say a few words about the basic physics of the problem. When a cycle becomes longer due to the slowing of the meridional circulation, two competing effects take place. The differential rotation has more time to generate more toroidal field, trying to make the cycle stronger. On the other hand, diffusion has also more time to act on

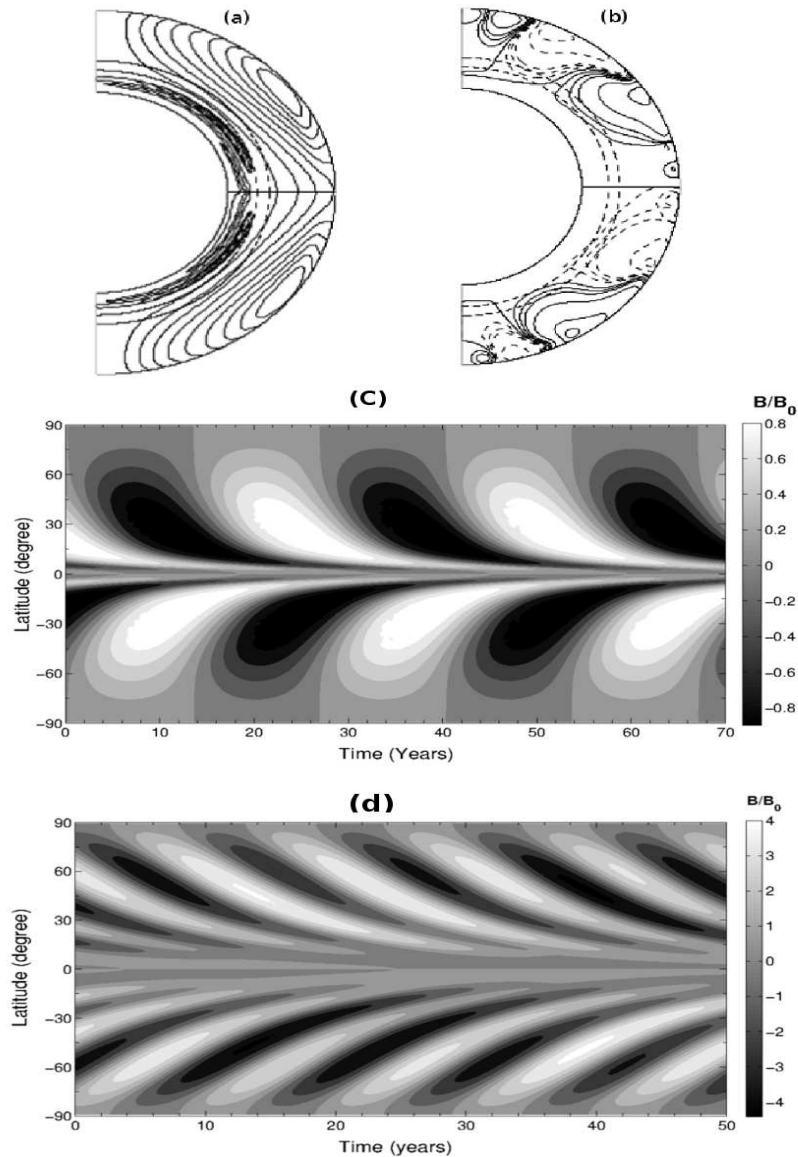


Fig. 2.2 (a) and (b) Poloidal field lines at a particular instant of time in two solar dynamo simulations. Both use the same combination of parameters which were used to generate the standard model in § 4 of [Chatterjee et al. \(2004\)](#). The only difference between the two runs is that (a) was generated by using local buoyancy treatment and (b) was generated by using the non-local buoyancy treatment. Whereas (a) is taken from Fig. 14 of [Chatterjee et al. \(2004\)](#), (b) is taken from Fig. 1 of [Choudhuri et al. \(2005\)](#). (c) and (d) are the time-latitude plots of the toroidal field at the bottom of the convection zone for these two cases. It may be noted that, in the local treatment of magnetic buoyancy adopted by [Chatterjee et al. \(2004\)](#), the flux eruptions are treated explicitly and one can generate a theoretical butterfly diagram of sunspots, as shown in Fig. 13 of [Chatterjee et al. \(2004\)](#). Since this is not possible in the non-local treatment, we have plotted the values of toroidal field in both the cases for the sake of easy comparison.

the magnetic field and tries to make the cycle weaker. Which of these two effects wins over depends on the assumed value of the turbulent diffusion coefficient in the convection zone.

Most of the calculations in our group were done with a value of turbulent diffusion around $10^{12} \text{ cm}^2 \text{ s}^{-1}$ consistent with mixing length argument (Parker, 1979, p. 629; Jiang et al. (2007)). With such a value of turbulent diffusion, the effect of diffusion trying to make the longer cycle weaker wins over the effect of differential rotation trying to make longer cycles stronger. As a result, longer cycles tend to be weaker. This naturally leads to an explanation of the Waldmeier effect that the rise time of the cycle is inversely correlated with the strength of the cycle (Karak & Choudhuri, 2011). On the other hand, several papers from Dikpati and her collaborators (Charbonneau & Dikpati, 2000; Dikpati & Charbonneau, 1999; Dikpati & Gilman, 2006) used a value of turbulent diffusion about 50 times smaller. With such a value of turbulent diffusion, the effect of differential rotation trying to make longer cycles stronger wins over, giving the opposite of the Waldmeier effect.

The better agreement with observational data on using the higher value of turbulent diffusion clearly indicates that this higher value must be closer to reality. However, we realized only recently that an appropriate handling of magnetic buoyancy is also required to get a match with observational data. We basically need diffusion to be dominant so that longer cycles are weaker. When we use a higher value of diffusion and treat magnetic buoyancy through local α parameterization, this happens and we are able to explain effects like the Waldmeier effect beautifully. However, when we use the non-local buoyancy method, we get into trouble even on taking the higher value of diffusion. In our calculations with local α parameterization, toroidal flux is removed from the bottom of the convection zone as a result of magnetic buoyancy. On the other hand, in the non-local buoyancy formulation used in several papers (Charbonneau & Dikpati, 2000; Dikpati & Charbonneau, 1999), the toroidal flux is never depleted as a result of magnetic buoyancy. Because of this, the toroidal field keeps becoming stronger when the cycle is longer and, even with a high value of diffusion, we find that longer cycles tend to be stronger, giving the opposite of the Waldmeier.

Since this aspect of the problem was realized only recently and has not yet been reported in regular journal publications, we present some new results here. Figure 2.3(a) shows the Waldmeier effect (i.e. the anti-correlation between the rise time and the strength of the cycles) obtained with a dynamo model with a high value of diffusion in the convection zone on using the local α parameterization. If we treat magnetic buoyancy through the non-local method as given by Eq. 2.4, while keeping all other things of the dynamo unchanged, then we get the opposite of the Waldmeier effect, i.e. a correlation rather than an anti-correlation. This is shown in Figure 2.3(b). To verify that this is indeed caused by not including the depletion of the toroidal field by magnetic buoyancy, if we now modify the non-local method slightly by

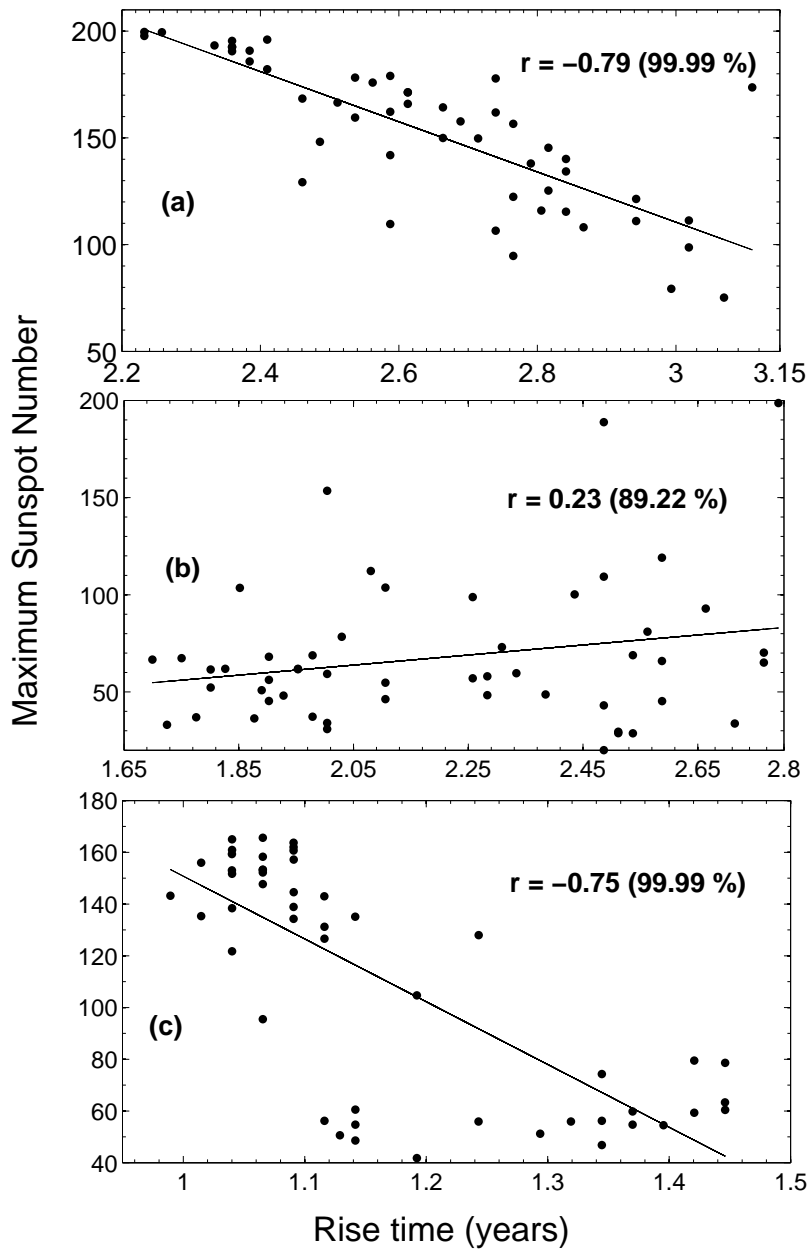


Fig. 2.3 The correlation between the rise and the strength of the solar cycle from a theoretical solar dynamo model using the same combination of parameters as the high diffusivity model presented by [Karak & Choudhuri \(2011\)](#). Only fluctuations in the meridional circulation are included. The panels (a) and (b) are obtained by using respectively the local treatment and the non-local treatment (without depletion in the toroidal flux) of magnetic buoyancy. The last panel (c) obtained by using the non-local treatment of magnetic buoyancy in which the toroidal field is not allowed to grow larger than a critical value B_c . The panel (a) essentially the same plot as Fig. 4(a) of [Karak & Choudhuri \(2011\)](#) obtained with a different realization of the randomness.

putting the restriction that the toroidal field is not allowed to grow beyond a limiting value B_c (i.e. we put a specification in the code that whenever $B > B_c$ we set $B = B_c$), then we again get back the Waldmeier effect. The result is shown in Figure 2.3(c) which is obtained by using the non-local buoyancy with the restriction that B is never allowed to grow beyond B_c . We thus have a rather peculiar situation. Although the non-local magnetic buoyancy method is more robust and works for a wide range of parameters, if this method is used blindly while studying irregularities caused by the variations in the meridional circulation, we are likely to get completely wrong results. This should make it clear that none of the presently used methods of treating magnetic buoyancy is completely satisfactory. Each method has its limitations and we have to keep these limitations in mind when interpreting the results obtained with a particular method.

2.5 The latitudinal distribution problem

So far we have discussed problems of a realistic 2D formulation of magnetic buoyancy, which is an intrinsically 3D process. Now we mention another problem connected possibly with magnetic buoyancy, which is still very poorly understood. In a helioseismic map of differential rotation (see, for example, Schou et al. (1998)), it is clearly seen that the radial differential rotation is concentrated more strongly at high latitudes than at low latitudes—the sign being different at high and low latitudes. Because of this, the generation of the toroidal magnetic field from the poloidal magnetic field is supposed to be more pronounced at the high latitudes. At the low latitudes, the differential rotation present there first has to ‘unwind’ the toroidal field produced by the differential rotation of the opposite sign at high latitudes and brought to the low latitudes by the equatorward meridional circulation. Only after that, the differential rotation at low latitudes can build up the toroidal field. Hence, when we use the differential rotation discovered by helioseismology, there is a propensity of stronger toroidal field being produced at the high latitudes. If this strong toroidal field is allowed to rise to the surface there due to magnetic buoyancy, then we find sunspots at latitudes higher than where they are seen. The first authors to use helioseismically determined differential rotation already noticed this problem (Dikpati & Charbonneau, 1999; Küker et al., 2001)

Nandy & Choudhuri (2002) proposed a solution to this problem. They suggested that the meridional circulation penetrates slightly below the bottom of the convection zone, where the temperature gradient is stable against convection and magnetic buoyancy is suppressed to a large extent. If this is the case, then the strong toroidal field created in the high-latitude tachocline may be pushed below the bottom of the convection zone and may not be able to rise to the surface due to the suppression of magnetic buoyancy there, thereby inhibiting formation

of sunspots at high latitudes. Then the toroidal field would be advected equatorward by the meridional circulation through layers slightly below the bottom of the convection. Then, when the penetrating meridional circulation again enters the convection zone at low latitudes, the toroidal field is brought into the convection zone and magnetic buoyancy again takes over to produce sunspots at low latitudes. This Nandy–Choudhuri hypothesis became a source of controversy—[Gilman & Miesch \(2004\)](#) arguing that it is not possible for the meridional circulation to penetrate into the stable layers below the bottom of the convection zone, whereas [Garaud & Brummell \(2008\)](#) pointed out that some penetration to a limited extent is possible. In many dynamo calculations from our group, we have made the meridional circulation slightly penetrating in order to confine sunspots to low latitudes. As [Chakraborty et al. \(2009\)](#) pointed out, one strong support for the Nandy–Choudhuri hypothesis comes from the observation that torsional oscillations begin at higher latitudes before the start of a sunspot cycle. Since torsional oscillations are presumably driven by the Lorentz force of the dynamo-generated magnetic field, this observation clearly suggests that the strong toroidal field builds up in the high-latitude tachocline a few years before this field is advected to low latitudes and is able to produce sunspots, in accordance with the Nandy–Choudhuri hypothesis.

In a study of the evolution of the poloidal field (in which the dynamo equation was not solved), [Dikpati & Choudhuri \(1994\)](#) mimicked the behavior of the dynamo by restricting the source term of the poloidal field to low latitudes. Within the last few years, several authors have solved the dynamo equation by artificially restricting the Babcock–Leighton source term to low latitudes in this fashion ([Hotta & Yokoyama, 2010](#); [Muñoz-Jaramillo et al., 2010](#)). While this procedure produces nice-looking butterfly diagrams with sunspots restricted to low latitudes, these authors provide no physical justification for this procedure. An analysis by [Schüssler et al. \(1994\)](#) suggested that flux tubes stored at the bottom of the convection zone are more likely to be unstable at lower latitudes. It is possible that such considerations may provide a justification for restricting the Babcock–Leighton process to low latitudes. Curiously, based on their study magneto-rotational instability at the bottom of the convection zone, [Parfrey & Menou \(2007\)](#) concluded that the lower latitudes are more stable—which were found to be unstable in the analysis of [Schüssler et al. \(1994\)](#). [Parfrey & Menou \(2007\)](#) argued that this stability is important for restricting the dynamo action at lower latitudes. Certainly this issue needs to be studied in more detail. In our opinion, we still do not have a proper understanding of why sunspots are restricted only to low latitudes. Although this is an old problem and no significant progress has been made in the last few years, we decided to add this Section because the existence of this problem is nowadays often not appreciated or acknowledged. We should keep this problem in mind and should not sweep it under the rug.

2.6 Conclusion

Our discussion has been restricted to kinematic dynamo models in which the velocity field is assumed to be given. Although we so far do not have anything that can be called the standard model of the solar dynamo even within the framework of kinematic models (Choudhuri, 2008), flux transport dynamo models developed by different groups have lots of common features. While there is a controversy on the nature of the meridional circulation at present, it is still not clear whether a serious revision of existing dynamo models will be required. Another uncertainty about the value of turbulent diffusion seems to be resolved now in favor of higher diffusivity (such that the diffusion time scale is a few years) because only with such diffusivity it is possible to model various aspects of cycle irregularities (Choudhuri, 2015). Whether turbulent pumping is important for the solar dynamo is another question. However, since the inclusion of turbulent pumping does not change the results of high-diffusion dynamo models too much (Karak & Nandy, 2012), this is presumably not a large source of uncertainty.

As we have discussed here, the biggest uncertainty in the flux transport dynamo at the present time arises from the treatment of magnetic buoyancy. There have been two widely used procedures for treating magnetic buoyancy in 2D kinematic models of the flux transport dynamo: (i) the non-local treatment in which the toroidal field at the bottom of the convection zone is assumed to contribute directly to the generation of the poloidal field, without itself being depleted, and (ii) the local treatment in which a part of the toroidal field from the bottom of the convection zone is shifted to the top whenever it exceeds a critical value. With magnetic buoyancy treated in either of these ways, it is possible to arrange the parameters of the model in such a way that the dynamo solution reproduces various characteristics of the solar cycle. However, for the same set of parameters, we get very different results on using these different treatments of magnetic buoyancy. The non-local treatment is more robust and is preferred when we want to study the behaviour of our system over a wide range of parameters. On the other hand, the local treatment with the toroidal field depletion at the bottom of the convection zone allows the proper reproduction of results under irregular situations (such as the Waldmeier effect) and appears the more physically realistic treatment.

This is certainly an unsatisfactory situation and presumably we cannot model magnetic buoyancy sufficiently well if we restrict ourselves only to strictly 2D situations. It may be noted that, in the early studies of magnetic buoyancy based on thin flux tube equation (Choudhuri, 1990; Spruit, 1981), some physical effects could be studied through 2D calculations (Choudhuri & D'Silva, 1990; Choudhuri & Gilman, 1987; D'Silva & Choudhuri, 1991). However, a proper study of the tilt of bipolar sunspot regions (which is responsible for the Babcock–Leighton process) could be carried out only when the calculations were carried out in 3D (Caligari et al., 1995; D'Silva & Choudhuri, 1993; Fan et al., 1993). Essentially, magnetic buoyancy is

inherently a 3D process and cannot be included very satisfactorily in 2D kinematic dynamo models. Further advances in 2D kinematic models are unlikely to solve the problems we are facing now.

The ultimate goal of solar dynamo models is to construct fully dynamically consistent 3D models, in which the velocity fields are also calculated from the fundamental equations (Karak et al., 2014a). Beyond 2D kinematic models, however, there is an intermediate possibility—3D kinematic models, in which the mean velocity fields (such as differential rotation and meridional circulation) are supposed to be axisymmetric and are specified (i.e. not calculated from the basic fluid equations), but the magnetic field is treated in a full 3D fashion and is allowed to evolve non-axisymmetrically so that we are able to model the formation of tilted bipolar sunspots and the Babcock–Leighton process more realistically. The relatively few citations (according to ADS) to the first paper suggesting this approach (Yeates & Muñoz-Jaramillo, 2013) indicate that the importance of this approach is not generally recognized. But we believe that this is going to be the next important step in flux transport dynamo theory beyond 2D kinematic model. Only a few authors have so far presented results with this approach (Miesch & Dikpati, 2014). This approach, when developed and integrated with a realistic dynamo model, should be more satisfactory than the currently widely used two treatments of magnetic buoyancy in 2D kinematic models. However, a 3D kinematic model is not expected to immediately solve all the problems connected with magnetic buoyancy in the 2D kinematic model. For example, we have discussed in Section 2.5 the problem of why sunspots appear in lower latitudes. This problem will not be solved with the 3D formulation of magnetic buoyancy. Rather, we shall need a better understanding of the physics of the tachocline to address this question. We thus expect a combination of more realistic calculation of magnetic buoyancy coupled with a better understanding of the tachocline to put the flux transport dynamo on a more satisfactory footing.

“The true adventurer goes forth aimless and uncalculating to meet and greet unknown fate.”

–O. Henry

3

Explaining various Irregular Properties of the Solar Cycle

Using different proxies of solar activity, we have studied the following features of solar cycle. (i) A linear correlation between the amplitude of cycle and its decay rate, (ii) a linear correlation between the amplitude of cycle n and the decay rate of cycle $(n - 1)$ and (iii) an anti-correlation between the amplitude of cycle n and the period of cycle $(n - 1)$. Features (ii) and (iii) are very useful because they provide precursors for future cycles. From 90 years of persistent Kodaikanal sunspot area data, the decay rate correlations (i), (ii) and Waldmeier effects are also reproduced. We have explained these features using a flux transport dynamo model with stochastic fluctuations in the Babcock-Leighton α effect and in the meridional circulation. Only when we introduce fluctuations in meridional circulation, we are able to reproduce different observed features of solar cycle. We discuss the possible reasons for these correlations

3.1 Introduction

Solar cycles are asymmetric with respect to their maxima, the rise time being shorter than the decay time. While the cycle amplitude (peak value) and the duration have cycle-to-cycle

variations, we find some correlations among different quantities connected with the solar cycle. Since 1935, it has been realized that the stronger cycles take less time to rise than the weaker ones (Waldmeier, 1935). This anti-correlation between rise times and peak values of the solar cycle is popularly known as the Waldmeier effect. Karak & Choudhuri (2011) have defined this aspect of the Waldmeier effect as WE1, whereas the correlation between the rise rates and the peak values is called WE2 (see also Cameron & Schüssler (2008)). Although WE2 is a more robust feature of the solar cycle, Karak & Choudhuri (2011) have shown that both WE1 and WE2 exist in many proxies of the solar cycle. We have also shown that the Waldmeier effects (both WE1 and WE2) exist in the 90 years persistent sunspots area data from Kodaikanal observatory. WE2 provides a valuable precursor for predicting solar cycles because one can predict the strength of a cycle once it has just started (see Kane (2008); Lantos (2000)).

The declining phase of the cycle also provides important clues for understanding long-term variations. We find that stronger cycles not only rise rapidly but also fall rapidly (shorter decay time). This results in a good correlation between the decay rate and amplitude of the same cycle. However, defining the decay rate differently, Cameron & Schüssler (2008) did not find a significant correlation between the decay rate and amplitude. Furthermore, we find a strong correlation between the decay rate of the current cycle and the amplitude of the next cycle, which was also found by Yoshida and Yamagishi (2010). The decay time, however, is found to have no correlation with the amplitude of the same cycle. Another important feature observed is that the amplitude of the cycle is inversely correlated with the period of the previous cycle (Hathaway et al., 2002; Ogurtsov & Lindholm, 2011; Solanki et al., 2002b). These two correlations again provide promising precursors to predict the strength of the future cycle (Solanki et al., 2002b; Watari, 2008).

Apart from showing these correlations from observational data, we also attempt to provide theoretical explanations for them. A dynamo mechanism operating in the solar convection zone is believed to be responsible for producing the solar cycle. It is generally accepted that the strong toroidal field (responsible for the formation of bipolar sunspots) is produced from the poloidal field by differential rotation in the solar convection zone (Parker, 1955b). This is the first part of solar dynamo theory. Due to magnetic buoyancy (Parker, 1955a) the flux tubes of toroidal field erupt out through the surface to form bipolar sunspot regions. These bipolar sunspots acquire tilts due to the action of the Coriolis force during their journey through the convection zone, giving rise to Joy's law (D'Silva & Choudhuri, 1993). To complete dynamo action, the toroidal field has to be converted back into the poloidal field. One possible mechanism for generating the poloidal field is the Babcock–Leighton (B-L) process (Babcock, 1961; Leighton, 1969), for which we now have strong observational support (Dasi-Espuig et al., 2010a; Kitchatinov & Olemskoy, 2011a; Muñoz-Jaramillo et al., 2013). In this process, the

fluxes of tilted bipolar active regions spread on the solar surface through different processes (diffusion, meridional circulation, differential rotation) to produce the poloidal field. A model of the solar dynamo that includes a coherent meridional circulation and this B-L mechanism for the generation of the poloidal field is called the flux transport dynamo model. This model was proposed in the 1990s (Choudhuri et al., 1995; Durney, 1995; Wang et al., 1991) and has been successful in reproducing many observed regular as well as irregular features of the solar cycle (Charbonneau & Dikpati, 2000; Chatterjee et al., 2004; Choudhuri & Karak, 2009; Guerrero & Muñoz, 2004; Hotta & Yokoyama, 2010; Karak & Choudhuri, 2013; Küker et al., 2001; Nandy & Choudhuri, 2002). Recently Charbonneau (2010), Choudhuri (2011b) and Karak et al. (2014a) have reviewed this dynamo model.

An important ingredient in flux transport dynamo is the meridional circulation, which is not completely constrained either from observations or from theoretical studies. Until recently not much was known about the detailed structure of the meridional circulation in the convection zone (Schad et al., 2013; Zhao et al., 2013). Therefore, most of the dynamo models use a single-cell meridional circulation in each hemisphere. However, we have shown in Chapter 4 that a complicated multi-cellular meridional circulation also retains many of the attractive features of the flux transport dynamo model if there is an equator-ward propagating meridional circulation near the bottom of the convection zone or if there is an equator-ward turbulent pumping (Guerrero & de Gouveia Dal Pino, 2008; Hazra & Nandy, 2016). While most of the calculations in this study are done for a single-cell meridional circulation, we show that the results remain qualitatively similar for more complicated meridional circulations.

Since we want to do a theoretical study of the irregularities in the solar cycle, let us consider the sources of irregularities in the flux transport dynamo model that make different solar cycles unequal. At present we know two major sources: (i) variations in the poloidal field generation due to fluctuations in the B-L process (Choudhuri et al., 2007; Goel & Choudhuri, 2009) and (ii) variations in the meridional circulation (Karak, 2010; Karak & Choudhuri, 2011). Direct observations of the polar field during last three cycles (Svalgaard et al., 2005), as well as its proxies such as the polar faculae and the active network index available for about last 100 years (Muñoz-Jaramillo et al., 2013; Priyal et al., 2014), indicate large cycle-to-cycle variations of the polar field. The poloidal field generation mechanism mainly depends on the tilts of active regions, their magnetic fluxes and the meridional circulation, all of which have temporal variations. Particularly the scatter of tilt angles around the mean, caused by the effect of convective turbulence on rising flux tubes (Longcope & Choudhuri, 2002), has been studied by many authors (Dasi-Espuig et al., 2010a; Wang & Sheeley, 1989). Recently Jiang et al. (2014b) found that the tilt angle scatter led to a variation in the polar field by about 30% for cycle 17. In fact, even a single big sunspot group with large tilt angle and large area appearing

near the equator can change the polar field significantly (Cameron *et al.*, 2013). On the other hand, for the meridional circulation, we have some surface measurements for about last 20 years, showing significant temporal variations (Chou & Dai, 2001; Hathaway & Rightmire, 2010). Although our theoretical understanding of the meridional circulation is very limited, all existing spherical global convection simulations do show significant variations in the meridional circulation (Karak *et al.*, 2015; Passos *et al.*, 2012). Introducing randomness in the poloidal field generation and in the meridional circulation, Karak & Choudhuri (2011) have been able to reproduce the Waldmeier effect in their high diffusivity dynamo model. When the meridional circulation becomes weaker, the cycle period and hence the rise time becomes longer. The longer cycle period allows the turbulent diffusion to act for a longer time, making the cycle amplitude weaker (Karak, 2010; Yeates *et al.*, 2008) and leading to the Waldmeier effect. The variation of the meridional circulation is crucial in reproducing this effect.

The motivation of the present work is to explore how the decay rates of cycles are related to their amplitudes in a flux transport dynamo model, with the aim of explaining the observed correlations mentioned earlier. The presentation of the chapter is following. In the next section, we summarize some of the features of solar cycle that are often considered as precursors of the solar cycle. In Section 3.3, we present a brief summary of our flux transport dynamo model and then in Section 3.4 we introduce suitable stochastic fluctuations in the poloidal field and the meridional circulation, in order to reproduce various observed features of the solar cycle. Finally the last section summarizes our conclusions.

3.2 Observational Studies

We have used three different observational data sets: (i) Wolf sunspot number¹ (cycles 1–23), (ii) sunspot area² (cycles 12–23), and (iii) 10.7 cm radio flux³ (available only for the last five cycles). These parameters are very good proxies of magnetic activity and are often used to study the solar cycle (Hathaway *et al.* 2002). To minimize the noise while keeping the underlying properties unchanged, we smooth these monthly data using a Gaussian filter having a full-width at half maximum (FWHM) of 1 year. We also average the data with FWHM of 2 years to check how the results change with the filtering. Apart from these three data sets, in Section 3.2.4, we present some new irregular properties of solar cycle along with some existent irregular properties using recently digitized 90 years sunspot area data from Kodaikanal Observatory, India (Mandal *et al.*, 2017a).

¹http://solarscience.msfc.nasa.gov/greenwch/spot_num.txt

²http://solarscience.msfc.nasa.gov/greenwch/sunspot_area.txt

³<http://www.ngdc.noaa.gov/stp/solar/flux.html>

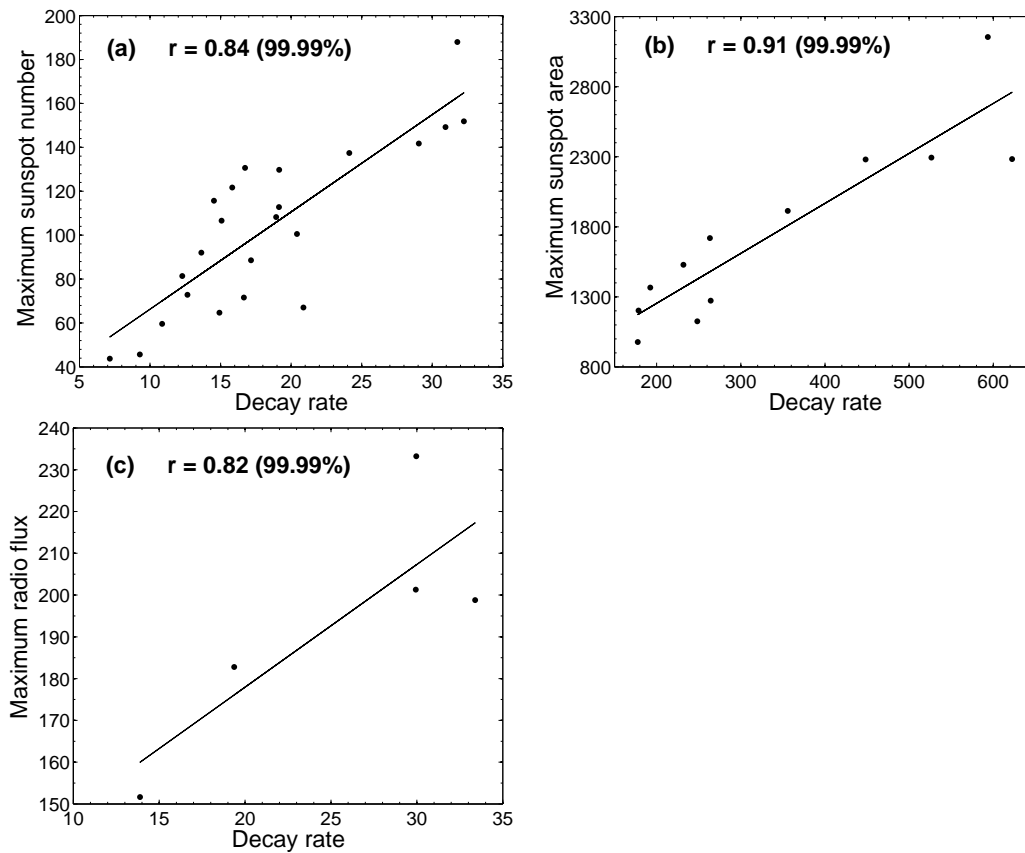


Fig. 3.1 Scatter plots of the decay rate and the amplitude of the same cycle computed from (a) sunspot number, (b) sunspot area, and (c) 10.7 cm radio flux data. In all these cases the original monthly data are smoothed using a Gaussian filter with FWHM of 2 years. The straight line in each plot is best linear fit of data. The correlation coefficients (r) and the significance levels are also given in each plot.

3.2.1 Correlation between the Decay Rate and the Cycle Amplitude

We have calculated the decay rate at three different phases of the descending phase of the cycle, namely, early phase, late phase and entire phase. For the early phase, the decay rate is taken as the slope between two points with a separation of 1 year with the first point one year after the cycle peak, whereas for the late phase the second point is taken 1 year before the cycle minimum. Here we exclude one year after the maximum when computing decay rate for the early phase because sometimes the cycle peaks are not so prominent. While computing the decay rate for the late phase we also exclude 1 year before the minimum just to avoid the effect of overlapping between two cycles during solar minimum. Finally, the decay rate of the entire decay part (*i.e.*, entire phase) is taken as the average of the individual decay rates computed at four different locations with a separation of one year starting from early phase to the late phase.

Table 3.1 Correlation coefficients between different quantities of the solar cycle.

Data set	FWHM	Correlation coefficients of the decay rate with the amplitude of					Correlation between the amplitude and the previous cycle period	
		Entire phase	Same cycle		Early Phase	Next cycle		
			Our value	CS08's value		Entire phase	Late phase	
Sunspot number	1 yr	0.79	0.21	0.22	0.67	0.55	0.65	-0.64
	2 yr	0.86	0.45	–	0.86	0.61	0.83	-0.67
Sunspot area	1 yr	0.84	0.20	0.11	0.69	0.14	0.37	-0.49
	2 yr	0.91	0.53	–	0.92	0.39	0.66	-0.60
Radio flux	1 yr	0.86	-0.11	0.14	0.93	-0.42	0.64	0.11
	2 yr	0.82	0.24	–	0.95	-0.43	0.46	0.09

In Figure 3.1 (a), (b) and (c), we show the correlations of the cycle amplitudes with the decay rates of the entire phase computed from sunspot number, sunspot area and 10.7 cm radio flux data, respectively.

We would like to point out that [Cameron & Schüssler \(2008\)](#) have computed the decay rate from the intervals of two fixed values of solar activity and they did not get significant correlation between the decay rate and the amplitude (see right column, Figure 2 of their paper). The reason of not finding significant correlation is that they have calculated the decay rate in the late phase of the cycle, *i.e.* near the tail of the cycle where the rate of decay is really very small. We find that their values are comparable with our decay rates computed in the late phase. In 4th and 5th columns of Table 3.1 we have listed our values and the values computed following [Cameron & Schüssler \(2008\)](#) method (hereafter referred as CS08). It is interesting to note that even for the radio flux data for which we have only five data points, we get strong correlation; see Table 3.1 for details. Therefore we can see that if we determine the decay rates from the entire phase of the solar cycle or the early phase, we find strong correlation with the amplitude. Thus, to determine the decay rate from descending part of the solar cycle, we need to consider the entire decay phase of the cycle, which provides a better estimate than CS08.

3.2.2 Correlation between the Decay Rate and the Next Cycle Amplitude

Next we find that there is a significant correlation between the amplitude of cycle and the decay rate of the previous cycle. Again we find this correlation for all the data sets considered here (see Table 3.1). However in Figure 3.2(a) we show this correlation only for sunspot number. Note that here the decay rates have been calculated from the entire decay phase as discussed in

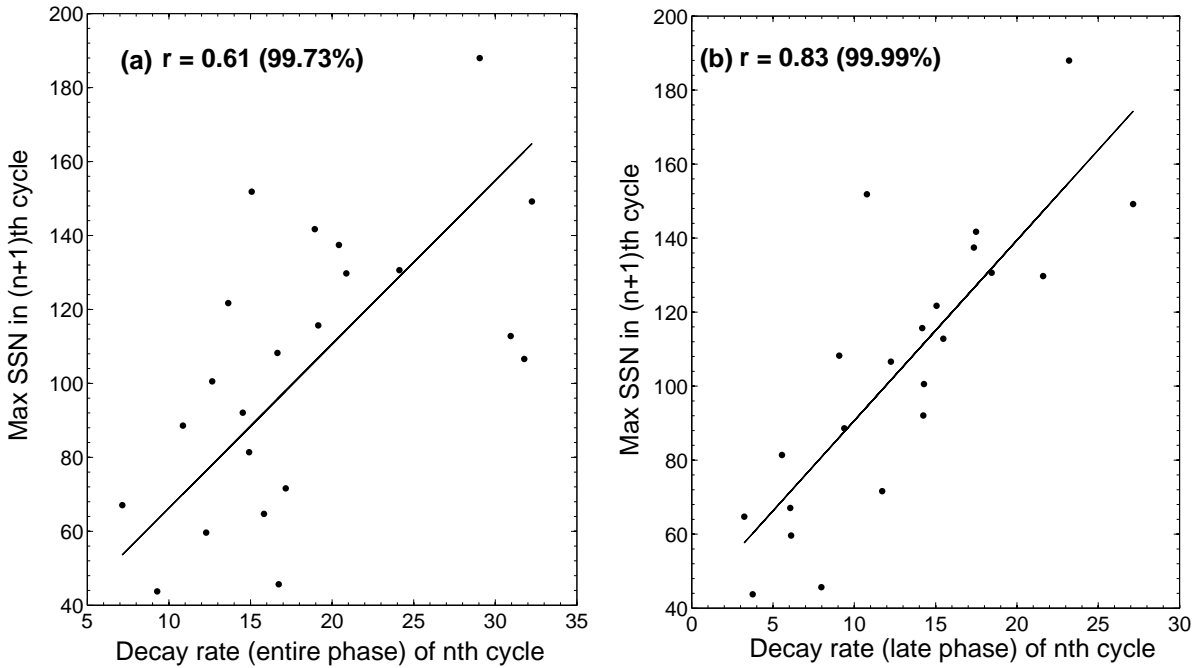


Fig. 3.2 Scatter plots showing the correlation of the amplitude vs. the decay rate of the previous cycle computed from sunspot number data (smoothed with FWHM of 2 year). In (a) the decay rate is computed from the entire decay phase, whereas in (b) it is at late decay phase.

Section 3.2.1. This correlation suggests that the decay rate of a cycle carries some information of the strength of the next cycle. It is interesting to note that when we look at this correlation with the decay rate computed in the late phase, the correlations become even stronger; see Figure 3.2(b). In 7th and 8th column of Table 3.1, we show both correlations for all three data sets. These results suggest that particularly the late phase of the cycle carries more information of the forthcoming cycle. This correlation of decay rate with the amplitude of succeeding cycle is already reported in [Yoshida & Yamagishi \(2010\)](#). They have shown this correlation for only sunspot number data and their methodology for calculation of decay rate (rate of decrease in sunspot number over some time) is somewhat different from our methodology. They have studied decay rate in six different cases (see their Figures 1(a)-(f)). They have obtained the decay rate from the decrease of sunspot number (SSN) over the period of 1, 2, 3, 4, 5 and 6 years before the minima of the cycle in the six different cases of study respectively. Since solar cycles sometimes have overlapping regions during minima and it is difficult to ascertain the actual minima, there are some uncertainties in the methodology of [Yoshida & Yamagishi \(2010\)](#). The correlation coefficient ($r = 0.70$) obtained in the second case of their study (see their Figure 1(b)) should be the same with what we obtained during late phase correlation ($r =$

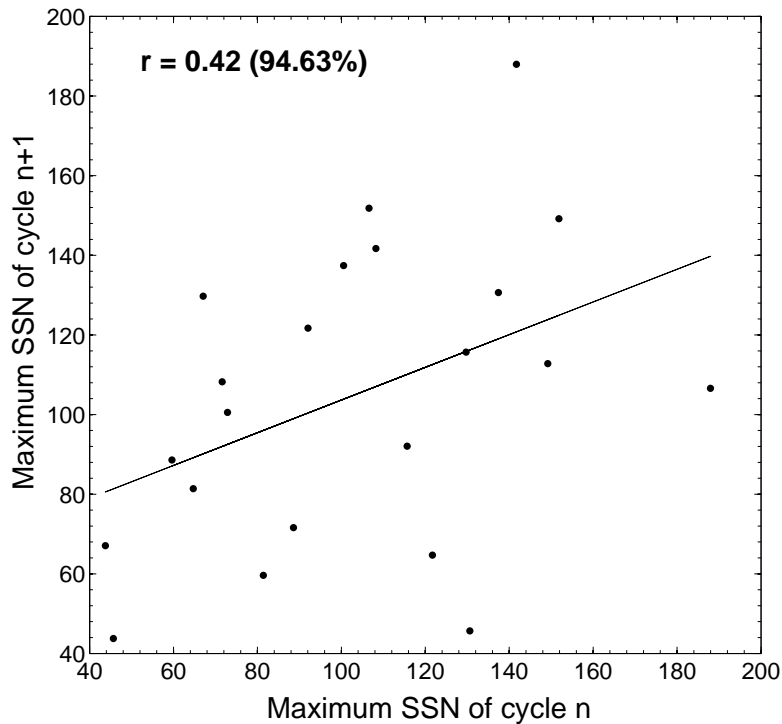


Fig. 3.3 Scatter plot of n th cycle amplitude and the amplitude of the next $n + 1$ cycle from sunspot number data (smoothed with FWHM of 2 years).

0.83). Since they have not considered the overlapping region between the minima and used monthly smoothed SSN, the value of the correlation coefficient is slightly different.

[Cameron & Schüssler \(2007\)](#) (also see [\(Brown, 1976\)](#)) have observed similar feature that the activity level during the solar minimum is an indicator for the strength of the next solar cycle and argued that this is caused by overlap between two cycles during solar minimum.

In all our theoretical calculations (subsequent section), while studying the correlation between the amplitude and the decay rate of the same cycle, we shall consider the decay rate of the entire phase, but for the correlation with the next cycle we shall consider only the late-phase decay rate.

Since the decay rate of the cycle n is correlated both with the amplitude of cycle n (Figure 3.1) and the amplitude of cycle $n + 1$ (Figure 3.2), one question that naturally arises is whether the amplitude of cycle n and the amplitude of cycle $n + 1$ are themselves correlated. We show a correlation plot between these amplitudes in Figure 3.3, demonstrating that there is not a significant correlation. The challenge before a theoretical model is, therefore, to explain

how the decay rate of cycle n is correlated both with the amplitude of cycle n and the amplitude of cycle $n + 1$, while these amplitudes themselves do not have a strong correlation.

3.2.3 Correlation between the Cycle Period and the Next Cycle Amplitude

Finally, we also find that the shorter cycles are followed by stronger cycles and vice versa. This produces an anti-correlation between the amplitude of a cycle and the period of the previous cycle (Hathaway et al., 2002; Ogurtsov & Lindholm, 2011; Solanki et al., 2002b). Figure 3.4 shows this correlation from sunspot number data (smoothed using a Gaussian filter with FWHM of 2 years). The correlation coefficients from other data are listed in Table 3.1. For all data we have taken the period of the cycle just as the time difference between two successive minima.

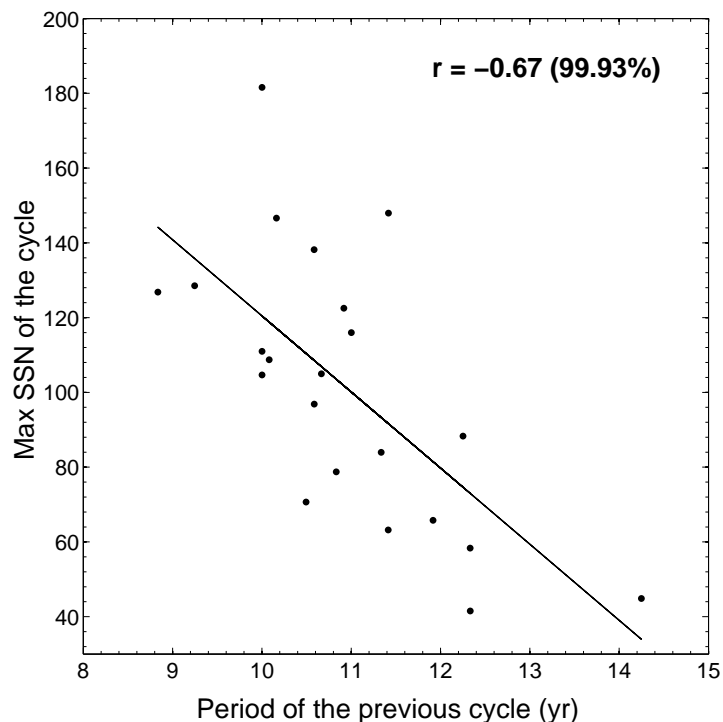


Fig. 3.4 Scatter plot showing the anti-correlation between the cycle amplitude and the period of the previous cycle from sunspot number data (smoothed with FWHM of 2 years).

3.2.4 Some irregular features of solar cycle from century long sunspot area data of Kodaikanal Observatory

Kodaikanal Solar Observatory (Hasan et al., 2010) is observing the Sun since 1904. This century long observation has been carried out in three different wavelength bands, white-light (since 1904), Ca-K (since 1907) and in H-alpha (since 1912). Among these three wavelengths, white-light observations were taken without any changes of the telescope optics since 1918. This makes the data set very efficient for long term solar studies. Kodaikanal white-light images have been used in the past by many authors to study the time evolution of different sunspot parameters. Sivaraman et al. (1993) used the white-light data, for a period of 45 years (1940-1985), and compared their results with Mount Wilson white-light data. In the subsequent years, various aspects of the sunspot and their variation with the solar cycles have been studied using this data set. Solar rotation rates (Gupta et al., 1999; Howard et al., 1999), axial tilt of the sunspot groups (Sivaraman et al., 1999), tilt angle and size variation of the sunspot groups (Howard et al., 2000), rotational rate variation with the age of the sunspot groups (Sivaraman et al., 2003) are some of the highlighted works produced from this data set. Here, we have calculated various correlations during ascending and descending phase of the solar cycles from this data set (1921-2011) and reproduced all the irregular features in those phases as given below.

3.2.4.1 Waldmeier Effect: The correlations in ascending phase of the solar cycle

Although the irregular properties of the solar cycles are well established but doubts are always expressed about their existence. Are they really properties of solar cycles or just statistical artifacts (Dikpati et al., 2008)? Time variation of daily sunspot area data or even the monthly averaged sunspot area data are so scattered that it is very difficult to calculate the required quantities like rise time and rise rate to validate their specific properties. So we need do the data smoothing. Here we have also smoothed our data by using a Gaussian filter having FWHM = 1 year and FWHM = 2 years. In figure 3.5(a) and figure 3.5(b) we have shown 1 year averaged and two years averaged solar cycles respectively. Red vertical dotted lines represents the minima which is calculated only for 1 year averaged solar cycle and green vertical dotted line shows the minima for 2 years averaged dataset. If we see figure 3.5 carefully then we can understand that determining solar minima for each cycle is always very sensitive to the filtering window and minima calculated using 1 year averaged data is not exactly same with the minima of the 2 years averaged data. This is true for determination of solar maxima also. It is also found that there is always an overlap between two successive cycles and the position of cycle minima depends on this overlapping (Cameron & Schüssler, 2007). Thus, defining the solar cycle

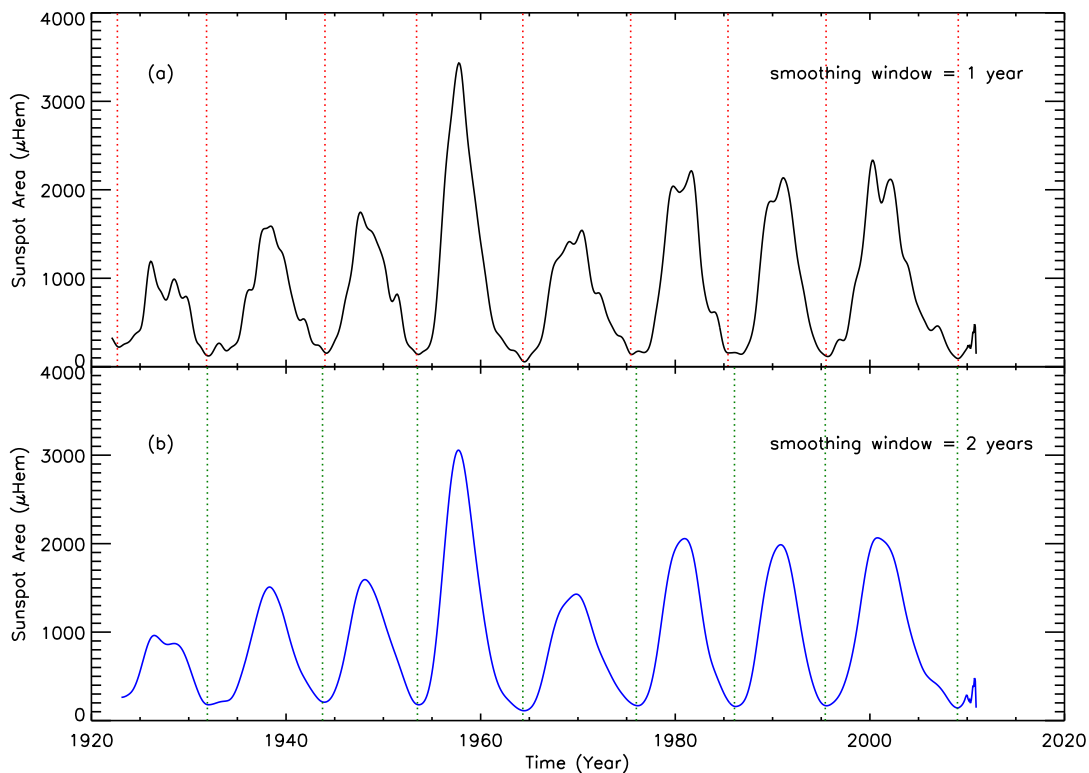


Fig. 3.5 Panel (a) shows the yearly averaged solar cycle from kodaikanal sunspot area data. (b) 2 year averaged solar cycle from kodaikanal sunspot area data

minima and maxima becomes very difficult. So the procedure which is followed in literature to determine Waldmeier effect is somewhat arbitrary. (Dikpati et al., 2008) had taken a straight forward approach to calculate rise time and rise rate. They have calculated the rise time as the time difference from minima to maxima for each cycle and ended up with no significant correlations between rise time and amplitude of the cycle (WE1). They concluded that “*the inverse correlation between cycle peak and rise time originally found in Wolf sunspot number data by Waldmeier (1935) is not present in another solar cycle index, namely sunspot area data*”. Karak & Choudhuri (2011) then slightly changed the procedure of determination of rise time and they calculated the rise time by taking the time difference between which the solar cycle reaches to $0.8P$ from $0.2P$, where P = peak amplitude of the cycle. When they defined the rise time in this way they got a good correlation (See fig1(b) of Karak & Choudhuri (2011)) which was not found in Dikpati et al. (2008) calculations. We want to reconfirm the Waldmeier effect from the Kodaikanal sunspot area data. The reconfirmation of Waldmeier effect from completely different sunspot area data set is not only important for the prediction of the peak amplitude when cycle is in the early stage but also it is important to validate our existing

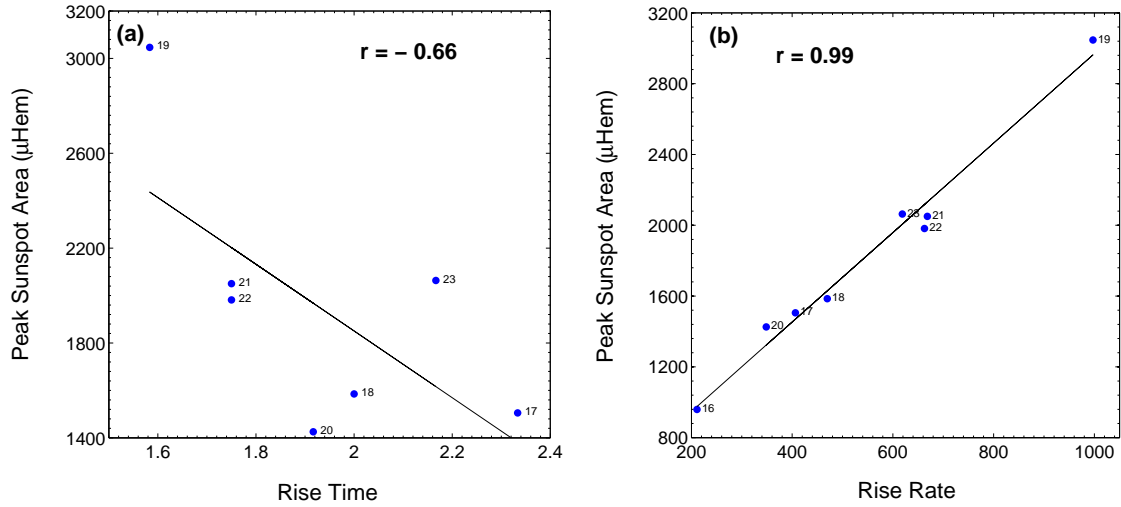


Fig. 3.6 Panel (a) shows the scatter plot of rise time (in years) and the peak amplitude of same solar cycle (FWHM=2 year). Solid line represents best linear fit. Scatter plot of rise rate ($\mu\text{Hem}/\text{year}$) and the peak amplitude of same solar cycle (FWHM=2 year) is shown in panel (b). Solar cycle numbers also marked beside each of the blue circles.

dynamo models. Following [Karak & Choudhuri \(2011\)](#), we have calculated the rise time as the time differences between the time where solar cycle reaches to $0.8P$ from $0.2P$, where P the peak sunspot area. On the other hand rise rate is defined as the slope between two points separated by one year and the first point is chosen one year before the cycle maxima. These calculation are done for both the 1 year and 2 years average dataset. Panel (a) in Figure 3.6 shows the plot between the rise time and the peak amplitude (WE1) of the cycle for 2 years average dataset. We see an anti-correlation ($r = -0.66$) between these two parameters and we can confirm that the Waldmeier effect is a true property of the solar cycle. Since the minima of the cycle 16 is not captured in 2 years averaged data (see Fig 3.5b), so we have plotted this correlation (WE1) with 7 data points for 7 cycles only. Similarly in panel (b) in Figure 3.6, the correlation between the rise rate and cycle amplitude is calculated and it is evident from the figure that WE2 is also well reproduced with correlation coefficients $r = 0.99$. Here we should mention that these correlation coefficient which we have calculated here are the normal Pearson correlation coefficient, and normal Pearson correlation coefficients are statistically significant when we have a large number of data points but for all our calculations we have only data points for 8 cycles. So are these correlation coefficients statistically significant? Yes, they are. The normal practice for calculating the correlation coefficient with less data points is

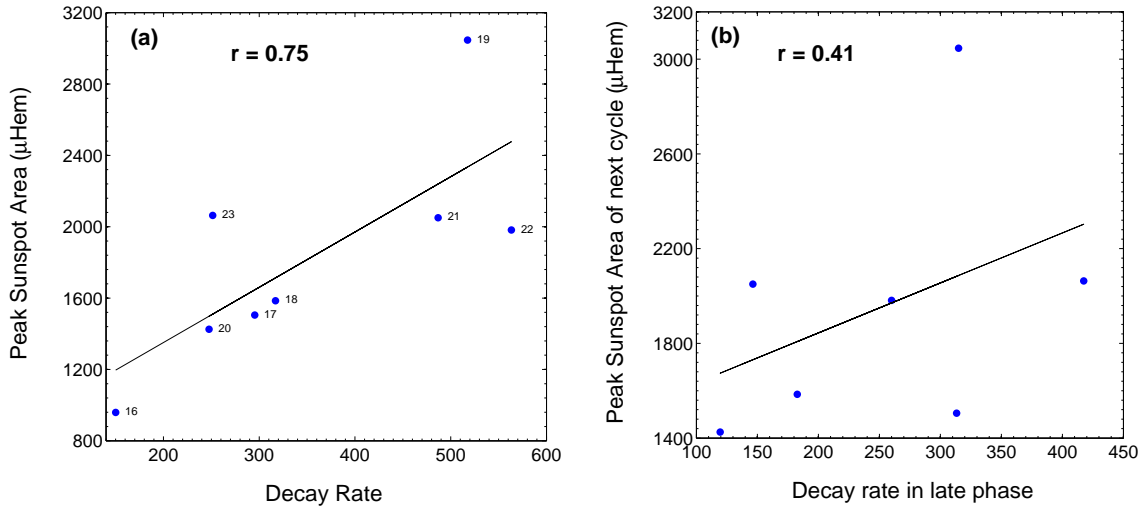


Fig. 3.7 Panel (a) shows the scatter plot of decay rate and the peak amplitude of same solar cycle (FWHM=2 year). Best linear fit is shown with the solid line. Panel (b) shows the scatter plot of decay rate at late phase and the peak amplitude of the next cycle.

to calculate the adjusted Pearson correlation coefficient (r_{adj}) which is given below

$$r_{adj}^2 = 1 - (1 - r^2) \frac{n-1}{n-p-1} \quad (3.1)$$

where r is the normal correlation coefficient, n is the number of data points and p is the independent variables. So the calculated values of adjusted coefficient for $r = -0.66$ (WE1) and $r = -0.99$ (WE2) become $r_{adj} = -0.57$ and $r_{adj} = 0.99$ respectively. So if you are dealing with a statistically high correlation coefficient then adjusted correlation coefficients give almost similar value. In Table 3.2 we have summarized the different correlation coefficient values which are calculated using Gaussian filter with a FWHM of 1 year. The correlations with 2 years averaged data is also enlisted in the Table for comparison. It is found that the statistical trends are almost similar for both the cases but the value of correlation coefficients differs slightly.

3.2.4.2 The correlations in descending phase of the solar cycle

In the previous section we mentioned that the presence of small fluctuations and the double peaks in the solar cycle makes it difficult to identify the actual minima and maxima of a cycle. To avoid this discrepancy, we have excluded the actual cycle minima and the maxima in our decay rate calculation. The final decay rate of a particular cycle has been determined by

Table 3.2 Correlation coefficients at different phase of solar cycle

Smoothed data with FWHM	Correlations during rising phase of the cycle between		Correlations during decaying phase of the cycle between	
	Rise time and cycle amplitude (WE1)	Rise rate and cycle amplitude (WE2)	Decay rate and cycle amplitude	Decay rate at late phase and cycle amplitude of next cycle
1 year	-0.63	0.92	0.57	0.56
2 years	-0.66	0.99	0.75	0.41

averaging over the individual decay rates calculated at four different locations as described in Section 3.2.1. Hence these decay rates are the decay rate for the entire phase of the cycle. For correlations of decay rate with next cycle amplitude, we have calculated decay rate at late phase. In panel (a) of Figure 3.7 we have shown the correlations between the final decay rate of a cycle with the cycle amplitude using 2 years average sunspot area data. The correlations of decay rate calculated at the late phase of cycle with the amplitude of the next cycle is shown in panel (b) of Figure 3.7. We obtain a correlation coefficients $r = 0.75$ for the correlation between decay rate and cycle amplitude for same cycle whereas we get $r = 0.41$ for decay rate at late phase with next cycle amplitude. The correlation coefficients obtained from one year averaged data (FWHM = 1 year) is also given in Table 3.2. From the values given in the Table 3.2, we notice that the correlation coefficients are of comparable values. During the calculation of the decay rates correlations with less data points one should calculate ‘adjusted correlation coefficient’ as we mentioned in the previous section and when we calculate adjusted correlation coefficient, it does not vary much for high value of correlation coefficient. So we keep the normal Pearson correlation coefficients here. This reconfirmations of various correlations from persistent century long kodaikanal sunspot area data help to understand that they are the true nature of the solar cycle and no statistical artifact.

3.3 Theoretical Framework of the Dynamo Model

We carry out our theoretical studies using the flux transport dynamo model originally presented by Chatterjee et al. (2004). In this model, the evolution of the axisymmetric two-dimensional magnetic field is governed by following two equations:

$$\frac{\partial A}{\partial t} + \frac{1}{s}(\mathbf{v} \cdot \nabla)(sA) = \eta_p \left(\nabla^2 - \frac{1}{s^2} \right) A + S_{BL}(r, \theta; B), \quad (3.2)$$

$$\frac{\partial B}{\partial t} + \frac{1}{r} \left[\frac{\partial}{\partial r}(rv_r B) + \frac{\partial}{\partial \theta}(v_\theta B) \right] = \eta_t \left(\nabla^2 - \frac{1}{s^2} \right) B + s(\mathbf{B}_p \cdot \nabla)\Omega + \frac{1}{r} \frac{d\eta_t}{dr} \frac{\partial B}{\partial r}, \quad (3.3)$$

where $s = r \sin \theta$, $B(r, \theta, t)$ is the toroidal component of the magnetic field, $A(r, \theta, t)$ is the vector potential of the poloidal field, $\mathbf{v} = v_r \hat{\mathbf{r}} + v_\theta \hat{\boldsymbol{\theta}}$ is the velocity of the meridional flow, Ω is the internal angular velocity of the Sun and η_t , η_p are the turbulent diffusivities of the toroidal and the poloidal fields. Since the detailed discussion of the parameters and boundary conditions are given in [Chatterjee et al. \(2004\)](#) and [Karak & Choudhuri \(2011\)](#), here we do not discuss them again. We only make a few remarks about magnetic buoyancy and about the term $S_{\text{BL}}(r, \theta; B)$ appearing in Equation (3.2), which captures the longitude averaged B-L mechanism.

Let us discuss how the magnetic buoyancy is treated in this model. When the toroidal field above the tachocline ($r = 0.71R_\odot$) at any latitude exceeds a certain value, a fraction of it is reduced there and the equivalent amount of this field is added on the solar surface. Then this local toroidal field near the surface is multiplied by a factor α to give the poloidal field. The source term in Equation (3.2), therefore, is

$$S_{\text{BL}}(r, \theta; B) = \alpha B(r, \theta, t), \quad (3.4)$$

where

$$\alpha = \frac{\alpha_0}{4} \cos \theta \left[1 + \operatorname{erf} \left(\frac{r - 0.95R_\odot}{0.03R_\odot} \right) \right] \left[1 - \operatorname{erf} \left(\frac{r - R_\odot}{0.03R_\odot} \right) \right], \quad (3.5)$$

with $\alpha_0 = 30 \text{ m s}^{-1}$. Now our job is to use this model to study the observed features of solar cycle reported in previous sections. To study any irregular feature of the solar cycle, we have to make the cycles unequal by introducing randomness in this regular dynamo model, as we discuss in the following sections.

In most of our calculations, we have followed [Chatterjee et al. \(2004\)](#) in assuming the meridional circulation to consist of one cell. Of late, this assumption has been questioned, although the exact nature of the meridional circulation in the deeper layers of the convection zone is still not known. We have shown in Section 3.4.4 that we can retain the attractive features of our results with more complicated meridional circulation ([Hazra et al., 2014](#)). We have also included the near-surface shear layer in the calculations presented in Section 3.4.4

3.4 Results of Theoretical Modeling

3.4.1 Fluctuations in the Poloidal Field Generation

We have discussed in the Introduction that the Sun does not produce equal amount of poloidal field at the end of every cycle and that the generation of the poloidal field involves randomness. Therefore, similar to adding stochastic fluctuations in the traditional mean-field alpha ([Choud-](#)

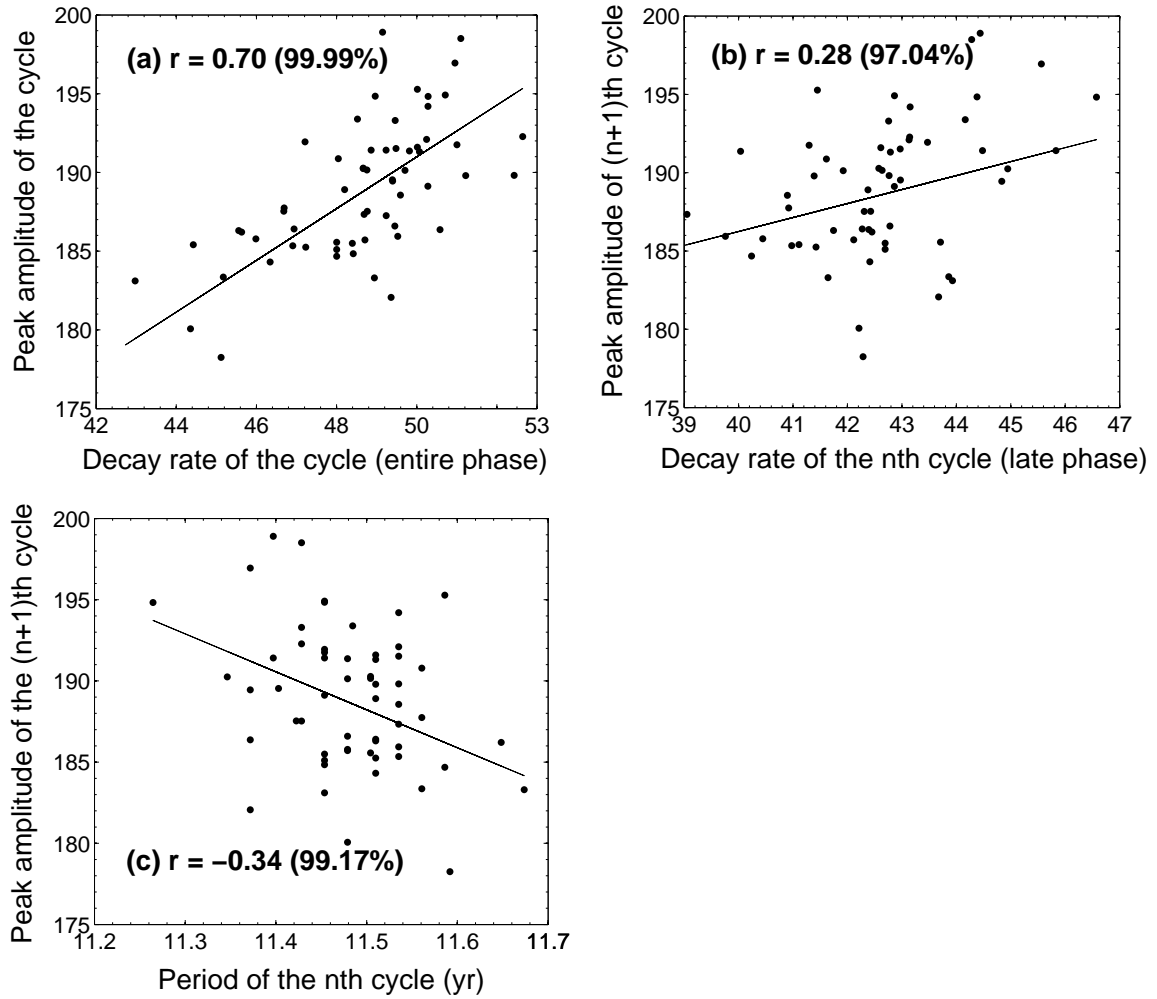


Fig. 3.8 Results from stochastically forced dynamo model with B-L α fluctuations: Scatter plots showing the correlations between (a) the decay rate and the amplitude of cycle n , (b) the decay rate of cycle n and the amplitude of cycle $n + 1$, (c) the period of cycle n and the amplitude of cycle $n + 1$.

huri, 1992), adding stochastic fluctuations in the B-L α has become a standard practice in the flux transport dynamo community (Charbonneau & Dikpati, 2000; Jiang et al., 2007; Karak & Nandy, 2012). In the present work, first we introduce stochastic noise in the B-L α in the following way:

$$\alpha_0 \rightarrow \alpha_0 + \sigma(t, \tau)\alpha'_0, \quad (3.6)$$

where τ is the coherence time during which the fluctuating component remains constant and σ

is a uniformly distributed random number in the interval $[-1, 1]$. Considering the typical decay time of the active regions by surface flux transport process, we fix the coherence time within 0.5 – 2 months. To see a noticeable effect, we add 75% fluctuations in α (*i.e.*, $\alpha'_0/\alpha_0 = 0.75$) with coherence time of 1 month. From this stochastically forced model we have to calculate a measure of the theoretical sunspot number. We consider the magnetic energy density (B^2) of toroidal field at latitude 15° at the base of the convection zone ($r = 0.7R_\odot$) as a proxy of sunspot number (this was done by Charbonneau & Dikpati (2000)). Note that absolute value of the theoretical sunspot number does not have any physical meaning. Therefore, we scale it by an appropriate factor to match it with the observed sunspot number. From the time series of theoretical sunspot number, we calculate the cycle periods and decay rates in the same way as we have done for the observational data.

In Figure 3.8(a) we show the correlation between the decay rates and the amplitudes of the same cycles. We see a positive correlation as in the observed data presented in Figure 3.1. It is easy to understand the reason behind getting this positive correlation. Since we have kept meridional circulation fixed, the periods of the solar cycle do not vary much but the cycle strengths do vary due to the fluctuations in the poloidal field generation. Therefore, when the amplitude of a cycle increases while its period remains approximately fixed, the cycle has to decay rapidly. Hence we find that the stronger cycles decay faster than the weaker cycles, producing the positive correlation seen in Figure 3.8(a). However, we see in Figure 3.8(b) that there is not much correlation between the decay rate of the cycle n and the amplitude of the next cycle $n + 1$ and we are unable to explain the observed correlation seen in Figure 3.2. Note that for Figure 3.8(a) the decay rates are calculated from the entire decaying part of the cycle which is more appropriate definition of the decay rate as we argued in Section 3.2, whereas for Figure 3.8(b) it is computed at the late decay phase because observationally we find strong correlation when decay rate is computed in late decay phase only. Finally we see in Figure 3.8(c) that in this study the observed anti-correlation between the period of cycle n and the amplitude of cycle $n + 1$ (shown in Figure 3.4) is also not reproduced. Note that the period does not vary too much when the meridional circulation is kept constant.

To sum up, when we introduce fluctuations in the poloidal field generation mechanism, we can explain the observed correlation between the decay rate and the amplitude of the cycle shown in Figure 3.1, but we cannot explain the other observed correlations presented in Figures 3.2 and 3.4.

3.4.2 Fluctuations in the Meridional Circulation

Next we introduce the other important source of fluctuations in the flux transport dynamo model, namely, variations of the meridional circulation. Although we have some observational

results of the meridional circulation variations near the solar surface for the last 15 – 20 years, we do not have long data to conclude the nature of long-term variations (Chou & Dai, 2001; Hathaway & Rightmire, 2010). However, there are indirect evidences for the variation of the meridional circulation over a long time (Karak, 2010; Lopes & Passos, 2009; Passos & Lopes, 2012). Particularly, Karak & Choudhuri (2011) have used the durations of the past cycles to argue that the meridional circulation has long-term variations with the coherence time of probably 20 – 45 years. There can also be short-term variations in the meridional circulation whose time scale may be related to the convective turnover time of the solar convection zone. Such variations with the time scale from a few months to a year are also observed in global magnetohydrodynamic simulations (Karak et al., 2014c). In this work, we vary the amplitude of the meridional circulation in the same way as we have done for the α term but with a different coherence time. We show the results of simulations with 30% fluctuations in the meridional circulation with coherence time of 30 years. We shall discuss later that various observed correlations can be explained only if the coherence time is assumed to be not much less than the cycle period. While fluctuations of shorter duration (along with spatial variations) are likely to be present in the meridional circulation, we believe that they do not play any role in producing the correlations we are studying. With 30% level of fluctuations with a coherence time of 30 years, we get variations of the amplitude and of the period in our theoretical model comparable to the observational data. As in Section 3.4.1, we take the time series (B^2) at latitude 15° at the base of the convection zone as our proxy of sunspot activity and calculate the required correlations from it. The relevant correlation plots are shown in Figure 3.9. We see in Figure 3.9(a) that now the correlation between the decay rates and the cycle amplitudes has improved. Importantly, the other correlations are also correctly reproduced in Figures 3.9(b) and 3.9(c) and can be compared with the observational plots Figure 3.2(b) and Figure 3.4. These correlations did not appear at all when the fluctuations in poloidal field generation was introduced (*cf.* Figures 3.8(b) and 3.8(c)). To show how the correlations change on changing the correlation time or the level of fluctuations, we tabulate the values of correlations coefficients under different situations in Table 3.3. Each correlation coefficient is calculated from a run of 50 cycles. It should be kept in mind that there is some statistical noise in the values of correlation coefficients. If the correlation coefficient for exactly the same set of parameters is calculated from different independent runs, the values for different runs will be a little bit different. Keeping this in mind, we note that there is no clear trend of the correlation coefficients increasing or decreasing with increasing levels of fluctuations (other things being the same). However, all the correlation coefficients tend to decrease on decreasing the coherence time.

It is not difficult to understand how the correlation in Figure 3.9(a) arises. For a stronger cycle, the sunspot number has to decrease by a larger amount during the decay phase, making the

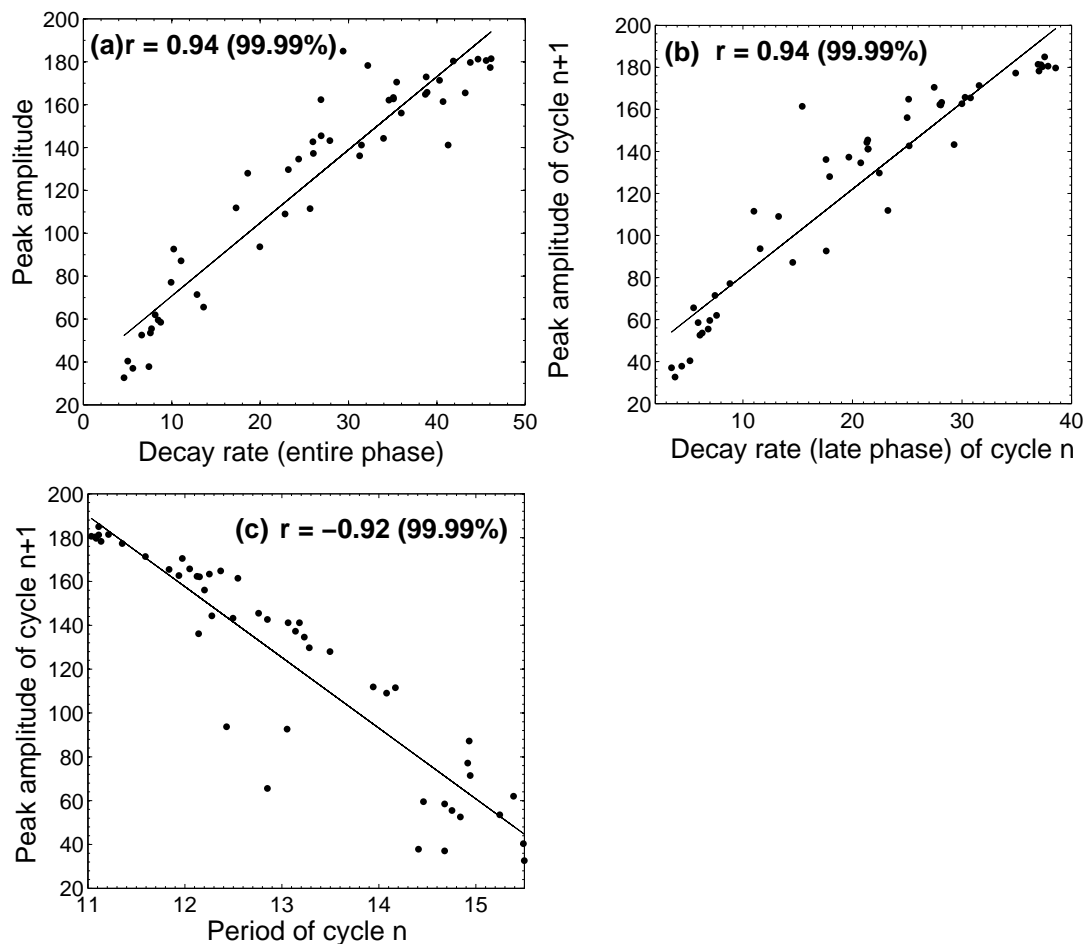


Fig. 3.9 Same as Figure 3.8 but with meridional circulation fluctuations.

decay rate faster. However, to understand the physical reason behind the other two correlations seen in Figures 3.9(b) and 3.9(c), more subtle arguments are needed. Karak & Choudhuri (2011) extended the arguments of Yeates et al. (2008) and pointed out that a weaker meridional circulation, which makes the cycles longer, will have two effects. Firstly, the differential rotation has more time to generate more toroidal field and tends to make the cycles stronger. Secondly, the turbulent diffusivity gets more time to act on the fields and tends to make the cycles weaker. When the diffusivity is high (as in our model), the second effect dominates over the first and the longer cycles are weaker (the opposite is true for dynamo models with low diffusivity). Karak & Choudhuri (2011) showed that this led to an explanation of the Waldmeier effect for dynamo models with high diffusivity. We now point out that this tendency (longer

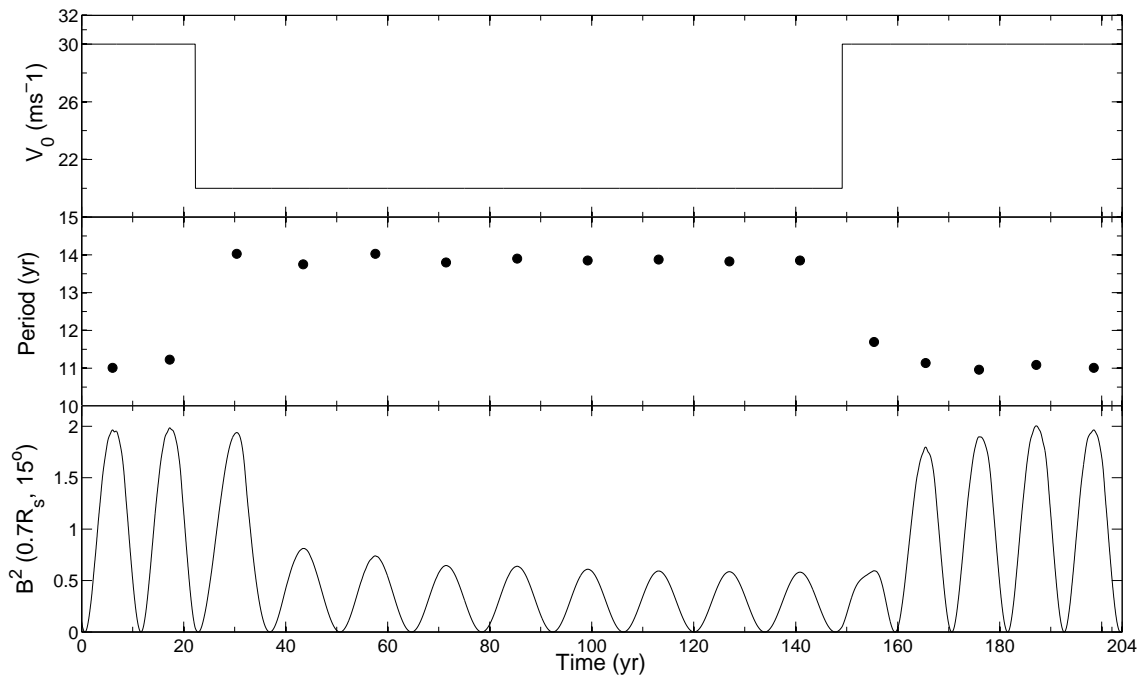


Fig. 3.10 Plots showing how the variation of meridional circulation, measured by v_0 , with time (upper panel) changes the period of the cycle (middle panel) and strength of the magnetic field (shown by B^2 in the lower panel).

cycles tending to be weaker) is also crucial in our understanding of the correlations seen in Figures 3.9(b) and 3.9(c).

If the meridional circulation keeps fluctuating with a coherence time of 30 years, it would happen very often that the meridional circulation would have a certain value during a cycle (say cycle n) and the early rising phase of the next cycle (say cycle $n+1$). This is less likely to happen when the coherence time is reduced. Suppose the meridional circulation is weaker during cycle n and the rising phase of cycle $n+1$. Then cycle n will tend to be longer and to have a weaker decay rate. The following cycle $n+1$ will have a tendency of being weaker. This will produce the correlations seen in Figures 3.9(b) and 3.9(c). On decreasing the coherence time, it will happen less often that the meridional circulation will be the same during cycle n and the rising phase of the next cycle $n+1$. Hence the correlations degrade on decreasing the coherence time of the meridional circulation.

We have realized that there is also a memory effect, which enhances the correlations explained in the previous paragraph. To illustrate this memory effect, we make a run of our dynamo code in which the meridional circulation is decreased suddenly during a sunspot minimum and then brought back to its original value during another sunspot minimum a

few cycles later. The meridional circulation and the resulting sunspot activity are plotted in Figure 3.10. The periods of successive cycles are also indicated in the middle panel of Figure 3.10. On changing the meridional circulation, it is found that the periods of cycles begin changing almost immediately. However, there seems to be a memory effect as far as the amplitudes of the cycles are concerned. Even after the meridional circulation changes, the amplitude of the next cycle is very similar to the amplitude corresponding to the earlier value of the meridional circulation. This memory effect will certainly enhance the correlations we are discussing. Suppose the meridional circulation is weaker during the cycle n , making its period longer and decay rate weaker. Even if the meridional circulation becomes stronger by the rising phase of the next cycle $n + 1$, the memory effect will ensure the amplitude of the cycle $n + 1$ will still be weak, thereby producing the correlation.

At this point, we would like to mention a misconception behind the correlation between cycle n period and cycle $n + 1$ amplitude. It may be thought that the overlap between two cycles during solar minimum is the cause of this correlation. If the next cycle is stronger, then it starts early and the overlap with the present cycle is more. This makes the present cycle shorter. However we believe that this is not the source of this correlation because if this is so, then we would have seen this correlation in Figure 3.8(c) also, where cycle strengths were varied by fluctuations in the poloidal field generation. So the overlap is not the reason behind this correlation and we only get this in high diffusivity dynamo model with fluctuating meridional circulation.

3.4.3 Fluctuations in the Poloidal Field Generation and the Meridional Circulation

Finally we add fluctuations in both the poloidal field generation process and the meridional circulation of the regular model, which is the realistic scenario. We add the same amount of fluctuations in poloidal field generation and in meridional circulation that we had added earlier in the individual cases (*i.e.*, 75% fluctuations in the poloidal field generation with a coherence time of 1 month and 30% fluctuations in the meridional circulation with a coherence time of 30 years). The results are shown in Figures 3.11. In this figure, we see that the scatters in the correlation plots are very close to what we find in actual observations. It is perhaps not a big surprise that all the correlations are reproduced correctly, because they were already reproduced on introducing fluctuations in meridional circulation alone.

A correct theoretical model also should explain the lack of correlation seen in Figure 3.3 between peaks of two successive cycles. Figure 3.12(a) shows the correlation between the amplitude of cycle n and the amplitude of cycle $n + 1$ for the same level of fluctuations which

Table 3.3 Correlation coefficients at different levels of fluctuations and coherence time of meridional circulation.

Coherence time (year)	Fluctuations (%)	Correlation of decay rate with cycle amplitude of		Correlation of previous cycle period with amplitude
		Same cycle (Entire phase)	Next cycle (Late phase)	
30	10	0.92	0.92	-0.97
	20	0.86	0.92	-0.95
	30	0.87	0.89	-0.96
	40	0.92	0.96	-0.73
	50	0.87	0.91	-0.94
20	10	0.79	0.85	-0.95
	20	0.86	0.86	-0.98
	30	0.93	0.96	-0.97
	40	0.90	0.87	-0.88
	50	0.89	0.90	-0.97
11	10	0.78	0.74	-0.90
	20	0.88	0.77	-0.97
	30	0.90	0.85	-0.92
	40	0.82	0.74	-0.89
	50	0.82	0.84	-0.83
5.5	10	0.70	0.63	-0.87
	20	0.83	0.74	-0.86
	30	0.81	0.79	-0.84
	40	0.81	0.57	-0.85
	50	0.80	0.81	-0.78
1	10	0.57	0.48	-0.78
	20	0.58	0.59	-0.64
	30	0.61	0.67	-0.80
	40	0.73	0.25	-0.65
	50	0.69	0.38	-0.72
	75	0.64	0.39	-0.58
	100	0.65	0.73	-0.76
0.5	10	0.42	0.62	-0.80
	20	0.56	0.69	-0.78
	30	0.68	0.47	-0.74
	40	0.62	0.56	-0.67
	50	0.61	0.56	-0.79
	75	0.64	0.50	-0.81
	100	0.64	0.60	-0.87

were used to generate Figure 3.11, whereas Figure 3.12(b) gives the same correlation when the fluctuation in B-L α is raised to 100% from 75%. It is found that the correlations between these amplitudes is weak and becomes weaker still on increasing the fluctuation in the B-L α . A physical interpretation is not difficult to give. A coherence time of 30 years in meridional circulation implies that very often the meridional circulation will be the same during two successive cycles, trying to produce a correlation between the cycles. On the other hand, a fluctuation in the B-L α will definitely try to reduce the correlation. Certainly this fluctuation would try to reduce the correlations seen in Figure 3.11 as well. However, for our choice of parameters, we are able to theoretically reproduce the three observed correlations as shown in Figure 3.11, whereas the correlation between successive cycles is much weaker in conformity with observations. We may mention that we also get an anti-correlation between the amplitude of a cycle and its duration. Our theoretical correlation coefficient ($r = -0.65$) is somewhat stronger than what Charbonneau and Dikpati (2000) obtained from the observational data ($r = -0.37$).

3.4.4 Robustness of the Results on Changing the Meridional Circulation and Differential Rotation Profiles

So far, our earlier computations are performed using a single-cell meridional circulation in each hemisphere. However, recent observations, helioseismic inversions and convection simulations suggest the possibility that the meridional circulation may have a complicated multi-cellular structure rather than being single-cellular (Karak et al., 2015; Zhao et al., 2013). In Hazra et al. (2014), we have shown that the flux transport dynamo model can reproduce most of basic features of solar cycle using multi-structured meridional circulation as long as there is an equator-ward flow near the bottom of the convection zone. Therefore we are curious to know whether the correlations studied in this chapter are also reproduced with multi-structured circulation. To answer this question, we perform a simulation with three radially stacked circulation cells, exactly the same as used in Section 3 of Hazra et al. (2014). For the differential rotation in all our previous works, we have used a simplified profile of the observed differential rotation that does not capture the near-surface shear layer (see *e.g.* Figure 1 of Chatterjee et al. (2004)). Although it is expected that the near-surface shear layer does not produce significant effect on global large-scale fields in the flux transport dynamo (Dikpati et al., 2002), just for the sake of completeness we use a somewhat improved profile of differential rotation captured by the following analytical formula

$$\Omega(r, \theta) = \sum_{j=0}^2 \cos\left(2j\left(\frac{\pi}{2} - \theta\right)\right) \sum_{i=0}^4 c_{ij}(r/R_{\odot})^i. \quad (3.7)$$

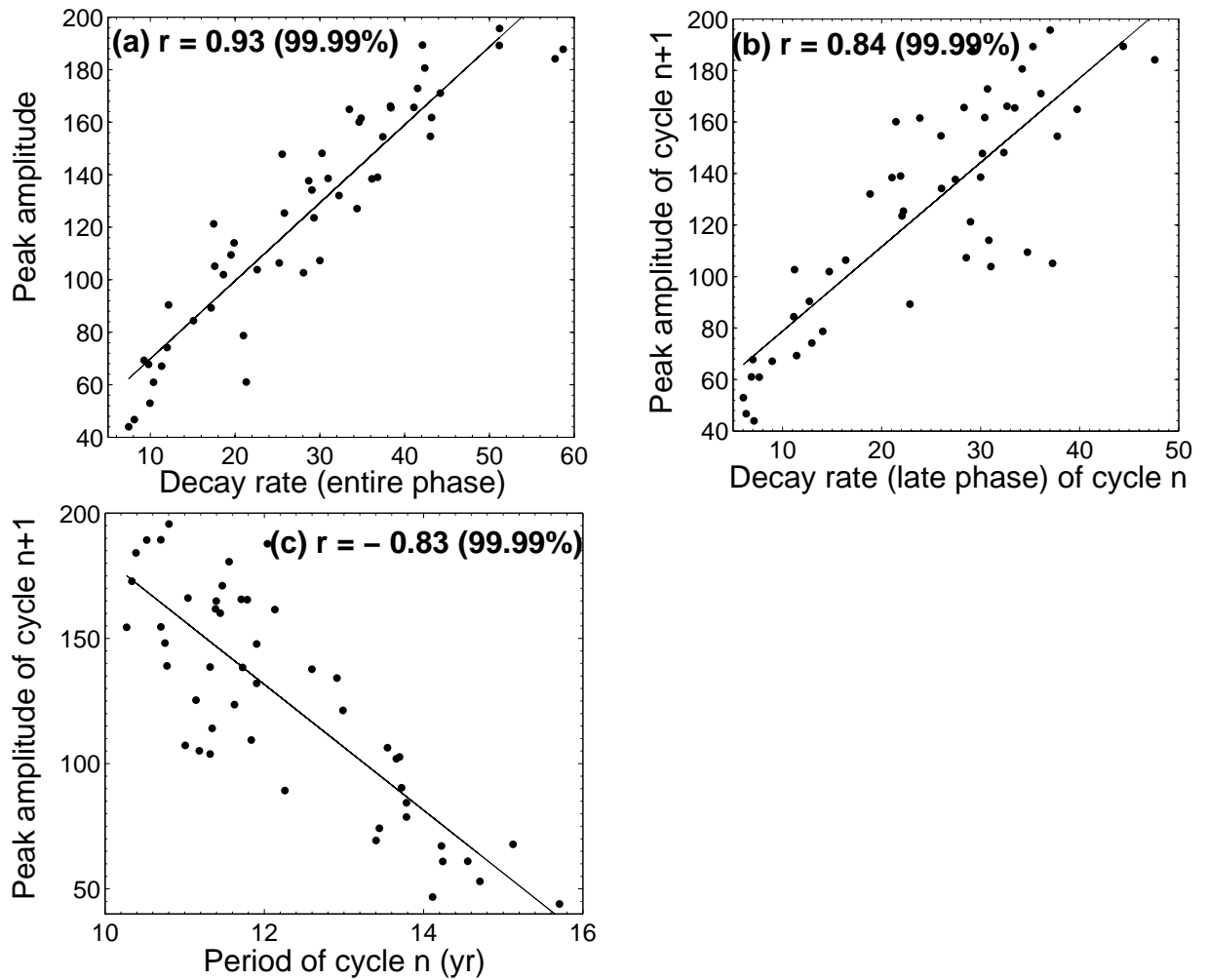


Fig. 3.11 Same as Figure 3.8 but with both B-L α and meridional circulation fluctuations.

For the coefficients c_{ij} see Table 1 of [Belvedere et al. \(2000\)](#), (see also their Figure 1 for the comparison with observed profile).

With these new profiles of the meridional circulation and the differential rotation, we perform a dynamo simulation by adding the same amount of stochastic fluctuations in B-L α and in meridional circulation as done in the previous section. In the results presented earlier, magnetic buoyancy was treated by moving a part of the toroidal magnetic field to the surface whenever it became larger than a critical value. However, as pointed out in [Hazra et al. \(2014\)](#) and [Karak et al. \(2014b\)](#), this way of treating magnetic buoyancy is not very robust under a large change in parameters and model ingredients. Therefore, for the computations of this section we use the ‘non-local’ magnetic buoyancy as used in [Charbonneau & Dikpati \(2000\)](#), and in many other works.

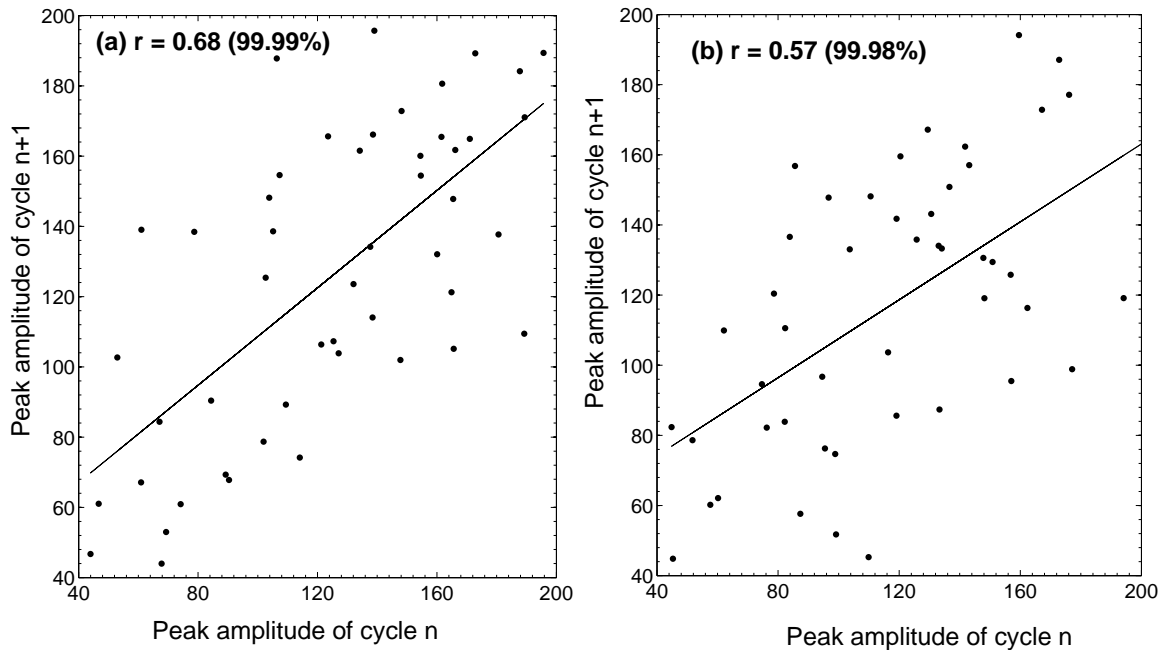


Fig. 3.12 (a) Scatter plot of the amplitude of cycle n with the amplitude of cycle $n + 1$ with 75% fluctuation in B-L α . (b) Same as (a) but with 100% fluctuation in B-L α .

Final results from this computation are shown in Figure 3.13. We observe that even with the *unconventional* meridional flow profile (three radial cells) and addition of near-surface shear layer, the correlations do not disappear. Although the correlations in Figures 3.13(b) and 3.13(c) become a little weaker compared to what we have found for the usual single-cell circulation (Figure 3.11), they show the correct general features as found in observations. The values of the correlations might be improved a little bit by tuning the amount of imposed fluctuations; we do not want to do that here, rather we have used same amount of fluctuations as we used in earlier sections.

We make a few remarks about the two ways of treating magnetic buoyancy. The behavior of the dynamo can become substantially different on treating magnetic buoyancy in these two different ways (see Chapter 2 for detail). Since some magnetic field is removed due to magnetic buoyancy, one would expect the strength of the toroidal field at the bottom of the convection zone to be depleted due to the action of magnetic buoyancy. One unphysical aspect of the non-local treatment of magnetic buoyancy is that this effect is usually not taken into account. As we have repeatedly pointed out, one requirement for obtaining the Waldmeier effect as well as the correlations discussed in this study is that the effect of diffusivity has to be more

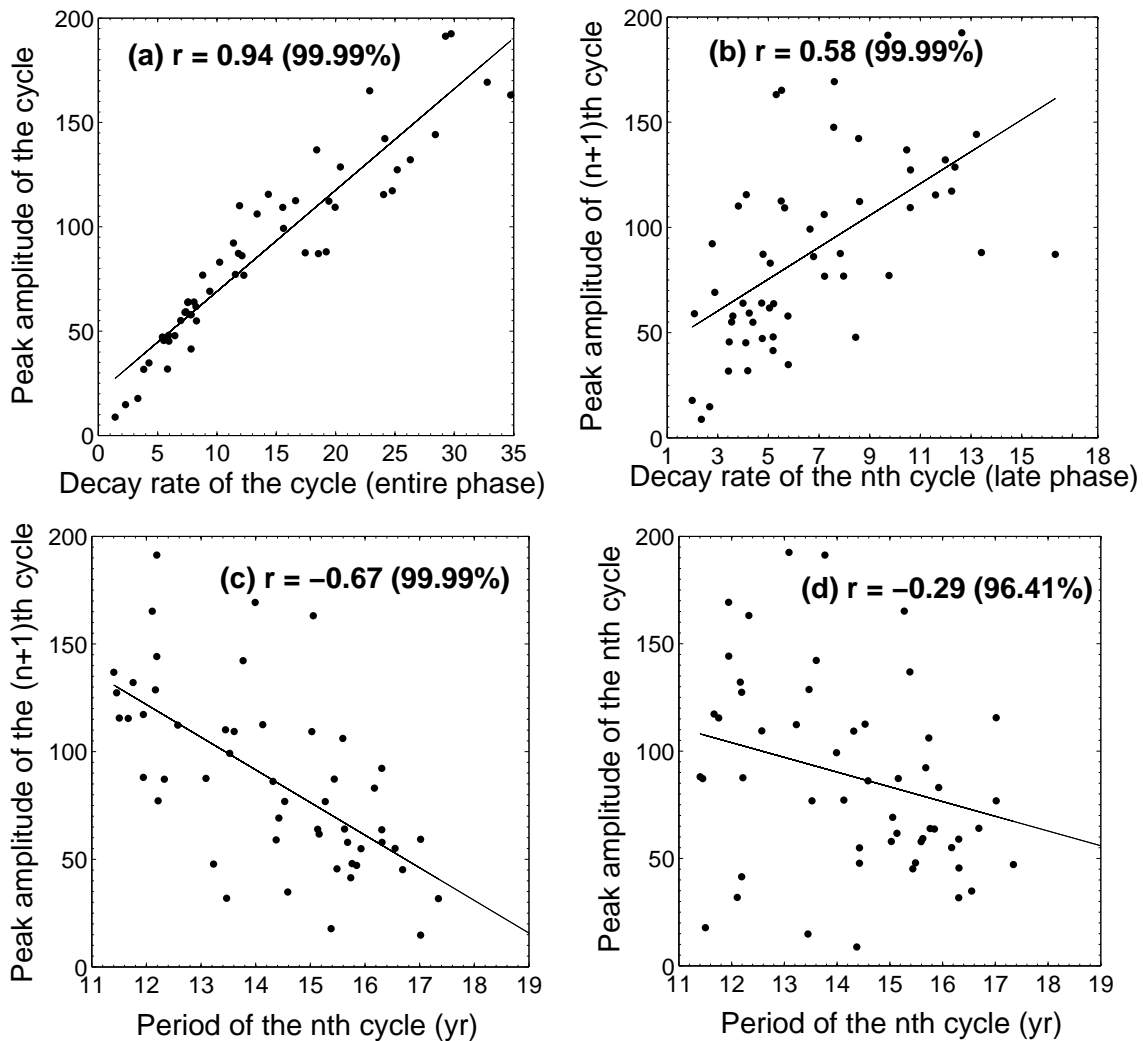


Fig. 3.13 Same as Figure 3.11 but in this model, the large-scale flow has three cells radially stacked in the solar convection zone and the differential rotation includes near surface shear layer.

important than the effect of toroidal field generation. Since the first method of treating magnetic buoyancy (used in the earlier subsections) puts a cap on the strength of the toroidal field but not the second non-local method, toroidal field generation remains unrealistically strong in the second method and it is more difficult to get the correlations properly in this method. We have taken the magnetic energy density (B^2) at latitude 15° at the bottom of the convection zone as the proxy of the sunspot number. In the first method of treating magnetic buoyancy (with the single-cell meridional circulation, as presented in Section 3.4.1–3.4.3), we found that all the correlations come out robustly if we use the magnetic energy density (B^2) in a wide

range of latitudes as a proxy of the sunspot number. However, on using the second method of non-local magnetic buoyancy, we find that the magnetic energy density (B^2) has to be taken in a narrow band of low latitudes, with the correlations disappearing or even reversing if we use the magnetic energy density at higher latitudes. To sum up, the second non-local method of treating magnetic buoyancy is a more robust method and keeps the dynamo stable over a wide range of parameters (which is not the case with the first method). However, it is more difficult to reproduce various observed correlations of the solar cycle with this non-local buoyancy method because the depletion of magnetic field due to buoyancy is not included.

3.5 Conclusion

We have discussed three important features of solar cycle – i) a linear correlation between the amplitude of cycle and its decay rate, ii) a linear correlation between the amplitude of cycle n and the decay rate of cycle $n - 1$ and iii) an anti-correlation between the amplitude of cycle n and the period of cycle $n - 1$. We have seen that all these correlations exist in all the data sets considered here. Last two correlations involve characteristics of one cycle and the amplitude of the next. So they provide useful precursors for predicting a future cycle. Just by measuring the period and the decay rate of a cycle, we can get an idea of the strength of the next cycle.

We have also explored whether these features can be explained in a B-L type flux transport dynamo model. We have first introduced stochastic fluctuations in the poloidal field generation (B-L α term) and we find that only the correlation between the decay rate and the cycle amplitude is reproduced. However when we added fluctuations in the meridional circulation, we found that all three correlations are reproduced in qualitative agreement with observational data. In our high diffusivity dynamo model, strong meridional circulation makes the period shorter and the decay rate faster, but it also makes the next cycle stronger—especially because the cycle strength displays a memory effect, depending on the meridional circulation a few years earlier. The opposite case happens when meridional circulation becomes weaker. Therefore the fluctuations in the meridional circulation are essential to reproduce the observed features. This study is consistent with earlier studies for modeling the cycle durations and strengths of observed cycles (Karak, 2010), the Waldmeier effect (Karak & Choudhuri, 2011), grand minima (Choudhuri & Karak, 2012) and few others (Passos, 2012) which indicate that the variable meridional circulation is crucial in modeling many aspects of the solar cycle. We have found that the observed correlations are reproduced even when the meridional circulation is assumed to be more complicated than the one-cell pattern used in most flux transport dynamo models. However, the coherence time of the fluctuations in the meridional circulation has to be not less than the cycle period in order to produce the correlations. The correlations disappear

on making the coherence time too short, implying that fluctuations in the meridional circulation having coherence time of the order of convective turnover time cannot be the cause of the observed correlations. The theory of meridional circulation is still very poorly understood and we have no understanding of what may cause the fluctuations in meridional circulation with long coherence time. However, the pattern in the periods of the past cycles indicate the presence of such fluctuations ([Karak & Choudhuri, 2011](#)) and the fact that only such fluctuations can explain the various observed correlations of the solar cycle convinces us that such fluctuations in the meridional circulation with long coherence time must exist.

We have pointed out that the period or the decay rate of a cycle may be used to predict the next cycle, since these quantities indicate the strength of the meridional circulation which also determines the amplitude of the next cycle a few years later (due to the memory effect). It seems that the decay rate during the late phase of the cycle is the most reliable precursor for the next cycle, as found in [Figure 3.2\(b\)](#)—presumably because the decay rate during this phase is the best indicator of the meridional circulation during the particular interval of time which is most crucial in determining the amplitude of the next cycle. However, fluctuations in the poloidal field generation process degrades all the observed correlations. As a result, even [Figure 3.2\(b\)](#)—displaying the correlation between the decay rate during the late phase and the amplitude of the next cycle—has considerable scatter, limiting our ability to predict the next cycle in this way.

“We should be unwise to trust scientific inference very far when it becomes divorced from opportunity for observational test”

–Sir Arthur Stanley Eddington, *The Internal Constitution of the Stars*

4

Multi-cell Meridional Circulation in Flux Transport Dynamo Models

The solar activity cycle is successfully modeled by the flux transport dynamo, in which the meridional circulation of the Sun plays an important role. Most of the kinematic dynamo simulations assume a one-cell structure of the meridional circulation within the convection zone, with the equatorward return flow at its bottom. In view of the recent claims that the return flow occurs at a much shallower depth, we explore whether a meridional circulation with such a shallow return flow can still retain the attractive features of the flux transport dynamo (such as a proper butterfly diagram, the proper phase relation between the toroidal and poloidal fields). We consider additional cells of the meridional circulation below the shallow return flow—both the case of multiple cells radially stacked above one another and the case of more complicated cell patterns. As long as there is an equatorward flow in low latitudes at the bottom of the convection zone, we find that the solar behavior is approximately reproduced. However, if there is either no flow or a poleward flow at the bottom of the convection zone, then we cannot reproduce solar behavior. Although this conclusion may change if there is suitable turbulent pumping in the equatorward direction. On making the turbulent diffusivity low, we still find periodic behavior, although the period of the cycle becomes unrealistically large. Also, with a low diffusivity, we do not get

the observed correlation between the polar field at the sunspot minimum and the strength of the next cycle, which is reproduced when diffusivity is high. On introducing radially downward pumping, we get a more reasonable period and more solar-like behavior even with low diffusivity.

4.1 Introduction

The most extensively studied theoretical model of the solar activity cycle in the last few years is the flux transport dynamo model, originally proposed in the 1990s (Choudhuri et al., 1995; Durney, 1995; Wang et al., 1991), and recently reviewed by several authors (Charbonneau, 2010; Choudhuri, 2011b). This model had a remarkable success in explaining various aspects of the solar cycle and its irregularities. However, in spite of its success, doubts are often expressed if this success is merely accidental or if this is the really correct model. Basically this hinges on the question whether the various assumptions used in this model are correct.

Let us consider the crucial assumptions of the model. The toroidal magnetic field is assumed to be produced from the poloidal field by the differential rotation that is mapped by helioseismology, leaving no scope for any doubts. This toroidal field rises due to magnetic buoyancy to the solar surface, where the poloidal magnetic field is produced from it by the Babcock–Leighton mechanism (Babcock, 1961; Leighton, 1964), for which there is now strong observational support (Dasi-Espuig et al., 2010a; Kitchatinov & Olemskoy, 2011a; Muñoz-Jaramillo et al., 2013). It is true that magnetic buoyancy and the Babcock–Leighton mechanism are inherently three-dimensional processes and their representation in a two-dimensional kinematic model can never be fully realistic (Muñoz-Jaramillo et al., 2010; Yeates & Muñoz-Jaramillo, 2013). There are also considerable uncertainties in the values of some parameters, such as the turbulent diffusivity inside the convection zone. The Boulder group (Dikpati et al., 2004) and the Bangalore group (Chatterjee et al., 2004) used values of turbulent diffusivity which differ by a factor of about 50. The higher diffusivity used by the Bangalore group has now got strong support due to the success in explaining various aspects of the observational data (Chatterjee & Choudhuri, 2006; Chatterjee et al., 2004; Choudhuri & Karak, 2009, 2012; Goel & Choudhuri, 2009; Hotta & Yokoyama, 2010; Jiang et al., 2007; Karak, 2010; Karak & Choudhuri, 2011, 2012, 2013; Miesch et al., 2012a; Muñoz-Jaramillo et al., 2013). Because of these uncertainties in the treatment of the Babcock–Leighton mechanism and in the value of turbulent diffusivity, it is necessary to interpret the results of the flux transport dynamo model with some degree of caution. However, these uncertainties do not invalidate the model. After all, different treatments of the Babcock–Leighton mechanism and a range of values for the turbulent diffusivity seem to give qualitatively similar results. The only other important ingredient of the

flux transport dynamo model is the meridional circulation. Because the nature of the meridional circulation in the deeper layers of the convection zone is not yet observationally established, the main source of doubt about the flux transport dynamo model at the present time concerns the question of whether the Sun really has the kind of meridional circulation which is assumed in the flux transport dynamo models.

Let us consider the role of the meridional circulation in flux transport dynamo models. In order for sunspots to form at lower and lower latitudes with the progress of the cycle, a condition known as the Parker–Yoshimura sign rule was expected to be satisfied (Parker (1955b); Yoshimura (1975) see also Choudhuri (1998), Section 16.6). According to this condition, $\alpha \partial\Omega/\partial r$ has to be negative in the northern hemisphere. It follows from observations of solar surface that α corresponding to the Babcock–Leighton mechanism is positive in the northern hemisphere. Helioseismology shows that $\partial\Omega/\partial r$ is also positive in the lower latitudes where sunspots are seen (except in a shear layer just below the solar surface). So clearly the Parker–Yoshimura sign rule is not satisfied and it may be expected that the dynamo wave will propagate in the poleward direction, contrary to observations. Choudhuri et al. (1995) showed that an equatorward meridional circulation at the bottom of the convection zone can overcome the Parker–Yoshimura sign rule and make the dynamo wave propagate in the correct direction. This is the main role of the meridional circulation in the flux transport dynamo models. The second role of the meridional circulation is that the poleward meridional circulation near the solar surface advects the poloidal field poleward, as seen in the observations. In dynamo models with low turbulent diffusivity, the meridional circulation has a third important role. It brings the poloidal field created near the surface to the bottom of the convection zone where the strong differential rotation can act on it to create the toroidal field. In dynamo models with high turbulent diffusivity, however, the poloidal field can diffuse from the surface to the bottom of the convection zone in typically about 5 yr and this third role of the meridional circulation is redundant (Jiang et al., 2007). If there is radial pumping as suggested by some authors (Karak & Nandy, 2012), then that further eliminates the role of meridional circulation for bringing the poloidal field to the bottom of the convection zone. Because we will be using a higher value of turbulent diffusivity in many of our calculations, the twin roles of the meridional circulation in our model will be the equatorward advection of the toroidal field at the bottom of the convection zone and the poleward advection of the poloidal field near the surface.

The simplest kind of meridional circulation assumed in most of the theoretical models consists of one cell encompassing a hemisphere of the convection zone, with a poleward flow in the upper layers and an equatorward flow in the lower layers. This kind of meridional circulation successfully plays the twin roles expected of it in a flux transport dynamo model. Observations show a poleward meridional circulation near the surface, so there is absolutely

no doubt that this part of the meridional circulation advects the poloidal field poleward. The only remaining question is whether the cell of the meridional circulation really penetrates to the bottom of the convection zone where the equatorward flow branch has to be located for the equatorward advection of the toroidal field. Early helioseismic investigations going to a depth of $0.85R_{\odot}$ could not find any evidence of the equatorward return flow until that depth (Braun & Fan, 1998a; Giles et al., 1997). However, recently Hathaway (2012b), assuming that the supergranules are advected by the meridional circulation, analyzed the observational data to conclude that the return flow occurs at depths as shallow as 50–70 Mm. Zhao et al. (2013) also claim on the basis of their helioseismic inversion that the equatorward return flow exists between radii $0.82R_{\odot}$ and $0.91R_{\odot}$. On the other hand, Schad et al. (2013) from the study of global helioseismic analysis find the indication of multi-cell meridional circulation in the whole convection zone. If these results are supported by other independent groups and really turn out to be true, then the very important question is whether the attractive aspects of the present flux transport dynamo models can be retained with such a meridional circulation. In this chapter, we explore whether additional cells of meridional circulation below the shallow return flow can help us solve the problem.

So far only a few theoretical studies of the flux transport dynamo with a meridional circulation more complicated than a single cell have been carried out. The effects of two cells in the latitudinal direction have been considered by Bonanno et al. (2006). However, we now want to consider a more complicated structure of the meridional circulation in the radial direction, including the possibility of multiple cells in the radial direction. Such a study was first carried out by Jouve & Brun (2007). In their calculations, they always had poleward meridional circulation at the bottom of the convection zone in the lower latitudes where sunspots are seen. They were able to get periodic solutions, but the butterfly diagrams were always in the wrong sense, implying poleward migration of the toroidal field. They concluded that “the resulting butterfly diagram and phase relationship between the toroidal and poloidal fields are affected to a point where it is unlikely that such multicellular meridional flows persist for a long period of time inside the Sun, without having to reconsider the model itself” (Jouve & Brun (2007), p. 239). If this conclusion was generally true for any meridional circulation more complicated than the simple single-cell circulation, then the results of Hathaway (2012b); Schad et al. (2013); Zhao et al. (2013), if supported by independent investigations by other groups, would indeed be bad news for flux transport dynamo models. Guerrero & de Gouveia Dal Pino (2008) considered a single cell confined to the upper layers of the convection zone. On introducing strong radial and latitudinal pumping, they were able to get correct butterfly diagrams. However, whether such equatorward latitudinal pumping really exists to give the right kind of butterfly diagram, needs to be studied rigorously. Another recent attempt of saving the flux transport

dynamo has been made by [Pipin & Kosovichev \(2013\)](#), who use the near-surface shear layer found in helioseismology and an equatorward return flow of meridional circulation just below it. Since $\partial\Omega/\partial r$ is negative within this shear layer, such a dynamo would have equatorward propagation according to the Parker–Yoshimura sign rule even in the absence of an equatorward meridional circulation in the right place. However, we are unable to accept this model of [Pipin & Kosovichev \(2013\)](#) as a satisfactory model of the solar cycle for the following reasons. It is known for a long time that magnetic buoyancy is particularly destabilizing in the upper layers of the convection zone and it is impossible to store magnetic fields generated there for sufficient time for dynamo amplification ([Moreno-Insertis, 1983](#); [Parker, 1975](#)). Also, the scenario that the toroidal field is generated within the tachocline and then parts of it rise to produce active regions can explain many aspects of active regions including Joy’s law rather elegantly ([Caligari et al., 1995](#); [Choudhuri, 1989](#); [D’Silva & Choudhuri, 1993](#); [Fan et al., 1993](#)). We find no compelling reason to discard the scenario that the toroidal magnetic field is produced in the tachocline where magnetic buoyancy is suppressed in the regions of sub-adiabatic temperature gradient ([Moreno-Insertis et al., 1992](#)).

The main aim of the present study is to address the question whether a meridional circulation with a return flow at a relatively shallow depth would allow us to retain the attractive features of the flux transport dynamo, without introducing such assumptions as strong equatorward pumping and without abandoning the scenario in which the toroidal field is generated and stored in the tachocline from where it rises to produce active regions. If there is a return flow at a shallow depth and there are no flows underneath it, then we find that the solar cycle cannot be modeled properly with such a flow. However, if there are additional cells of meridional circulation below the shallow return flow, we find that we can retain most of the attractive features of the flux transport dynamo model as long as there is a layer of equatorward flow in low latitudes at the bottom of the convection zone. The existence of such an equatorward flow at the bottom of the convection zone is consistent with the findings of [Zhao et al. \(2013\)](#), who are unable to extend their inversion below $0.75R_{\odot}$ using their limited data set. Also, [Passos et al. \(2015\)](#) have shown that there should be an equatorward flow at the base of the convection zone at mid-latitudes, below the current maximum depth helioseismic measures can probe ($0.75R_{\odot}$) using three-dimensional global simulations of solar convection. Since our knowledge of the meridional circulation either from observational or theoretical considerations is limited, in this study we take the meridional circulation as a free parameter that can be assumed to have any form involving multiple cells and explore the dynamo problem with different kinds of meridional circulation.

We discuss the mathematical formulation of our dynamo model in Section 4.2. Then in Section 4.3 we present our results for several cells of meridional circulation in the radial

direction, whereas Section 4.4 presents results for more complicated meridional circulation with multiple cells in both radial and latitudinal directions. Whether the results get modified for low turbulent diffusivity will be discussed in Section 4.5. The effect of turbulent pumping will be discussed in Section 4.6. Finally we summarize our conclusions in Section 4.7.

4.2 Mathematical formulation

In the two-dimensional kinematic flux transport dynamo model, we represent the magnetic field as

$$\mathbf{B} = B\hat{\mathbf{e}}_\phi + \nabla \times (A\hat{\mathbf{e}}_\phi), \quad (4.1)$$

where $B(r, \theta, t)$ and $A(r, \theta, t)$ respectively correspond to the toroidal and poloidal components which satisfy the following equations:

$$\frac{\partial A}{\partial t} + \frac{1}{s}(\mathbf{v} \cdot \nabla)(sA) = \eta_p \left(\nabla^2 - \frac{1}{s^2} \right) A + S(r, \theta, t), \quad (4.2)$$

$$\frac{\partial B}{\partial t} + \frac{1}{r} \left[\frac{\partial}{\partial r}(rv_r B) + \frac{\partial}{\partial \theta}(v_\theta B) \right] = \eta_t \left(\nabla^2 - \frac{1}{s^2} \right) B + s(\mathbf{B}_p \cdot \nabla)\Omega + \frac{1}{r} \frac{d\eta_t}{dr} \frac{\partial(rB)}{\partial r} \quad (4.3)$$

where $s = r \sin \theta$. Here \mathbf{v} is velocity of the meridional flow, Ω is the internal angular velocity of the Sun, η_p and η_t are turbulent diffusivities and $S(r, \theta, t)$ is the coefficient which describes the generation of poloidal field at the solar surface from the decay of bipolar sunspots. These equations have to be solved with the boundary conditions $A = B = 0$ at $\theta = 0, \pi$, whereas at the top boundary $B = 0$ and A matches a potential field above (Dikpati & Choudhuri, 1995). The bottom boundary condition does not affect the solutions as long as the bottom of the integration region is taken sufficiently below the bottom of the convection zone. Once the parameters Ω , η_p , η_t , \mathbf{v} and $S(r, \theta, t)$ are specified, Equation 4.2 and 4.3 can be solved with the code *Surya* to obtain the behavior of the dynamo (Chatterjee et al., 2004; Nandy & Choudhuri, 2002). Chatterjee et al. (2004) present a detailed discussion how the parameters were specified in their simulations. However, Karak (2010) made some small changes in the parameters. In the calculations in this chapter, we use the Ω , η_p and η_t as Karak (2010), except that Section 4.5 and Section 4.6 present some discussion with different diffusivities which will be explained in Section 4.5. In this chapter we carry out dynamo simulations with different kinds of meridional circulation \mathbf{v} . Before coming to the meridional circulation, let us describe how we specify the poloidal source term $S(r, \theta, t)$.

The effects of the magnetic buoyancy and the Babcock–Leighton mechanism have to be incorporated by suitably specifying the poloidal source term $S(r, \theta, t)$. There are two widely used procedures of specifying magnetic buoyancy. In the first procedure, whenever the toroidal field B at the bottom of the convection zone crosses a critical value, a part of it is brought to the solar surface. In the second procedure, the Babcock–Leighton coefficient α in the source term multiplies the toroidal magnetic field at the bottom of the convection zone rather than the local toroidal field. Although the two procedures with all the other parameters kept the same do not give identical results (see Chapter 2 for details), both the procedures reproduce the qualitative behaviors of the solar cycle. Since we believe the first procedure to be more realistic, we had used it in the majority of calculations from our group (Chatterjee et al., 2004; Choudhuri et al., 2007; Karak, 2010). However, it sometimes becomes difficult to introduce this procedure in a stable way when the meridional circulation is made very complicated. Because we are studying the behavior of the dynamo with various complicated meridional circulations, we have opted for the second procedure. We specify the poloidal source term in Equation 4.2 in the following way:

$$S(r, \theta; B) = \frac{\alpha(r, \theta)}{1 + (\bar{B}(r_t, \theta)/B_0)^2} \bar{B}(r_t, \theta), \quad (4.4)$$

where $\bar{B}(r_t, \theta)$ is the value of the toroidal field at latitude θ averaged over the tachocline from $r = 0.685R_\odot$ to $r = 0.715R_\odot$. We take

$$\alpha(r, \theta) = \frac{\alpha_0}{4} \left[1 + \operatorname{erf} \left(\frac{r - 0.95R_\odot}{0.05R_\odot} \right) \right] \left[1 - \operatorname{erf} \left(\frac{r - R_\odot}{0.01R_\odot} \right) \right] \sin \theta \cos \theta \quad (4.5)$$

$$\times \left[\frac{1}{1 + e^{-30(\theta - \pi/4)}} \right]$$

Note that the last factor in Equation 4.5 suppresses α in the higher latitudes and constrains the butterfly diagram from extending to very high latitudes. We are following many previous authors who also suppressed α in high latitudes by such means (Hotta & Yokoyama, 2010; Muñoz-Jaramillo et al., 2010). Since this suppression of α is not based on a clear physical reason, we have not used such a suppression of α in the previous calculations from our group using the first procedure of treating magnetic buoyancy outlined above. However, on treating magnetic buoyancy by the second procedure, flux eruptions tend to occur at higher latitudes (Choudhuri et al., 2005) and it becomes necessary to suppress eruptions at high latitudes to get more reasonable butterfly diagrams. For calculations presented in Section 4.3 and 4.4 using high diffusivity, we use $\alpha_0 = 8.0 \text{ m s}^{-1}$. In the low diffusivity case presented in Section 4.5, we use a lower value $\alpha_0 = 0.5 \text{ m s}^{-1}$. When we include the effect of radial turbulent pumping in Section 4.6 we use $\alpha_0 = 0.1 \text{ m s}^{-1}$. Note that the parameter B_0 in Equation 4.4 introduces

the only nonlinearity in the problem and determines the amplitude of the magnetic field. We will later present magnetic fields in units of B_0 .

Below we discuss how the meridional circulation is prescribed. The meridional circulation is always defined in terms of stream function ψ which is given by

$$\rho \mathbf{v} = \nabla \times [\psi(r, \theta) \mathbf{e}_\phi], \quad (4.6)$$

with the density profile given by

$$\rho = C \left(\frac{R_\odot}{r} - 0.95 \right)^{3/2}, \quad (4.7)$$

We can generate different types of meridional circulation by choosing ψ suitably. For example, the one-cell meridional circulation used in many of the recent works from our group (Karak, 2010) is obtained by taking

$$\psi r \sin \theta = \psi_0 (r - R_p) \sin \left[\frac{\pi(r - R_p)}{(R_\odot - R_p)} \right] \{1 - e^{-\beta_1 \theta^\varepsilon}\} \times \{1 - e^{\beta_2(\theta - \pi/2)}\} \times e^{-((r - r_0)/\Gamma)^2} \quad (4.8)$$

with $\beta_1 = 1.5$, $\beta_2 = 1.3$, $\varepsilon = 2.0000001$, $r_0 = (R_\odot - R_b)/3.5$, $\Gamma = 3.47 \times 10^8$ m, $R_p = 0.635R_\odot$. The value of ψ_0/C determines the amplitude of the meridional circulation. On taking $\psi_0/C = 0.95 \times 15.0$, the poleward flow near the surface at mid-latitudes peaks around $v_\theta = 15.0$ m s⁻¹. The cell of the meridional circulation is confined between R_p and R_\odot . By making R_p larger (but less than R_\odot), we can make the meridional circulation confined in the upper layers of the convection zone.

In order to have N cells of meridional circulation, we can take a stream function of the form

$$\psi = \psi_1 + \psi_2 + \dots + \psi_N, \quad (4.9)$$

where each term in the stream function gives rise to a cell of meridional circulation. Here we describe how we generate a two-cell meridional circulation pattern, used in some of our simulations. The details of how we generate three-cell and more complicated patterns are given in the Appendix. Since Zhao et al. (2013) claim that the upper cell of the meridional circulation is confined above $0.82R_\odot$, we do some calculations with two cells above and below $R_m = 0.82R_\odot$. To generate such a pattern of meridional circulation, we use the stream function

$$\psi = \psi_u + \psi_l \quad (4.10)$$

The stream function ψ_u which generates the upper cell is given by

$$\psi_u = \psi_{0u} \left[1 - \operatorname{erf} \left(\frac{r - 0.91R_\odot}{1.0} \right) \right] (r - R_{m,u}) \sin \left[\frac{\pi(r - R_{m,u})}{(R_\odot - R_{m,u})} \right] \{1 - e^{-\beta_1 \theta^\varepsilon}\} \times \{1 - e^{\beta_2(\theta - \pi/2)}\} e^{-((r-r_0)/\Gamma)^2} \quad (4.11)$$

where the parameters have the following values: $\beta_1 = 3.5, \beta_2 = 3.3, r_0 = (R_\odot - R_b)/3.5, \Gamma = 3.4 \times 10^8$ m, $R_{m,u} = 0.815R_\odot$. The stream function ψ_l which generates the lower cell is given by

$$\psi_l = \psi_{0l} \left[1 - \operatorname{erf} \left(\frac{r - 0.95R_{m,l}}{1.8} \right) \right] (r - R_p) \sin \left[\frac{\pi(r - R_p)}{(R_{m,l} - R_p)} \right] \{1 - e^{-\beta_1 \theta^\varepsilon}\} \times \{1 - e^{\beta_2(\theta - \pi/2)}\} e^{-((r-r_0)/\Gamma)^2} \quad (4.12)$$

where the parameters have the following values: $\beta_1 = 3.2, \beta_2 = 3.0, r_0 = (R_\odot - R_b)/3.5, \Gamma = 3.24 \times 10^8$ m, $R_p = 0.65R_\odot, R_{m,l} = 0.825R_\odot$. We choose ψ_{0u}/C and ψ_{0l}/C in such a way that the velocity amplitudes in the upper and lower cells are around 20.0 m s^{-1} and 4.0 m s^{-1} respectively.

The two-cell meridional circulation given by the above expressions is shown in the upper part of Figure 4.2. Figure 4.2(a) shows the streamlines of flow, whereas Figure 4.2(b) shows how v_θ varies with r at the mid-latitude. The vertical dashed lines in Figure 4.2(b) indicate bottoms and tops of the two cells. It may be noted that both the cells have anti-clockwise flow patterns. This means that the flows at the bottom of the upper cell and at the top of the lower cell (which are adjacent to each other) are in opposite directions involving a jump in the value of v_θ from one cell to the next, as seen in Figure 4.2(b). If we replace ψ_l by $-\psi_l$, then we can avoid such a jump in the value of v_θ . This flow pattern is shown in the upper part of Figure 4.3. However, in this case, the meridional circulation at the tachocline is in the poleward direction. We shall see in Section 4.3 that this case will not give solar-like solutions. If we want the meridional circulation to be poleward at the surface and equatorward at the tachocline, and additionally we want to avoid a jump in v_θ , then we need at least three cells stacked one above the other in the radial direction. The flows in the top and bottom cells have to be counter-clockwise, whereas the flow in the middle cell has to be clockwise. The Appendix presents the steam function that would give such a flow, which is shown in the upper part of Figure 4.4. The results with all these flow patterns are presented in the next Section, whereas results with a more complicated flow will be presented in Section 4.4. When we discuss the

effects of changing the turbulent diffusivity in Section 4.5, we shall describe how the diffusivity will be changed. Similarly, in Section 4.6 where we discuss the effects of turbulent pumping, we shall explain how pumping is included in the mathematical theory.

4.3 Results with radially stacked cells

Let us first consider the situation that the meridional circulation has a return flow at the middle of the convection zone and there are no flows underneath it. We generate such a meridional circulation by taking $\psi = \psi_u$ with ψ_u given by Equation 4.11. The upper part of Figure 4.1 shows the streamlines and the profile of v_θ as a function of r at the mid-latitude. The middle part of Figure 4.1 is the ‘butterfly diagram’, which is essentially a time-latitude plot of B at the bottom of the convection zone. The bottom part shows the radial field at the solar surface as function of time and latitude. In the butterfly diagram, we find that the belt of strong B propagates poleward rather than equatorward at the low latitudes, although there is a slight tendency of equatorward propagation at the high latitudes. This result can be easily understood from the Parker–Yoshimura sign rule, which holds when there is no flow at the bottom of the convection zone. We have α positive in the northern hemisphere. Since $\partial\Omega/\partial r$ is positive in the low latitudes and negative in the high latitudes (see Figure 1 of Chatterjee et al. (2004) showing the differential rotation we are using), the Parker–Yoshimura sign rule implies poleward propagation at the low latitudes and equatorward propagation at the high latitudes. In this case, we are completely unable to reproduce the solar behavior. It may be noted that Guerrero & de Gouveia Dal Pino (2008) obtained solar-like behavior with a meridional circulation similar to what we have used by including equatorward latitudinal pumping at the bottom of the convection zone. However, observationally it is difficult to find evidence for latitudinal pumping, there are few numerical simulations (Augustson et al., 2015; Käpylä et al., 2006; Racine et al., 2011; Warnecke et al., 2016) which find latitudinal pumping at low latitudes in the bottom half of the convection zone in highly stratified rotating solar convection.

Next we consider the two-cell pattern given by Equations 4.10–4.12. For this case, Figure 4.2 provides plots of the same things that are shown in Figure 4.1 for the earlier case. We see that there is an equatorward flow at the bottom of the convection zone, although there is a jump in v_θ between the cells. We find that the equatorward flow at the bottom forces an equatorward transport of B in accordance with what we see in the Sun. Looking at the lowest part of Figure 4.2, we also see that the polar field changes sign at the time of the sunspot maximum, in accordance with the observations. Thus, on using the two-cell pattern with an equatorward flow at the bottom of the convection zone, we can reproduce the equatorward migration of the sunspot zone as well as the correct phase relationship between the toroidal and

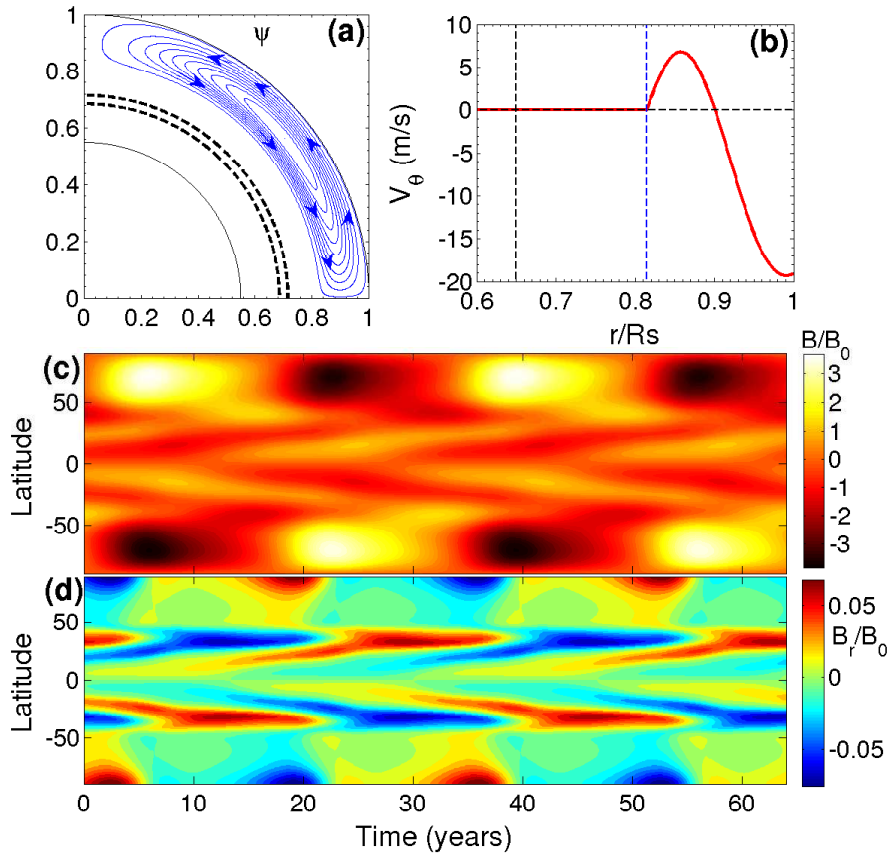


Fig. 4.1 (a) Streamlines of the shallow meridional circulation with no flow underneath. (b) v_θ as a function of r/R_\odot at the mid-latitude $\theta = 45^\circ$. (c) Butterfly diagram i.e, the time-latitude plot of the toroidal field at the bottom of the convection zone ($r = 0.70R_\odot$). (d) Time-latitude plot of the radial field at the surface of the Sun. All the toroidal and radial fields are in the unit of B_0 .

poloidal fields. It is true that the butterfly diagram starts at a somewhat high latitude compared to what we see in the Sun. It is well known that the butterfly diagram can be confined more to lower latitudes by making the meridional circulation a more penetrating (Nandy & Choudhuri, 2002) and playing with other parameters. We had not bothered to fine-tune the parameters to achieve this, since our main aim in this chapter is to study the qualitative behavior of the system under various kinds of meridional circulation. Note from Figures 4.2(c)–(d) that the maximum B at the bottom of the convection zone and the maximum B_r at the surface bear a ratio of about 100. It should be emphasized that this ratio corresponds to smoothed mean field values of B and B_r , which can have very different values inside flux concentrations (Choudhuri, 2003).

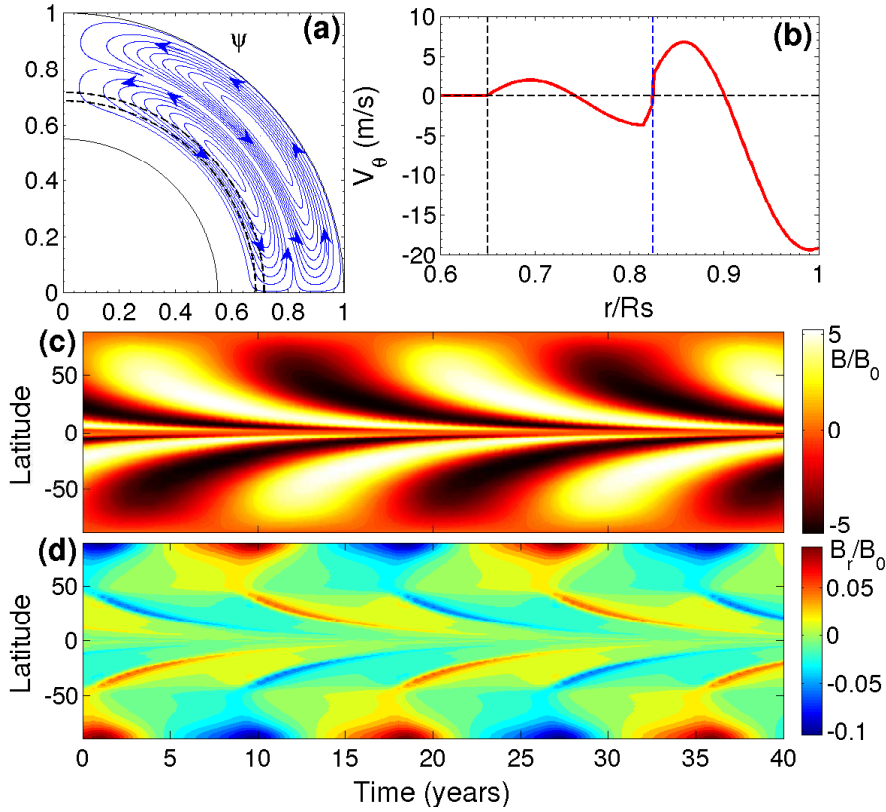


Fig. 4.2 (a) Streamlines for two radially stacked cells of meridional circulation. Arrows show the direction of the flow. (b), (c) and (d) are the same plots as in Figure 4.1, for this meridional circulation.

We can avoid the jump in the value of v_θ seen in Figure 4.2(b) by using a two-cell meridional circulation in which ψ_l is replaced by $-\psi_l$. Since the flow at the bottom of the convection zone is poleward in this case, a study of this case also throws light on the behavior of the dynamo with such a flow. Our results are shown in Figure 4.3. The butterfly diagram indicates poleward migration and the solar behavior is not reproduced in this case. The two-cell meridional circulation we have used is very similar to what was used by Jouve & Brun (2007) in one of their cases (see their Figure 2 and Figure 3). The butterfly diagram we have got is quite similar to what they got.

If we want to avoid a jump in v_θ and also to have a equatorward flow at the bottom of the convection zone, then we need at least three cells of meridional circulation stacked one over the other in the radial direction. The Appendix provides the mathematical prescription for generating such a meridional circulation. Figure 4.4 presents the results. Since there is an

equatorward flow at the bottom of the convection zone, we again find that the solar behavior is reproduced, in the sense of having a butterfly diagram showing equatorward migration as well as the correct phase relationship between the toroidal and poloidal fields.

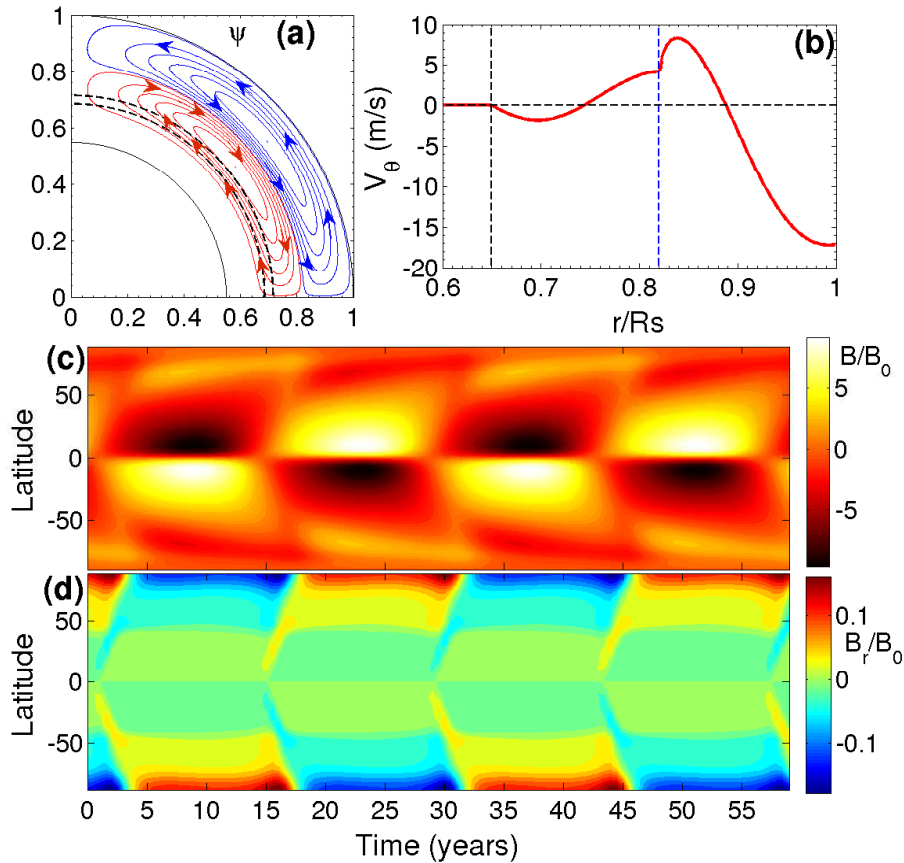


Fig. 4.3 (a) Streamlines for two radially stacked cells of meridional circulation with circulations in the opposite sense. Arrows show the direction of the flow. (b), (c) and (d) are the same plots as in Figure 4.1, for this meridional circulation.

One of the important results for the flux transport dynamo with a single cell of meridional circulation is that the period of the dynamo decreases when the meridional circulation is made faster (Dikpati & Charbonneau, 1999; Karak, 2010). To explore how the dynamo period depends on the flow velocity in the multi-cell situation, we have carried out a study for the case of three cells presented in Figure 4.4. We have carried out numerical experiments by varying the flow amplitude of one cell, while keeping the flows in the other two cells constant. Figure 4.5 shows how the dynamo period changes with the change of the flow speed in each of the three cells. It is clearly seen that the flow speeds in the upper two cells have very minimal effect on

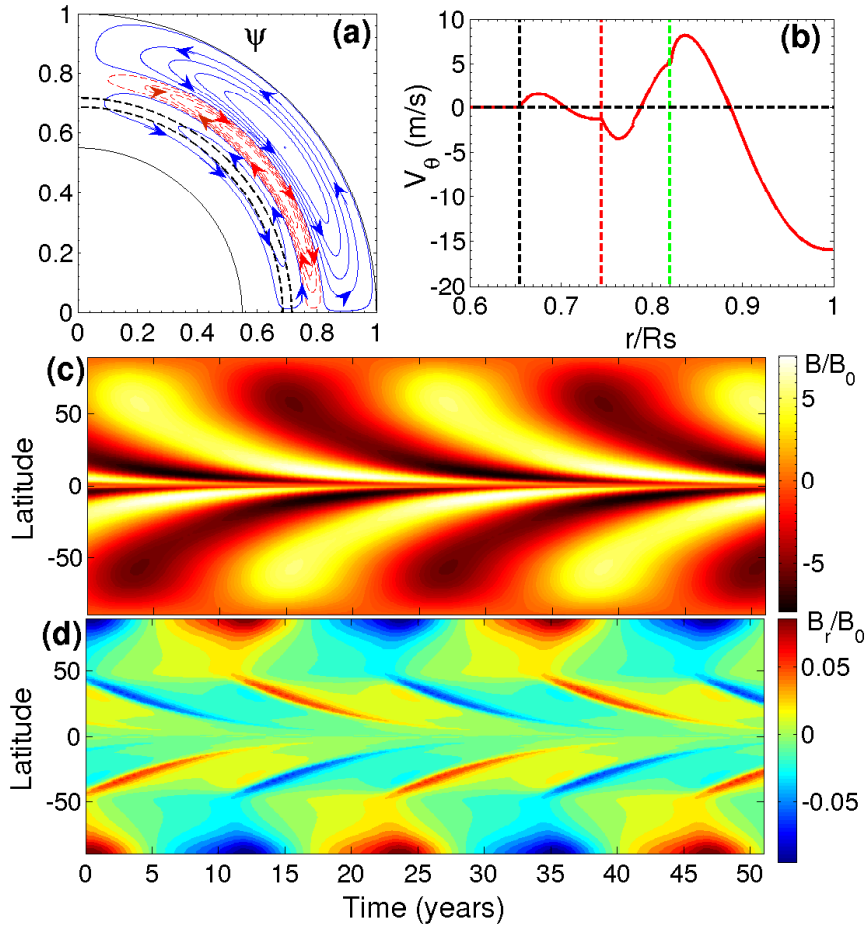


Fig. 4.4 (a) Streamlines for three radially stacked cells of meridional circulation. Directions are shown by arrows. (b), (c) and (d) are the same plots as in Figure 4.1, for this meridional circulation.

the dynamo period. It is the flow speed in the lowermost cell which determines the dynamo period and we find the period to decrease with the increase in this flow speed ($T \sim v_{0,l}^{-0.72}$). This result can be easily understood from common sense, since the flow in the lowermost cell causes the equatorward migration of B (giving solar-like butterfly diagram), and it is no wonder that the period becomes shorter on making this flow faster.

To sum up, as long as there is an equatorward flow at the bottom of the convection zone (the cases of Figure 4.2 and Figure 4.4), we are able to get solar-like behavior of the dynamo even if there is a complicated multi-cell structure of the meridional circulation, the period being determined by the flow in the cell at the bottom of the convection zone. Thus, even with a return flow of the meridional circulation at a shallow depth, the flux transport dynamo model can be made to work in this situation. On the other hand, if there is no flow at the bottom

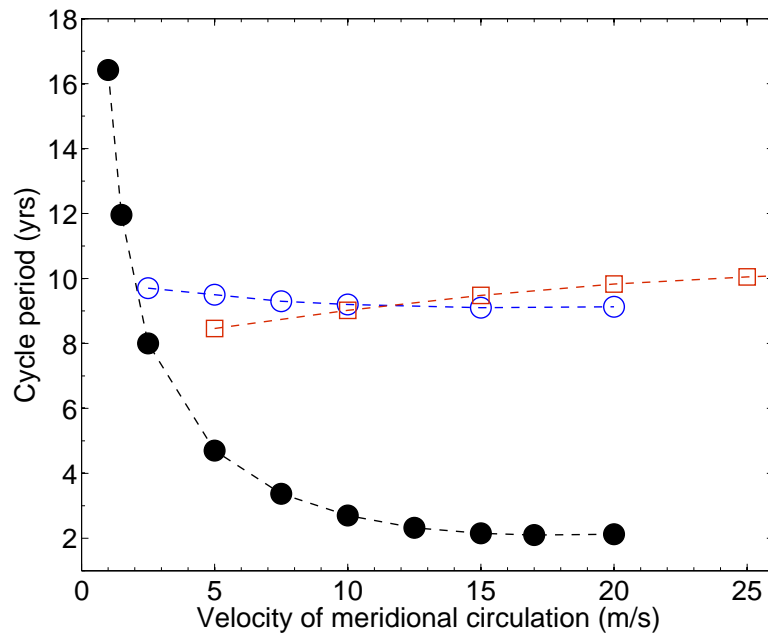


Fig. 4.5 Variation of solar cycle period with the velocity amplitudes of the three different cells shown in Figure 4.4(a). Black filled circles show the variation of the cycle period with velocity amplitude of the lower cell while keeping velocities of other cells constant. Similarly blue circles show the variation of period with velocity amplitude of middle cell and red boxes for upper cell.

of the convection zone (the case of Figure 4.1) or if there is a poleward flow there (the case of Figure 4.3), then the dynamo model fails to reproduce solar behavior. This conclusion was obtained by considering multiple cells only in the radial direction. We consider more complicated flows in the next Section and show that our main conclusion still holds.

4.4 Results with more complicated cells

We have carried out some simulations with fairly complicated multi-cell meridional circulation, which reinforced our main conclusion of the previous Section: we can have solar-like dynamo solutions as long as there is an equatorward flow in low latitudes at the bottom of the convection zone. For the very complicated meridional circulation pattern shown in Figure 4.6(a), we present the results in Figure 4.7. The Appendix indicates how this complicated flow is obtained from a suitable stream function. Since there is an equatorward flow in low latitudes at the bottom of the convection zone, we get solar-like butterfly diagrams even with such a flow. It may be noted that the lowermost cell in Figure 4.6(a) from the equator does not go all the

way to the pole, but the cell ends at some high latitude. We find that this cell has to extend sufficiently to reasonably high latitudes in order to give a solar-like butterfly diagram. If the cell does not extend beyond mid-latitudes, then we are unable to get very solar-like butterfly diagrams. In Figure 4.6(b), we show a meridional circulation with the lower cell not extending to high latitudes. Results for this case are presented in Figure 4.8. We see that the butterfly diagram is much less realistic compared to the butterfly diagram presented in Figure 4.7. It is clear from Figure 4.7 and Figure 4.8 that the requirement for a solar-like butterfly diagram is that there has to be an equatorward flow at the bottom of the convection zone having a sufficient latitudinal extent from the equator to a reasonably high latitude.

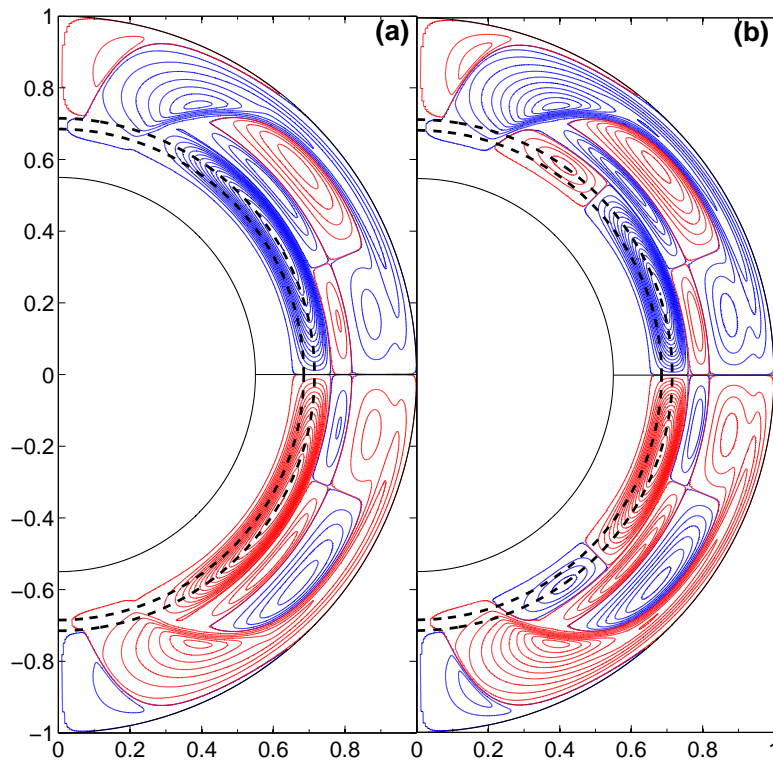


Fig. 4.6 Streamlines for two complicated meridional circulation patterns. The blue contours imply anti-clockwise circulation, whereas the red contours imply clockwise circulation. The lowest cell in (a) extends from the equator to fairly high latitudes, whereas this cell in (b) extends only to mid-latitudes.

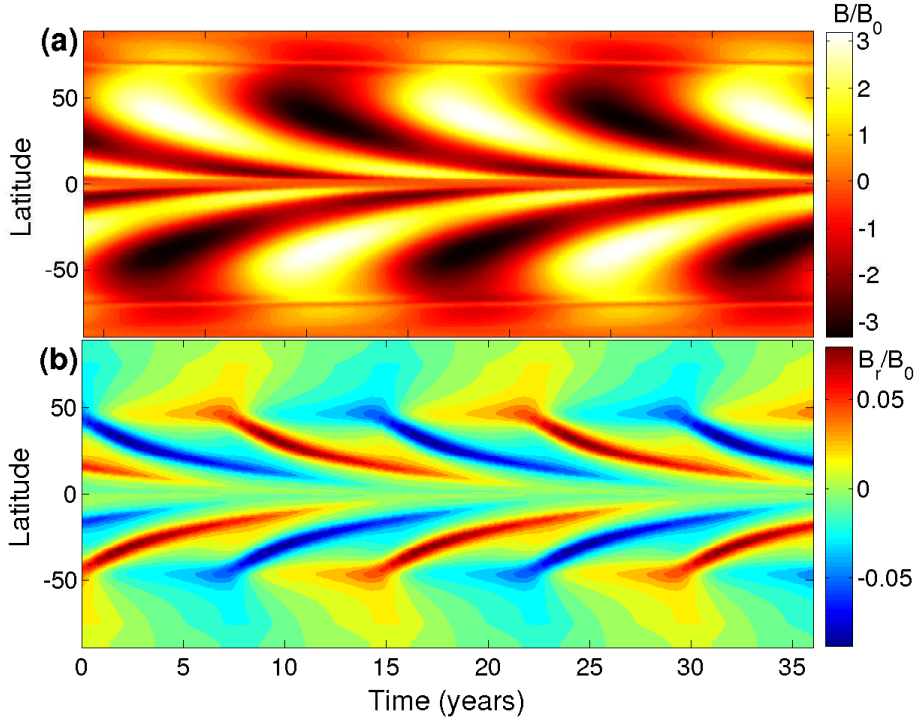


Fig. 4.7 (a) and (b) are the same plots as (c) and (d) in Figure 4.1, for the meridional circulation given in Figure 4.6(a).

4.5 Results for low diffusivity versus high diffusivity

We have pointed out that the nature of the dynamo depends quite a bit on whether the turbulent diffusivity within the convection zone is assumed to be high or low (Hotta & Yokoyama, 2010; Jiang et al., 2007; Karak, 2010; Karak & Choudhuri, 2011; Yeates et al., 2008). So far all the calculations in this chapter have been carried out with a diffusivity on the higher side. With such diffusivity, the poloidal field generated near the surface by the Babcock–Leighton mechanism reaches the bottom of the convection zone primarily due to diffusion and this process is not affected by the presence of multiple cells. However, when the diffusivity is low, it is the meridional circulation which has to transport the poloidal field from the surface to the bottom of the convection zone and such transport becomes more complicated when there are multiple cells. Now we come to the question whether our main conclusion in the previous two sections holds when the diffusivity is low. Following Chatterjee et al. (2004), we specify the diffusivity for the high diffusivity case in the following way:

$$\eta_p(r) = \eta_{RZ} + \frac{\eta_{SCZ}}{2} \left[1 + \operatorname{erf} \left(\frac{r - 0.7R_\odot}{0.03R_\odot} \right) \right] \quad (4.13)$$

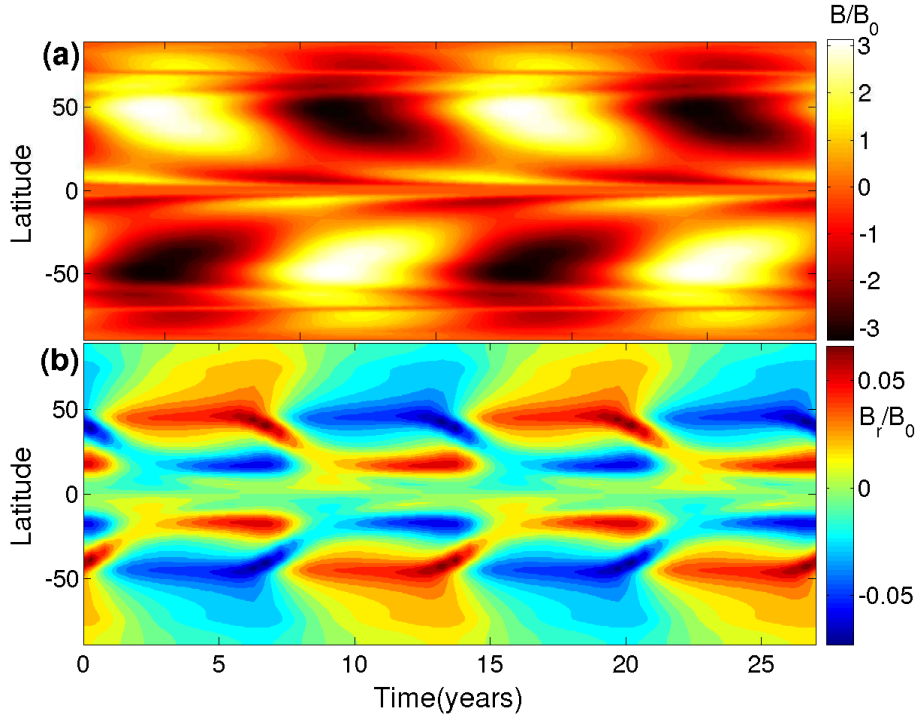


Fig. 4.8 Same as Figure 4.7, for the meridional circulation given in Figure 4.6(b).

$$\eta_t(r) = \eta_{RZ} + \frac{\eta_{SCZ1}}{2} \left[1 + \operatorname{erf} \left(\frac{r - 0.725R_\odot}{0.03R_\odot} \right) \right] + \frac{\eta_{SCZ}}{2} \left[1 + \operatorname{erf} \left(\frac{r - 0.975R_\odot}{0.03R_\odot} \right) \right] \quad (4.14)$$

Here η_{RZ} is the diffusivity below the bottom of the convection zone which is assumed to be small, whereas η_{SCZ} and η_{SCZ1} are respectively the diffusivities of the poloidal and the toroidal components within the body of the convection zone. Since the toroidal magnetic field is believed to be much stronger than the poloidal magnetic field, the diffusivity η_{SCZ1} of the toroidal field is assumed to be less than the diffusivity η_{SCZ} of the poloidal field. For high diffusivity case (all the results presented in Section 4.3 and Section 4.4), the values of the parameters for η_p are $\eta_{RZ} = 2.2 \times 10^8 \text{ cm}^2 \text{ s}^{-1}$, $\eta_{SCZ} = 2.2 \times 10^{12} \text{ cm}^2 \text{ s}^{-1}$, and for η_t are $\eta_{SCZ1} = 4.0 \times 10^{10} \text{ cm}^2 \text{ s}^{-1}$. Figure 4.9 shows these diffusivities as functions of r , which have been used in the calculations of Section 4.3 and Section 4.4. Now our aim in this Section is to study the case when the diffusivity of the poloidal field is less. To achieve this, we now take both η_p and η_t to be equal to η_t in the high diffusivity case, as given by Eq. 4.14. This means that the diffusivity of the poloidal field within the main body of the convection zone is now reduced by a factor of more than 50 (from $2.2 \times 10^{12} \text{ cm}^2 \text{ s}^{-1}$ to $4.0 \times 10^{10} \text{ cm}^2 \text{ s}^{-1}$) for the studies presented in this Section.

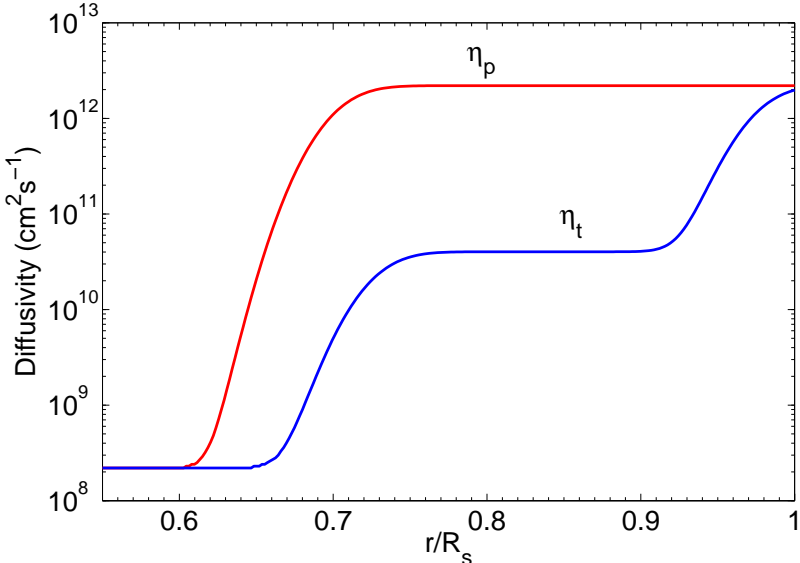


Fig. 4.9 Plots of $\eta_p(r)$ and $\eta_t(r)$ as given by (13) and (14). For the low diffusivity case, we take $\eta_p = \eta_t$.

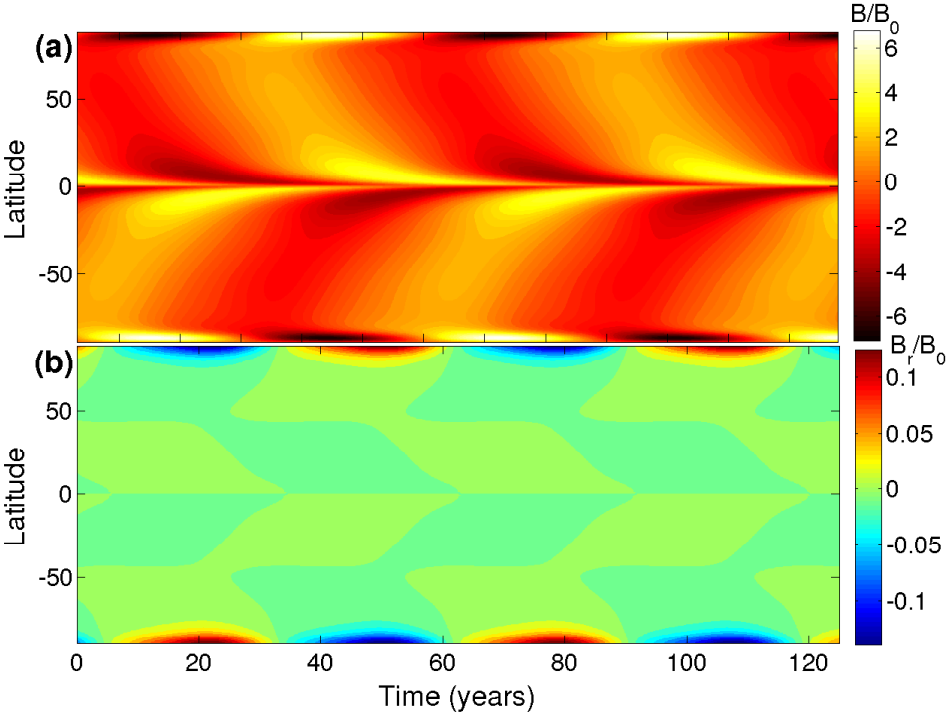


Fig. 4.10 Same as Figure 4.7, for the case of three radially stacked cells used in Figure 4.4 except that the diffusivity of the poloidal field is now lowered by making $\eta_p = \eta_t$.

To understand the effect of lowering the diffusivity, we carry on calculations for the case of three radially stacked cells (the case shown in Figure 4.4) by changing the diffusivity from the higher value to the lower value as mentioned above. While reducing the diffusivity, we also reduce the strength of the α -coefficient as pointed out in Section 4.2. All the other parameters are kept unchanged. Figure 4.10 presents the results. Although we still find solar-like butterfly diagrams, we find that the period has become much larger on reducing the diffusivity. This is not surprising. When the diffusivity is low, the poloidal field generated by the Babcock–Leighton mechanism near the surface is transported to the bottom of the convection zone (where the toroidal field is generated from it) by the meridional circulation. If there is only one cell, then this is easily accomplished. However, when there are three radially stacked cells as we are considering, the situation becomes much more complicated. The uppermost cell brings the poloidal field from the surface to its bottom. From there, the middle cell has to advect the poloidal field to its bottom. Finally, the lowermost cell takes the poloidal field to the bottom of the convection zone. In this process, the period of the dynamo gets lengthened. Figure 4.11 shows how the poloidal field lines evolve with the cycle for the case of three radially stacked cells—both when the diffusivity is high (the case of Figure 4.4) and when the diffusivity is low (the case of Figure 4.10). In the high diffusivity case, the poloidal field generated at the surface is transported downwards to the bottom of the convection zone by diffusion. Hence, in this case, we find that the poloidal field lines still are not very different from what we find in the case of meridional circulation with one cell, as shown in Figure 4 of Jiang et al. (2007). However, when the diffusivity is low, the poloidal field is nearly frozen during a cycle and is advected by the meridional circulation. In a three-cell meridional circulation, we find that the poloidal field becomes very complicated, as seen in the right column of Figure 4.11.

It has been pointed out that, when we introduce fluctuations to model irregularities of solar cycle, the dynamo models with high and low diffusivities behave completely differently (Jiang et al., 2007; Karak & Choudhuri, 2011). In the high diffusivity model, the fluctuations diffuse all over the convection zone in time scale comparable to the period of the dynamo. On the other hand, fluctuations in the low diffusivity model remain frozen during the period of the dynamo. Jiang et al. (2007) explained how the observed correlation between the polar field during a sunspot minimum and the strength of the next cycle arises in the high diffusivity model. This correlation, which forms the basis of solar cycle prediction in the high diffusivity model, does not exist in the low diffusivity model. We now check if these results hold even when we have multiple cells of the meridional circulation. Choudhuri et al. (2007) identified the fluctuations in the Babcock–Leighton process as the main source of irregularity in the sunspot cycles. These fluctuations arise from the scatter in the tilt angles of sunspots caused by the effect of convective turbulence on rising flux tubes (Longcope & Choudhuri, 2002). To model

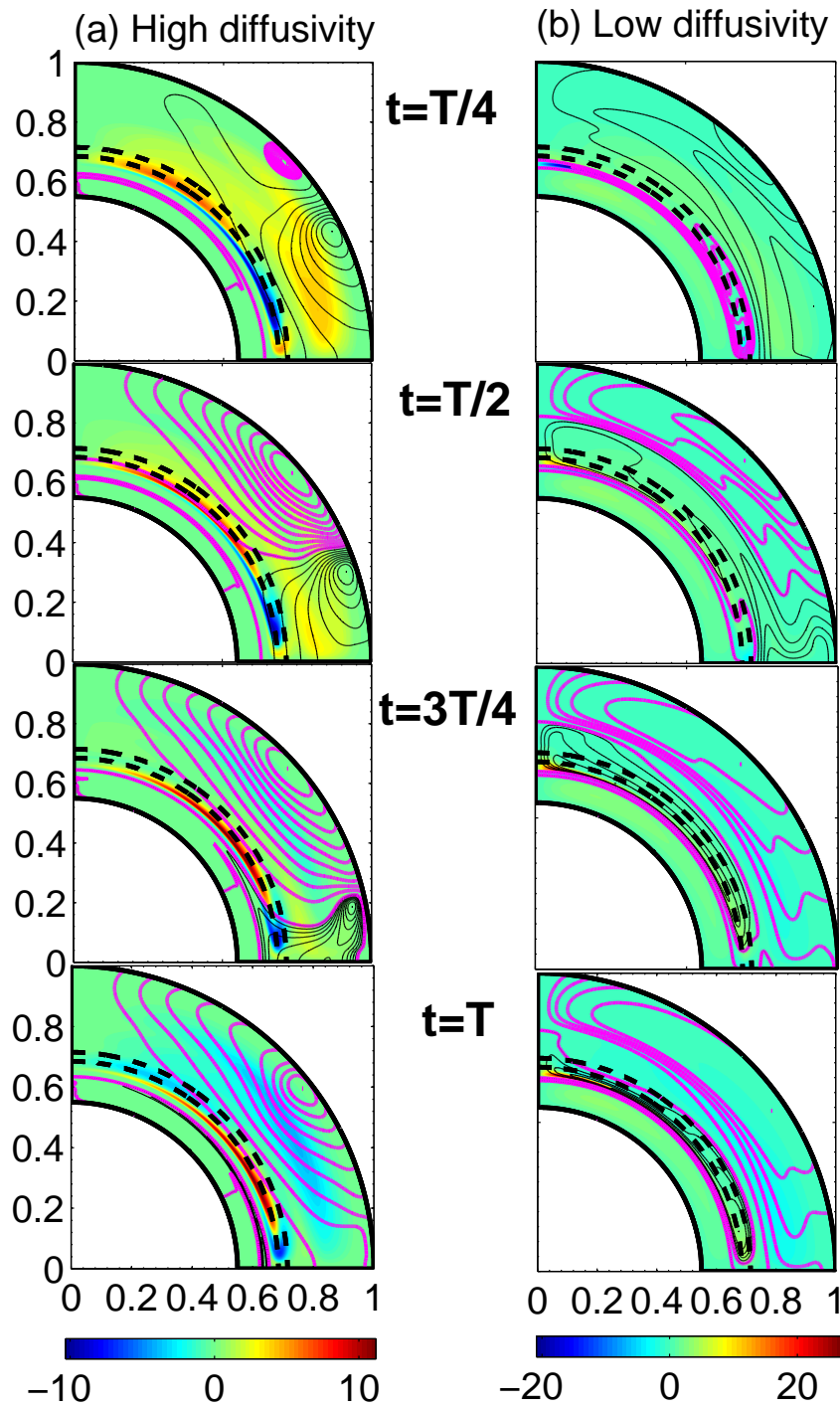


Fig. 4.11 The poloidal field lines at four different stages of a solar cycle for the cases of (a) high diffusivity and (b) low diffusivity. The magenta and the black colors respectively indicate the clockwise and anti-clockwise sense of field lines. The background colors indicate the strength of the toroidal field .

these fluctuations, we introduce stochastic fluctuations in α_0 appearing in Equation 4.5. We set

$$\alpha_0 \equiv \overline{\alpha_0}[1 \pm 0.75\sigma(\tau_{cor})], \quad (4.15)$$

where σ is a uniformly generated random number within 0 to 1 which changes value after a coherence time $\tau_{cor} = 1$ month. This makes α_0 to fluctuate randomly around its mean value $\overline{\alpha_0}$ with 75% amplitude of fluctuations. A simulation with such stochastic fluctuations in α in a traditional $\alpha\Omega$ dynamo model was first presented by Choudhuri (1992).

To study the correlation between the polar field and the strength of the next cycle, we consider the procedure of Yeates et al. (2008). We calculate the correlation between the peak of the surface radial flux ϕ_r at high latitudes of a cycle with that of the peak value of the deep-seated toroidal flux ϕ_{tor} of next cycle. We take ϕ_r as the flux of radial field over the solar surface from latitude 70° to 89° , and ϕ_{tor} as the flux of toroidal field over the region $r = 0.677R_\odot - 0.726R_\odot$ and latitude 10° to 45° . In the case of a one-cell meridional circulation (not presented in detail in this study), we get a strong correlation between the high-latitude radial flux at the end of a cycle with the toroidal flux of the next cycle, with a correlation coefficient of 0.79, which is comparable to the result of Jiang et al. (2007) (see their Figure 5) and Yeates et al. (2008) (see their Fig. 11b). Interestingly, for radially stacked three cells also, we get a strong correlation of 0.75 for the high diffusivity case. Figure 4.12 shows this result, along with the result for the low diffusivity case. For the low diffusivity case, the correlation is substantially poorer. Thus, a multi-cell meridional circulation not only reproduces the regular periodic features of a simple flux transport dynamo model, it also reproduces some of the irregular features of the cycle if the diffusivity is high, in accordance with the results presented in Chapter 3 with multi-cell meridional circulation. The methodology for predicting the next cycle developed by Choudhuri et al. (2007); Jiang et al. (2007) should work approximately the same way in the high diffusivity model even when the meridional circulation has a complicated multi-cell structure.

4.6 The effect of turbulent pumping

One possible mechanism for transporting magnetic fields across the solar convection zone which we have so far not included in our study is turbulent pumping. Many theoretical as well as numerical studies indicated that, in the strongly stratified solar convection zone, the magnetic fields can be pumped preferentially downward towards the base of the convection zone (Brandenburg et al., 1996; Tobias et al., 1998). Several magnetoconvection simulations have detected a downward pumping speed of a few meters per second in the solar convection

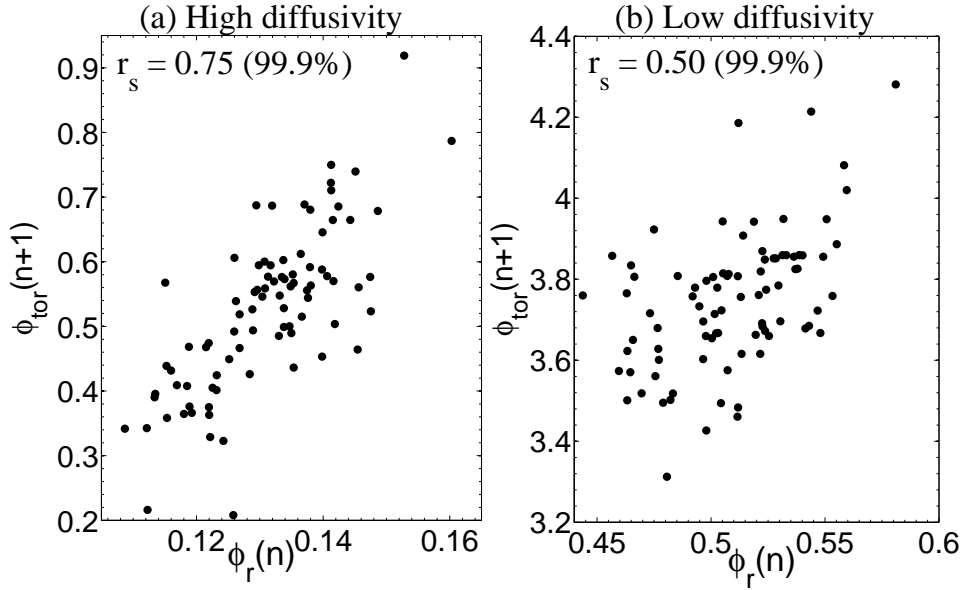


Fig. 4.12 Correlation between peak polar flux strength at the end of the n -th cycle and the peak toroidal flux strength of the $(n+1)$ -th cycle for (a) high diffusivity and (b) low diffusivity cases.

zone (Käpylä et al., 2006; Ossendrijver et al., 2002; Racine et al., 2011). Guided by these studies, we now include the effect of turbulent pumping in our dynamo model by introducing the following downward pumping velocity:

$$\gamma_r = -0.1854 \left[1 + \operatorname{erf} \left(\frac{r - 0.715R_\odot}{0.015R_\odot} \right) \right] \left[\exp \left(\frac{r - 0.715R_\odot}{0.25R_\odot} \right)^2 \cos\theta + 1 \right], \quad (4.16)$$

the unit being m s^{-1} . The variations of γ_r as functions of radius and co-latitude are shown in the upper part of Figure 4.13. Turbulent pumping appears as an advective term in the magnetic field equations. Therefore in Equations 4.2 and 4.3 we add this extra term γ_r in the radial velocity, i.e., we take $v_r \equiv v_r + \gamma_r$. As in Jiang et al. (2013); Karak & Nandy (2012); Kitchatinov & Olemskoy (2012), we first present results including only the radial pumping and not the latitudinal pumping.

Since the downward transport of the poloidal field by diffusion is reasonably efficient in the high diffusivity model, the effect of downward turbulent pumping is not very pronounced in this model. However, in the low diffusivity model, the poloidal field is advected by the meridional circulation in the absence of turbulent pumping and the addition of downward pumping can have quite dramatic effects. Karak & Nandy (2012) found that many of the differences between the high and the low diffusivity models disappear on inclusion of downward turbulent pumping.

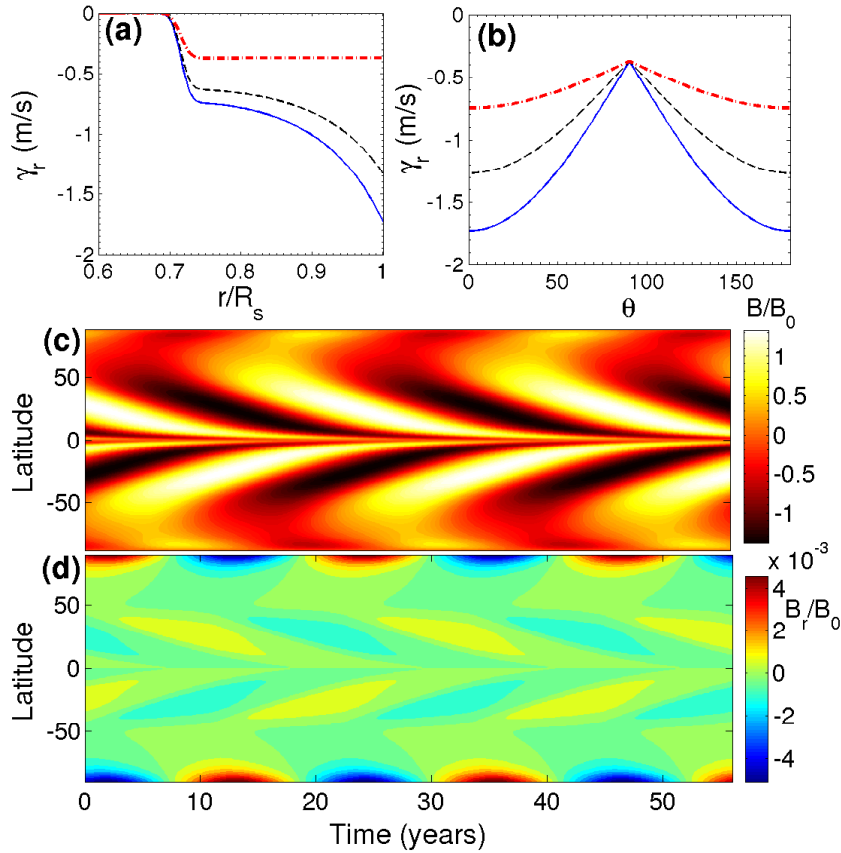


Fig. 4.13 (a) Radial pumping γ_r as a function of radius at different co-latitudes (θ). The solid (blue), the dashed (black) and the dash-dotted (red) lines correspond to $\theta = 90^\circ$, 45° and 0° respectively. (b) γ_r as a function of θ at different radii. The solid (blue), the dashed (black) and the dash-dotted (red) lines correspond to $r = R_\odot$, $0.95R_\odot$ and $0.75R_\odot$ respectively. (c) and (d) are the same as (a) and (b) in Figure 4.10 with the radial pumping added now.

We have seen in Section 4.5 that the low diffusivity model with multi-cell meridional circulation gives results which do not match observations as closely as the results obtained with high diffusivity. Although the case of meridional circulation with three radially stacked cells even with low diffusivity produces reasonably good equatorward propagation of toroidal field at low latitude, the solar cycle period becomes very long (see Figure 4.10). We now repeat this calculation for the low diffusivity case by including the downward pumping. The butterfly diagram is shown in the middle of Figure 4.13. We find that the period has become much shorter and the butterfly diagram looks quite similar to the butterfly diagram of Figure 4.4 in the high diffusivity case. Thus, even when multiple cells are present in the meridional circulation,

the inclusion of downward turbulent pumping makes the results of the low diffusivity case quite similar to the results of the high diffusivity case.

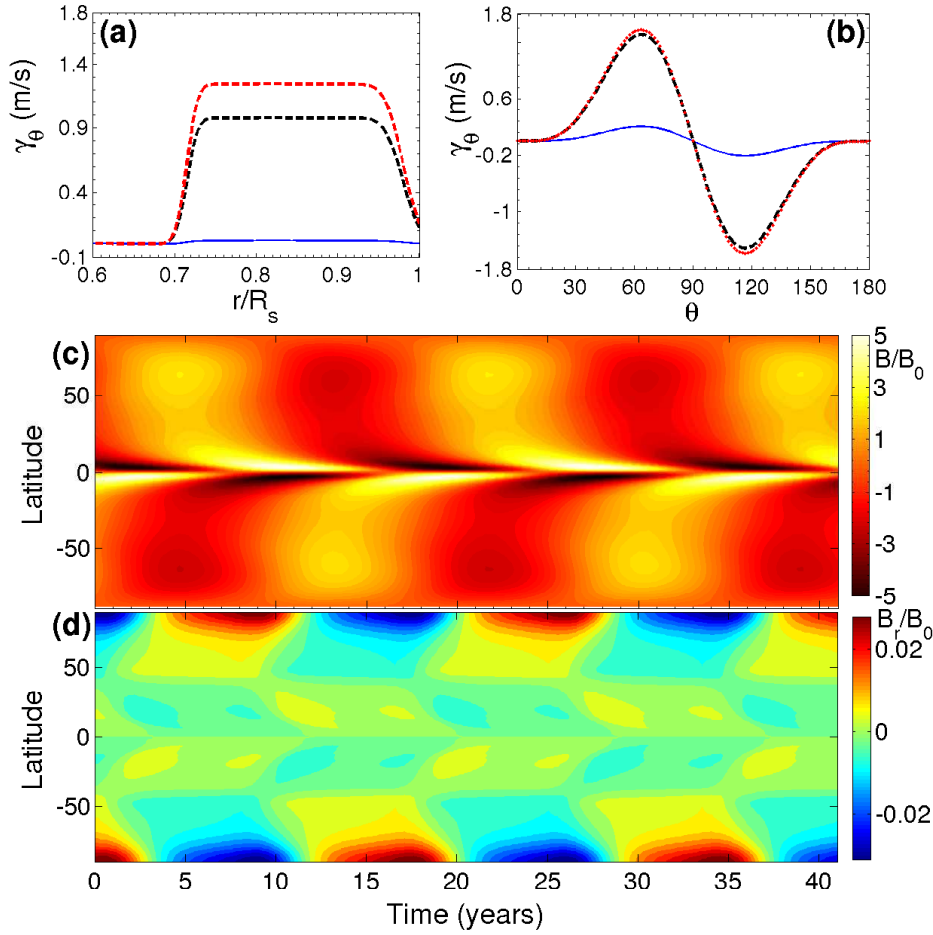


Fig. 4.14 (a) Latitudinal pumping γ_θ as function of radius at different θ . The solid blue, black dashed and red dashed lines correspond to $\theta = 15^\circ, 45^\circ$ and 75° respectively. (b) γ_θ as a function of θ at different radii. The solid (blue), the dashed (black) and the dash-dotted (red) lines correspond to $r = R_\odot, 0.95R_\odot$ and $0.75R_\odot$ respectively. (c) and (d) are same as Figure 4.1(c) and Figure 4.1(d) respectively with radial and latitudinal pumping added.

A few magnetoconvection simulations (Augustson et al., 2015; Käpylä et al., 2006; Ossendrijver et al., 2002; Racine et al., 2011) have detected a latitudinal turbulent pumping when rotation becomes important. Just to demonstrate that a latitudinal pumping can make many results significantly different, we show that our model reproduces the results of Guerrero & de Gouveia Dal Pino (2008). We take the equatorward latitudinal pumping profile as given below:

$$\gamma_\theta = 1.380 \left[1 + \operatorname{erf} \left(\frac{r - 0.715R_\odot}{0.0150R_\odot} \right) \right] \times \left[1 - \operatorname{erf} \left(\frac{r - 0.980R_\odot}{0.0250R_\odot} \right) \right] \cos \theta \sin^4 \theta, \quad (4.17)$$

the unit being m s^{-1} . This is very similar to what [Guerrero & de Gouveia Dal Pino \(2008\)](#) had taken. We now do a run for the case of a single cell of shallow meridional circulation (the case of [Figure 4.1](#)), now combined with radial pumping given by [Eq. 4.16](#) and latitudinal pumping given by [Eq. 4.17](#). The profiles of γ_θ as well as the results of the run are presented in [Figure 4.14](#). On comparing with [Figure 5](#) of [Guerrero & de Gouveia Dal Pino \(2008\)](#), It has been found that we qualitatively reproduce their results. In other words, if there is suitable equatorward pumping at the bottom of the convection zone, that can clearly help in producing solar-like butterfly diagram. This result is also supported by [Hazra & Nandy \(2016\)](#), who use the equatorward latitudinal turbulent pumping profile motivated by the study of magnetoconvection simulation of [Warnecke et al. \(2016\)](#).

4.7 Conclusion

In the flux transport dynamo model which has been very successful in modeling different aspects of the solar cycle, the meridional circulation of the Sun is a crucial ingredient. The major uncertainty in the flux transport dynamo model at the present time is our lack of knowledge about the nature of the meridional circulation in the deeper layers of the convection zone. Although two-dimensional models can never treat magnetic buoyancy and the Babcock–Leighton mechanism in a fully satisfactory way, we believe that these uncertainties are not so serious because different treatments of magnetic buoyancy and the Babcock–Leighton mechanism give qualitatively similar results ([Choudhuri et al., 2005](#); [Nandy & Choudhuri, 2001](#)). Since the meridional circulation arises out of a delicate imbalance between the centrifugal forcing and the thermal wind ([Kitchatinov & Olemskoy, 2011b](#)), it is challenging to model it theoretically. Models of differential rotation based on a mean field treatment of turbulence give rise to a meridional circulation ([Kitchatinov & Olemskoy, 2011b](#); [Kitchatinov & Ruediger, 1995](#); [Rempel, 2005](#)). MHD simulations of convection with the dynamo process also produce meridional circulations ([Brown et al., 2010](#); [Käpylä et al., 2013a](#); [Racine et al., 2011](#); [Warnecke et al., 2013](#)). In such simulations, the meridional circulation is often found to have several cells and to vary rapidly with time. We are still far from having a definitive theoretical model of the Sun’s meridional circulation.

Most of the flux transport dynamo models are based on the assumption of a single-cell meridional circulation having a return flow at the bottom of the convection zone. While a support for such a return flow may have been missing, this assumption of a deeply penetrating single-cell meridional circulation was at least consistent with all the observational data available till about a couple of years ago. The equatorward propagation of the sunspot belt was indeed regarded as indicative of the meridional circulation flow velocity at the bottom of the convection

zone (Hathaway et al., 2003). Only recently there are claims that the meridional circulation may have a return flow at a much shallower depth (Hathaway, 2012b; Zhao et al., 2013). If these claims are corroborated by independent investigations of other groups, then we shall have to conclude that the assumption of a deep one-cell meridional circulation is not correct. Since this assumption was extensively used in most of the kinematic flux transport dynamo models, a crucial question we face now is whether this assumption is so essential that the flux transport dynamo models would not work without this assumption or whether the flux transport dynamo models can still be made to work with a suitable modification of this assumption.

On the basis of our studies, we reach the conclusion that, in order to have a flux transport dynamo giving a solar-like butterfly diagram, we need an equatorward flow in low latitudes at the bottom of the convection zone. This flow is essential to overcome the Parker–Yoshimura sign rule and to advect the toroidal field generated in the tachocline in the equatorward direction. As long as there is such a flow, we find that the flux transport dynamo works even if the meridional circulation has a much more complicated structure than what has been assumed in the previous models. If there is a return flow at a shallow depth and there are no flows underneath, then the flux transport dynamo will not work. If there is a poleward flow at the bottom of the convection zone, then also we do not get solar-like butterfly diagrams. However, underneath a shallow return flow if we have multiple cells in such a way that there is an equatorward flow in low latitudes at the bottom of the convection zone, then the flux transport dynamo works without any serious problem. The assumption of such a multi-cell meridional circulation does not contradict any observational data available at the present time. MHD simulations also support the existence of a complicated multi-cell meridional circulation (Brown et al., 2010; Käpylä et al., 2013a; Racine et al., 2011; Warnecke et al., 2013). With such a multi-cell meridional circulation, we are able to retain all the attractive features of the flux transport dynamo model. The phase relation between the toroidal and the poloidal fields is correctly reproduced. The observed correlation between the polar field during a sunspot minimum and the strength of the next cycle is also reproduced when the diffusivity is high, although a reduced diffusivity diminishes this correlation.

One of the important processes in the operation of the flux transport dynamo is the transport of the poloidal field generated near the surface by the Babcock–Leighton mechanism to the bottom of the convection zone where the differential rotation can act on it. We have taken the diffusivity on the higher side in the calculations presented in Section 4.3–4.4 and we find that the poloidal field can diffuse from the surface to the bottom of the convection zone in a few years. A complicated multi-cell meridional circulation does not get in the way of this process. However, when the diffusivity is reduced, this transport has to be done by the meridional circulation. Interestingly, even in the case of low diffusivity with a multi-cell meridional

circulation, we are still able to get periodic solutions, although the poloidal field within the convection zone becomes very complicated and the cycle period is lengthened. A downward turbulent pumping helps in reducing the differences between the high and the low diffusivity models. Based on the few magnetoconvection simulations (Augustson et al., 2015; Käpylä et al., 2006; Racine et al., 2011; Warnecke et al., 2016) which found the equatorward latitudinal turbulent pumping near the bottom half of the Convection zone, we reproduce the result of Guerrero & de Gouveia Dal Pino (2008) that an equatorward pumping at the bottom of the convection zone can make the flux transport dynamo work even in the absence of a flow there.

To sum up, we do not think that the recent claims of an equatorward return flow at a shallow depth pose a threat to the flux transport dynamo model. Especially, we see no reason to give up the attractive scenario that the strong toroidal field is produced and stored in the stable regions of the tachocline, from which parts of this toroidal field break away to rise through the convection zone and produce sunspots. The crucial assumption needed to make the flux transport dynamo work is an equatorward flow in low latitudes at the bottom of the convection zone. At present, we do not have observational data either supporting or contradicting it. Since the flux transport dynamo has been so successful in explaining so many aspects of the solar cycle, we expect this assumption of equatorward flow in low latitudes at the bottom of the convection zone to be correct and we hope that future observations will establish it. Only if future observations show this assumption to be incorrect, a drastic revision of our current ideas about the solar dynamo will be needed at that time.

Appendix

Stream functions for the three-cell and more complicated meridional circulation

To get three radially stacked cells shown in Figure 4.4(a), we take the stream function as

$$\Psi = \Psi_u + \Psi_m + \Psi_l \quad (4.18)$$

The stream function which generates the upper cell is given by

$$\begin{aligned} \Psi_u = \Psi_{0u} \left[1 - \operatorname{erf} \left(\frac{r - 0.87R_\odot}{1.5} \right) \right] (r - R_{m,u})^{0.3} \sin \left[\frac{\pi(r - R_{m,u})}{(R_\odot - R_{m,u})} \right] \{ 1 - e^{-\beta_1 \theta^\varepsilon} \} \\ \times \{ 1 - e^{\beta_2(\theta - \pi/2)} \} e^{-((r-r_0)/\Gamma)^2} \end{aligned} \quad (4.19)$$

where the parameters have the following values: $\beta_1 = 3.5, \beta_2 = 3.3, r_0 = (R_\odot - R_b)/3.5, \varepsilon = 2.0000001, \Gamma = 3.4 \times 10^8 \text{ m}, R_{m,u} = 0.82R_\odot$. The stream function for middle cell is given by

$$\begin{aligned} \psi_m = \psi_{0m} \left[1 - \operatorname{erf} \left(\frac{r - 0.85R_{m,u}}{1.5} \right) \right] (r - R_{m,l}) \sin \left[\frac{\pi(r - R_{m,l})}{(R_{m,u} - R_{m,l})} \right] \{1 - e^{-\beta_1 \theta^\varepsilon}\} \\ \times \{1 - e^{\beta_2(\theta - \pi/2)}\} e^{-((r-r_0)/\Gamma)^2} \end{aligned} \quad (4.20)$$

where the parameters have the following values: $\beta_1 = 1.9, \beta_2 = 1.7, r_0 = (R_\odot - R_b)/3.5, \Gamma = 3.4 \times 10^8 \text{ m}, R_{m,l} = 0.75R_\odot, R_{m,u} = 0.82R_\odot$. Finally, the stream function which generates lower cell is

$$\begin{aligned} \psi_l = \psi_{0l} \left[1 - \operatorname{erf} \left(\frac{r - 0.75R_{m,l}}{0.8} \right) \right] (r - R_p) \sin \left[\frac{\pi(r - R_p)}{(R_{m,l} - R_p)} \right] \{1 - e^{-\beta_1 \theta^\varepsilon}\} \\ \times \{1 - e^{\beta_2(\theta - \pi/2)}\} e^{-((r-r_0)/\Gamma)^2} \end{aligned} \quad (4.21)$$

where the parameters have the following values: $\beta_1 = 1.5, \beta_2 = 1.3, r_0 = (R_\odot - R_b)/3.5, \Gamma = 3.47 \times 10^8 \text{ m}, R_p = 0.65R_\odot, R_{m,l} = 0.76R_\odot$. We choose $\psi_{0u}/C, \psi_{0m}/C$ and ψ_{0l}/C in such a way that v_0 for upper cell, middle cell and lower cell are around $17.0 \text{ m s}^{-1}, 5.5 \text{ m s}^{-1}$ and 2.0 m s^{-1} respectively.

In order to get the complicated meridional circulation as shown in Figure 4.6, we choose our stream function as given below.

$$\Psi = \psi_l + \psi_{lm} + \psi_m + \psi_u + \psi_{uc} \quad (4.22)$$

where, $\psi_l, \psi_{lm}, \psi_m, \psi_u$ and ψ_{uc} generate respectively the lower cell, lower middle cells, middle cells, the complicated upper cell and the upper corner cell. To give an idea about the kind of stream function we use in order to get a complicated cell, we write down the stream function ψ_u for the most complicated upper cell:

$$\begin{aligned} \psi_u = \psi_{0u} \left[1 + \operatorname{erf} \left(\frac{r - R_c}{0.02R_\odot} \right) \right] \sin \left[\frac{\pi(r - R_p)}{(R_\odot - R_p)} \right] (r - R_p) \{1 - e^{-\beta_1 \theta^\varepsilon}\} \\ \times \{1 - e^{\beta_2(\theta - \pi/2)}\} e^{-((r-r_0)/\Gamma)^2}, \end{aligned} \quad (4.23)$$

where

$$R_c = \frac{1}{2} \left[1 + \operatorname{erf} \left(\frac{\theta - \pi/24}{\pi/7} \right) \right] \times 0.95R_\odot$$

and the parameters have the following values:

$\beta_1 = 0.45, \beta_2 = 1.3, r_0 = (R_\odot - R_b)/3.5, \Gamma = 3.1 \times 10^8 \text{ m}, R_p = 0.65R_\odot$. Here do not write down the other stream functions, which are constructed along similar lines.

“The World is full of obvious things which nobody by any chance ever observes”

-Arthur Conan Doyle, The Hound of the Baskervilles

5

Why does Meridional Circulation Vary with the Solar Cycle?

Observations of the meridional circulation of the Sun, which plays a key role in the operation of the solar dynamo, indicate that its speed varies with the solar cycle, becoming faster during the solar minima and slower during the solar maxima. To explain this variation of the meridional circulation with the solar cycle, we construct a theoretical model by coupling the equation of the meridional circulation (the ϕ component of the vorticity equation within the solar convection zone) with the equations of the flux transport dynamo model. We consider the back reaction due to the Lorentz force of the dynamo-generated magnetic fields and study the perturbations produced in the meridional circulation due to it. This enables us to model the variations of the meridional circulation without developing a full theory of the meridional circulation itself. We obtain results which reproduce the observational data of solar cycle variations of the meridional circulation reasonably well. We get the best results on assuming the turbulent viscosity acting on the velocity field to be comparable to the magnetic diffusivity (i.e. on assuming the magnetic Prandtl number to be close to unity). We have to assume an appropriate bottom boundary condition to ensure that the Lorentz force cannot drive a flow in the subadiabatic layers below the bottom of the

tachocline. Our results are sensitive to this bottom boundary condition. We also suggest a hypothesis how the observed inward flow towards the active regions may be produced.

5.1 Introduction

The meridional circulation is one of the most important large-scale coherent flow patterns within the solar convection zone, the other such important flow pattern being the differential rotation. A strong evidence for the meridional circulation came when low-resolution magnetograms noted that the ‘diffuse’ magnetic field (as it appeared in low resolution) on the solar surface outside active regions formed unipolar bands which shifted poleward, implying a poleward flow at the solar surface (Howard & Labonte, 1981; Wang et al., 1989c). A further confirmation for such a flow came from the observed poleward migration of filaments formed over magnetic neutral lines (Makarov & Sivaraman, 1989; Makarov et al., 1983). Efforts for direct measurement of the meridional circulation also began in the 1980s (Labonte & Howard, 1982; Ulrich et al., 1988). The maximum velocity of the meridional circulation at mid-latitudes is of the order of 20 m s^{-1} .

After the development of helioseismology, there were attempts to determine the nature of the meridional circulation below the solar surface (Braun & Fan, 1998b; Giles et al., 1997). The determination of the meridional circulation in the lower half of the convection zone is a particularly challenging problem. Since the meridional circulation is produced by the turbulent stresses in the convection zone, most of the flux transport dynamo models in which the meridional circulation plays a crucial role assume the return flow of the meridional circulation to be at the bottom of the convection zone. In the last few years, several authors presented evidence for a shallower return flow (Hathaway, 2012b; Schad et al., 2013; Zhao et al., 2013). However, Rajaguru & Antia (2015) argue that helioseismic data still cannot rule out the possibility of the return flow being confined near the bottom of the convection zone.

Helioseismic measurements indicate a variation of the meridional circulation with the solar cycle. (Basu & Antia, 2010; Beck et al., 2002; Chou & Dai, 2001; Komm et al., 2015). These results are consistent with the surface measurements of Hathaway & Rightmire (2010), who find that the meridional circulation at the surface becomes weaker during the sunspot maximum by an amount of order 5 m s^{-1} . One plausible explanation for this is the back-reaction of the dynamo-generated magnetic field on the meridional circulation due to the Lorentz force. The aim of this study is to develop such a model of the variation of the meridional circulation and to show that the results of such a theoretical model are in broad agreement with observational data.

The theory of the meridional circulation is somewhat complicated. The turbulent viscosity in the solar convection zone is expected to be anisotropic, since gravity and rotation introduce two preferred directions at any point within the convection zone. A classic paper by [Kippenhahn \(1963\)](#) showed that an anisotropic viscosity gives rise to meridional circulation along with differential rotation. This work neglected the ‘thermal wind’ that would arise if the surfaces of constant density and constant pressure do not coincide. A more complete model based on a mean field theory of convective turbulence is due to [Kitchatinov & Ruediger \(1995\)](#) and extended further by [Kitchatinov & Olemskoy \(2011b\)](#). These authors argue that, in the high Taylor number situation appropriate for the Sun, the meridional circulation should arise from the small imbalance between the thermal wind and the centrifugal force due to the variation of the angular velocity with z (the direction parallel to the rotation axis). See the reviews by Kitchatinov ([Kitchatinov, 2011, 2013](#)) for further discussion. If the meridional circulation really comes from a delicate imbalance between two large terms, one would theoretically expect large fluctuations in the meridional circulation. Numerical simulations of convection in a shell presenting the solar convection zone produce meridional circulation which is usually highly variable in space and time ([Featherstone & Miesch, 2015](#); [Karak et al., 2014c](#); [Passos et al., 2017](#)). It is still not understood why the observed meridional circulation is much more coherent and stable than what such theoretical considerations would suggest. There are also efforts to understand whether mean field models can produce a meridional circulation more complicated than a single-cell pattern ([Bekki & Yokoyama, 2017](#)).

The meridional circulation plays a very critical role in the flux transport dynamo model, which has emerged as a popular theoretical model of the solar cycle. This model started being developed from the 1990s ([Chatterjee et al., 2004](#); [Choudhuri et al., 1995](#); [Dikpati & Charbonneau, 1999](#); [Durney, 1995](#); [Nandy & Choudhuri, 2002](#); [Wang et al., 1991](#)) and its current status has been reviewed by several authors ([Charbonneau, 2014](#); [Choudhuri, 2011b, 2014a](#); [Karak et al., 2014a](#)). The poloidal field in this model is generated near the solar surface from tilted bipolar sunspot pairs by the Babcock–Leighton mechanism and then advected by the meridional circulation to higher latitudes ([Choudhuri & Dikpati, 1999](#); [Dikpati & Choudhuri, 1994, 1995](#)). This poleward advection of the poloidal field is an important feature of the flux transport dynamo model and helps in matching various aspects of the observational data. The poloidal field eventually has to be brought to the bottom of the convection zone, where the differential rotation of the Sun acts on it to produce the toroidal field. If the turbulent diffusivity of the convection zone is assumed low, then the meridional circulation is responsible for transporting the poloidal field to the bottom of the convection zone. On the other hand, if the diffusivity is high, then diffusivity can play the dominant role in the transportation of the poloidal field across the convection zone ([Jiang et al., 2007](#); [Yeates et al., 2008](#)). We shall

discuss this point in more detail later in the chapter. Most of the authors working on the flux transport dynamo assumed a one-cell meridional circulation with an equatorward flow at the bottom of the convection zone. This equatorward meridional circulation plays a crucial role in the equatorward transport of the toroidal field generated at the bottom of the convection zone, leading to solar-like butterfly diagrams. In the absence of the meridional circulation, one finds a poleward dynamo wave (Choudhuri et al., 1995). When several authors claimed to find evidence for a shallower meridional circulation, there was a concern about the validity of the flux transport dynamo model. Hazra et al. (2014) showed that, even if the meridional circulation has a much more complicated multi-cell structure, still we can retain most of the attractive features of the flux transport dynamo as long as there is a layer of equatorward flow at the bottom of the convection zone. In the present work, we assume a one-cell meridional circulation.

Most of the papers on the flux transport dynamo are of kinematic nature, in which the only back-reaction of the magnetic field which is often included is the so-called “ α -quenching”, i.e. the quenching of the generation mechanism of the poloidal field. Usually kinematic models do not include the back-reaction of the magnetic field on the large-scale flows. We certainly expect the Lorentz force of the dynamo-generated magnetic field to react back on the large-scale flows. From observations, we are aware of two kinds of back-reactions on the large-scale flows: solar cycle variations of the differential rotation known as torsional oscillations and solar cycle variations of the meridional circulation (Choudhuri, 2011a). There have been several calculations showing how torsional oscillations are produced by the back-reaction of the dynamo-generated magnetic field (Bushby, 2006; Chakraborty et al., 2009; Covas et al., 2000; Durney, 2000). Rempel (2006) presented a full mean-field model of both the dynamo and the large-scale flows. This model produced both torsional oscillations and the solar cycle variation of the meridional circulation. However, apart from Figure 4(b) in the paper showing the time-latitude plot of v_θ near the bottom of the convection zone, this paper does not study the time variation of the meridional circulation in detail. To the best of our knowledge, this is the only mean-field calculation of magnetic back-reaction on the meridional circulation before our work.

The back-reaction on the meridional circulation should mainly come from the tension of the dynamo-generated toroidal magnetic field. Suppose we consider a ring of toroidal field at the bottom of the convection zone. Because of the tension, the ring will try to shrink in size and this can be achieved most easily by a poleward slip (van Ballegooijen & Choudhuri, 1988). It is this tendency of poleward slip that would give rise to the Lorentz force opposing the equatorward meridional circulation. We show in our calculations based on a mean field model that this gives rise to a vorticity opposing the normal vorticity associated with the meridional

circulation and, as this vorticity diffuses through the convection zone, there is a reduction in the strength of the meridional circulation everywhere including the surface. In order to circumvent the difficulties in our understanding of the meridional circulation itself, we develop a theory of how the Lorentz force produces a modification of the meridional circulation with the solar cycle. The important difference of our formalism from the formalism of [Rempel \(2006\)](#) is the following. In Rempel's formalism, one requires a proper formulation of turbulent stresses to calculate the full meridional circulation in which one sees a cycle variation due to the dynamo-generated Lorentz force. On the other hand, in our formalism, we have developed a theory of the modifications of the meridional circulation due to the Lorentz force so that we can study the modifications of the meridional circulation without developing a full theory of the meridional circulation.

The mathematical formulation of the theory is described in the next Section. Then Section 5.3 presents the results of our simulation. Our conclusions are summarized in Section 5.4.

5.2 Mathematical Formulation

Our main aim is to study how the Lorentz force due to the dynamo-generated magnetic field acts on the meridional circulation. We need to solve the dynamo equations along with the equation for the meridional circulation.

We write the magnetic field in the form

$$\mathbf{B} = B_\phi(r, \theta, t)\hat{e}_\phi + \nabla \times [A(r, \theta, t)\hat{e}_\phi] \quad (5.1)$$

where B_ϕ is the toroidal component of magnetic field and A is the magnetic vector potential corresponding to the poloidal component of the field. Then the dynamo equations for the toroidal and the poloidal components are

$$\frac{\partial A}{\partial t} + \frac{1}{s}(\mathbf{v}_m \cdot \nabla)(sA) = \eta_p \left(\nabla^2 - \frac{1}{s^2} \right) A + S(r, \theta, t), \quad (5.2)$$

$$\begin{aligned} \frac{\partial B_\phi}{\partial t} + \frac{1}{r} \left[\frac{\partial}{\partial r}(rv_r B_\phi) + \frac{\partial}{\partial \theta}(v_\theta B_\phi) \right] &= \eta_t \left(\nabla^2 - \frac{1}{s^2} \right) B_\phi + s(\mathbf{B}_p \cdot \nabla)\Omega \\ &+ \frac{1}{r} \frac{d\eta_t}{dr} \frac{\partial(rB_\phi)}{\partial r}, \end{aligned} \quad (5.3)$$

where v_r and v_θ are components of the meridional flow \mathbf{v}_m , Ω is the differential rotation and

$s = r \sin \theta$, whereas $S(r, \theta, t)$ is the source function which incorporates the Babcock-Leighton mechanism and magnetic buoyancy as explained in Chatterjee et al. (2004) and Choudhuri & Hazra (2016). We have kept most of the parameters the same as in Chatterjee et al. (2004). In the kinematic approach, both $\mathbf{v}_m = v_r \mathbf{e}_r + v_\theta \mathbf{e}_\theta$ and Ω are assumed to be given.

To understand the effect of the Lorentz force on the meridional circulation, we need to consider the Navier-Stokes equation with the Lorentz force term, which is

$$\frac{\partial \mathbf{v}}{\partial t} + (\mathbf{v} \cdot \nabla) \mathbf{v} = -\frac{1}{\rho} \nabla p + \mathbf{g} + \mathbf{F}_L + \mathbf{F}_v(\mathbf{v}) \quad (5.4)$$

where \mathbf{v} is the total plasma velocity, \mathbf{g} is the force due to gravity, \mathbf{F}_L is the Lorentz force term and $\mathbf{F}_v(\mathbf{v})$ is the turbulent viscosity term corresponding to the velocity field \mathbf{v} . We would have $\mathbf{F}_v(\mathbf{v}) = \nu \nabla^2 \mathbf{v}$ if the turbulent viscosity ν is assumed constant in space, but $\mathbf{F}_v(\mathbf{v})$ can be more complicated for spatially varying ν . For simplicity we have considered turbulent viscosity as a scalar quantity but, in reality, it is a tensor and can be a quite complicated quantity: see Kitchatinov & Olemskoy (2011b). It may be noted that the tensorial nature of turbulent viscosity is quite crucial in the theory of the unperturbed meridional circulation and it cannot be treated as a scalar in the complete theory. To study torsional oscillations, we have to consider the ϕ component of Eq. 5.4 as done by Chakraborty et al. (2009). To consider variations of the meridional circulation, however, we need to focus our attention on the r and θ components of Eq. 5.4. A particularly convenient approach is to take the curl of Eq. 5.4 (noting that $(\mathbf{v} \cdot \nabla) \mathbf{v} = -\mathbf{v} \times (\nabla \times \mathbf{v}) + \frac{1}{2} \nabla(v^2)$) and consider the ϕ component of the resulting equation. This gives

$$\frac{\partial \omega_\phi}{\partial t} - [\nabla \times \{\mathbf{v} \times (\nabla \times \mathbf{v})\}]_\phi = \frac{1}{\rho^2} [\nabla \rho \times \nabla p]_\phi + [\nabla \times \mathbf{F}_L]_\phi + [\nabla \times \mathbf{F}_v(\mathbf{v}_m)]_\phi. \quad (5.5)$$

where $\omega = \nabla \times \mathbf{v}$ is the vorticity, of which the ϕ component comes from the meridional circulation \mathbf{v}_m only. Writing $\mathbf{v} = \mathbf{v}_m + r \sin \theta \Omega$, a few steps of straightforward algebra give

$$[\nabla \times \{\mathbf{v} \times (\nabla \times \mathbf{v})\}]_\phi = -r \sin \theta \nabla \cdot \left(\mathbf{v}_m \frac{\omega_\phi}{r \sin \theta} \right) + r \sin \theta \frac{\partial \Omega^2}{\partial z} \quad (5.6)$$

Substituting this in Eq. 5.5, we have

$$\frac{\partial \omega_\phi}{\partial t} + s \nabla \cdot \left(\mathbf{v}_m \frac{\omega_\phi}{s} \right) = s \frac{\partial \Omega^2}{\partial z} + \frac{1}{\rho^2} (\nabla \rho \times \nabla p)_\phi + [\nabla \times \mathbf{F}_L]_\phi + [\nabla \times \mathbf{F}_v(\mathbf{v}_m)]_\phi. \quad (5.7)$$

We now break up the the meridional velocity into two parts:

$$\mathbf{v}_m = \mathbf{v}_0 + \mathbf{v}_1, \quad (5.8)$$

where \mathbf{v}_0 is the regular meridional circulation the Sun would have in the absence of magnetic fields and \mathbf{v}_1 is its modification due to the Lorentz force of the dynamo-generated magnetic field. The azimuthal vorticity ω_ϕ can also be broken into two parts corresponding to these two parts of the meridional circulation:

$$\omega_\phi = \omega_0 + \omega_1. \quad (5.9)$$

It is clear from Eq. 5.7 that the regular meridional circulation of the Sun in the absence of magnetic fields, which is assumed independent of time in a mean field model, should be given by

$$s\nabla \cdot \left(\mathbf{v}_0 \frac{\omega_0}{s} \right) = s \frac{\partial \Omega^2}{\partial z} + \frac{1}{\rho^2} (\nabla \rho \times \nabla p)_\phi + [\nabla \times \mathbf{F}_v(\mathbf{v}_0)]_\phi. \quad (5.10)$$

This is the basic equation which has to be solved to develop a theory of the regular meridional circulation. The first term in R.H.S is the centrifugal force term, whereas the second term, which can be written as

$$\frac{1}{\rho^2} (\nabla \rho \times \nabla p)_\phi = -\frac{g}{c_p r} \frac{\partial S}{\partial \theta}, \quad (5.11)$$

is the thermal wind term. This is the term which couples the theory to the thermodynamics of the Sun. So we need to solve the energy transport equation of the Sun in order to develop a theory of the regular meridional circulation, making the problem particularly difficult. In the pioneering study of [Kippenhahn \(1963\)](#), the thermal wind term was neglected. However, we now realize that for the Sun, in which the Taylor number is large, this term has to be important and of the order of the centrifugal term ([Kitchatinov & Ruediger, 1995](#)). It may be mentioned that, in the model of the meridional circulation due to [Kitchatinov & Ruediger \(1995\)](#) and [Kitchatinov & Olemsky \(2011b\)](#), the advection term on the L.H.S. of Eq. 5.10 was neglected. On inclusion of this term, the results were found not to change much (L. Kitchatinov, private communication).

We now subtract Equation 5.10 from 5.7, which gives

$$\frac{\partial \omega_1}{\partial t} + s\nabla \cdot \left(\mathbf{v}_0 \frac{\omega_1}{s} \right) + s\nabla \cdot \left(\mathbf{v}_1 \frac{\omega_0}{s} \right) = [\nabla \times \mathbf{F}_L]_\phi + [\nabla \times \mathbf{F}_v(\mathbf{v}_1)]_\phi \quad (5.12)$$

on neglecting the quadratic term in perturbed quantities $\mathbf{v}_1 \omega_1$ and assuming that $\mathbf{F}_v(\mathbf{v})$ is linear in \mathbf{v} , which is the case if we use the standard expressions of the viscous stress tensor. We have also assumed that the dynamo-generated magnetic fields do not affect the thermodynamics significantly, making the thermal wind term to drop out of Eq. 5.12. This is what makes the theory of the modification of the meridional circulation decoupled from the thermodynamics of

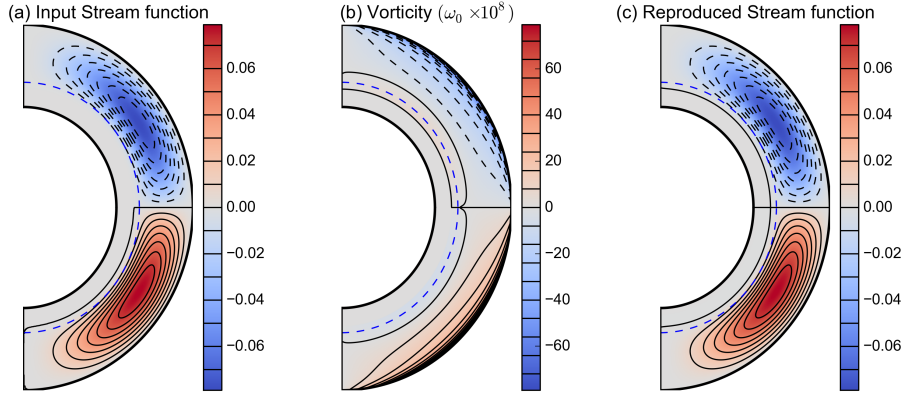


Fig. 5.1 (a) The input stream function for the unperturbed meridional circulation which is used in all of our simulations. The streamlines are indicated by contours—solid contours indicating clockwise flow and dashed contours indicating anti-clockwise flow. (b) The unperturbed vorticity calculated from the stream function shown in (a). Solid and dashed contours indicate positive and negative vorticity. (c) The stream function by inverting the vorticity shown in (b) with the help of Eq. 5.14. This has to be compared with (a). Blue dashed line represents the tachocline in all plots

the Sun and simpler to handle than the theory of the unperturbed meridional circulation. We have also not included the centrifugal force term, on the assumption that the temporal variations in Ω with the solar cycle do not significantly affect our model of the meridional circulation perturbations. The existence of torsional oscillations indicates that this may not be a fully justifiable assumption. In a future work, we plan to include torsional oscillations in the theory along with the meridional circulation perturbations.

In order to study how the meridional circulation evolves with the solar cycle due to the Lorentz force of the dynamo-generated magnetic fields, we need to solve Equation 5.12 along with Equations 5.2 and 5.3. A solution of Eq. 5.12 first yields the perturbed vorticity ω_1 at different steps. We can then compute the perturbed velocity \mathbf{v}_1 in the following way. Since $\nabla \cdot \rho \mathbf{v}_1 = 0$, we can write \mathbf{v}_1 in terms of a stream function:

$$\mathbf{v}_1 = \frac{1}{\rho} \nabla \times [\psi(r, \theta, t) \hat{e}_\phi]. \quad (5.13)$$

Putting this in $\omega_1 = \nabla \times \mathbf{v}_1$, we get

$$\frac{1}{\rho} [\nabla \rho \times \{\nabla \times (\psi \hat{e}_\phi)\}]_\phi + \left(\nabla^2 - \frac{1}{s^2} \right) \psi = -\rho \omega_1. \quad (5.14)$$

This is similar to Poisson's equation and we solve it for a given vorticity to get the stream function. After obtaining the stream function, it is very trivial to get the velocity fields. There are various methods to solve this vorticity-stream function equation (Eq. 5.14), but we choose to solve it using Alternating Direction Implicit (ADI) method. The advantage of this method is that it will take less iterations than the other relaxation methods (e.g, Jacobi iteration method) to achieve the same accuracy level. To check whether this method is giving us the correct results, we take the vorticity of the unperturbed meridional circulation that we use in our dynamo calculations. We invert this vorticity to obtain the velocity field by solving Eq. 5.14 and then cross check if we have succeeded in reproducing the original input meridional circulation. The stream function corresponding to the input velocity field is in shown in Figure 5.1(a). Here black solid contours surrounding regions of positive stream function (indicated by red) imply clockwise flow and black dashed contours surrounding regions of negative stream function (indicated by blue) imply anti-clockwise flow. We calculate the vorticity (Fig 5.1(b)) from this given velocity field and solve Eq. 5.14 to get back the stream function. The stream function obtained in this process is shown in Fig 5.1(c). As we can see, it is almost indistinguishable from the original given stream function. While solving Eq. 5.14, we have set the tolerance level to 10^{-5} , which is found to be sufficient enough to get accurate results. As meridional circulation cannot penetrate much below the tachocline, we have used $v_r = 0$ at $r = 0.65R_{\odot}$ as our bottom boundary condition.

It may be noted that a realistic specification of density ρ is more important for studying the meridional circulation than for the dynamo problem. It is the density stratification which determines how strong the poleward flow at the surface will be compared to the equatorward flow at the bottom of the convection zone. We use a polytropic, hydrostatic, adiabatic stratification for density that matches the standard solar model quite well (Jones et al., 2011):

$$\bar{\rho} = \rho_i \left(\frac{\zeta(r)}{\zeta(r_1)} \right)^n \quad (5.15)$$

where

$$\zeta(r) = c_0 + c_1 \frac{r_2 - r_1}{r} \quad (5.16)$$

$$c_0 = \frac{2\zeta_0 - \beta - 1}{1 - \beta} \quad (5.17)$$

$$c_1 = \frac{(1 + \beta)(1 - \zeta_0)}{(1 - \beta)^2} \quad (5.18)$$

and

$$\zeta_0 = \frac{\beta + 1}{\beta \exp(N_\rho/n) + 1} \quad (5.19)$$

Here $\rho_i = \rho(r_1) = 0.1788 \text{ g cm}^{-3}$, $\beta = r_1/r_2 = 0.55$ is the aspect ratio, $n = 1.5$ is the polytropic index, and $N_\rho = 5$ is the number of density scale heights across the computational domain, which extends from $r_1 = 0.55R_\odot$ to $r_2 = R_\odot$.

To solve Eq. 5.12, we need explicit expressions of $[\nabla \times \mathbf{F}_L]_\phi$ and $[\nabla \times \mathbf{F}_v(\mathbf{v}_1)]_\phi$. If the magnetic field is given by Eq. 5.1, then we have

$$\begin{aligned} [\nabla \times \mathbf{F}_L]_\phi &= \left[\nabla \times \left(\frac{(\nabla \times \mathbf{B}) \times \mathbf{B}}{4\pi\rho} \right) \right]_\phi \\ &= \left[\frac{1}{4\pi\rho} \nabla \times \{(\nabla \times \mathbf{B}) \times \mathbf{B}\} \right]_\phi - \left[\{(\nabla \times \mathbf{B}) \times \mathbf{B}\} \times \nabla \left(\frac{1}{4\pi\rho} \right) \right]_\phi \end{aligned} \quad (5.20)$$

It is straightforward to show that

$$\begin{aligned} \nabla \times [\{(\nabla \times \mathbf{B}) \times \mathbf{B}\}]_\phi &= \left[\frac{1}{r} \frac{\partial}{\partial r} \left(\frac{j_\phi}{s} \right) \frac{\partial(sA)}{\partial\theta} - \frac{1}{r} \frac{\partial}{\partial\theta} \left(\frac{j_\phi}{s} \right) \frac{\partial(sA)}{\partial r} \right] \\ &+ \left[\frac{1}{r} \frac{\partial}{\partial\theta} \left(\frac{B_\phi}{s} \right) \frac{\partial(sB_\phi)}{\partial r} - \frac{1}{r} \frac{\partial}{\partial r} \left(\frac{B_\phi}{s} \right) \frac{\partial(sB_\phi)}{\partial\theta} \right] \end{aligned} \quad (5.21)$$

where $j_\phi = (\nabla \times \mathbf{B})_\phi$ is ϕ component of current density, which is associated only with the poloidal field. It is clear from Eq. 5.21 that the Lorentz forces due to the poloidal field and due to the toroidal field clearly separate out. In typical flux transport dynamo simulations, the toroidal magnetic field turns out to be about two orders of magnitude stronger than the poloidal magnetic field. Since the Lorentz force goes as the square of the magnetic field, the Lorentz force due to the toroidal field should be about four orders of magnitude stronger than that due to the poloidal field. So we include the Lorentz force due to the toroidal field alone in our calculations. We also have to keep in mind that the magnetic field in the convection zone is highly intermittent with a filling factor, say f . The Lorentz force is significant only inside the flux tubes and a mean field value of this has to be included in the equations of our mean field theory. This point was discussed by [Chakraborty et al. \(2009\)](#), who showed that, if we use mean field values of the magnetic field in our equations, then the mean field value of the quadratic Lorentz force will involve a division by f . Keeping this in mind, the expression of $[\nabla \times \mathbf{F}_L]_\phi$ to be used when solving Equation 5.12 is obtained from Equations 5.20 and 5.21:

$$[\nabla \times \mathbf{F}_L]_\phi = \frac{1}{4\pi\rho f} \left[\frac{1}{r^2} \frac{\partial}{\partial\theta} (B_\phi^2) - \frac{\cot\theta}{r} \frac{\partial}{\partial r} (B_\phi^2) \right] + \frac{1}{4\pi\rho^2 f} \frac{d\rho}{dr} \frac{B_\phi}{r \sin\theta} \frac{\partial(\sin\theta B_\phi)}{\partial\theta} \quad (5.22)$$

The expression for $[\nabla \times \mathbf{F}_v(\mathbf{v}_1)]_\phi$ happens to be rather complicated (even when the turbulent diffusivity ν is assumed to be a scalar) and will be discussed in Appendix A. We carry on our calculations assuming a simpler form of the viscosity term:

$$[\nabla \times F_v(\mathbf{v}_1)]_\phi = \nu \left(\nabla^2 - \frac{1}{r^2 \sin^2 \theta} \right) \omega_1. \quad (5.23)$$

As we shall show in Appendix A, this simple expression of $[\nabla \times \mathbf{F}_v(\mathbf{v}_1)]_\phi$, which is easy to implement in a numerical code, captures the effect of viscosity reasonably well.

To study the variations of the meridional circulation with the solar cycle, we need to solve Equations 5.2, 5.3 and 5.12 simultaneously, with $[\nabla \times \mathbf{F}_L]_\phi$ and $[\nabla \times \mathbf{F}_v(\mathbf{v}_1)]_\phi$ in Eq. 5.12 given by Eq. 5.22 and Eq. 5.23 respectively. It is the term $[\nabla \times \mathbf{F}_L]_\phi$ in Eq. 5.12 which is the source of the perturbed vorticity ω_1 and gives rise the variations of the meridional circulation with the solar cycle. The toroidal field field B_ϕ obtained at each time step from Eq. 5.3 is used for calculating $[\nabla \times \mathbf{F}_L]_\phi$ as given by Eq. 5.22.

The numerical procedure for solving Equations 5.2 and 5.3 has been discussed in detail by Chatterjee et al. (2004). We solve Eq. 5.12 also in a similar way. Note that this equation consists of two advection terms in the LHS and one diffusion term along with the source term in the RHS. It is also basically an advection-diffusion equation similar to Eq. 5.2 and 5.3. We solve Equation 5.12 to obtain the axisymmetric perturbed vorticity ω_1 in the $r - \theta$ plane of the Sun with 256×256 grid cells in latitudinal and radial directions. As in the case of Equations 5.2 and 5.3, we solve Eq. 5.12 by using Alternating Direction Implicit (ADI) method of differencing, treating the diffusion term through the Crank–Nicholson scheme and the advection term through the Lax–Wendroff scheme (for more detail please see the guide of *Surya* code which is publicly available upon request. Please send e-mail to arnab@physics.iisc.ernet.in). We have used $\omega_1 = 0$ as the boundary condition at the poles $\theta = 0$ and π . The radial boundary conditions are also $\omega_1 = 0$ on the surface ($r = R_\odot$) and below the tachocline ($r = 0.70R_\odot$).

We now make one important point. By solving Eq. 5.12, we obtain the perturbed vorticity ω_1 at each time step. If we need the perturbed velocity \mathbf{v}_1 also at a time step, then we further need to solve Eq. 5.14 over our 256×256 grid points. If this is done at every time step, then the calculation becomes computationally very expensive. It is much easier to run the code if we do not need \mathbf{v}_1 at each time step. In a completely self-consistent theory, the meridional flow appearing in the dynamo Equations 5.2 and 5.3 should be given by Eq. 5.8, with \mathbf{v}_1 inserted at each time step. As we pointed out, this is computationally very expensive. If \mathbf{v}_1 is assumed small compared to \mathbf{v}_0 , then the dynamo Equations 5.2 and 5.3 can be solved much more easily by using $\mathbf{v}_m = \mathbf{v}_0$. Additionally, \mathbf{v}_1 appears in the third term on the LHS of Eq. 5.12. We discuss this term in Appendix B, where we argue that our results should not change qualitatively on not

including this term. If we neglect this term along with using $\mathbf{v}_m = \mathbf{v}_0$ in the dynamo equations 5.2 and 5.3, then we do not require \mathbf{v}_1 at each time step. The calculations in the present study are done by following this approach, which is computationally much less intensive. This has enabled us to explore the parameter space of the problem more easily and understand the basic physics issues. We are now involved in the much more computationally intensive calculations in which \mathbf{v}_1 is calculated at regular time intervals and the dynamo equations 5.2 and 5.3 are solved by including \mathbf{v}_1 in the meridional flow. The results of these calculations will be presented in future work.

Finally, before presenting our results, we want to point out a puzzle which we are so far unable to resolve. Our calculations suggest that the variations of the meridional circulation should be about two orders of magnitude larger than what they actually are! Since a larger f would reduce the Lorentz force given by Eq. 5.22, we can make the variations of the meridional circulation to have the right magnitude only if we take the filling factor f larger than unity, which is clearly unphysical. We show that this problem becomes apparent even in a crude order-of-magnitude estimate. We expect ω_1 to be of order V/L , where V is the perturbed velocity amplitude and L is the length scale. Then $\partial\omega_1/\partial t$ has to be of order V/LT . Taking T to be the solar cycle period and L to be the depth of the convection zone, a value $V \approx 5 \text{ m s}^{-1}$ gives

$$\left| \frac{\partial\omega_1}{\partial t} \right| \approx 10^{-16} \text{ s}^{-2}. \quad (5.24)$$

The curl of the Lorentz force is the source of this term and should be of the same amplitude. Now the curl of the Lorentz force is of order $|B_\phi^2/4\pi f\rho L^2|$. In a mean field dynamo model, the magnetic field should be scaled such that the mean polar field comes out to have amplitude of order 10 G. Then the mean toroidal field at the bottom of the toroidal field turns out to be about 10^3 G. On using such a value, the curl of the Lorentz force is of order $10^{-15}/f \text{ s}^{-2}$. This would become equal to 10^{-16} s^{-2} given in Eq. 5.24 only if f is of order 10—a completely unphysical result. If we take f less than 1 as expected, then the theoretical value of the perturbed meridional circulation would be much larger than what is observed. One may wonder if the same problem would be there in the theory of torsional oscillations. It turns out that the torsional oscillations have the same amplitude 5 m s^{-1} as variations in the meridional circulation. However, torsional oscillations are driven by the component $\approx |B_r B_\phi/L|$ of the magnetic stress rather than the component $\approx |B_\phi^2/L|$ relevant for meridional circulation variations. Since $|B_r|$ turns out to be about 100 times smaller $|B_\phi|$ in mean field dynamo calculations, things come out quite reasonably in the theory of torsional oscillations (Chakraborty et al., 2009). Here is then the puzzle. Since the variations in the meridional circulation are driven by the magnetic stress $\approx |B_\phi^2/L|$ which is about 100 times larger than the magnetic stress $\approx |B_r B_\phi/L|$ driving

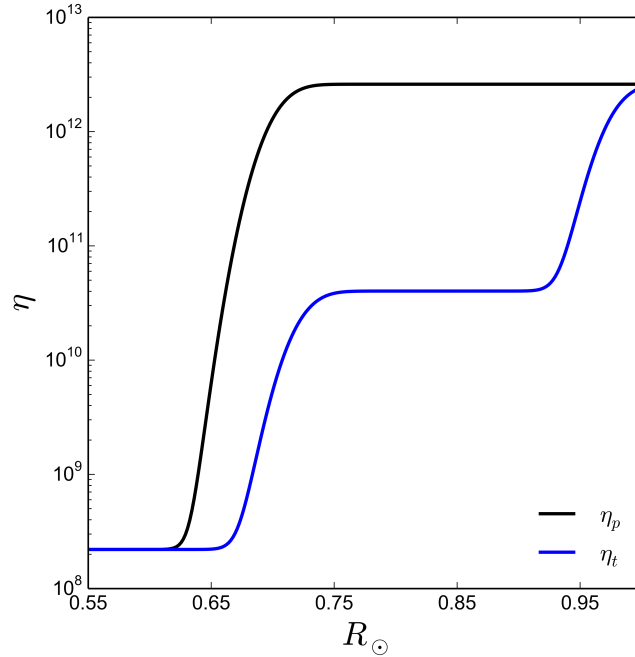


Fig. 5.2 Magnetic diffusivities ($\text{cm}^2 \text{s}^{-1}$) used in our flux transport model. The black solid line shows the turbulent diffusivity for the poloidal magnetic field, and the blue solid line shows the same for the toroidal magnetic field.

torsional oscillations, one would naively expect the meridional circulation variations to have an amplitude about 100 times larger than the amplitude of torsional oscillations. But why are their observational values found comparable? In the present study, we do not attempt to provide any solution to this puzzle and merely present this as an issue that requires further study. We point out that, even in non-magnetic situations, some terms in the equations tend to produce a much faster meridional circulation than what is observed (Dikpati, 2014; Durney, 1996). Presumably, such a fast meridional circulation would upset the thermal balance and, as a back reaction, a thermal wind force would arise to ensure that such a large meridional circulation does not take place. Also, the cyclic alterations of meridional flow may occur indirectly (other than the Lorentz force associated with the large-scale magnetic field) via magnetically mediated changes in other dynamical drivers e.g., Reynolds stresses, Maxwell stresses. Some MHD simulations (Beaudoin et al. (2013) and reference therein) suggest that this is the case for the rotational torsional oscillation and since meridional circulation and differential rotation are strongly coupled, one might expect similar things may happen for variation of the meridional flow.

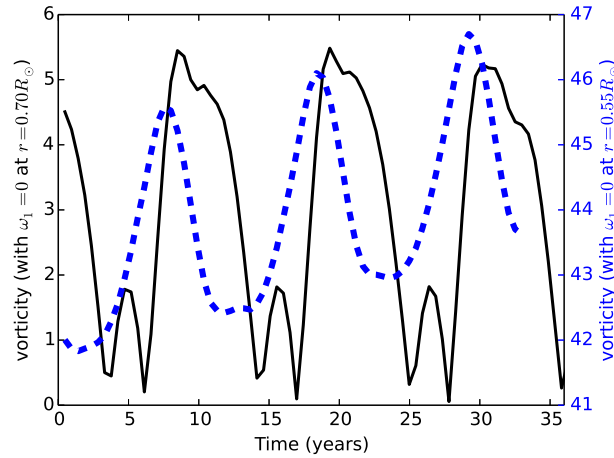


Fig. 5.3 The perturbed vorticity at a point within the convection zone is plotted against time for the two cases with different boundary conditions. The black solid line shows the absolute value of the perturbed vorticity ω_1 at 15° latitude and at depth $0.75R_\odot$, with the bottom boundary condition $\omega_1 = 0$ at $r = 0.7R_\odot$. The blue dashed line shows the absolute value of perturbed vorticity ω_1 at 15° latitude and at depth $0.71R_\odot$, with the bottom boundary condition $\omega_1 = 0$ at $r = 0.55R_\odot$. The values of the vorticity which is shown in blue dashed line are given on the right y-axis with blue color.

5.3 Results

We now present results obtained by solving the dynamo equations 5.2 and 5.3 simultaneously with Eq. 5.12 for perturbed vorticity. The various dynamo parameters—the source function $S(r, \theta, t)$, the differential rotation Ω , the meridional circulation \mathbf{v}_m and the turbulent diffusivities η_p , η_t —are specified as in Chatterjee et al. (2004). As we have pointed out, calculations in this study are based on using the unperturbed meridional circulation \mathbf{v}_0 in the dynamo equations 5.2 and 5.3. We also follow Chatterjee et al. (2004) in assuming different diffusivity for the poloidal and the toroidal components of the magnetic field as shown in Fig. 5.2. The justification for the reduced diffusivity of the toroidal component is that it is much stronger than the poloidal component and the effective turbulent diffusivity experienced by it is expected to be reduced by the magnetic quenching of turbulence. The unquenched value of turbulent diffusivity used for the poloidal field inside the convection zone is what is expected from simple mixing length arguments (Parker (1979), p. 629). A much smaller value of turbulent diffusivity was assumed in some other flux transport dynamo models (Dikpati & Charbonneau, 1999). However, a higher value appears much more realistic on the ground that only with such a higher value it is possible to model many different aspects of observational data: such as the dipolar parity (Chatterjee et al., 2004; Hotta & Yokoyama, 2010), the lack of significant hemispheric

asymmetry (Chatterjee & Choudhuri, 2006; Goel & Choudhuri, 2009), the correlation of the cycle strength with the polar field during the previous minimum (Jiang et al., 2007) and the Waldmeier effect (Karak & Choudhuri, 2011). For solving the vorticity Equation 5.12 we need to specify the turbulent viscosity ν . From simple mixing length arguments, we would expect the turbulent magnetic diffusivity η_p and the turbulent viscosity ν to be comparable, i.e, we would expect the magnetic Prandtl number $P_m = \nu/\eta_p$ to be close to 1. We first present results obtained with $P_m = 1$ in Section 5.3.1. How our results get modified on using a lower value of the magnetic Prandtl number P_m will be discussed in the Section 5.3.2.

We know that the toroidal field B_ϕ changes its sign from one cycle to the next. Since the Lorentz force depends on the square of B_ϕ , as seen in Eq. 5.22, the Lorentz force should have the same sign in different cycles. As a result, one may think that the perturbed vorticity ω_1 driven by the Lorentz force will tend to grow. However, results presented in Sections 5.3.1 and 5.3.2 are obtained with the boundary condition $\omega_1 = 0$ at $r = 0.7R_\odot$, which ensures that ω_1 cannot grow indefinitely. Asymptotically, we find ω_1 to have oscillations as the Lorentz force increases during solar maxima and decreases during solar minima. In Fig. 5.3 we have shown the time variation of perturbed vorticity (at 15° latitude and $r = 0.75R_\odot$) for this case with the black solid line. The calculations presented in Sec. 5.3.3 were done by taking the boundary condition $\omega_1 = 0$ at $r = 0.55R_\odot$. In this situation, we found that ω_1 has oscillations around a mean which keeps growing with time (see the blue dashed line plot of Fig. 5.3 which does not saturate even after running the code for several cycles).

5.3.1 Results with $P_m = 1$

The meridional circulation in a poloidal cut of the Sun's northern hemisphere is anti-clockwise, implying a negative vorticity ω_0 . If the meridional circulation is to be weakened by the Lorentz forces at the time of the sunspot maximum, then we need to generate a positive perturbed vorticity ω_1 at that time. Fig. 5.4 explains the basic physics of how this happens. The three rows of this figure plot three quantities in the $r - \theta$ plane: the toroidal field B_ϕ , the ϕ -component of the curl of the Lorentz force $[\nabla \times \mathbf{F}_L]_\phi$ and the perturbed vorticity ω_1 along with the associated streamlines. The five vertical columns correspond to five time intervals during a solar cycle. The second column corresponds to a time close to the sunspot maximum, whereas the the fourth column corresponds to the sunspot minimum.

Our discussion of Figure 5.4 below will refer to the part in the northern hemisphere. Signs will have to be opposite for some quantities in the southern hemisphere. We see in the top row that B_ϕ , produced primarily in the tachocline by the strong differential rotation there, is concentrated in a layer at the bottom of the solar convection zone. Since $-\partial(B_\phi^2)/\partial r$ will be positive at the top of this layer and will be negative at the bottom of this layer, we expect from

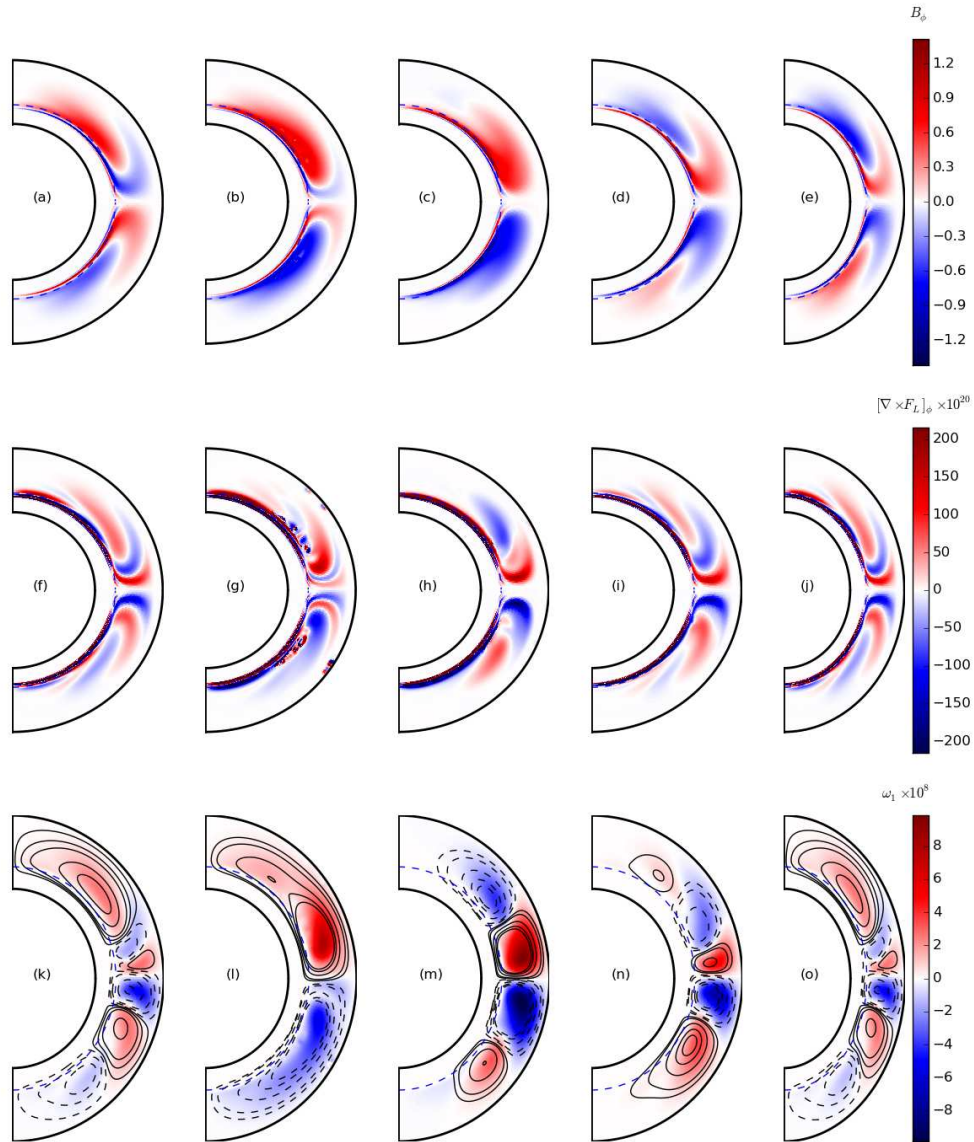


Fig. 5.4 Snapshots in the $r - \theta$ plane of different quantities spanning an entire solar cycle: the toroidal field B_ϕ , the ϕ component of the curl of the Lorentz force $[\nabla \times \mathbf{F}_L]_\phi$ and the perturbed vorticity ω_1 with streamlines are shown in the first row (a)-(e), the second row (f)-(j), and the third row (k)-(o) respectively. The five columns represent time instants during the midst of the rising phase, the solar maximum, the midst of the decay phase and the solar minimum, followed by the midst of the rising phase again. In the third row (k)-(o), the solid black contours represent clockwise flows and the dashed black contours represent anti-clockwise flows. The unit of toroidal fields in the first row is given in terms of B_c . The Lorentz forces in the second row also are calculated from toroidal fields in the unit of B_c . The vorticities are given (third row) in s^{-1} . Here B_c is the critical strength of magnetic fields above which the fields are magnetically buoyant and create sunspots (Chatterjee et al., 2004). All the plots are for the magnetic Prandtl number $P_m = 1$ with the bottom boundary condition $\omega_1 = 0$ at $r = 0.7R_\odot$.

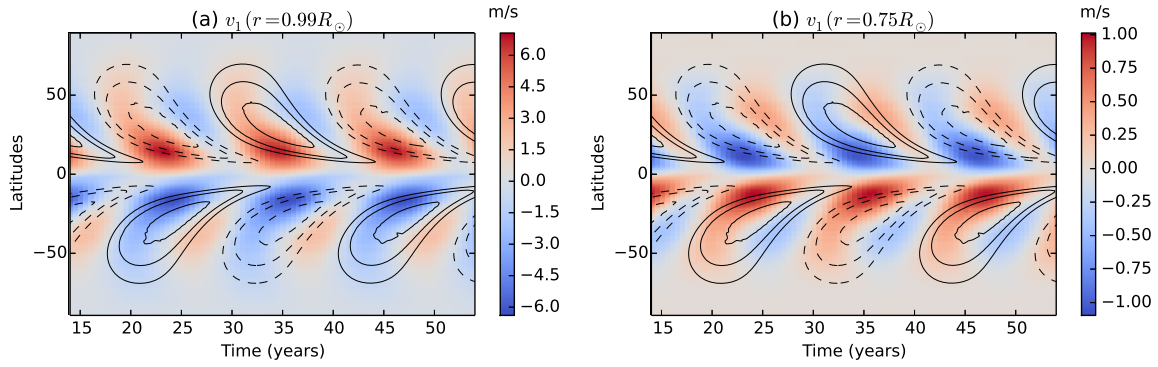


Fig. 5.5 The time–latitude plot of perturbed velocities v_θ (a) near the surface ($r = 0.99R_\odot$) and (b) at the depth $r = 0.75R_\odot$. In the northern hemisphere, positive red color shows perturbed flows towards the equator and the negative blue color shows flows towards pole. It is opposite in the southern hemisphere. Toroidal fields at the bottom of the convection zone are overplotted in both of the plots by line contours. Black solid contours indicate positive polarity and black dashed contours are for negative polarity. All the plots are for the magnetic Prandtl number $P_m = 1$ with the bottom boundary condition $\omega_1 = 0$ at $r = 0.7R_\odot$.

Eq. 5.22 that $[\nabla \times \mathbf{F}_L]_\phi$ will also respectively have positive and negative values in these regions. This expectation is borne out as seen in the second row of Fig. 5.4 plotting $[\nabla \times \mathbf{F}_L]_\phi$. Where the layer of the toroidal field ends at low latitudes, we have negative $\partial(B_\phi^2)/\partial\theta$ and we see from Eq. 5.22 that this will lead to negative $[\nabla \times \mathbf{F}_L]_\phi$. This is also seen in the second row of Fig. 5.4. We now note from Eq. 5.12 that $[\nabla \times \mathbf{F}_L]_\phi$ is the main source of the perturbed vorticity ω_1 . We expect that the positive $[\nabla \times \mathbf{F}_L]_\phi$ above the tachocline (i.e. at the top of the layer of concentrated toroidal field) will give rise to positive ω_1 , implying a clockwise flow opposing the regular meridional circulation. We see in the third row (k)-(o) of Fig. 5.4 that the distribution of ω_1 inside the convection zone follows the distribution of $[\nabla \times \mathbf{F}_L]_\phi$ (as shown in the second row (f)-(j)) fairly closely. We see that positive ω_1 is particularly dominant within the convection zone near the time of the sunspot maximum (second column). This corresponds to streamlines with clockwise flow, which will oppose the regular meridional circulation at the time of the sunspot maximum and will lead to a decrease in the overall amplitude of the meridional circulation at the solar surface, in accordance with the observational data. It may be interesting to compare Fig. 5.4 with Fig. 3 of Passos et al. (2017), where they present some results on the variation of the meridional circulation with the solar cycle on the basis of a full numerical simulation. Our results obtained from a mean field theory show a spatially smoother perturbed velocity field (perhaps in better agreement with observational data?) than what is found in the full simulation.

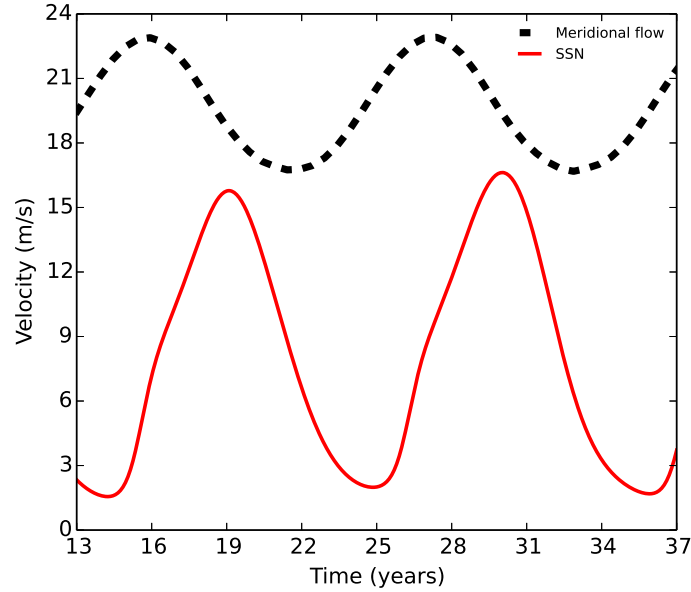


Fig. 5.6 The variation of the total meridional circulation with time is plotted with solar cycle. The yearly averaged solar cycle is plotted in the red solid line, whereas the black dashed line shows the total meridional circulation just below the surface at 25° latitude.

We wish to make one important point here. A careful look at the second row of Fig. 5.4 shows that there is a thin layer of negative $[\nabla \times \mathbf{F}_L]_\phi$ at the bottom of the tachocline where $-\partial(B_\phi^2)/\partial r$ is negative. This layer of negative $[\nabla \times \mathbf{F}_L]_\phi$ will try to create a negative vorticity driving a counter-clockwise flow below the tachocline. However, we know that it is not easy to drive a flow below the tachocline where the temperature gradient is stable (Gilman & Miesch, 2004). The physics of this is taken into account by using the bottom boundary condition that $\omega_1 = 0$ at $r = 0.7R_\odot$. As we shall see in Section 5.3.3, results can change dramatically on changing this boundary condition. Our boundary condition ensures that the negative $[\nabla \times \mathbf{F}_L]_\phi$ at the bottom of the tachocline cannot produce negative vorticity there (as seen in the third row of Fig. 5.4) and cannot drive a flow below the tachocline. We thus see that, while the distribution of ω_1 follows the distribution of $[\nabla \times \mathbf{F}_L]_\phi$ fairly closely within the convection zone, this is not the case at the bottom of the tachocline.

The strength of the perturbed meridional circulation certainly depends on the strength of $[\nabla \times \mathbf{F}_L]_\phi$, which is controlled by the filling factor f as seen in Eq. 5.22. We have followed the dynamo model of Chatterjee et al. (2004) in which the scale of the magnetic field is set by the critical value B_c above which the toroidal field becomes buoyant in the convection zone. As pointed out by Jiang et al. (2007) and followed by Chakraborty et al. (2009), we take $B_c = 108$ G to ensure that the mean polar field has the right amplitude. With the unit of the magnetic field

fixed in this way, we find that $f = 53$ gives surface values of the perturbed meridional circulation of the order of 5 m s^{-1} comparable to what is seen in the observational data. Such a value of the filling factor f , which should be less than 1, is completely unphysical. We anticipated this problem on the basis of the order-of-magnitude estimate presented in Section 5.2. Chakraborty et al. (2009) needed $f = 0.067$ to model torsional oscillations, whereas Choudhuri (2003) estimated that it should be about $f \approx 0.02$. Since f appears in the denominator of the Lorentz force term in Eq. 5.22, a large value of f means that we have to reduce the Lorentz force in an artificial manner to match theory with observations. We are not sure about the significance of this. All we can say now is that, if we reduce the Lorentz force in this manner, then we find theoretical results to be in good agreement with observational data.

Fig. 5.5 shows time-latitude plots of the perturbed v_θ just below the surface and in the lower part of the convection zone. Fig. 5.5(a) can be directly compared with Fig. 11 of Komm et al. (2015). When the perturbed meridional circulation near the surface has an amplitude of about 5 m s^{-1} near the surface (comparable to what we find in observational data), its amplitude at the bottom of the convection zone turns out to be about 0.75 m s^{-1} . This is a significant fraction of the amplitude of the meridional circulation at the bottom of the convection zone, which is of order 2 m s^{-1} . In other words, the ratio of the amplitude at the bottom of the convection zone to the amplitude at the top of the convection zone for the perturbed meridional circulation (≈ 0.15) is somewhat larger than this ratio for the regular meridional circulation (≈ 0.08). The reason behind this becomes clear on comparing the distribution of ω_0 , as seen in Fig. 5.1(b), with the distribution of ω_1 , as seen in Fig. 5.4(1), i.e. the second figure in the third row of Fig. 5.4. This ratio is small when the vorticity is concentrated near the upper part of the convection zone and streamlines in the lower part of the convection zone are fairly spread out. On the other hand, with ω_1 distributed throughout the body of the convection zone, this ratio for the perturbed meridional circulation is not so small. The perturbed meridional circulation at the bottom of the convection zone (which is in the poleward direction) will reduce the value of the equatorward meridional circulation there considerably at the time of the sunspot maximum. This will presumably affect the behavior of the dynamo, in such ways as lengthening its period (since a slower meridional circulation at the bottom of the convection zone during certain phases of the cycle is expected to lengthen the cycle). We are certainly not fully justified in solving the dynamo equations 5.2–5.3 by using the regular meridional circulation \mathbf{v}_0 . However, as we have pointed out in Section 5.2, in order to include the perturbed meridional circulation in these equations, we need to evaluate the perturbed velocity field at every time step (i.e. not only the perturbed vorticity ω_1), which will require considerably more computational efforts. We are currently doing these calculations and will present the results in a future work. The aim of the present exploratory study is to elucidate the basic physics of the problem and not

to construct a very complete model. Figure 5.6 shows the time evolution of the total v_θ at 25° degree latitude just below the surface along with the sunspot number. We see that the meridional circulation reaches its minimum a little after the sunspot maximum. This figure can be compared with Fig. 4 of Hathaway & Rightmire (2010).

One important aspect of observational data is an inward flow towards the belt of active regions at the time of the sunspot maximum (Cameron & Schüssler, 2010; Komm et al., 2015). We now come to the question whether our model can provide any explanation for this. This inward flow means that the meridional circulation is enhanced in the low latitudes below the sunspot belt and reduced in the higher latitudes. It is thought that the cooling effect of sunspots may drive this inward flow (Gizon & Rempel, 2008; Spruit, 2003). Since this idea is not yet fully established through detailed and rigorous calculations, it is worthwhile to look for alternative explanations. We would like to draw the reader's attention to the first figure in the bottom row of Fig. 5.4. In the northern hemisphere, we see positive ω_1 (implying clockwise flow) extending over latitudes higher than where sunspots are usually seen. However, we see a region of negative ω_1 (implying counter-clockwise flow) at lower latitudes. It is clear that the perturbed meridional circulation is of the nature of an inward flow at the latitudes between the region of positive ω_1 on the high-latitude side and the region of negative ω_1 on the low-latitude side. We are thus able to obtain an inward flow at the latitudes where sunspots are typically seen, but unfortunately we are getting this at the wrong time—shortly after the sunspot minimum (when there would be no sunspots in that region) rather than at the sunspot maximum. A look at Fig. 5.5(a) also makes it clear that this inward flow occurs slightly after the sunspot minimum. We are now exploring the question whether, by changing some parameters of the model, it is possible to get this inward flow at the right latitudes at the right phase (around the sunspot maximum) of the solar cycle. If our interpretation is correct, then the inward flow has nothing to do with the actual physical presence of sunspots. While the Lorentz force above the tachocline tends to produce positive vorticity, the low-latitude edge of the toroidal magnetic field belt can be a source of negative vorticity. If the sunspot belt merely happens to be a region having positive ω_1 on the high-latitude side and negative ω_1 on the low-latitude side, then it will be a region of apparent inward flow. We suggest this as a tentative hypothesis which requires further study. This similar pattern for the meridional circulation is also found in the MHD simulations of Passos et al. (2017) (see Fig 1(F) of their paper) supporting the fact that sunspot may appear in a region having a positive ω_1 on the high-latitude side and negative ω_1 on the low-latitude side. We shall argue in Appendix B that the advection term $s\nabla \cdot (\mathbf{v}_1 \omega_0 / s)$ not incorporated in the present study (the third term on the LHS of Eq. 5.12) may be quite important for modeling the inward flow in active regions.

5.3.2 Results with low Prandtl number ($P_m < 1$)

In order to study how the nature of the perturbations in the meridional circulation will change on changing the turbulent viscosity ν , we now present results obtained by taking $\nu = \eta_t$ (shown by the blue solid line in Fig. 5.2) rather than $\nu = \eta_p$ which was the case for the results presented in Section 5.3.1. This makes the magnetic Prandtl number defined as ν/η_p (note that η_p rather than η_t represents the unquenched turbulent diffusivity) much smaller than unity within the body of the convection zone.

We now want to present our results in the meridional plane of the Sun. Since there have been no changes in the dynamo equations 5.2 and 5.3, the toroidal field B_ϕ and the ϕ -component of the curl of the Lorentz force $[\nabla \times \mathbf{F}_L]_\phi$ will be the same as in the first two rows of Fig. 5.4 if we take the snapshots at the same instants of time. To facilitate easy comparison with the perturbed vorticity ω_1 generated, we again plot $[\nabla \times \mathbf{F}_L]_\phi$ in the top row of Figure 5.7. This is the same as the middle row of Fig. 5.4. Then the bottom row of Figure 5.7 shows the perturbed vorticity ω_1 along with the streamlines of the perturbed velocity. This bottom row should be compared to the bottom row of Fig. 5.4. When ν is higher (the case of Fig. 5.4), the perturbed vorticity ω_1 spreads more evenly within the convection zone. On the other hand, when ν is lower (the case of Figure 5.7), the perturbed vorticity ω_1 tends to be frozen where it is created by $[\nabla \times \mathbf{F}_L]_\phi$. As a result, ω_1 follows $[\nabla \times \mathbf{F}_L]_\phi$ more closely in Figure 5.7 rather than in Fig. 5.4. We thus see a more complicated distribution of ω_1 in Figure 5.7 implying a more complicated velocity field.

To make the perturbed meridional circulation near the surface comparable to what we find in the observational data, we need to choose $f = 5.3 \times 10^2$ in this case of low P_m . This is even more unphysical than what we needed for the case $P_m = 1$ ($f = 53$) with all the other dynamo parameters same. Basically, on reducing viscosity, vorticity tends to get piled up and we need to reduce the strength of the Lorentz force further to match observations. The perturbed velocities near the surface and near the bottom of the convection zone are shown in Fig. 5.8(a) and 5.8(b) respectively. The requirement that the perturbed velocity at the surface compares with observational data forces the perturbed velocity at the bottom of the convection zone as seen in Fig. 5.8(b) of order 1.5 m s^{-1} , which makes it almost comparable to the unperturbed velocity (though they are in opposite directions). This shows that solving the dynamo equations 5.2 and 5.3 with the unperturbed meridional circulation \mathbf{v}_0 is more unjustified in this case than in the case of $P_m = 1$.

We do not know how large the perturbations to the meridional circulation at the bottom of the convection zone actually are. If they were comparable to the unperturbed meridional circulation, then probably we would see some effects on the dynamo. Since this problem has not been studied before, we do not know what those effects may be like. As, on theoretical

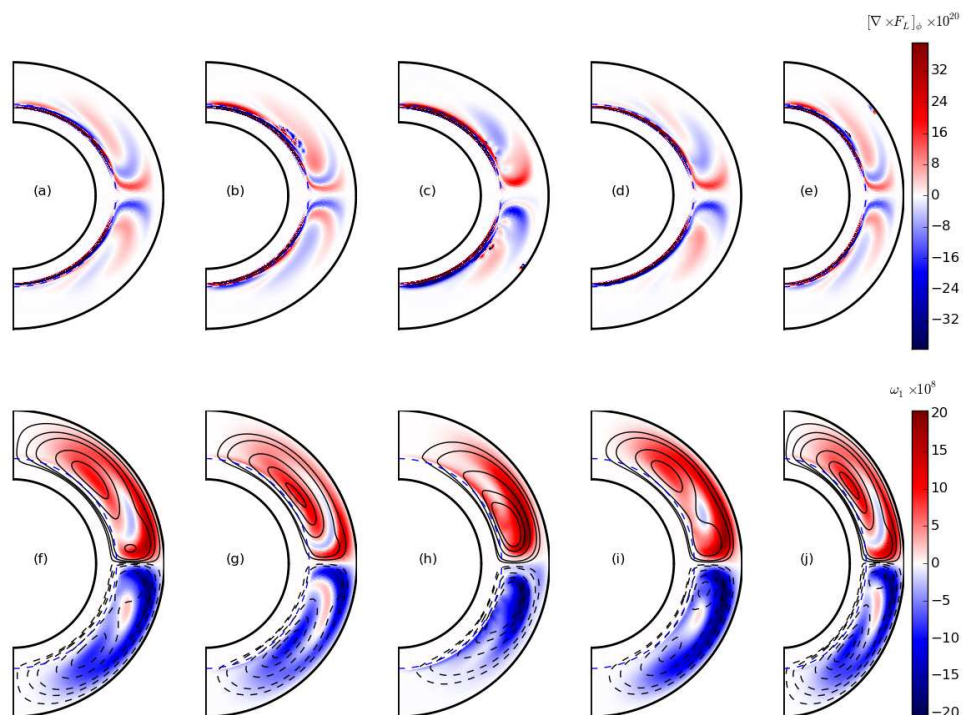


Fig. 5.7 Results obtained with low Prandtl number plotted in the same way as Fig. 5.4. The top row plotting $[\nabla \times \mathbf{F}_L]_\phi$ is the same as the second row of Fig. 5.4. The bottom row shows the vorticity ω_1 with streamlines.

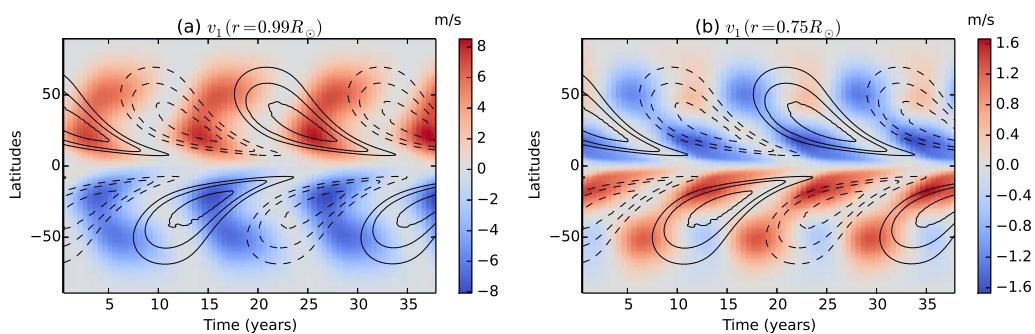


Fig. 5.8 Same as Fig. 5.5 but with low Prandtl number P_m .

grounds also we expect P_m to be of order unity, we believe that the model with $P_m = 1$ presented in Section 5.3.1 is probably a more realistic depiction of what is happening inside the Sun rather than the model with low P_m .

5.3.3 Dependence of the results on lower radial boundary condition

While discussing Fig. 5.4, we have pointed out that the Lorentz force at the bottom of the tachocline would have a tendency of producing a perturbed vorticity with the same sign as the unperturbed vorticity. This will tend to drive a counter-clockwise flow (in the northern hemisphere) below the tachocline. Since on physical grounds we do not expect such a flow to be driven in a region of stable temperature gradient, we have used the boundary condition $\omega_1 = 0$ at $r = 0.70R_\odot$ in Sections 5.3.1 and 5.3.2 to suppress this flow. We found that our results are quite sensitive to this bottom boundary condition. We now discuss what we get on changing the boundary condition to $\omega_1 = 0$ at $r = 0.55R_\odot$.

Again the solutions of the dynamo equations 5.2 and 5.3 remain the same as in Section 5.3.1 and 5.3.2. We present the solutions of the perturbed vorticity at the same time instants as the time instants in Figure 5.4. Only the third row of this figure will be replaced by what is shown in Figure 5.9. When we had taken the boundary condition $\omega_1 = 0$ at $r = 0.70R_\odot$ earlier, ω_1 was restrained from growing indefinitely. Now, on pushing the boundary well below the bottom of the convection zone, we found that ω_1 kept growing for many cycles for which we ran the code (see Fig. 5.3). This is the reason why the values of ω_1 given in the color scale in Figure 5.9 are rather large. We would expect the growing perturbed vorticity to have the opposite sign of the original unperturbed vorticity. But this is not the case now. The growing perturbed vorticity has the same sign as the original unperturbed vorticity. This means that the Lorentz force strengthens the original meridional circulation (This is also seen in the MHD simulation of Passos et al. (2012)) rather than opposing it! Presumably this is because the effect of the Lorentz force at the bottom of the tachocline (which tries to produce a perturbed vorticity of the same sign as the original vorticity) overwhelms the effect of the Lorentz force at the top of the tachocline which opposes the unperturbed meridional circulation. These results show that the bottom boundary condition is quite crucial. If we allow the Lorentz force to create a perturbed vorticity below the bottom of the tachocline, we may get totally unphysical results.

5.4 Conclusion

The meridional circulation of the Sun plays a crucial role in the flux transport dynamo model, the currently favored theoretical model for the solar cycle. Presumably an equatorward flow

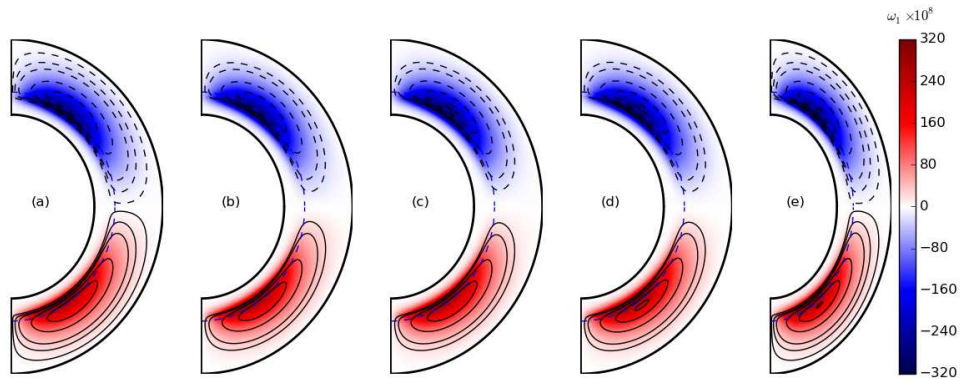


Fig. 5.9 On changing the bottom boundary condition to $\omega_1 = 0$ at $r = 0.55R_\odot$, the third row of Fig. 5.4 would get changed to this.

at the bottom of the convection zone is responsible for the equatorward migration of the sunspot belts (Choudhuri et al., 1995; Hazra et al., 2014). The poleward flow at the surface builds up the polar field of the Sun by bringing together the poloidal field generated by the Babcock–Leighton mechanism from the decay of active regions (Hazra et al., 2017). We now have growing evidence that similar flux transport dynamos operate in other solar-like stars as well (Choudhuri, 2017). Our lack of understanding of the meridional circulation in such stars is the major stumbling block for building theoretical models of stellar dynamos (Choudhuri, 2017; Karak et al., 2014b). The mathematical theory of the meridional circulation involves a centrifugal term and a thermal wind term. The centrifugal term couples the theory of the meridional circulation to the theory of differential rotation and the thermal wind term couples the theory to the thermodynamics of the star—making it a very complex subject.

We now have evidence that the meridional circulation of the Sun varies with the solar cycle, becoming weaker around the sunspot maximum (Beck et al., 2002; Chou & Dai, 2001; Hathaway & Rightmire, 2010; Komm et al., 2015). We believe that this is caused by the back-reaction of the Lorentz force of the dynamo-generated magnetic field. We show that the theory of the perturbations to the meridional circulation caused by the Lorentz force can be decoupled from the theory of the unperturbed meridional circulation itself. Especially, this theory becomes decoupled from any thermodynamic considerations if we assume that the magnetic fields do not affect the thermodynamics of the Sun. This makes the theory of the perturbations to the meridional circulation much simpler than the theory of the meridional circulation itself. Even without having a theory of the unperturbed meridional circulation, we are able to develop a theory of how the meridional circulation gets affected by the Lorentz force of the dynamo-generated magnetic fields.

The most convenient way of developing a theory of the meridional circulation is by considering the equation for the ϕ -component of vorticity ω_ϕ . We solve the equation for the perturbed vorticity along with the standard axisymmetric mean field equations of the flux transport dynamo. For the unperturbed meridional circulation, ω_ϕ is negative in the northern hemisphere of the Sun. If the Lorentz force can produce some positive vorticity there, then we expect the meridional circulation to become weaker during the sunspot maxima. Our calculations show that positive vorticity is indeed produced near the top of the tachocline. Our theoretical results are able to explain many aspects of observational data presented by [Hathaway & Rightmire \(2010\)](#) and [Komm et al. \(2015\)](#). We get best results when the turbulent viscosity ν is taken to be comparable to the turbulent diffusivity η_p of the magnetic field, i.e. when the magnetic Prandtl number P_m is close to unity. Our results are sensitive to the boundary condition at the bottom of the convection zone. At the bottom of the tachocline, the Lorentz force tends to produce vorticity with the same sign as the unperturbed vorticity and this has to be suppressed with a suitable boundary condition to incorporate the important physics that it is very difficult to drive flows in the stable subadiabatic layers below the tachocline.

One intriguing observation is that of an inward flow towards active regions during the sunspot maxima ([Cameron & Schüssler, 2010](#); [Komm et al., 2015](#)). While we have not been able to construct a satisfactory model of this inward flow, we suggest a possibility how this flow may be produced. We would have such a flow if the northern hemisphere has a positive perturbed vorticity at latitudes above the mid-latitudes and a negative perturbed vorticity at lower latitudes. We propose a scenario how this can happen. The Lorentz force at the top of the tachocline tends to produce positive vorticity, whereas the Lorentz force at the edge of the toroidal field belt at low latitudes tends to produce negative vorticity. In our model, we found an inward flow towards typical sunspot latitudes at a wrong phase of the solar cycle. It remains to be seen whether the phase can be corrected by changing the parameters of the problem.

One puzzle we encounter is that we have to reduce the strength of the Lorentz force artificially by about two orders of magnitude to make theory fit with observations. While we do not have a proper explanation for this, we make one comment. While the overall strength of the Lorentz force varies with the solar cycle, it does not change sign between cycles. As a result, the Lorentz force would always tend to drive a very strong clockwise flow in the northern hemisphere (anti-clockwise in the south), if it is not reduced sufficiently. Now, in the theory of the unperturbed meridional circulation, we know that we need some force trying to drive such a flow—to make the surfaces of constant angular velocity depart from cylinders and to balance the centrifugal term. Normally, the thermal wind caused by anisotropic heat transport in the Sun is believed to do this ([Kitchatinov & Olemskoy, 2011b](#); [Kitchatinov & Ruediger, 1995](#)). Is it possible that the expected large Lorentz force also plays an important role in the force balance?

To address this question, one has to carry on a much more complicated analysis than what we have attempted in this chapter, without separating the equations of unperturbed and perturbed meridional circulation. While we do not attempt such an analysis, our analysis brings out many basic physics issues rather clearly and raises intriguing questions like this.

The equation of the perturbed meridional circulation gives us the perturbed vorticity at different times. In order to get the perturbed velocity from the perturbed vorticity, we need to solve a Poisson-type equation. If we want to do this at every time step, then running the code becomes computationally very expensive. On the hand, if we are satisfied only with the perturbed vorticity at all steps and do not require the perturbed velocity, then we need much less computer time. This is what we have done in this chapter in which our aim was to carry out a parameter space study to understand the basic physics. However, we have to pay a price for not calculating the perturbed velocity at all time steps. We keep solving the dynamo equations by using the unperturbed velocity of the meridional circulation. This is certainly a questionable approximation. If we want to make the perturbed velocity at the surface comparable to what is found in observational data ($\approx 5 \text{ m s}^{-1}$), then the perturbed velocity at the bottom of the convection zone turns out to be $\approx 0.75 \text{ m s}^{-1}$. This is certainly smaller than the unperturbed velocity there ($\approx 2 \text{ m s}^{-1}$), but is not completely negligible. While we feel reassured that the perturbed velocity at the bottom of the convection zone is smaller than the unperturbed velocity and probably will not necessitate a major revision of the flux transport dynamo, the effect of this perturbed velocity on the dynamo needs to be investigated. We are now in the process of including this perturbed velocity in the dynamo equations. This will need finding the perturbed velocity from the perturbed vorticity at different time intervals—pushing up the computational requirements significantly. Once we do that, we shall be able to include another advection term involving \mathbf{v}_1 in the computations which had been left out in this study because of computational difficulties. This term may be important for modeling the inward flow towards active regions.

Not including the back-reactions on the meridional circulation in the dynamo equations is not a limitation of this study alone, but a limitation of nearly all hitherto published studies on the flux transport dynamo based on 2D kinematic mean field formulation. To the best of our knowledge, only [Karak & Choudhuri \(2012\)](#) studied this problem by modeling the back-reaction on the meridional circulation due to the Lorentz force through a simple parameterization (though see [Passos et al. \(2012\)](#) who have included back-reaction in a simple low-order dynamo model). Although such a back-reaction on the meridional circulation can have dramatic effects on the dynamo if the magnetic diffusivity is low, [Karak & Choudhuri \(2012\)](#) found that the effect is not much on a high-diffusivity dynamo (like what we present in this study). However, it is now important to go beyond such simple parameterization and include the properly computed

perturbed velocity in the dynamo equations and study its effects. We hope that we shall be able to present our results in the near future.

5.5 Appendix A: Calculation of the Viscosity Term

The calculation of the viscous term becomes immensely complicated if $\nabla \cdot \mathbf{v}$ is not set equal to zero. Although we are dealing with a situation in which we rather have $\nabla \cdot (\rho \mathbf{v}) = 0$, the meridional circulation velocities are everywhere highly subsonic and the role of compressibility in viscous dissipation is expected to be negligible. So we shall assume $\nabla \cdot \mathbf{v} = 0$ to make the calculations manageable. For a velocity field

$$\mathbf{v} = v_r(r, \theta, t) \mathbf{e}_r + v_\theta(r, \theta, t) \mathbf{e}_\theta$$

the non-zero components of the viscous stress tensor are

$$\begin{aligned} \sigma_{rr} &= 2\nu \frac{\partial v_r}{\partial r}, \sigma_{\theta\theta} = 2\nu \left(\frac{1}{r} \frac{\partial v_\theta}{\partial \theta} + \frac{v_r}{r} \right), \\ \sigma_{\phi\phi} &= 2\nu \left(\frac{v_r}{r} + \frac{v_\theta \cot \theta}{r} \right), \sigma_{r\theta} = \nu \left(\frac{1}{r} \frac{\partial v_r}{\partial \theta} + \frac{\partial v_\theta}{\partial r} - \frac{v_\theta}{r} \right) \end{aligned} \quad (5.25)$$

The r and θ components of the viscosity term in Navier–Stokes equation are given by

$$F_{v,r} = \frac{1}{r^2} \frac{\partial}{\partial r} (r^2 \sigma_{rr}) + \frac{1}{r \sin \theta} \frac{\partial}{\partial \theta} (\sin \theta \sigma_{r\theta}) - \frac{\sigma_{\theta\theta} + \sigma_{\phi\phi}}{r}, \quad (5.26)$$

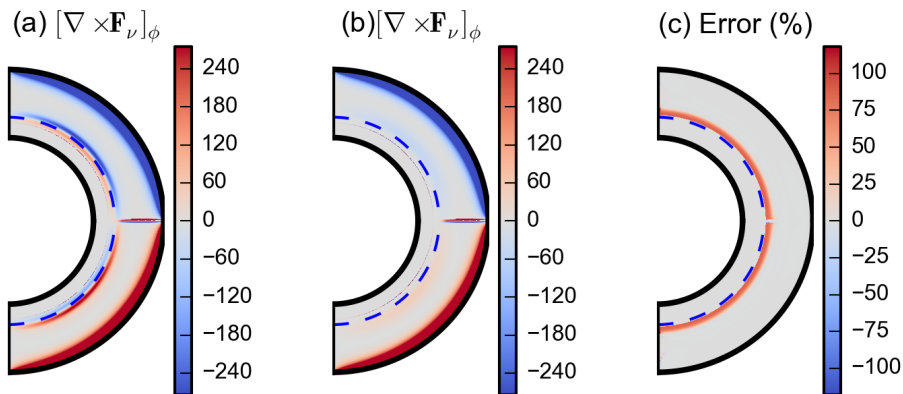


Fig. 5.10 $[\nabla \times \mathbf{F}_\nu]_\phi$ calculated using full expression (Eq. 5.30) and using approximated expression (Eq. 5.23) are shown in (a) and (b) respectively. The difference between the values of case (a) and (b) are shown in percentage in (c).

$$F_{v,\theta} = \frac{1}{r^2} \frac{\partial}{\partial r} (r^2 \sigma_{r\theta}) + \frac{1}{r \sin \theta} \frac{\partial}{\partial \theta} (\sin \theta \sigma_{\theta\theta}) + \frac{\sigma_{r\theta}}{r} - \frac{\sigma_{\phi\phi} \cot \theta}{r}, \quad (5.27)$$

We now substitute from Eq. 5.25 in Equations 5.26 and 5.27. On making use of $\nabla \cdot \mathbf{v} = 0$, we get after a few steps of algebra

$$F_{v,r} = \nu \left[\nabla^2 v_r - \frac{2}{r^2} \frac{\partial v_\theta}{\partial \theta} - \frac{2v_r}{r^2} - \frac{2 \cot \theta v_\theta}{r^2} \right] + 2 \frac{d\nu}{dr} \frac{\partial v_r}{\partial r}, \quad (5.28)$$

$$F_{v,\theta} = \nu \left[\nabla^2 v_\theta + \frac{2}{r^2} \frac{\partial v_r}{\partial \theta} - \frac{v_\theta}{r^2 \sin^2 \theta} \right] + \frac{d\nu}{dr} \left[\frac{1}{r} \frac{\partial v_r}{\partial \theta} + \frac{\partial v_\theta}{\partial r} - \frac{v_\theta}{r} \right]. \quad (5.29)$$

To solve Equation 5.12, we need $[\nabla \times \mathbf{F}_v]_\phi$, which is given by

$$[\nabla \times \mathbf{F}_v]_\phi = \frac{1}{r} \left[\frac{\partial}{\partial r} (r F_{v,\theta}) - \frac{\partial F_{v,r}}{\partial \theta} \right]. \quad (5.30)$$

On substituting Equations 5.28 and 5.29 into Eq. 5.30, we get a rather complicated analytical expression for the viscosity term. It is extremely challenging to incorporate this complicated expression in the time evolution code to solve Eq. 5.12—especially if we want to handle the diffusion terms through Crank-Nicholson scheme which is partly implicit, to avoid very small time steps. Since there are many uncertainties in this problem—including the uncertainty in the value of turbulent viscosity ν —we felt that it is not worthwhile to make an enormous effort to incorporate a completely accurate expression of the viscous term in our code to solve Eq. 5.12. In order to capture the effect of viscosity in the problem, we have used the simpler approximate expression given in Eq. 5.23. The question is whether we make a very large error in doing this simplification. To address this question, we take the unperturbed meridional circulation shown in Fig. 5.1(a) and calculate $[\nabla \times \mathbf{F}_v]_\phi$ for this velocity field both by the approximate expression in Eq. 5.23 and the full expression in Eq. 5.30. To calculate the value of $[\nabla \times \mathbf{F}_v]_\phi$ at different grid points by the full expression in Eq. 5.30, we first calculate $F_{v,r}$ and $F_{v,\theta}$ at different grid points by using Equations 5.28 and 5.29. Then we use these numerical values of $F_{v,r}$ and $F_{v,\theta}$ to calculate $[\nabla \times \mathbf{F}_v]_\phi$ by using a simple difference scheme to handle Eq. 5.30. The values obtained for $[\nabla \times \mathbf{F}_v]_\phi$ by using the full expression (Eq. 5.30) and the approximate expression (Eq. 5.23) are shown in Figure 5.10(a) and Figure 5.10(b) respectively. We see that both the expressions give fairly close values within the main body of the convection zone. Only at the bottom of the convection zone where radial derivatives of ν included in the full expression are important, the two expressions give somewhat different values—though the values are of the same order of magnitude (see Fig 5.10(c)). In Figure 5.10(c), we have shown percentage differences of $[\nabla \times \mathbf{F}_v]_\phi$ values calculated in two cases (Figures 5.10(a) and (b)) in

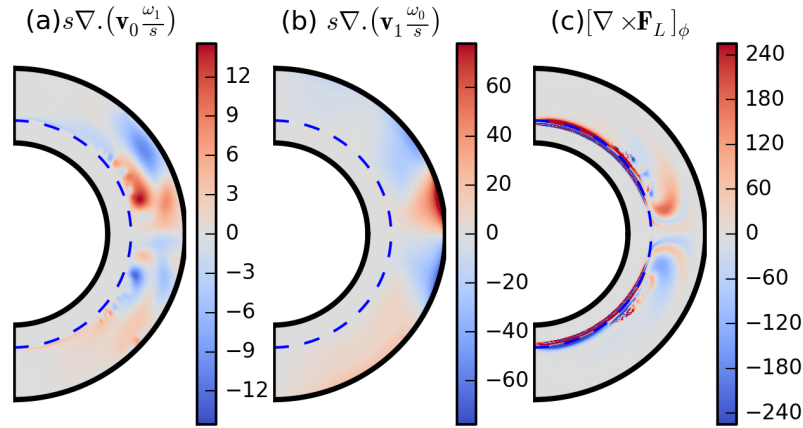


Fig. 5.11 The advective terms in LHS of Eq. 5.12 are shown in (a) and (b), where $s = r \sin \theta$. The ϕ component of the curl of the Lorentz force is shown in (c). All terms are calculated at a particular time step near a solar maximum.

our integration region above $r > 0.7R_{\odot}$. Note that things change much more at the bottom of the convection zone on changing the bottom boundary condition slightly. We thus conclude that, by using the approximate expression in Eq. 5.23 for $[\nabla \times \mathbf{F}_v]_{\phi}$, we do not make a large error and get everything within the correct order of magnitude.

5.6 Appendix B: Importance of various advective terms

In the calculations presented in this chapter, we have neglected the term $s\nabla \cdot (\mathbf{v}_1 \frac{\omega_0}{s})$ while solving Eq. 5.12, because its evaluation requires the perturbed velocity \mathbf{v}_1 in every time step which is computationally very expensive to obtain. Now we calculate the two advective terms in Eq. 5.12 separately using simple finite difference scheme at a particular time step near a solar maximum to see their relative importance with respect to the Lorentz force term $[\nabla \times \mathbf{F}_L]_{\phi}$. The values of the two advection terms involving unperturbed velocity $s\nabla \cdot (\mathbf{v}_0 \frac{\omega_1}{s})$ and involving perturbed velocity $s\nabla \cdot (\mathbf{v}_1 \frac{\omega_0}{s})$ in the $r - \theta$ plane are shown in Fig. 5.11(a) and 5.11(b) respectively. The ϕ component of the curl of the Lorentz force $[\nabla \times \mathbf{F}_L]_{\phi}$ is shown in Fig. 5.11(c). The color table for curl of the Lorentz force is clipped to 240 to show its value in the convection zone (where it has much smaller values compared to the tachocline) but its maximum value is about 3000. Thus, in comparison to the curl of the Lorentz force, the other terms are small but not negligible. The advective term $s\nabla \cdot (\mathbf{v}_0 \frac{\omega_1}{s})$ which we already included is important within the convection zone, but the other term with perturbed velocity $s\nabla \cdot (\mathbf{v}_1 \frac{\omega_0}{s})$ which we plan to include in our future work is important near the surface at low latitudes. The dynamics of vorticity presented in the Section 5.3.1 clearly reflect the fact that

the time evolution of vorticity is mostly determined by the Lorentz force term $[\nabla \times \mathbf{F}_L]_\phi$ (see Fig. 5.4((k)-(o))) even when the advective term $s\nabla \cdot (\mathbf{v}_0 \frac{\omega_1}{s})$ is included. However, since the $s\nabla \cdot (\mathbf{v}_1 \frac{\omega_0}{s})$ term becomes appreciable in the regions where we have inward flow towards active regions during the sunspot maximum, this term may have some importance in modeling this inward flow. We plan to investigate this further in future.

"We must not think of the things we could do with, but only of the things that we can't do without"

—Jerome k Jerome, Three men in a boat

6

3D Flux Transport Dynamo Model and Build up of Solar Polar Field

We develop a three-dimensional kinematic self-sustaining model of the solar dynamo in which the poloidal field generation is from tilted bipolar sunspot pairs placed on the solar surface above regions of strong toroidal field by using the SpotMaker algorithm and then the transport of this poloidal field to the tachocline is primarily caused by turbulent diffusion. We obtain a dipolar solution within a certain range of parameters. We use this model to study the build-up of the polar magnetic field and show that some insights obtained from surface flux transport (SFT) models have to be revised. We present results obtained by putting a single bipolar sunspot pair in a hemisphere and two symmetrical sunspot pairs in two hemispheres. We find that the polar fields produced by them disappear due to the upward advection of poloidal flux at low latitudes, which emerges as oppositely-signed radial flux and which is then advected poleward by the meridional flow. We also study the effect that a large sunspot pair violating Hale's polarity law would have on the polar field. We find that there would be some effect—especially if the anti-Hale pair appears at high latitudes in the mid-phase of the cycle—though the effect is not very dramatic.

6.1 Introduction

The flux transport dynamo model, which started being developed from the 1990s (Choudhuri et al., 1995; Durney, 1995; Wang et al., 1991), has emerged as an attractive theoretical model for explaining the solar cycle and has been extensively reviewed by several authors (Charbonneau, 2014; Choudhuri, 2011b; Karak et al., 2014a). In any dynamo model, the toroidal magnetic field is generated from the poloidal field by the differential rotation, which has now been mapped by helioseismology (Thompson et al., 1996). The distinctive features of the B-L flux transport dynamo model are that the meridional circulation plays a crucial role in this model and the poloidal magnetic field is generated by the Babcock–Leighton (BL) process involving the decay of tilted bipolar sunspots. Bipolar sunspots are assumed to form due to the buoyant rise of the toroidal magnetic flux through the convection zone (Parker, 1955a) and their tilts result from the action of the Coriolis force on the rising flux tubes (Choudhuri, 1989; D’Silva & Choudhuri, 1993; Fan et al., 1993) leading to Joy’s law (Hale et al., 1919). When a tilted pair of bipolar sunspots decays, turbulent diffusion spreads the magnetic flux to produce a poloidal magnetic component (Babcock, 1961; Leighton, 1964). An over-all poloidal field develops from the contributions due to many bipolar sunspots and is advected to the poles by the meridional circulation, which is poleward in the upper layers of the convection zone. The polar magnetic field of the Sun is built up in this process.

The BL process—which involves the production of tilted bipolar sunspot pairs and the generation of the poloidal field from their decay—is an inherently 3D process and can be modeled in 2D only through drastically simplified crude approximations (Choudhuri & Hazra, 2016). Still an understanding of how the poloidal field builds up by the BL process historically came from two distinct classes of 2D theoretical models: the 2D flux transport dynamo model and the surface flux transport (SFT) model. In the 2D flux transport dynamo model, we average over the azimuthal direction ϕ and solve the axisymmetric dynamo equation in the r - θ plane. On the other hand, in the SFT model, we focus our attention only on the B_r component of the magnetic field at the solar surface spanned by the θ - ϕ coordinates and study its evolution on this surface under the joint action of diffusion, meridional circulation and differential rotation. Neither of these approaches provides a fully satisfactory depiction of the BL process and each approach has its own limitations.

If a tilted bipolar sunspot pair at the solar surface is averaged over the azimuthal direction ϕ , then we get two rings of opposite magnetic polarity at slightly different latitudes. Durney (1995, 1997) advocated the development of the flux transport dynamo model by using such double rings as the source of the poloidal component. However, a more popular approach has been to introduce an α -coefficient reminiscent of the α -effect of the mean field dynamo theory (Chapter 16, Choudhuri (1998); Parker (1955b); Steenbeck et al. (1966)), although this now

has a completely different interpretation. The source term of the poloidal field is taken as the product of this α -coefficient and the toroidal field that has risen from the tachocline due to magnetic buoyancy. Choudhuri & Hazra (2016) review how different authors achieve this, with references to the original papers. Nandy & Choudhuri (2001) showed that the double ring approach and the treatment through α -coefficient give qualitatively similar results, although Muñoz-Jaramillo et al. (2010) argued that the double ring approach is more realistic. In any case, the 2D kinematic dynamo models do not give a detailed picture of how the poloidal field builds up from the contributions of many individual bipolar sunspot pairs, since such pairs get smeared over when we average over the azimuthal direction. Also, as most of these dynamo models rely on a mean field approach, flux tubes or sunspots are not handled properly in these models (Choudhuri, 2003).

Starting from the pioneering work of Wang et al. (1989a,d), the surface flux transport (SFT) model has been made more sophisticated in several recent studies (Baumann et al., 2004, 2006; Cameron et al., 2010; Jiang et al., 2014b, 2015; Schrijver et al., 2002; Upton & Hathaway, 2014a; van Ballegoijen et al., 1998). In this model, recently reviewed by Jiang et al. (2014a), one can study in detail how individual sunspot pairs contribute in building up the poloidal field and can address such questions as to how this process depends on such factors as the latitudinal positions of the sunspot pairs and the distribution in their tilt angles. The main limitation of this model is that several important aspects of physics get left out by ignoring the vectorial nature of the magnetic field and by not including any subsurface processes. By studying the time evolution of an axisymmetric poloidal field, Dikpati & Choudhuri (1994, 1995) and Choudhuri & Dikpati (1999) showed that the subduction of the poloidal field by the meridional circulation sinking underneath the surface at the polar region plays an important role in the dynamics of the magnetic field. Since this process cannot be included in the SFT models, flux of B_r tends to get piled up in the polar regions and has to be neutralized by flux of opposite sign advected there. If additional flux of opposite sign is not brought there, then the polar field may reach an asymptotic value as seen in Figure 6 of Jiang et al. (2014b). When one tries to model several successive cycles through an SFT model, one may get a ‘secular drift’ of the polar field if the flux of the succeeding cycle is unable to properly neutralize the polar flux of the preceding cycle, as seen in Figure 1 of Baumann et al. (2006). A way of fixing this problem proposed by Baumann et al. (2006) involves adding an ad hoc decay term corresponding to the radial diffusion not included in the SFT model. In spite of the tremendously important historical role the SFT model has played in elucidating the BL process, this model has the inherent limitation that it cannot adequately handle the magnetic field dynamics in the Sun’s polar region.

We believe that the next step forward is the 3D kinematic flux transport dynamo model. In this model, the fluid motions (differential rotation, meridional circulation) are specified

and the evolution of the magnetic field is calculated in 3D. Such a model has the promise of incorporating the attractive features of both the 2D flux transport dynamo model and the SFT model, while being free from the limitations of both these models. It can handle the BL process much more realistically than the 2D flux transport dynamo model where we average over the azimuthal direction and cannot include tilted bipolar sunspots properly. On the other hand, this model incorporates the vectorial nature of the magnetic field and the subsurface processes which are left out in the SFT models.

Efforts of constructing 3D kinematic flux transport dynamo models began only within the last few years. In a landmark paper, [Yeates & Muñoz-Jaramillo \(2013\)](#) developed a method of treating the buoyant rise of a flux tube in their 3D dynamo model by simultaneously applying a radially outward and a vortical velocity to a localized part of an azimuthal flux tube at the bottom of the convection zone. Although they did not present a self-excited dynamo solution, they simulated a solar cycle by incorporating bipolar sunspot eruptions by this method at the actual locations where bipolar sunspots were observationally seen. [Miesch & Dikpati \(2014\)](#) succeeded in producing a self-excited dynamo by identifying the locations (in latitude and longitude) at the bottom of the convection zone where the toroidal field was the strongest (in the theoretical model) and then putting tilted bipolar sunspot pairs above those locations with loop-like magnetic structures both above and below the surface (by using an algorithm which they named SpotMaker). More details of this model have been given by [Miesch & Teweldebirhan \(2016\)](#). After a part of the toroidal flux tube rises to the surface to produce bipolar sunspots, the magnetic field underneath these sunspots has to be detached at some stage from the bottom of the convection zone before the magnetic flux of the sunspots is dispersed freely by diffusion and carried poleward by the meridional circulation ([Longcope & Choudhuri, 2002](#)). Our lack of understanding of this process is the main difficulty in constructing realistic 3D dynamo models at the present time. Presumably, the approach of [Yeates & Muñoz-Jaramillo \(2013\)](#) captures the physics of the early phase soon after the bipolar sunspots emerge, whereas the approach of [Miesch & Dikpati \(2014\)](#) is more appropriate for the later phase when the magnetic field below the sunspot pairs has become detached from the bottom of the convection zone.

The aim of this study is to use a modified version of the model of [Miesch & Dikpati \(2014\)](#) to study the build-up of the Sun's polar magnetic field by the BL process in more detail. The model of [Miesch & Dikpati \(2014\)](#) uses values of parameters (such as turbulent diffusion) which are probably not very realistic for the Sun. We use the same dynamo code named as STABLE (i.e. Surface flux Transport And Babcock LEighton Model) to first construct a model of the solar dynamo based on more realistic values of parameters and then use this model for our study. Since the BL process has been studied most extensively by the SFT models, we

especially address the question whether the insights gained about various aspects of this process from the SFT models are borne out by the 3D model or have to be revised significantly. We shall see that the accumulation of magnetic flux at the poles seen in the SFT models does not occur when the low-latitude advection and emergence of oppositely-signed radial flux is taken into account. Thus, the problem of ‘secular drift’ is automatically eliminated. One insight from the SFT models is that the fluxes of leading sunspots at lower latitudes get canceled across the equator and the fluxes from the following sunspots are then advected to the poles, building up a dipole moment of the Sun. We shall see that this insight also will have to be modified significantly. SFT models indicate that even a few large sunspot pairs with anti-Hale or wrong polarity (i.e. opposite of what is expected of sunspot pairs in that cycle) may have significant effect on the polar field (Jiang et al., 2015). We shall be able to study this effect more realistically in our 3D model.

After discussing the mathematical formulation of the problem in the next section, the standard model of the solar dynamo which we shall use is presented in Section 6.3. Then the build-up of the polar field is studied in Section 6.4, whereas the effects of large anti-Hale sunspot pairs are discussed in Section 6.5. Our conclusions are summarized in Section 6.6.

6.2 Mathematical Formulation

In this section, we explain the basic formulation of the STABLE dynamo model which is first reported in Miesch & Dikpati (2014) and in more detail in Miesch & Teweldebirhan (2016). This model is a 3D generalization of the pre-existing axisymmetric 2D flux transport dynamo models and it solves the induction equation in full 3D rotating spherical shell with radius ranges from $r = 0.69R$ to $r = R$ of the Sun:

$$\frac{\partial \mathbf{B}}{\partial t} = \nabla \times (\mathbf{v} \times \mathbf{B} - \eta_t \nabla \times \mathbf{B}) + S(\theta, \phi, t) \quad (6.1)$$

where \mathbf{v} is the velocity field, $\eta_t(r)$ is the turbulent diffusion in the solar convection zone and $S(\theta, \phi, t)$ is the source function which captures the effect of the BL mechanism. As we shall discuss in detail later, the source function $S(\theta, \phi, t)$ is of the nature of an impulsive forcing term which becomes non-zero only at the instants when we allow a bipolar sunspot pair to be put at the solar surface. Though this model is fully 3D and no axisymmetric assumption is considered but still this model is kinematic and we provide the velocity field motivated from helioseismology and observations. We solve equation (6.1) using Anelastic Spherical Harmonic (ASH) code (Brun et al., 2004; Miesch et al., 2000). ASH is a well-established pseudospectral code which has been used extensively for 3D solar and stellar convection

simulations, instabilities, tachocline confinement and many other aspects of solar and stellar internal dynamics. The ASH code has capability to solve the velocity equation and magnetic induction equation together but for our kinematic model we bypass the velocity equation solver and only solve the induction equation by providing observationally motivated velocity fields. The version of the code used for 3D kinematic dynamo modeling is named STABLE (i.e. Surface flux Transport And Babcock LEighton Model).

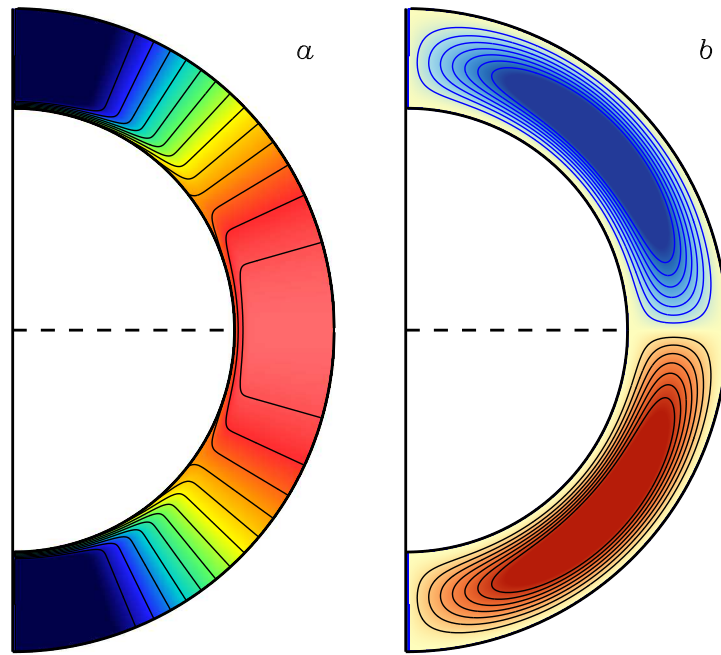


Fig. 6.1 (a). Differential rotation profile with color table ranging from 350-480 nHz from blue to red, (b) Streamlines for the meridional flow. Blue and red contours show the poleward flow at the surface, and an equatorward flow at the bottom of the convection zone in northern and southern hemisphere respectively. The amplitude of the meridional circulation is taken as 20.40 m/s on the surface and 1.64 m/s at the lower convection zone.

The mean velocity field \mathbf{v} in the Sun can be written as the summation of the part from differential rotation Ω and the meridional circulation v_p . Whereas the exact differential rotation is mapped from helioseismology quite well (Schou et al., 1998), the structure of the meridional circulation in the solar convection zone is still under study. Recently different helioseismology groups have reported substantially different structures of the meridional circulation in the solar convection zone (Rajaguru & Antia, 2015; Schad et al., 2013; Zhao et al., 2013). In response to these observational claims, Hazra et al. (2014) carried on calculations with different types of meridional circulation structure and showed that flux transport dynamo works quite well as long as there is an equatorward flow at the bottom of the convection zone. Recently Karak &

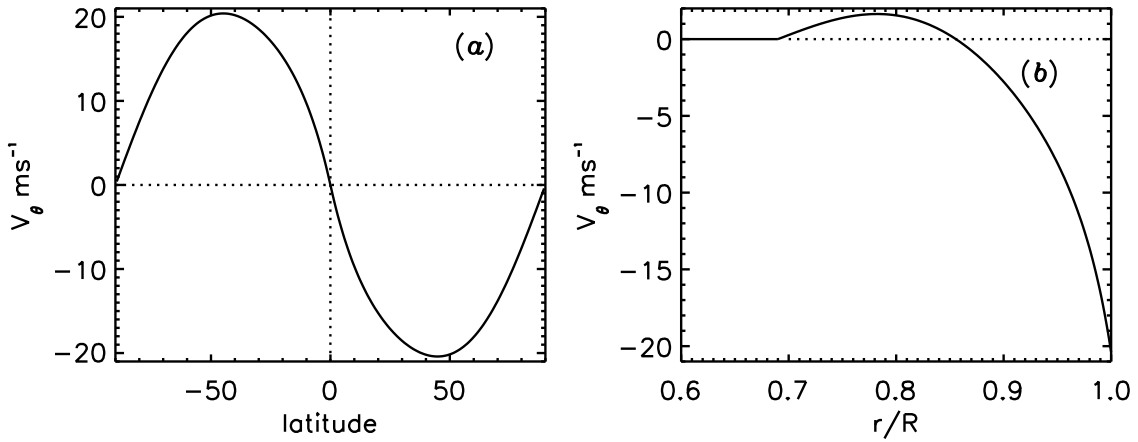


Fig. 6.2 Variation of latitudinal component of meridional circulation V_θ with latitude on the surface (a) and with radius at 45° latitude (b).

Cameron (2016) showed that in the presence of appropriate profile of downward pumping in the solar convection zone, the flux transport solar dynamo works with even shallow meridional circulation. Since there is still no compelling reason (Rajaguru & Antia, 2015) to give up the simple single-cell profile of meridional circulation used by many previous authors (Chatterjee et al. (2004), Miesch & Dikpati (2014)), we use a single cell profile of the meridional circulation having a poleward flow at the surface and an equatorward return flow at the bottom of the convection zone. The stream function corresponding to the meridional circulation which we use here is

$$\psi r \sin \theta = \psi_0 (r - R_p) \sin \left[\frac{\pi (r - R_p)}{(R_\odot - R_p)} \right] \{1 - e^{-\beta_1 r \theta^\varepsilon}\} \{1 - e^{\beta_2 r (\theta - \pi/2)}\} e^{-((r - r_0)/\Gamma)^2} \quad (6.2)$$

with $\beta_1 = 0.3 \times 10^{-10} \text{ cm}^{-1}$, $\beta_2 = 0.5 \times 10^{-10} \text{ cm}^{-1}$, $\varepsilon = 2.0000001$, $r_0 = (R_\odot - R_b)/4.0$, $\Gamma = 3.5 \times 10^{10} \text{ cm}$, $R_p = 0.69R_\odot$. The value of ψ_0 determines the amplitude of the meridional circulation. On taking $\psi_0 = 12.0$, the poleward flow near the surface at mid-latitudes peaks around $v_0 = 20.40 \text{ m s}^{-1}$. The contour plot for the meridional circulation is shown in figure 6.1(b) and the variation of V_θ with latitude on the surface and variation V_θ with radius at mid-latitude (45°) are shown in figure 6.2(a) and 6.2(b) respectively. For differential rotation we have used the analytical formula given in (Dikpati & Charbonneau, 1999) which is a good fit to the observational data (Figure 6.1(a)).

Turbulent diffusivity is another important parameter. After the BL process generates the poloidal field near the solar surface, it has to reach the tachocline where the differential rotation acts on it to produce the toroidal field. This can happen in two ways. The poloidal field may

first be advected by the meridional circulation to the pole and then underneath the surface to the mid-latitude tachocline from where the first sunspots of cycle rise. The time scale for this is close to 20 yr for a reasonable profile of the meridional circulation. The second possibility is that the poloidal field diffuses from the surface to the bottom of the convection zone to be acted upon by the differential rotation of the tachocline. The Green's function for the diffusion equation suggests that the diffusion time across a length L is $L^2/4\eta_t$ (see, for example, [Parker \(1979\)](#), p. 32). If the turbulent diffusivity within the convection zone is assumed to be $5 \times 10^{11} \text{ cm}^2 \text{ s}^{-1}$ as we shall do, then this diffusion time turns out to be about 7 yr if we take L to be the thickness of the convection zone. The value of the turbulent diffusivity determines whether the poloidal field is transported across the convection zone primarily by meridional circulation or by turbulent diffusion, and the behavior of the dynamo is very different in the two situations ([Jiang et al., 2007](#); [Yeates et al., 2008](#)). Over the years, we have got more and more evidence that the turbulent diffusivity has to be sufficiently high to make the poloidal field transport primarily by diffusion in order to explain many aspects of the solar cycle, such as the dipolar parity ([Chatterjee et al., 2004](#); [Hotta & Yokoyama, 2010](#)), the lack of significant hemispheric asymmetry ([Chatterjee & Choudhuri, 2006](#); [Goel & Choudhuri, 2009](#)), the observed correlation between the polar field at the cycle minimum and the strength of the next cycle ([Jiang et al., 2007](#)), the Waldmeier effect ([Karak & Choudhuri, 2011](#)). Such a value of turbulent diffusivity is also consistent with mixing length arguments ([Parker \(1979\)](#), p. 629) and the theory of mean flows ([Miesch et al., 2012b](#)).

In most of the SFT models, a constant diffusivity $(2.5 - 3.0) \times 10^{12} \text{ cm}^2 \text{ s}^{-1}$ on the surface is used ([Jiang et al., 2014a](#)). The turbulent diffusivity is expected to be less within the convection zone and falls drastically at its bottom where convection is less vigorous. Except when stated explicitly otherwise, the calculations of this chapter assume the diffusivity to be given by

$$\eta_t = \eta_c + \frac{\eta_{mid}}{2} \left[1 + \operatorname{erf} \left(2 \frac{r - r_{da}}{d_a} \right) \right] + \frac{\eta_{top}}{2} \left[1 + \operatorname{erf} \left(2 \frac{r - r_{db}}{d_b} \right) \right] \quad (6.3)$$

where $\eta_c = 2 \times 10^{10} \text{ cm}^2 \text{ s}^{-1}$, $\eta_{mid} = 5 \times 10^{11} \text{ cm}^2 \text{ s}^{-1}$, $r_{da} = 0.725R_\odot$, $r_{db} = 0.956R_\odot$, and $d_b = 0.05R$. In [Figure 6.3](#) we have shown the diffusivity profile by the blue solid line. For comparison, the diffusivity profile used by [Miesch & Dikpati \(2014\)](#) is shown by the black solid line. It may be noted that some groups ([Dikpati & Charbonneau, 1999](#); [Dikpati & Gilman, 2006](#)), over the years, used a rather low value of diffusivity. As seen in [Figure 6.3](#), [Miesch & Dikpati \(2014\)](#) and [Miesch & Teweldebirhan \(2016\)](#) followed these authors in using a diffusivity which was, within the body of the convection zone, about one order of magnitude smaller than what we are using. In our case the diffusivity η_{mid} in the convection zone is $5 \times 10^{11} \text{ cm}^2 \text{ s}^{-1}$, whereas [Miesch & Dikpati \(2014\)](#) and [Miesch & Teweldebirhan \(2016\)](#) use

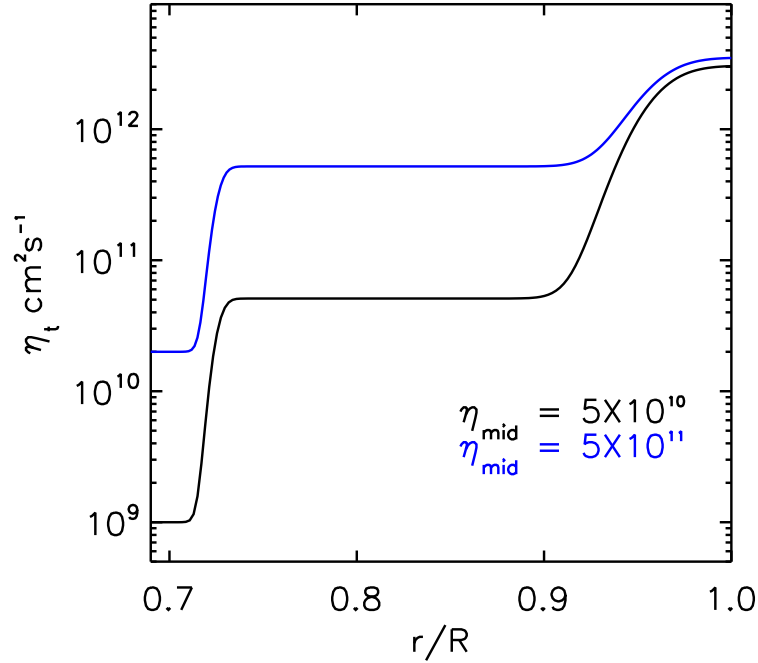


Fig. 6.3 High diffusivity profile used for most of our simulation is shown in blue solid line and the profile used for advection-dominated regime is shown in black solid line.

$5 \times 10^{10} \text{ cm}^2\text{s}^{-1}$. Such a lower value of diffusivity would make the diffusion time across the convection zone of the order of 70 yr and the advection by the meridional circulation would clearly be the dominant process for the transport of the poloidal field. [Miesch & Dikpati \(2014\)](#) presented a self-excited dynamo solution for this situation. For the value of diffusivity we are using, the diffusion across the convection zone is the primary process for bringing the poloidal field from the solar surface to the tachocline. We believe that we are the first to obtain a self-excited 3D kinematic dynamo solution for this case, which we contend is closer to reality.

We now discuss how the source term $S(\theta, \phi, t)$ in Eq. 6.1 is specified with the help of the SpotMaker algorithm to treat the BL process. This algorithm is mainly a 3D generalization of the Durney's double ring algorithm ([Durney, 1995, 1997](#)). In this algorithm, two suitable opposite-polarity spots are placed on the surface of the Sun in response to the dynamo-generated field near the base of the convection zone and then they are allowed to decay in the presence of mean flows (meridional circulation and differential rotation) and diffusivity. The first aim of this algorithm is to find out the suitable position for these spots to be placed on the surface. To do so, we calculate the mean toroidal flux $\bar{B}(\theta, \phi)$ near the bottom of the convection zone averaged over the tachocline thickness ([Miesch & Teweldebirhan, 2016](#)) and find out where this field is crossing the threshold value B_t . It is believed that if magnetic fields near the bottom of the convection zone are stronger than the threshold value B_t then they become magnetically

buoyant and create the bipolar sunspots on the surface (Parker, 1975). So the latitude and longitude of the spot pair is chosen randomly from all grid points where the mean toroidal flux exceeds B_t , subject to a mask that suppresses spots at high latitudes. When we are able to find the θ_s and ϕ_s where the dynamo-generated toroidal field is more than the threshold value B_t , we put two spots on the surface at that position. Once the position of the bipolar sunspots is decided, the next step is to specify the magnetic field there, by putting some tilt angle between the two sunspots according to Joy's law. For that we use the polynomial profile as given in Miesch & Dikpati (2014) and for tilt angle we follow the procedure given in Stenflo & Kosovichev (2012). We choose the tilt angle to be $\delta = 32.1^\circ \cos \theta$. We do not want to put these spots at each time step of our simulation. There are always certain time differences between the appearances of different sunspot groups. So we have used a time delay probability density function which allows us to put successive sunspot pairs having a random time delay between their appearances (Miesch & Teweldebirhan, 2016). Another thing we should mention here is that, as seen in the observed butterfly diagram, sunspots are found mostly on the lower latitudes and in our model we artificially suppress the sunspot formation at higher latitude using some masking function as given in equation (3) of the Miesch & Dikpati (2014). The flux content in the spots and the strength of the radial field are chosen based on the dynamo-generated field \bar{B} and the observed strength of the sunspots as given below.

$$\Phi = 2\alpha_{spot} \frac{|\hat{B}(\theta_s, \phi_s, t)|}{B_q} \frac{10^{23}}{1 + (\hat{B}(\theta, \phi)/B_q)^2} \text{Mx} \quad (6.4)$$

where $\hat{B} = g(\theta)\bar{B}$ is the toroidal field after using the masking function $g(\theta)$ to suppress sunspots at high latitude and B_q is the quenching field strength. Here α_{spot} is the parameter which determines whether the dynamo will be sub-critical or super-critical. Our ultimate aim would be to make the dynamo work with $\alpha_{spot} = 1$ so that the flux in a particular BMR will have a value of 10^{23} Mx as observed in case of the subsurface field strength equivalent to the quenching field strength. But if the subsurface field at the bottom of the convection zone is not close to the quenching field, then we have to increase the value of α_{spot} in order to get a working dynamo with bigger spots. In case of the diffusion-dominated dynamo, we are able to get a working dynamo with $\alpha_{spot} = 100$. While creating sunspot pairs by the SpotMaker algorithm, once the total flux is fixed by (6.4), we have the freedom of selecting either the magnetic field strength or the size. We choose the magnetic field strength inside the sunspots to be 3000 G, which fixes the size.

Since we are solving magnetic fields in 3D spherical shell, so we must have to specify the subsurface structure of the sunspots which are put on the surface using SpotMaker algorithm. As it is argued by Longcope & Choudhuri (2002) and Schüssler & Rempel (2005) that the

sunspots get quickly disconnected from the parent flux tube, we make a very simple potential field approximation for the sunspot fields (see Figure 2(a,b) of [Miesch & Teweldebirhan \(2016\)](#)). We ensure that the radial field becomes zero at some penetration depth ($r = 0.90R$) and it is equal to the imposed sunspot field at the surface ($r = R$). For the upper boundary condition, we take the magnetic field to be radial at the solar surface. Throughout our simulation we use $N_r = 200$, $N_\theta = 256$ and $N_\phi = 512$. All of the cases where we show the field lines above the solar surface ($r = R$) are the extrapolated fields using a free potential approximation.

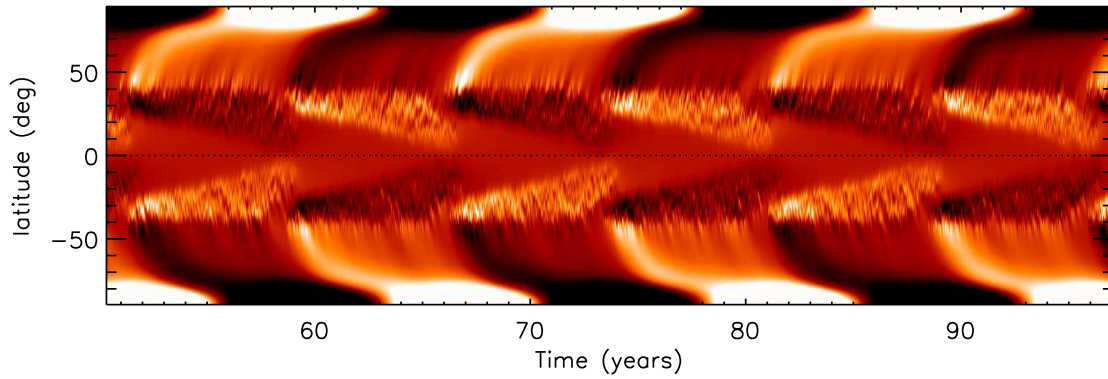


Fig. 6.4 Time-latitude plot of longitudinally averaged radial magnetic field on the surface ($r = R$) of Sun. Color table is set at ± 10 kG.

6.3 Our reference model

Now we present a self-excited solution from our reference model with parameters as prescribed in the previous section. To the best of our knowledge, this is the first self-excited 3D kinematic dynamo solution in which the diffusivity has been assumed sufficiently high to make sure that the poloidal field is transported from the surface to the tachocline primarily by diffusion. The earlier results presented by [Miesch & Dikpati \(2014\)](#) and [Miesch & Teweldebirhan \(2016\)](#) were obtained with a diffusivity one order of magnitude smaller and the transport of the poloidal field was due to the meridional circulation.

Figure 6.4 shows a butterfly diagram obtained by putting the longitude-averaged B_r in a time-latitude plot. One clearly sees the butterfly diagram of sunspots at lower latitudes and the poleward advection of the magnetic field by the meridional circulation at higher latitudes. Superficially this resembles Figure 6(a) of [Miesch & Teweldebirhan \(2016\)](#), although our solution is for the diffusion-dominated case in contrast to the solution of [Miesch & Teweldebirhan \(2016\)](#) obtained for the case dominated by advection due to the meridional

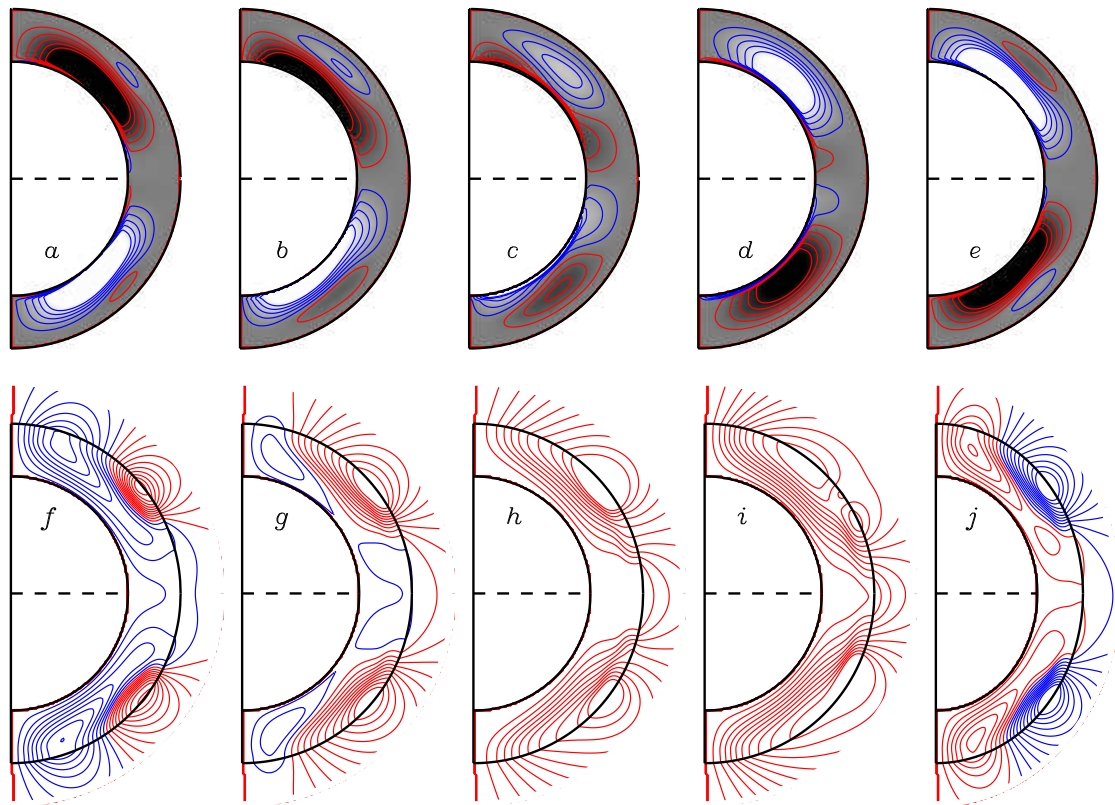


Fig. 6.5 Mean toroidal and poloidal field lines are shown for a particular solar cycle at five different time: $t = 60.0$ (a,f), 62.0 (b,g), 64.0 (c,h), 66.0 (d,i) and 68.0 years (e,j). Frames (a-e) show mean toroidal fields with red and blue lines indicating eastward and westward field respectively. Filled color also represents the mean toroidal fields. Color table is set in this case at ± 500 kG. Frames (f-g) represent poloidal magnetic potential with potential field extrapolation above the surface (upto $r = 1.25R$) where red and blue lines represent clockwise and anticlockwise directions. The maximum and minimum contour level is set corresponding to the poloidal field strength of ± 49 kG

circulation. The differences between the two cases become clear on looking at the distribution of the magnetic field. Figure 6.5 shows the evolution of the toroidal and the poloidal fields during a cycle. Comparing with Figure 8 of [Miesch & Teweldebirhan \(2016\)](#), we see some obvious differences. In the solution of [Miesch & Teweldebirhan \(2016\)](#), the oppositely directed toroidal fields on the two sides of the equator almost pressed against each other. Due to the low diffusivity, there would not be much diffusion of the toroidal field even when two opposite bands are brought so close to each other. In our model with higher diffusivity, however, there would be more diffusion of the toroidal field across the equator, making sure that the bands of concentrated opposite polarity are kept somewhat apart, as seen in Fig. 6.5.

The solar magnetic field is predominantly dipolar. One requirement of a theoretical solar dynamo model is that it should have dipolar parity. We have run our reference model for several cycles to ensure that the dipolar parity persisted. One important question is under what circumstances we would expect dipolar parity. This question has been studied thoroughly by [Chatterjee et al. \(2004\)](#) and [Hotta & Yokoyama \(2010\)](#) for the 2D kinematic dynamo model. A full study of this question requires running the code for many different combinations of parameters and running it for a large number of cycles for each such combination. This would require a huge amount of computer time for the 3D model. Because of the limited computer time available to us, we have not been able to study this question exhaustively. However, we have made a limited number of runs to explore the issue of parity a little bit. The best way to look at the issue of parity is to make a butterfly diagram of longitudinally averaged B_ϕ at the bottom of the convection zone, as done in Figure 7(a) of [Chatterjee et al. \(2004\)](#). In Figure 6.6(a) we show such a plot for our reference model, whereas Figure 6.6(b) shows a similar plot for the case in which the value of diffusivity within the convection zone has been changed from $5 \times 10^{11} \text{ cm}^2 \text{ s}^{-1}$ to $7 \times 10^{11} \text{ cm}^2 \text{ s}^{-1}$ while keeping all the other parameters exactly the same as in our reference model. We clearly see in Figure 6.6(b) that the nature of the solution is changing from a dipolar parity to a quadrupolar parity.

The surprising fact is that we now seem to get a result which is opposite of what [Chatterjee et al. \(2004\)](#) and [Hotta & Yokoyama \(2010\)](#) obtained for the 2D kinematic dynamo model. These authors found that the dipolar parity is preferred on increasing the diffusivity, whereas we now are finding the opposite of that. Let us look at the physics of the problem. In a dipolar mode, the poloidal magnetic field lines connect across the equator, whereas the toroidal field on the two sides of the equator has to be directed oppositely. In order for this to happen, we need diffusivity to have a big effect on the poloidal field, but not much effect on the toroidal field. In the model of [Chatterjee et al. \(2004\)](#), any strong toroidal field within the convection zone was removed by magnetic buoyancy and the toroidal field at the bottom of the convection zone was also depleted continuously to account for flux loss due to magnetic buoyancy. As a result, the toroidal magnetic field near the equator was naturally weak and the effect of diffusion was more important on the poloidal field than on the toroidal field. This ensured that higher diffusivity favored the dipolar mode. In the present calculation, the situation is rather different. The strong parts of the toroidal field are now allowed to hover in the middle of the convection zone and near the equator. On increasing diffusivity, the quadrupolar mode in which the toroidal field on the two sides of the equator has the same sign is favored. Here we should mention that the magnetic pumping can play a very important role to promote dipolar parity ([Guerrero & de Gouveia Dal Pino, 2008](#)). Another point to note is that [Chatterjee et al. \(2004\)](#) used a lower diffusivity of the toroidal field compared to the poloidal field, to account for the quenching

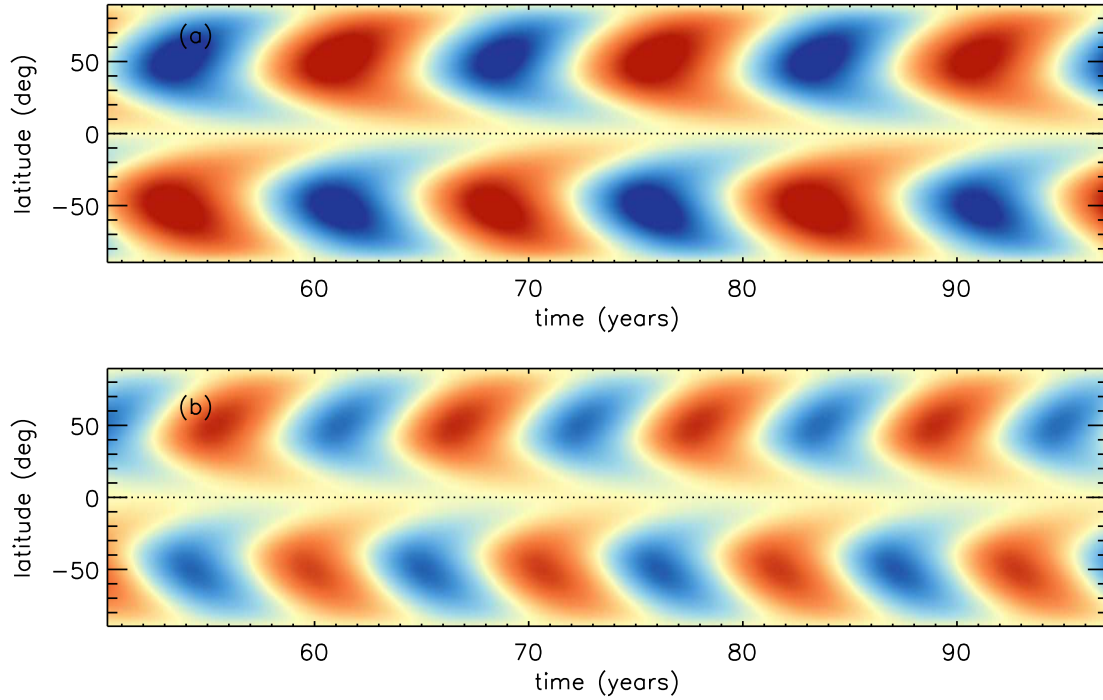


Fig. 6.6 Azimuthal averaged toroidal fields B_ϕ at the bottom of the convection zone ($r = 0.71R$) for two different values of diffusivity η_{mid} at the convection zone (a) $5 \times 10^{11} \text{ cm}^2 \text{ s}^{-1}$ and (b) $7 \times 10^{11} \text{ cm}^2 \text{ s}^{-1}$. Color table is set at $\pm 400 \text{ kG}$.

of turbulent diffusion due to the stronger toroidal magnetic field. This could be done in a 2D mean field model in which the evolution equations for the toroidal and poloidal fields neatly separate out, and one could use different values of diffusivity in the two equations. Since it is not possible to do this in a 3D non-axisymmetric model in which the equations for the toroidal and poloidal components do not split in this way, we have used a single diffusivity. It is possible that the weaker diffusivity of the toroidal field in [Chatterjee et al. \(2004\)](#) helped in producing a dipolar parity by allowing toroidal fields of opposite sign to exist on the two sides of the equator more easily. One way of capturing the physics of this in a 3D non-axisymmetric model may be to include a quenching of turbulent diffusivity in the regions of strong magnetic field. We plan to explore the effect of this in future.

With these two opposite results at hand, one crucial question is: which of the two results is closer to reality? Although we cannot assert this with confidence at this stage, we believe that the 2D kinematic dynamo result that the dipolar parity is preferred on increasing diffusivity is the more appropriate result. Although in this study we are taking account of the 3D nature of magnetic buoyancy and, in that sense, treating magnetic buoyancy more realistically, we still have not taken account of flux depletion from the convection zone and its bottom in an

appropriate way. This is probably one important reason why our results are not matching with the results of previous 2D models (Chatterjee et al., 2004; Hotta & Yokoyama, 2010). We are right now exploring possible schemes to take account of the flux depletion due to magnetic buoyancy in a realistic way. We believe that this flux depletion is quite important in the solar dynamo. Choudhuri & Hazra (2016) found that the Waldmeier effect cannot be reproduced from a theoretical dynamo model unless the flux depletion is taken into account. We have a future plan of incorporating flux loss due to magnetic buoyancy in a realistic way in our 3D kinematic dynamo model and then studying the parity issue more carefully.

Since we are interested in a dynamo solution which has dipolar parity, we have converged on the reference solution presented here. If we decrease diffusivity, then we are led to the case where the meridional circulation provides the main transport mechanism for the poloidal field. On the other hand, if we increase diffusivity, then we obtain the quadrupolar mode. This is what has led us to choose the value $5 \times 10^{11} \text{ cm}^2 \text{ s}^{-1}$ for diffusivity inside the convection zone.

6.4 The build-up of the polar field

After constructing the self-excited dynamo model, we now study how individual sunspot pairs contribute to the building up of the polar field and address the question whether our understanding gained from this study necessitates the revision of some insights we have from surface flux transport (SFT) models. For this study, we shall put individual sunspot pairs on the solar surface by hand and look at the evolution of the magnetic field. In other words, we shall now not try to construct self-excited periodic solutions, although we shall keep using the same values of different parameters that we had used for constructing the self-excited periodic solution.

We start our simulation by putting a single pair of bipolar sunspots in the northern hemisphere at different emergence angles λ_{emg} and let it evolve under the axisymmetric mean flows and diffusion to see the development of the polar field. We have chosen magnetic flux of $1 \times 10^{22} \text{ Mx}$ in each spot and its radius is taken to be 21.71 Mm (somewhat larger than actual sunspot radii, to make the results of the simulation more clearly visible) throughout our simulations. In the next set of our simulations, we shall put two pairs of sunspots symmetrically in the two hemispheres, which have the same amount of flux and radius as in the case of the single pair to see the effects of cross-equator diffusion of magnetic flux.

6.4.1 Polar field from one sunspot pair

We use the SpotMaker algorithm to put one sunspot pair at latitude 20° with tilt angle 40° . Then we allow our code to evolve the magnetic field from this sunspot pair leading to the build-up of the polar field. Figure 6.7 shows snapshots of B_r on the solar surface at different times during the evolution process. This figure can be compared with Figure 6 of Yeates & Muñoz-Jaramillo (2013). Although Yeates & Muñoz-Jaramillo (2013) assumed the sunspot pair to be initially connected to the toroidal flux system at the bottom of the convection zone, eventually this connection would be disrupted and the evolution of the magnetic field on the surface due to the sunspot pair in the northern hemisphere appears to be very similar to the evolution that we get by assuming a disconnection from the very beginning. The following sunspot at the higher latitude has the positive polarity and we clearly see that this positive polarity is preferentially transported to the higher latitudes. This positive polarity region gets stretched by the differential rotation into a belt going around the polar axis. When this belt reaches sufficiently high latitude, we see that it is followed by a belt of negative polarity coming from the leading sunspot which was taken at a lower latitude. The meridional circulation takes about 3 yr to bring the flux of B_r to create a positive patch on the pole surrounded a ring of negative polarity. The formation process of the negative polarity ring is clearly visible in Figure 6.7(d), but at later times it becomes weaker due to the action of diffusion and is not clearly visible. Since the meridional circulation sinks downward at the polar region, eventually both the positive and negative polarity magnetic fields are advected simultaneously below the surface. This becomes clear from the field line plots shown in Figure 6.8. At certain instants of time, we have averaged B_r and B_θ over the azimuthal direction ϕ to obtain the field lines.

It may be noted that the color scale for each plot in Figure 6.7 is set at \pm maximum values of the magnetic field in each case. This was necessary because the magnetic field becomes weak with time. Had we used the color scale of Figure 6.7 (a) for all cases shown in Figure 6.7, then the magnetic field would be completely invisible for the plots at later times. Though the magnetic fields in the sunspot pair remain concentrated for shorter time than what one may suspect from a casual look at Figure 6.7, the sunspots in our simulations are nevertheless live longer than real sunspots. This is expected because we have assumed the sizes of sunspots in our calculation to be larger than real sunspots. If sunspots decay by the action of turbulent diffusion, then a simple application of the diffusion equation suggests that the lifetime should go as the square of the size. A hypothetical sunspot 5 times larger than a real sunspot should live 25 times longer than a real sunspot.

It should be kept in mind that $\int \mathbf{B} \cdot d\mathbf{S}$ integrated over the whole solar surface has to be zero at any time (since $\nabla \cdot \mathbf{B} = 0$). This means that, during any time interval, equal amounts of positive and negative magnetic fluxes have to disappear below the surface due to the subduction

process. As a result, we see in Figure 6.7 that the white patch at the pole (representing positive flux) remains there till all fluxes disappear and is not replaced by the poleward migrating dark ring (representing negative flux, which gets subducted along with the positive flux). In the real Sun undergoing successive cycles, the polar field reverses only when fluxes of the following sunspots from the next cycle reach the pole. This subduction process has been seen before in axisymmetric Babcock-Leighton / Flux-Transport dynamo models but has not been well studied within the context of SFT models (though see Cameron et al. (2012); Yeates & Muñoz-Jaramillo (2013)). It relies on the upward advection of poloidal flux near the equator, which leads to the emergence of oppositely-signed radial field, as shown in Figure 6.8(f-j). This changes the net radial flux through the surface in each hemisphere and eats away at the polar field as it is advected poleward. Without this low-latitude emergence, the subduction of poloidal flux at the poles could not change the net flux through the outer surface.

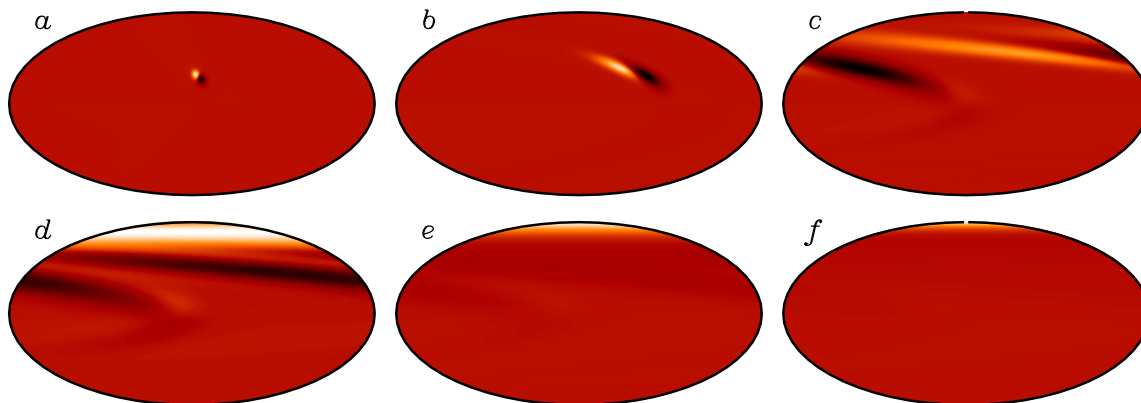


Fig. 6.7 Time evolution of radial fields on the surface of the sun with a single pair in the northern hemisphere for (a) 0.025 years, (b) 0.25 years, (c) 1.02 years, (d) 2.03 years, (e) 3.05 years and (f) 4.06 years. Here white color shows the outwards going radial field and black color represents inward going radial field. The color scale is set at \pm maximum values of the magnetic fields for each case. For example ± 4.66 G is the color scale for (a) and ± 0.10 G is the color scale for (f).

In the SFT model also, a tilted sunspot pair gives rise to a polar field with the polarity of the following sunspot surrounded by a belt of the opposite polarity. However, since the low-latitude emergence and subsequent subduction of the mean poloidal field is not included in the model, the net flux through each hemisphere can only change by means of cross-equatorial transport and diffusion. In a model of the solar magnetic field dynamics with realistic values of various parameters, usually the diffusion time for neutralizing the opposite magnetic polarities turns out to be much longer than the time for their disappearance due to low-latitude emergence and subduction by the meridional circulation. As we see in Figure 6.8, the magnetic fields tend to

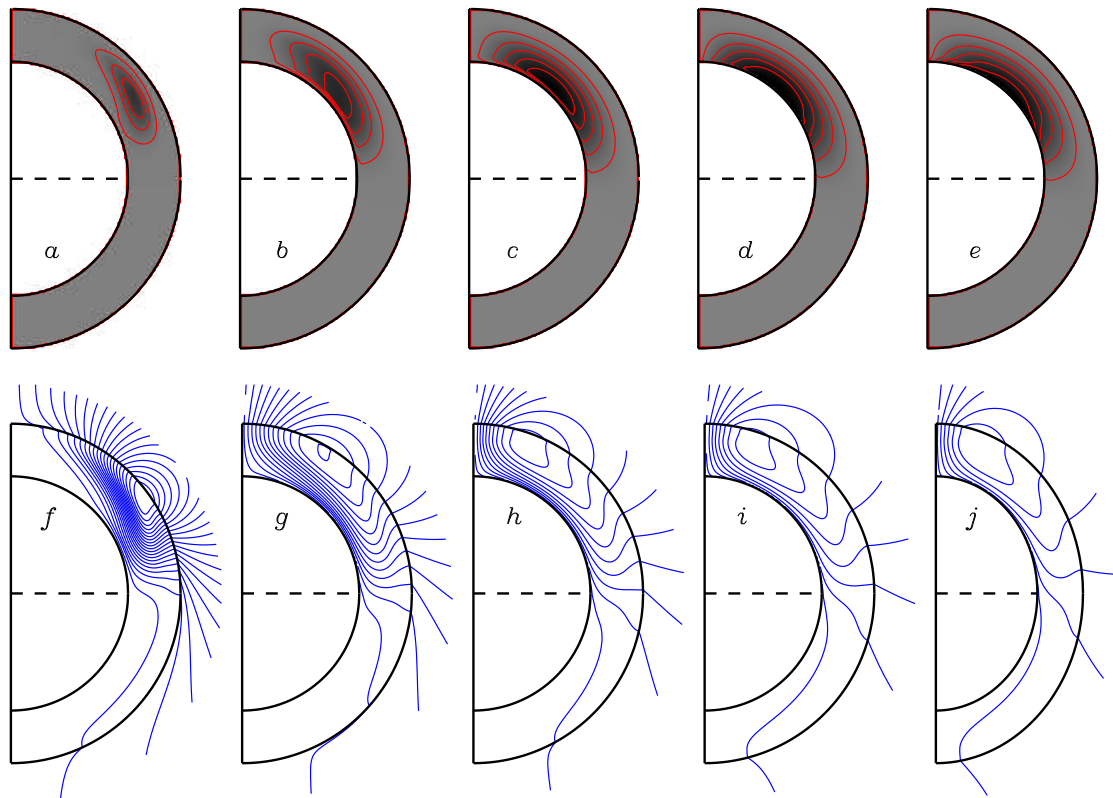


Fig. 6.8 Axisymmetric toroidal field lines (a-e) and axisymmetric poloidal field lines (f-j) are shown for 5 different times. Time spans are (a,f) = 1.02 years, (b,g)= 3.05 years, (c,h) = 5.08 years, (d,i) = 7.11 years and (e,j) = 9.15 years. Frames (a-e) represent $\langle B_\phi \rangle$ (azimuthal averaged) with red and blue indicating eastward and westward fields respectively. Filled contour also represents the mean toroidal fields. Here color scale is set at ± 1.5 G. Frames (f-j) represent the square root of poloidal magnetic potential with potential field extrapolation above the surface (upto $r = 1.25R$) and blue color contours denote the clockwise direction of the field. Maximum and minimum contour levels are set corresponding to potential field strength of ± 0.3 G respectively.

sink below the surface while they diffuse and the disappearance of the magnetic fields at the surface takes place in a time scale shorter than the diffusion time scale. We thus see that the evolution of the polar field in our 3D model is qualitatively different from what it is in the SFT model.

Figure 6.8 also shows the toroidal field generated in the convection zone. Since the poloidal field has not yet reached the tachocline to be acted upon by the radial differential rotation there, it may be worthwhile to comment how the toroidal field is generated. As soon as we put a sunspot pair on the surface by the SpotMaker algorithm, some toroidal field arises below the surface at once because the magnetic loop connecting the two sunspots below the surface would have a

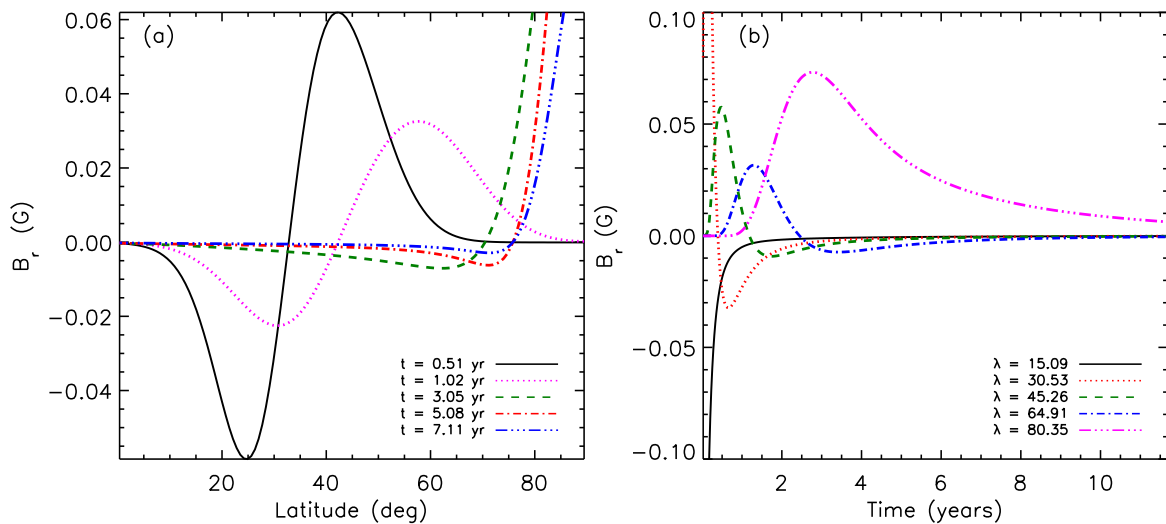


Fig. 6.9 (a) Behavior of radial field with latitude is plotted for different times. Radial field just after the emergence of the sunspot (at 20° latitude) are shown in black line at time $t = 0.51$ years. Magenta dotted, green dashed, red dash dotted and blue long dash dotted lines represent variation of radial magnetic field with latitude at time 1.02 years, 3.05 years, 5.08 years and 7.11 years respectively. (b) Time variations of radial magnetic field for different latitudes are plotted. Solid black, red dotted, green dash dotted, blue dash dotted and magenta long dash dotted lines are for latitude 15.09° , 30.53° , 45.26° , 64.91° and 80.35° respectively. All units of magnetic fields are given in gauss.

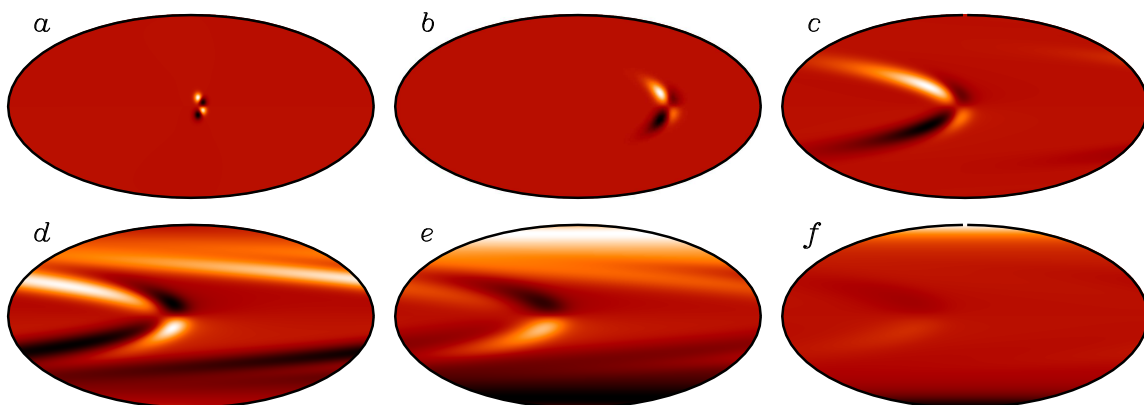


Fig. 6.10 Same as Figure 6.7 but for sunspot emergence in two hemispheres at $\pm 5^\circ$ latitudes. In this figure also color scale is set at \pm maximum value of the magnetic fields for each case.

toroidal component. Additionally, more toroidal field is produced by the latitudinal differential rotation within the convection zone. It has been known that the latitudinal differential rotation can play an important role in generating the toroidal field (Guerrero & de Gouveia Dal Pino, 2007). In reality, any strong magnetic field generated within the convection zone is expected to be quickly removed by magnetic buoyancy which is particularly effective within the convection zone (Moreno-Insertis, 1983; Parker, 1975). Since we do not allow magnetic buoyancy to remove the toroidal field in the present version of the code, the toroidal field remains where it is created. However, it may be noted that some fully dynamical simulations suggest persistent rings of toroidal flux within the convection zone (Brown et al., 2010).

Finally, Figure 6.9(a) shows B_r (averaged over ϕ) as a function of latitude for different times, whereas Figure 6.9(b) shows B_r as a function of time at different latitudes. A careful scrutiny of Figure 6.9(a) makes it clear that the poleward meridional circulation transports the magnetic flux to higher latitudes with time. After about 3 yr, the polar field starts building up. It is clear that the polar field becomes much stronger than the fields at mid-latitudes. This is purely a geometrical effect. Since magnetic flux from different longitudes is brought by the meridional circulation to the pole where it converges, it is natural that the magnetic field becomes stronger at the pole. It is also to be noted that we only have the polar field with polarity corresponding to the polarity of the following sunspot at the higher latitude (positive in the present case). Turning to Figure 6.9(b) now, we first look at the plots corresponding to the mid-latitudes ($\approx 30^\circ - 65^\circ$). At a mid-latitude, first the magnetic field corresponding to the polarity of the following sunspot (positive in the present case) is brought by the meridional circulation, followed by the magnetic field with opposite polarity from the leading sunspot (negative in the present case) a little bit later. This is seen in all the mid-latitude plots in Figure 6.9(b). But we should pay a special attention to the plots for latitudes 15° and 80° . At the latitude of 15° , the positive magnetic field from the following sunspot is never seen, because the following sunspot appeared at a higher latitude and the meridional circulation transported the flux from its decay towards the pole. On the other hand, at the latitude of 80° , we see only the positive magnetic field which has been brought there from following sunspot. The negative magnetic field from the leading sunspot forms a negative polarity belt around the pole, as we have already seen, and then it sinks below the surface, so the negative magnetic field is never seen at sufficiently high latitudes. Also, note that, although the peak value of the positive polarity field at 65° is less than that at 45° (due to the action of diffusion while the magnetic field is transported to higher latitudes), the positive polarity field again becomes strong at 80° due to the geometrical effect of converging flow bringing magnetic flux from different longitudes.

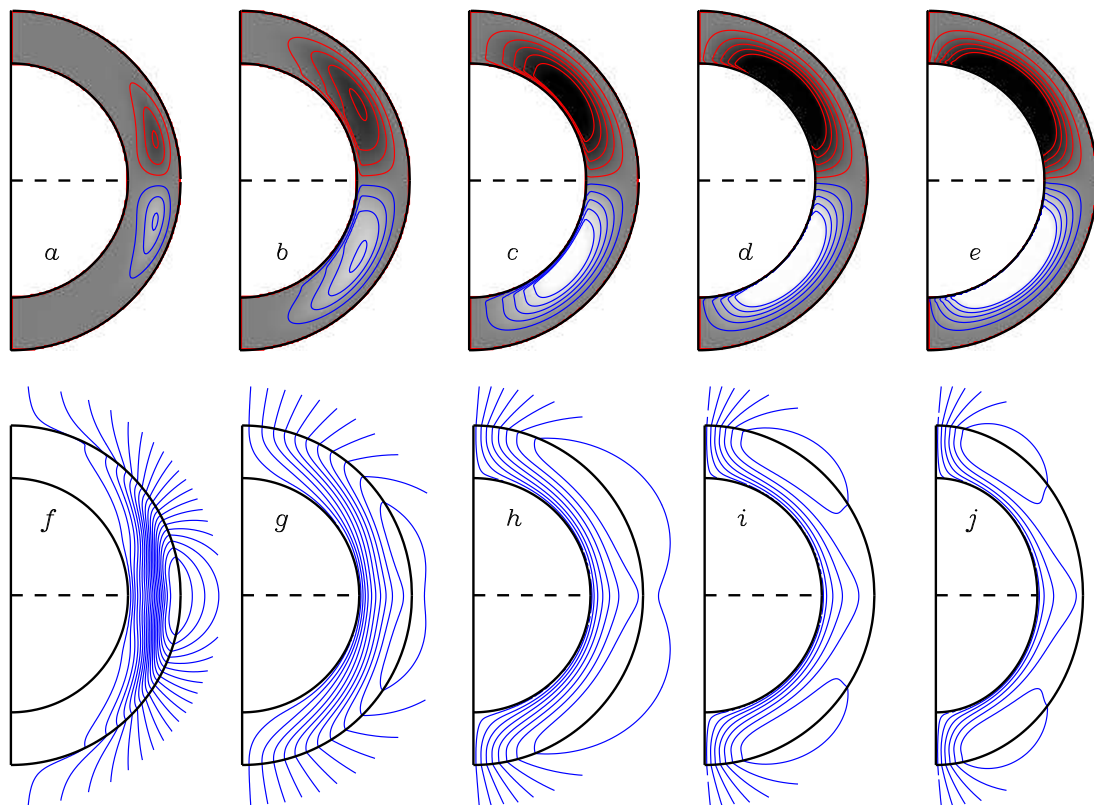


Fig. 6.11 Same as Figure 6.8 but for two pairs at two hemispheres at $\pm 5^\circ$ latitudes. Color scale for toroidal fields is set at $\pm 1.5G$ and contour levels corresponding to the poloidal fields strengths of $\pm 0.02 G$ are set as maximum and minimum respectively.

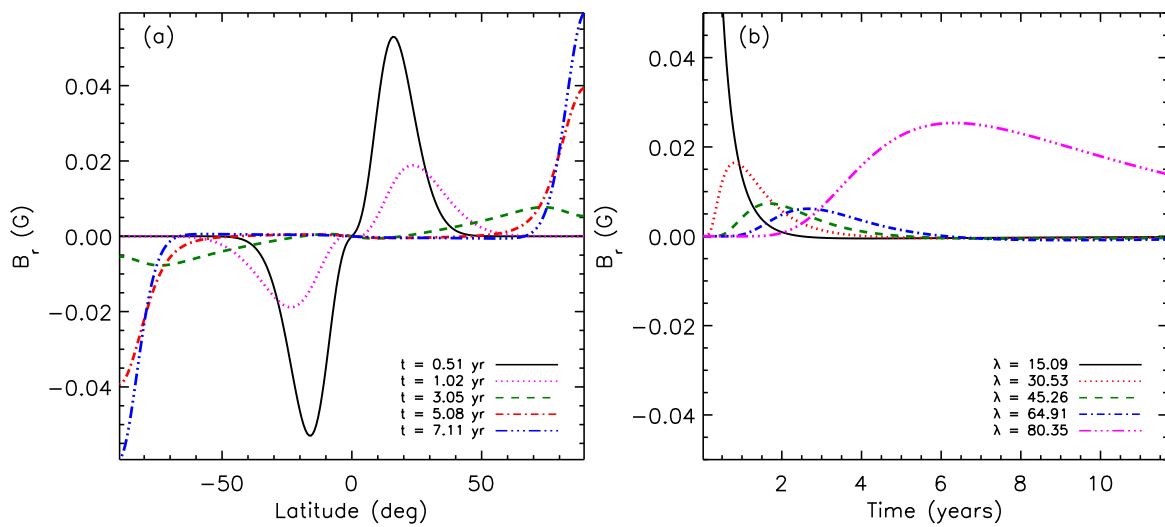


Fig. 6.12 Same as Figure 6.9 but with two pairs in two hemispheres at $\pm 5^\circ$ latitudes.

6.4.2 Polar fields from two sunspot pairs in two hemispheres

The results of the 3D model differ more dramatically from the results of the SFT model when we put two pairs of sunspots located symmetrically in the two hemispheres. If the two pairs are sufficiently close to the equator, then magnetic fluxes of the two leading sunspots get canceled by diffusion across the equator. In the SFT model, only the fluxes from the following polarities are advected to the two poles and we eventually get polar patches which are not surrounded by rings of opposite polarity as we found in the case of the single sunspot pair. When the outward spreading of magnetic field from the polar patches by diffusion is eventually balanced by the inward advection by the meridional circulation, we reach an asymptotic steady state in the SFT model, with an asymptotic magnetic dipole which does not change with time. This is seen in Figure 6 of [Jiang et al. \(2014b\)](#). As we shall discuss now, we get a completely different result from the 3D model.

We see in Figure 6.10 that polar magnetic patches form with the polarity of the succeeding sunspots. A careful look at this figure, shows some evidence of opposite polarity (i.e. opposite of what we see in the poles) at mid-latitudes even when we start from two sunspots placed symmetrically at sufficiently low latitudes in both the hemispheres. The physics of what is happening becomes clear from the plot of field lines shown in Figure 6.11. After the fluxes from the leading sunspots near the equator cancel, we see that initially we get poloidal field lines spanning both the hemispheres. A look at the field line plots makes it clear that we shall have B_r only at high latitudes in the early stages of the evolution of the magnetic field. As the meridional circulation drags the poloidal field towards the poles, we find that eventually the polar fields in the two hemispheres get detached, as a result of which B_r again appears at lower latitudes having the opposite polarity of B_r at high latitudes. This is purely a result of the 3D structure of the magnetic field and cannot happen in the SFT model. There would not be a source for creating B_r at low latitudes in the SFT model and such fields would never appear in that model. Because of the breakup of the poloidal field in the two hemispheres and the appearance of B_r with opposite polarity in the low latitudes, it is possible for the poloidal magnetic field in the 3D model to be subducted below the surface as the meridional circulation sinks downward in the polar regions. Thus, in contrast to the SFT model in which polar fields have nothing to cancel them and therefore persist, the polar field disappears after some time in the 3D model.

Though this result is notable, it may be offset to some extent by efficient magnetic pumping. Using a 2D (axisymmetric) model [Karak & Cameron \(2016\)](#) have shown that downward magnetic pumping due to strongly stratified convection in the solar surface layers can suppress the upward diffusion and advection of toroidal and poloidal fields. This, in turn, can produce

steady polar fields that might persist indefinitely. We will investigate the role of magnetic pumping in future work.

Figure 6.12(a) is similar to Figure 6.9(a) except that latitudes now cover from -90° to 90° . In this figure, we clearly see that around 1 yr, we had only positive B_r in the northern hemisphere and negative B_r in the southern hemisphere, but afterwards very weak B_r having sign opposite to the sign at the high latitudes developed at low latitudes. Figure 6.12(b), which is similar to Figure 6.9(b), shows that eventually B_r disappears at the surface in this 3D model, exactly similar to what happens when we put only one sunspot pair on the solar surface.

We carry on such calculations by putting two sunspot pairs symmetrically at different latitudes in the two hemispheres. Figure 6.13(a) shows how the polar field evolves with time for sunspot pairs placed at different latitudes. When the sunspot pairs are placed at high latitudes, the magnetic flux is brought to the poles without too much diffusion and the polar field is stronger. Eventually the polar field disappears in all the cases due to emergence and subduction by the meridional circulation, as we have already discussed. This figure can be compared with the left panel of Figure 6 of Jiang et al. (2014b). Such a comparison makes the difference between the 3D model and SFT model completely clear. In the SFT model, only if the sunspot pairs are put at sufficiently high latitudes so that cross-equatorial diffusion is negligible, fluxes of both polarity are advected to the polar regions and eventually the axial dipole moment becomes zero. If the sunspot pairs are put at low latitudes in the SFT model, only the fluxes from the following sunspots reach the poles and give rise to an asymptotic axial dipole. The situation is completely different in the 3D model, although we see that the polar field persists for a longer time when the initial sunspot pairs are put at lower latitudes. So, in that sense, sunspot pairs appearing in lower latitudes are somewhat more effective in creating the polar field even in the 3D model. This is in agreement with the claim of Dasi-Espuig et al. (2010a) that we have a better correlation between the average tilt of a cycle and the strength of the next cycle if more weight is given to sunspot pairs at low latitudes when computing the average tilt.

We have also calculated the polar magnetic flux for two sunspot pairs emerging on the two hemispheres, to find out how much flux from the sunspots reaches the poles. We calculate the polar flux by integrating B_r over only those regions of the surface between 60° latitude and the pole where B_r has one sign (positive in the north pole). While putting the sunspot pairs by hand using SpotMaker algorithm, we injected 1×10^{22} Mx flux in each spot. A normalized polar flux is estimated by dividing the signed flux by the input flux (1×10^{22} Mx). In Figure 6.13(b), we have shown the percentage of normalized polar flux with time for the spot pairs emerging at different latitudes. It is evident from this figure that around 1.76% of the input flux can reach the pole when the spot pair emerges at a high latitude like 40° , whereas 0.2% of the input flux can reach the pole when the spot pair is at a low latitude like 5° . Keeping in mind that we have

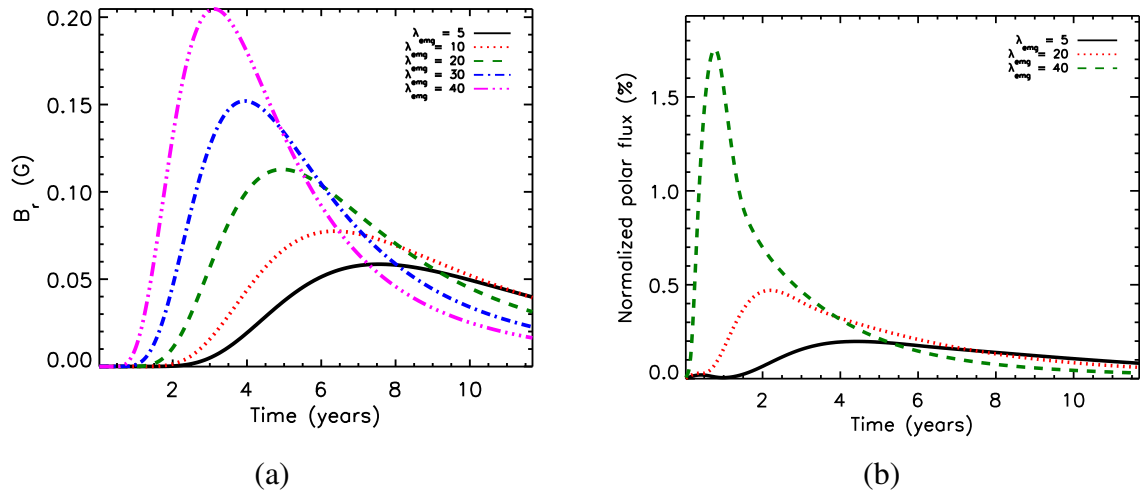


Fig. 6.13 (a) Polar field evolution with time for different emergence angle λ_{emg} of sunspot pairs in both the hemisphere. Black solid, red dotted, green dashed, blue dash dotted and magenta long dash dotted lines represent the polar field for the sunspot emergence at 5° , 10° , 20° , 30° and 40° respectively. Magnetic field is in mG and time is given in years. (b) Polar flux evolution with time for different emergence angle λ_{emg} of sunspot pairs in both the hemisphere. Black solid, red dotted, green dashed lines represent the percentage of normalized polar flux able to reach the pole for the sunspot emergence at 5° , 20° and 40° respectively.

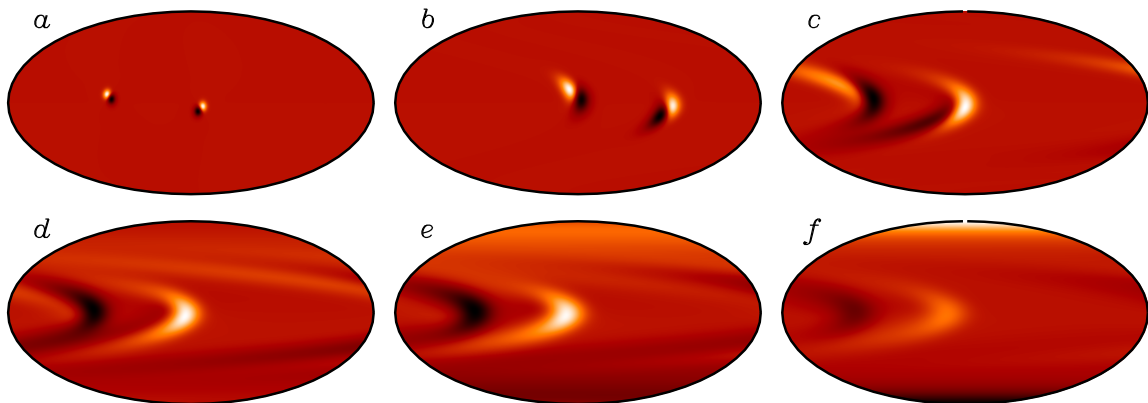


Fig. 6.14 Same as Figure 6.10 but sunspot pairs are placed at longitude 90° on northern hemisphere and at longitude 180° on southern hemisphere.

used an unrealistically high tilt of 40° , we point out that the flux reaching the poles will be less for more realistic tilts. It is instructive to compare our result with relevant observational data. Schrijver & Harvey (1994a) and Solanki et al. (2002a) analyzed the NSO Kitt Peak magnetograph data and estimated the maximum active regions flux during solar maxima to be around 5×10^{23} Mx. Muñoz-Jaramillo et al. (2012) calibrated century long polar faculae data

from Mount Wilson Observatory and estimated the time evolution of the polar flux, finding its maximum value to be around 1.5×10^{22} Mx for an average cycle. Although these values are not from a single dataset and many other observational constraints should be taken into account, a simple division of these values of flux quoted above suggests that around 3% of the sunspots flux can contribute in the polar flux. Our theoretical model gives a value having the same order of magnitude, although our theoretical values are a little bit on the lower side.

All the results presented so far for two sunspot pairs in different hemispheres were obtained by putting both the pairs in the same longitude. This helped in magnetic fluxes of the two leading sunspots canceling each other by diffusing across the equator. One important question is whether the final outcome will be different if the two sunspot pairs in the two hemispheres are widely separated in longitude. Figure 6.14 shows the surface evolution of magnetic flux in such a case, which can be compared with Figure 6.10. We find that the magnetic fluxes from the following sunspots in the two hemispheres are carried towards the pole exactly as in Figure 6.10. However, the evolution of magnetic fluxes from the leading sunspots is quite intriguing. Because of the gap in longitude, these fluxes cannot cancel with each other across the equator so easily. However, these fluxes still diffuse across the equator, as seen in Figure 6.14, and, if we average over longitude, the averaged values are found to be virtually identical with the averaged values that we get in the case of Figure 6.10. When we plotted figures similar to Figure 6.11 and Figure 6.12 for this case, they turned out to be indistinguishable from Figure 6.11 and Figure 6.12.

6.5 The contribution of bipolar sunspots not obeying Hale's law

Joy's law for tilts of sunspot pairs is only a statistically average law. We see a spread of tilt angles around Joy's law. This spread is believed to be caused by the action of turbulence on rising flux tubes (Longcope & Choudhuri, 2002; Weber et al., 2011) and is one of the main sources of irregularity in the solar cycle (Choudhuri, 2014b; Choudhuri & Karak, 2009; Choudhuri et al., 2007). It is well known that some bipolar sunspots appear with wrong magnetic polarities not obeying Hale's polarity law. Because of the spread in tilt angles around Joy's law, it is certainly expected that a few outliers in this spread would violate Hale's law. Stenflo & Kosovichev (2012) estimated that about 4% of medium and large sunspots violate Hale's law—see their Figure 7. Since the number of such sunspots is small, it is not surprising that due to statistical fluctuations more of such sunspots violating Hale's law may appear in some particular cycles compared to other cycles. This fact assumes significance in the light of

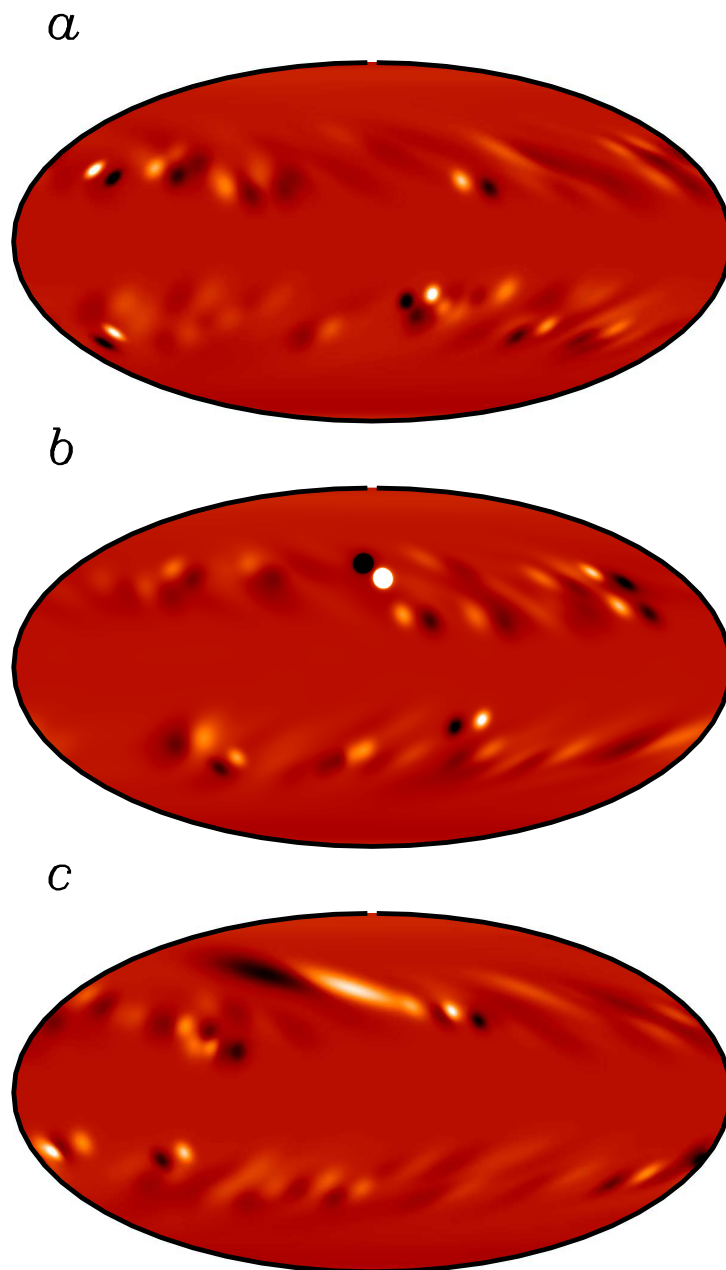


Fig. 6.15 Radial Magnetic field structures are shown for the case when “anti-Hale” sunspot pair appears at 40° latitude and at middle phase of the cycle. (a) Prior to 3 month before the anti-Hale sunspot pair to be appeared, (b) During the emergence of anti-Hale sunspot pair and (c) After 3 month of the anti-Hale sunspot pair has emerged. Here white color shows the outwards going radial fields and black color represents inward going radial fields. The color scale is set at ± 100 kG for all three cases.

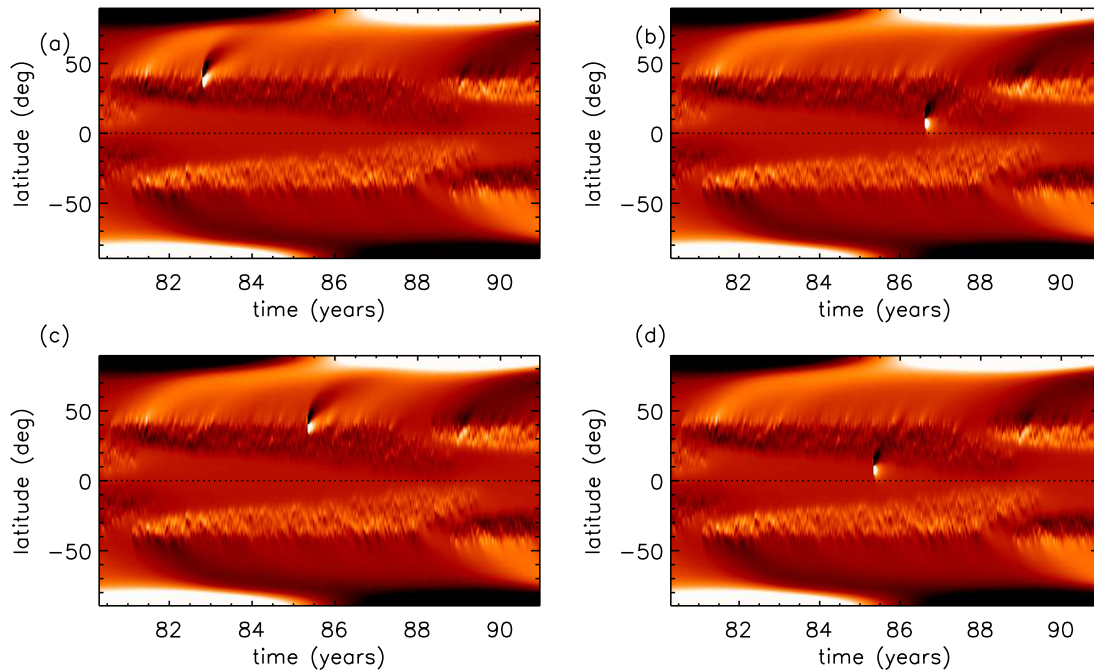


Fig. 6.16 Butterfly diagram with an “anti-Hale” sunspot pair at different latitude and at different phase of the solar cycle. (a) At early phase of the cycle and at 40° latitude. (b) Late phase of the cycle and at 10° latitude. (c) Middle phase and at 40° and (d) Middle phase and at 10° latitude. Color scale is set at ± 15 kG for all four cases.

the suggestion made by [Jiang et al. \(2015\)](#) on the basis of their SFT calculations that a few large “anti-Hale” sunspot pairs may significantly decrease the strength of the polar field produced at the end of the cycle. Especially, [Jiang et al. \(2015\)](#) suggested that the weak polar field at the end of cycle 23 was caused by a few prominent anti-Hale sunspot pairs present in that cycle. In contrast, they argue that not too many such anti-Hale sunspot pairs appeared in cycles 21 and 22, as a result of which such a decrease of the polar field did not happen in those cycles.

Since we have seen that some insights gained from SFT calculations have to be modified—especially results connected with the build-up of the polar field—on the basis of more realistic and complete 3D kinematic dynamo calculations, we now address the question whether anti-Hale sunspot pairs have a large effect on the polar field even in 3D kinematic dynamo models. We now use our reference model presented in Section 6.3 and put a large anti-Hale sunspot pair by hand to study its effect on the build-up of the polar field. To make its effect visible, we take this anti-Hale sunspot pair to carry 25 times the magnetic flux carried by the other regular sunspots and to have tilt angle 30° . We can say that the tilt angle is -30° , if we define the tilt angle by following the convention that its value is positive for sunspot pairs obeying Hale’s law.

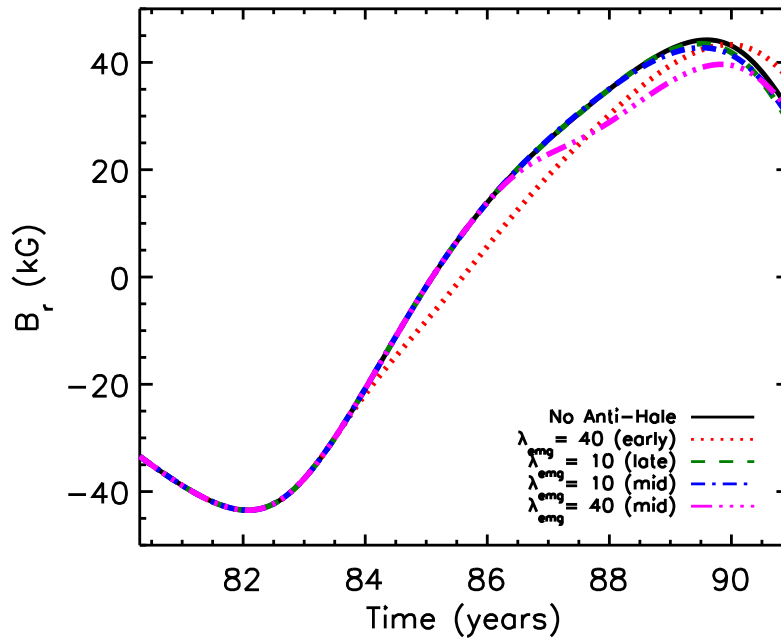


Fig. 6.17 Polar field evolution with time for one complete solar cycle with “anti-Hale” sunspot pair at different location and different time of the cycle. Solid black line represents the regular cycle with no anti-Hale sunspot pair. Red dotted line indicates the poloidal field evolution with an anti-Hale pair at 40° latitude at early phase of the cycle. Green dashed line represents poloidal field with an anti-Hale pair at 10° and late phase. blue dashed and magenta long dashed lines indicate the poloidal field with an anti-Hale pair at middle of the cycle but at 10° and at 40° latitude respectively.

We want to understand how the effect of the anti-Hale sunspot pair depends on the emergence latitude as well as the phase of the cycle when it makes its appearance. So we consider four different cases. Since sunspots appear at high latitudes in the early phase of the cycle and at low latitudes in the late phase, we consider one case by putting the anti-Hale sunspot pair at the high latitude of 40° in the early phase and another case by putting the pair at the low latitude of 10° in the late phase. The two other cases considered involve putting the large anti-Hale sunspot pair at 40° and 10° (in separate case studies) in the middle phase of the cycle. The radial fields on the surface in mollweide projection is shown for a case where “anti-Hale” sunspot pair is placed at 40° latitude during the middle phase of the cycle in the Figure 6.15. Figure 6.16 shows how B_r evolves in a time-latitude plot (a “butterfly diagram”) for these four cases. The effect on the polar field can be seen more clearly in Figure 6.17 where we plot the time evolution of the polar field for these four cases, along with the reference case without an anti-Hale sunspot pair.

It is clear from Figure 6.17 even a very large anti-Hale sunspot pair placed at a low latitude like 10° does not have much effect on the polar field. Presumably the opposite fluxes from the two sunspots neutralize each other before they reach the poles. This becomes quite apparent by looking at Figures 6.16(b) and 6.16(d). We see that the sunspot pairs at low latitudes produce a kind of “surge” behind them, but it does not reach the poles. The effect of anti-Hale pairs at higher latitudes is certainly much more pronounced. We see in Figures 6.16(a) and 6.16(c) that the surges behind these anti-Hale pairs reach the pole in these situations. If an anti-Hale sunspot pair appears at 40° in the early phase of the cycle, then we see in Figure 6.17 that the build-up of the polar field is weakened and delayed, but eventually the polar field reaches almost the strength we would expect in the absence of the anti-Hale sunspot pair. However, when the anti-Hale sunspot pair is put at 40° in the middle phase of the cycle, it is clear from Figure 6.17 that polar field can be reduced by about 17%. But remember that we get this large reduction by assuming the anti-Hale sunspot pair to be unrealistically large. Our conclusion is that anti-Hale sunspot pairs do affect the build-up of the polar field—especially if they appear at high latitudes in the middle phase of the cycle—but the effect does not appear to be very dramatic. As for the suggestion of Jiang et al. (2015) that the weakness of the polar field at the end of cycle 23 was due to the appearance of several anti-Hale sunspot pairs, we feel that this is an interesting suggestion which merits further detailed study in order to arrive at a firm conclusion.

6.6 Conclusion

Historically the evolution of the Sun’s magnetic field with the solar cycle has been studied extensively through two classes of 2D theoretical models: the 2D kinematic dynamo model and the surface flux transport (SFT) model. We argue that the 3D kinematic dynamo model incorporates the attractive aspects of both, while being free from the limitations of both. On the one hand, this model can treat the Babcock–Leighton mechanism more realistically in 3D, which is not possible in the 2D kinematic dynamo model. On the other hand, it includes the vectorial nature of the magnetic field and various subsurface processes which are left out in SFT models. Cameron et al. (2012) have pointed out that the results of SFT model agree with the results of 2D flux transport dynamo model on the inclusion of a downward pumping.

In order to study the build-up of the Sun’s polar field with a 3D kinematic dynamo model, we first construct an appropriate self-excited model. The poloidal field generated by the Babcock–Leighton mechanism near the solar surface has to be transported to the tachocline in order for the solar dynamo to work. This transport can be achieved in two ways: (i) due to advection by the meridional circulation; or (ii) due to diffusion across the convection zone.

There are reasons to believe that (ii) is the appropriate transport mechanism inside the Sun. The earlier papers by [Miesch & Dikpati \(2014\)](#) and [Miesch & Teweldebirhan \(2016\)](#) presented self-excited dynamo models dominated by advection by the meridional circulation. We believe that we are the first to construct self-excited 3D kinematic dynamo model dominated by diffusion. We have briefly looked at the question of parity, although the limitation of computer time prevented us from an exhaustive study of the subject.

We use this dynamo model to study how the polar field builds up from the decay of one tilted bipolar sunspot pair and two symmetrically situated bipolar sunspot pairs in the two hemispheres. We find that the polar field which arises from such sunspot pairs ultimately disappears due to the emergence of poloidal flux at low latitudes and its subsequent subduction by the meridional flow. This process is not included in the SFT models, in which the polar field can only be neutralized by diffusion with field of opposite polarity. So we conclude that SFT models do not capture the dynamics of polar fields realistically and one has to be cautious in interpreting the SFT results pertaining to polar magnetic fields. Our results differ most dramatically from the SFT results when we put two symmetric bipolar sunspot pairs in the two hemispheres very near the equator. Then the magnetic fields of the two leading sunspots on the two sides of the equator cancel each other. At the same time, the magnetic fields of the following sunspots which formed at higher latitudes are advected by the meridional circulation to the poles, ultimately causing a magnetic dipole of the Sun. In the SFT model, this is the whole story and we get an asymptotically steady dipole. In our 3D kinematic model, on the other hand, magnetic field lines between the two hemispheres can get detached when they are pulled by the meridional circulation in the opposite directions. As a result, radial magnetic fields with signs opposite to the polar fields develop in the lower latitudes. This is not possible in the SFT model in the absence of any source of radial magnetic field in the lower latitudes. Finally the detached magnetic loops in the two hemispheres are subducted underneath the surface by the meridional circulation, contradicting the SFT result that the magnetic dipole of the Sun would be asymptotically steady in this state. While the SFT models played a tremendously important historical role in our understanding of how the magnetic field on the solar surface evolves, we should keep in mind that these models cannot capture certain aspects of the dynamics of the Sun's polar magnetic fields due the intrinsic limitations of these models.

Finally, we look into the provocative question of whether a few large sunspot pairs violating Hale's law could have a large effect on the strength of the polar field. We find that such anti-Hale sunspot pairs do produce some effect on the Sun's polar field—especially if they appear at higher latitudes during the mid-phase of the solar cycle—but the effect is not very dramatic. The question of whether a few large anti-Hale sunspot pairs could be the principal

cause behind the weakness of the polar field at the end of some cycles like cycle 23 needs to be analyzed carefully.

“There is nothing new under the sun but there are lots of old things we don't know”

–Ambrose Bierce, The Devil's Dictionary

7

Incorporating Surface Convection into a 3D Flux Transport Dynamo Model

The observed convective flows on the photosphere (e.g., supergranulation, granulation) play a key role in the Babcock-Leighton (BL) process to generate large scale polar fields from sunspots fields. In most surface flux transport (SFT) and BL dynamo models, the dispersal and migration of surface fields is modeled as an effective turbulent diffusion. Recent SFT models have incorporated explicit, realistic convective flows in order to improve the fidelity of convective transport but, to our knowledge, this has not yet been implemented in previous BL models. Since most Flux-Transport (FT)/BL models are axisymmetric, they do not have the capacity to include such flows. We present the first kinematic 3D FT/BL model to explicitly incorporate realistic convective flows based on solar observations. Though we describe a means to generalize these flows to 3D, we find that the kinematic small-scale dynamo action they produce disrupts the operation of the cyclic dynamo. Cyclic solution is found by limiting the convective flow to surface flux transport. The results obtained are generally in good agreement with the observed surface flux evolution and with non-convective models that have a turbulent diffusivity on the order of $3 \times 10^{12} \text{ cm}^2 \text{ s}^{-1}$ ($300 \text{ km}^2 \text{ s}^{-1}$). However, we find that the use of a turbulent diffusivity underestimates the dynamo efficiency, producing weaker mean fields than in the convective

models. Also, the convective models exhibit mixed polarity bands in the polar regions that have no counterpart in solar observations. Also, the explicitly computed turbulent electromotive force (emf) bears little resemblance to a diffusive flux. We also find that the poleward migration speed of poloidal flux is determined mainly by the meridional flow and the vertical diffusion.

7.1 Introduction

Since it was discovered over a century ago that sunspots are regions of strong magnetic field (Hale, 1909) and solar cycles are thus manifestations of solar magnetic activity, researchers have been seeking an explanation for this cyclic magnetic activity. A major breakthrough in this history of research came with the work of Parker (1955b) who first demonstrated how helical plasma motions can generate large-scale magnetic fields. Steenbeck et al. (1966) later gave Parker's theory a more mathematical foundation with the development of mean field dynamo theory. The first dynamo simulations to produce a solar-like butterfly diagram (cyclic equatorward migration of toroidal field) were made by Steenbeck & Krause (1969) and subsequently by Roberts & Stix (1972). There are likely other papers from that time period achieving the same but the most notable in this time period would be Yoshimura (1975) and Stix (1976). All of these calculations were based on the kinematic, mean field formulation of the magnetohydrodynamic (MHD) induction equation.

Prior to the mid-1980s, when there was little observational information about the internal rotation profile of the Sun, theorists were free to adopt any profile that was needed in order to reproduce the observed butterfly diagram using the α - Ω dynamo waves of mean-field theory. However, by the mid 1990's the internal rotation profile of the Sun was well established (Thompson et al., 2003). But, the use of this differential rotation profile in mean-field dynamo models was problematic because it adversely affected the propagation of α - Ω dynamo waves. Choudhuri et al. (1995) showed that the inclusion of a meridional circulation can help to solve this problem by advecting toroidal flux toward the equator, thus promoting more solar-like butterfly diagrams. About the same time it was also argued that helical turbulence may not be as efficient at generating poloidal field as previously thought. This was based on non-kinematic effects associated with Lorentz-force back-reactions on both large and small scales. On large scales, it was argued that the toroidal field concentrations that give rise to sunspots may be too strong (super-equipartition fields of $\geq 10^4$ G) for convection to twist (D'Silva & Choudhuri, 1993). On small scales it was argued that the buildup of small-scale magnetic helicity may dramatically suppress the turbulent α -effect (Brandenburg, 2001; Gruzinov & Diamond, 1994; Vainshtein & Cattaneo, 1992).

These challenges to traditional mean-field dynamo theory led to the resurgence of solar dynamo models based on the so-called Babcock-Leighton (BL) process. The BL process (or BL mechanism) had been proposed decades earlier (Babcock, 1961; Leighton, 1969) as an alternative candidate for the poloidal field generation that does not rely on turbulent convection. In short, toroidal flux concentrations can destabilize and rise due to magnetic buoyancy, emerging from the photosphere as bipolar magnetic regions (BMRs). The action of the Coriolis force on the rising flux tube induces a twist that is manifested upon emergence as a preferential tilt of BMRs, known as Joy's law, such that the trailing edge is displaced poleward relative to the leading edge. The subsequent fragmentation and dispersal of these tilted BMRs after emergence due to turbulent diffusion, differential rotation, and meridional flow generates a dipole moment that, together with the Ω -effect due to differential rotation, sustains the dynamo (Charbonneau, 2010; Dikpati & Gilman, 2009; Karak et al., 2014a). Note that the fragmentation and dispersal of the BMRs are executed by the convective flows on the photosphere (e.g. supergranulation and granulation) and this process is modeled as a simple random of walk process which is treated as an effective turbulent diffusion (Leighton, 1964). In the last two decades Babcock-Leighton (BL) solar dynamo models have grown to become the most promising paradigms to explain the origin of solar magnetic cycle and its irregularities (Charbonneau, 2010; Chatterjee et al., 2004; Choudhuri et al., 1995; Dikpati & Charbonneau, 1999; Dikpati & Gilman, 2009; Karak, 2010; Karak & Choudhuri, 2011; Karak et al., 2014a). Yet, most of these models are still kinematic in the sense that they solve only the magnetohydrodynamic (MHD) induction equation with specified mean flows (differential rotation and meridional circulation) derived from observations.

Efforts to solve the fundamental MHD equations in the solar convection zone (CZ) from first principles in a more self-consistent manner date back to the pioneering work of Gilman & Miller (1981), Gilman (1983) and Glatzmaier (1984, 1985) and have made dramatic progress just in the last seven years. Convective dynamo simulations now exhibit many solar-like features, including self-organization of large-scale fields, magnetic cycles with periods on the order of a decade, equatorward migration of toroidal flux, torsional oscillations, long-term cycle modulation, and even hints of magnetic flux emergence (Augustson et al., 2015; Brown et al., 2011; Fan & Fang, 2014; Ghizaru et al., 2010; Hotta et al., 2016; Käpylä et al., 2012, 2013b, 2016; Karak et al., 2015; Nelson et al., 2013a,b; Passos & Charbonneau, 2014; Racine et al., 2011; Warnecke et al., 2014). However, these models operate in parameter regimes far removed from the real solar interior and they still fall short of reproducing the solar cycle with high fidelity. One reason may be that they do not yet have sufficient resolution to capture the full scope and complexity of the BL process. This would require faithfully capturing the formation, rise, and emergence of the magnetic flux structures in the deep CZ, as well as the

compressible, radiative MHD and small-scale convection in the surface layers responsible for the formation, fragmentation, and dispersal of active regions.

The amount of available flux emerging in BMRs each solar cycle, ($> 2 \times 10^{24}$ Mx [Schrijver & Harvey, 1994b](#); [Thornton & Parnell, 2011](#)) is two orders of magnitude larger than the amount of flux needed to reverse the dipole moment of the Sun, at least at the surface ($\sim 5 \times 10^{22}$ Mx [Muñoz-Jaramillo et al., 2012](#)). This alone suggests that the BL process may play an essential role in the solar dynamo. This conclusion is further supported by the observed evolution of magnetic flux in the solar photosphere as represented by magnetic butterfly diagrams, which suggest that the polar field reversals are triggered by the poleward migration of magnetic flux originating from the trailing edge of BMRs ([Hathaway, 2010](#)). Other lines of evidence in favor of the BL process include an observed correlation between the BL source term and cycle strength ([Dasi-Espuig et al., 2010b](#); [McClintock & Norton, 2013](#)), the flux budget in active regions ([Cameron & Schüssler, 2015](#)), and the phase relationship between poloidal and toroidal fields ([Charbonneau, 2010](#); [Dikpati & Gilman, 2009](#); [Karak et al., 2014a](#)).

The observed evolution of magnetic flux in the solar photosphere is well captured by Surface Flux Transport (SFT) models. SFT models are not dynamo models. Magnetic flux is injected by means of artificial source terms or 2D magnetograms which provide the radial field B_r as a function of latitude and longitude in some data assimilation window (typically the near side of the Sun). The model then follows the subsequent evolution of this flux by solving a 2D (latitude-longitude) version of the kinematic MHD induction equation [eq. (7.1) below] which includes differential rotation, meridional circulation, and turbulent diffusion by photospheric convection ([DeVore et al., 1984](#); [Wang & Sheeley, 1991](#)). As the evolution proceeds, the leading-polarity flux in low-latitude BMRs cancels across the equator while residual trailing-polarity flux is transported to the poles. The polarity of this trailing flux is opposite to the pre-existing polar flux so its accumulation at the poles from multiple BMRs eventually reverses the polar field and the global dipole moment. This is the surface manifestation of the BL process.

[Upton & Hathaway \(2014b,c\)](#) have recently developed an SFT model called AFT (Advective Flux Transport) that used the observed surface flows to improve the fidelity of the model. The distinguishing feature of AFT is that it uses explicit convective flow fields where other models use turbulent diffusion. These 2D convective flow fields (v_θ, v_ϕ) are designed to reproduce the observed photospheric power spectrum and cell lifetimes, with randomized phases, as described by [Hathaway \(2012a,b\)](#); [Hathaway et al. \(2000\)](#). [Upton & Hathaway \(2014b,c\)](#) showed that the use of these convective flows greatly improved the realism of the flux transport, reproducing the magnetic network and introducing stochastic variations that are not captured by a turbulent diffusion.

In this study we use explicit three-dimensional (3D) convective flow fields for the first time in a Babcock-Leighton dynamo model of the solar cycle. On the surface, these flow fields are identical to the empirical flow fields used in the AFT SFT model (Hathaway, 2012b; Upton & Hathaway, 2014b,c). However, here we extrapolate these flows below the surface to create a 3D rendition of surface convection that is responsible for the magnetic flux transport in the upper CZ. Furthermore, in this initial implementation, we use a time-independent snapshot of the convective flow instead of the evolving flow fields used by Upton & Hathaway. We will implement evolving convective and mean flows in future work.

We achieve this through the use of the Surface flux Transport And Babcock-LEighton (STABLE) solar dynamo model (Hazra et al., 2017; Miesch & Dikpati, 2014; Miesch & Teweldebirhan, 2016). STABLE is a 3D model that explicitly places BMRs on the surface in response to the dynamo-generated toroidal field near the base of the CZ so the BL process can operate more realistically than in previous 2D (axisymmetric) models that employ, for example, a non-local α -effect. STABLE can function both as a BL dynamo model and as an SFT model, although we have not yet assimilated observational data in the latter context. It is part of a next generation of 3D solar dynamo models that seek to capture the operation of the solar cycle with high fidelity by incorporating observational data and insights wherever possible. In the future we will include Lorenz-force feedbacks by solving the full MHD equations but here we take the pragmatic approach of previous 2D models and solve the kinematic MHD induction equation with specified, realistic flow fields. Since STABLE is 3D, these specified flow fields can include surface convection as well as differential rotation and meridional circulation. Note that no existing global MHD convection simulation has sufficient resolution and scope to realistically capture surface convection on the scales of granulation to supergranulation. So, our approach of specifying the convective velocity spectrum based on photospheric observations ensures that the surface convective motions are represented as realistically as is currently feasible.

Turbulent transport plays an important role in BL dynamo models, helping to regulate the cycle period and amplitude. 2D models typically represent it by a turbulent diffusivity and (sometimes) magnetic pumping but there are few observational constraints on how these coefficients vary with depth so models vary widely in the profiles they use (see, e.g. Muñoz-Jaramillo et al., 2011). Even SFT models vary in the coefficient they use to describe the observed dispersal of magnetic flux on the solar surface (Jiang et al., 2014a). In this study we investigate how realistic surface convection influences the behavior of a BL dynamo model. Furthermore, by comparing convective models with models based on turbulent diffusion, we assess the viability of the turbulent diffusion paradigm and estimate the effective diffusion coefficient, η_t . Our results suggest that the surface convection is approximately equivalent to a turbulent diffusion: $\eta_t \sim 3 \times 10^{12} \text{ cm}^2 \text{ s}^{-1}$ which is comparable with the values obtained from

observations: $\eta_t \sim 2\text{--}5 \times 10^{12} \text{ cm}^2 \text{ s}^{-1}$ (Chae et al., 2008; Jiang et al., 2014a; Mosher, 1977; Schrijver et al., 1996a; Topka et al., 1982)

The organization of the chapter is as follows. In Section 7.2 and 7.3, we describe the STABLE model and how we implement convective flow fields. In Sections 7.4 and 7.5 we describe dynamo simulations based on turbulent diffusion and explicit convective motions respectively. In Section 7.6 we compare and contrast these simulations in order to quantify the role of convective transport and estimate the effective turbulent diffusivity of the convective motions. We conclude and summarize our results in Section 7.7.

7.2 The Numerical Model

The Surface flux Transport And Babcock-LEighton (STABLE) dynamo model is a 3D generalization of previous 2D BL models. In particular, it can be classified as a Flux-Transport Dynamo (FTD) model (Choudhuri et al., 1995; Dikpati & Charbonneau, 1999; Dikpati & Gilman, 2009; Wang et al., 1991). FTD models are BL dynamo models in which the imposed meridional circulation plays an important role in transporting toroidal flux toward the equator, thus establishing the butterfly diagram. Toroidal field is generated by the stretching of poloidal field by the differential rotation (the Ω -effect) and the poloidal field is generated by the BL process (Sec. 7.1).

Many previous 2D models parameterize the BL process by means of an α -effect or similar poloidal source term that is nonlocal in the sense that the poloidal field generation is confined to the surface layers but depends on the toroidal flux near the base of the CZ (e.g. Dikpati & Charbonneau, 1999; Rempel, 2006). We take a different approach here, exploiting the 3D capabilities of STABLE to treat the inherently 3D BL process more realistically. In particular, we explicitly place tilted BMRs on the surface of the model and follow their subsequent evolution by solving the 3D kinematic MHD induction equation:

$$\frac{\partial \mathbf{B}}{\partial t} = \nabla \times (\mathbf{v} \times \mathbf{B} - \eta_t \nabla \times \mathbf{B}) \quad . \quad (7.1)$$

The BMRs are sheared out and dispersed by differential rotation and turbulent diffusion and advected poleward by the differential rotation, naturally generating mean poloidal field as originally described by Babcock (1961) and Leighton (1969) and as captured by SFT models (Sec. 7.1).

The numerical algorithm that places BMRs on the surface is called SpotMaker and is described in detail by Miesch & Dikpati (2014) and Miesch & Teweldebirhan (2016, hereafter MT16). Briefly, we define a spot-producing toroidal field $B^*(\theta, \phi, t)$ at any time t by integrating

the longitudinal field component $B_\phi(\theta, \phi, r, t)$ over a radial range near the base of the CZ (here spanning $0.7-0.71R$, where R is the solar radius) and applying a latitudinal mask that suppresses high latitudes. We then choose a random latitude and longitude from all points where $B^*(\theta, \phi, t)$ exceeds a threshold value (here equal to 1 kG). This is where we place a tilted BMR on the surface.

The tilt angle of each BMR follows Joy's law ($\delta = 32^\circ.1 \cos \theta$; Stenflo & Kosovichev 2012) and the subsurface spot structure is specified by means of a potential field extrapolation down to $r_p = 0.90R$. As discussed by MT16 (see also Longcope & Choudhuri, 2002; Schüssler & Rempel, 2005), this corresponds to the limit in which BMRs decouple quickly from their roots in the tachocline/lower CZ (on a time scale short compared with the solar cycle). The subsurface structure is a very idealized assumption but it serves to localize the BL process in the near-surface layers as in previous FTD models. In the future we will consider the opposite limit in which the BMR retains connectivity to the tachocline by implementing a lifting and twisting flow in SpotMaker as described by Yeates & Muñoz-Jaramillo (2013).

In its current rendition, SpotMaker is essentially a 3D generalization of Durney's Double ring algorithm (Durney, 1995, 1997; Muñoz-Jaramillo et al., 2010). It effectively serves as an explicit source term $S(r, \theta, \phi, t)$ added to equation (7.1):

$$\frac{\partial \mathbf{B}}{\partial t} = \nabla \times (\mathbf{v} \times \mathbf{B} - \eta_t \nabla \times \mathbf{B}) + S(r, \theta, \phi, t) \quad . \quad (7.2)$$

Expressed in this way, $S(r, \theta, \phi, t)$ would be composed of a series of δ functions in time, with several thousand instances in each 11-year cycle. The time interval between spot appearances in each hemisphere is chosen randomly from a lognormal probability distribution with a mean of 3 days and a mode of 2 days (see Fig. 2c in MT16).

The magnetic flux in each BMR is proportional to the toroidal flux at the base of the CZ, $B^*(\theta, \phi, t)$, and at the chosen location, θ_s, ϕ_s :

$$\Phi = 2\alpha_{spot} \frac{|\hat{B}(\theta_s, \phi_s, t)|}{B_q} \frac{10^{23}}{1 + (\hat{B}(\theta, \phi)/B_q)^2} \text{Mx} \quad (7.3)$$

We neglect the rise time of a flux tube, which is short (~ 1 month) compared to a cycle period (~ 11 years). We also currently neglect the deflection of the tube as it rises. So, the flux in each BMR is proportional to the instantaneous value of \hat{B} at the same time, latitude, and longitude, as described by MT16. For the simulations reported here we use a quenching field strength B_q of 100 kG.

Defining the flux content of the spots in this way (equation 7.3) has various advantages. The poloidal field generation is proportional to \hat{B} for weak fields, so it correctly mimics the

Babcock-Leighton α effect. For $\alpha_{spot} = 1$, the subsurface field at the quenching strength B_q will generate the biggest spots that are observed which have a flux content $\sim 10^{23}$ Mx. However, as discussed by MT16, it is sometimes necessary to artificially increase the BMR flux in order to achieve supercritical (non-decaying) dynamo solutions. This is done by choosing a value for $\alpha_{spot} > 1$. Hence, this parameter determines how much poloidal field will be generated from the subsurface toroidal field and helps to regulate the overall amplitude of the dynamo fields. We define the radius of a spot r_r based on its flux content, such that $\Phi = B_0 r_r^2$ (neglecting geometric factors of order unity; see Miesch & Dikpati, 2014). For the value of B_0 we choose a typical sunspot field strength of 3 kG. We impose a minimum value of r_r based on the spatial resolution.

We use the well-tested Anelastic Spherical Harmonic (ASH) code (Brun et al., 2004; Miesch et al., 2000) to solve only the 3D magnetic induction equation (7.2), with fixed velocity fields. This kinematic formulation follows the pragmatic approach of previous 2D FTD dynamo models that take advantage of solar observations and helioseismic inversions to make the flow fields as realistic as possible. We will consider Lorentz-force feedbacks in future work. The ASH code has been verified against both convective dynamo benchmarks (Jones et al., 2011) and axisymmetric FTD benchmarks (MT16).

The velocity field \mathbf{v} in eq. (7.2) includes differential rotation (DR) and meridional circulation (MC) profiles chosen to match helioseismic inversions and photospheric observations, where available. Despite a recent proliferation of research fueled by the availability of high-resolution HMI/SDO data and long time series from MDI/SOHO, the subsurface structure and amplitude of the MC is still uncertain. There is some possible evidence for multiple cells per hemisphere in latitude and radius but different methods do not yet provide a consistent picture (Hathaway, 2012b; Jackiewicz et al., 2015b; Rajaguru & Antia, 2015; Schad et al., 2013; Zhao et al., 2013). In light of this uncertainty and in order to be consistent with the vast majority of papers in the literature on FTD dynamos, we adopt an MC profile here with a single cell per hemisphere, with counter-clockwise circulation in the northern hemisphere (NH) and clockwise circulation in the southern hemisphere (SH). This yields a peak poleward flow of 25.5 m s^{-1} at mid-latitudes at the surface and an equatorward flow of $\sim 2 \text{ m s}^{-1}$ near the base of the CZ. For further details on the MC profile we use see Chatterjee et al. (2004) and Hazra et al. (2017, hereafter HCM17).

The DR profile is chosen to be independent of radius in the bulk of the CZ, with a latitudinal rotation rate varying from 460.7 nHz at the equator to 330.67 nHz at the poles. We do not include a near-surface shear layer but we do include a tachocline, expressed by means of an error function centered at $r_c = 0.7R$, with a thickness of $0.05 R$. This produces a sharp transition at the base of the CZ to uniform rotation rate of the radiative zone, which is set equal to 432.8 nHz. These values are based on the previous 2D FTD models of Dikpati & Charbonneau (1999)

and Chatterjee et al. (2004) and our implementation is described further by MT16 (see Fig. 1a). Dikpati et al. (2002) have argued that the near-surface shear layer does not contribute significantly to the operation of flux-transport solar dynamo, but Karak & Cameron (2016) have shown that it can promote equatorward propagation in conjunction with efficient magnetic pumping in the surface layers.

In this study for the first time, we also include a non-axisymmetric convective velocity component in \mathbf{v} . Our methodology for achieving this is described in Sec. 7.3. This convective flow is confined to the upper CZ ($r > 0.9R$) and is intended to capture magnetic flux transport by small-scale surface convection on scales from granulation to super-granulation. Transport in the deeper regions of the CZ (giant cells) is still handled by means of the turbulent diffusivity η_t , which is a function of radius alone. For the simulations described in Section 7.4 that do not include 3D convective motions we use a two-step diffusivity profile as in previous 2D FTD models (e.g. Hotta & Yokoyama, 2010). Example profiles are shown in Fig. 7.1 (see also Fig. 1c in MT16 and Fig. 3 in HCM17). The value of $\eta_t(r)$ at $r = R$, which we refer to as η_{top} , is varied between $1 \times 10^{10} \text{ cm}^2 \text{ s}^{-1}$ and $3.5 \times 10^{13} \text{ cm}^2 \text{ s}^{-1}$, as described in Sec. 7.4. The values of $\eta_t(r)$ in the lower CZ and radiative interior are respectively $5 \times 10^{10} \text{ cm}^2 \text{ s}^{-1}$, and $10^9 \text{ cm}^2 \text{ s}^{-1}$. For the simulations described in Sec. 7.5, we reduce the surface diffusion to $5 \times 10^{11} \text{ cm}^2 \text{ s}^{-1}$, one order of magnitude higher than the value in the mid CZ (black dotted line). This ensures that the transport in the upper CZ is dominated by the imposed convective motions.

Note that the value of η_t that we use in the mid CZ, $5 \times 10^{10} \text{ cm}^2 \text{ s}^{-1}$ puts us in the so-called advection-dominated regime of FTD models in the sense that the MC dominates the transport of poloidal magnetic flux from the surface layers to the base of the CZ (Jiang et al., 2007; Karak et al., 2014a; Yeates et al., 2008). STABLE can also operate in the diffusion-dominated regime in which turbulent diffusion is the dominant transport mechanism; for an example see HCM17. It has been argued on several different grounds that the diffusion-dominated regime may be more realistic (e.g. Choudhuri et al., 2007; Jiang et al., 2007; Karak & Choudhuri, 2011; Miesch et al., 2012c) and is less sensitive to the detailed structure of the MC, capable of producing solar-like cycles even for multi-cellular MC profiles (Hazra et al., 2014). However, an investigation of these issues lies outside the scope of this present study. Here we focus on how explicit convective transport affects the operation of FTD dynamo models and our chosen $\eta_t(r)$ profiles are sufficient for this purpose.

We also include a weak horizontal hyperdiffusion on the right-hand-side of eq. (7.2) to dissipate spurious small-scale fields and thus keep the code numerically stable. In spectral space this is expressed as $-\eta_h R^{-2} [\ell(\ell+1)]^2 \tilde{\mathbf{B}}$, where $\tilde{\mathbf{B}}$ is the spherical harmonic transform of \mathbf{B} . We use $\eta_h = 2 \times 10^8 \text{ cm}^2 \text{ s}^{-1}$ for the diffusive Cases A1-A8 (Sec. 7.4) and $\eta_h = 3 \times 10^{10} \text{ cm}^2 \text{ s}^{-1}$ for the convective Cases C1-C3 (Sec. 7.5).

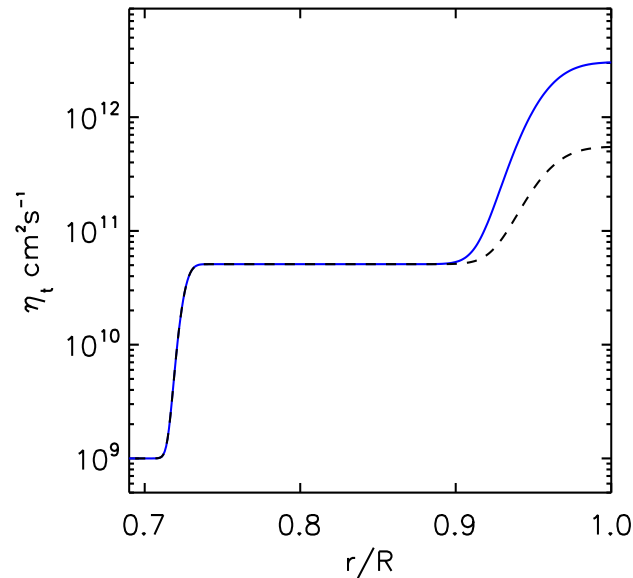


Fig. 7.1 Two step diffusivity profile used in our simulations. Shown are example diffusivity profiles used for simulations with convection (black dotted line) and without explicit convective motions (solid blue line), with $\eta_{top} = 3 \times 10^{12} \text{ cm s}^{-1}$ in the latter. The convective motions are confined to the upper convection zone and their role in the global dynamo is functionally equivalent to an enhanced turbulent diffusion.

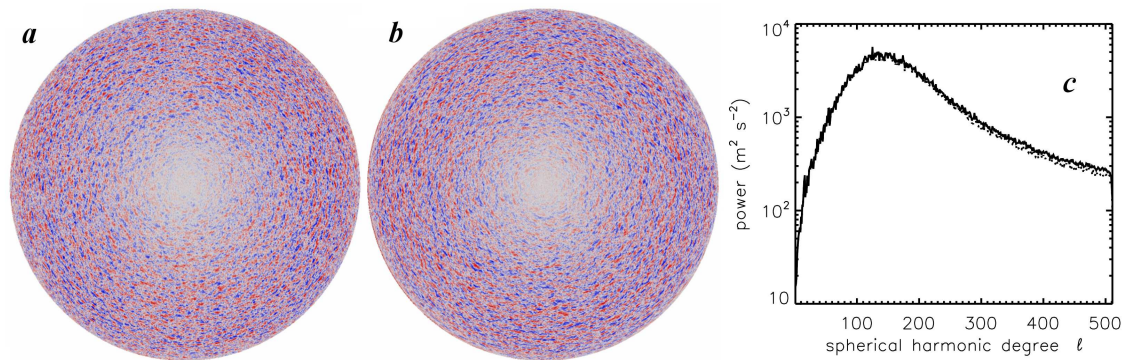


Fig. 7.2 (a) Line-of-sight (Doppler) velocity in the solar photosphere measured with the SOHO/MDI instrument on June 4, 1996. (b) Simulated line-of-sight velocity constructed from the empirical model of Hathaway et al. (2000) and Hathaway (2012a,b), which is designed to reproduce the observed horizontal Doppler velocity power spectrum, with randomized phases. (c) Horizontal velocity spectra for Hathaway's simulated flow field (solid line) and for the convective flow field used here (dotted line), at $r = R$. Small discrepancies at large ℓ arise because we only extract the divergent component (see text). Images and data courtesy of David Hathaway and Lisa Upton.

7.3 Incorporating Non-Axisymmetric Convective Flows into STABLE

7.3.1 Empirical Model for Surface Convection

Though ASH is fully capable of simulating global-scale convective motions, no global solar convection model can accurately capture smaller-scale convective motions near the surface such as granulation and supergranulation. This would require both extremely high resolution and including physical processes that are often neglected in global models, such as non-LTE radiative transfer, ionization, and the breakdown of the anelastic approximation. However, it is these small-scale convective motions that contribute most to the breakup and dispersal of BMRs and are thus most important from the perspective of the BL process.

For this reason, we wish to incorporate convection in a manner that is consistent with the pragmatic approach of kinematic dynamo modeling. In particular, we wish to exploit observational measurements of the convective power spectrum in the solar photosphere in order to ensure that the imposed convective flow fields near the surface are as realistic as possible. High-quality, full-disk measurements of the photospheric convection spectrum are now available from such instruments as the Helioseismic Magnetic Imager (HMI) onboard NASA's Solar Dynamics Observatory and the Michelson Doppler Imager (MDI) onboard NASA's SOLar and Heliospheric Observatory (SOHO). These measurements are typically based on Dopplergrams; 2D (latitude-longitude) maps of the line-of-sight velocity component on the solar surface (Fig. 7.2a).

Since the velocities in the solar photosphere are predominantly horizontal, these are the velocity components that are mainly sampled by the Dopplergrams; this leads to the dearth of power at disc center in Fig. 7.2a. Furthermore, at any point on the solar disc, only one horizontal direction is sampled. For example, Doppler velocities near the eastern limb are dominated by V_ϕ . In order to reconstruct the complete 2D flow field $V_\theta(\theta, \phi, t)$ and $V_\phi(\theta, \phi, t)$, some modeling is needed. Hathaway (2012a,b) has devised such a model (see also Hathaway et al., 2000). Hathaway's model is based on first subtracting off the differential rotation, the meridional circulation, and other unwanted signals such as convective blueshift, spacecraft motion and instrumental artifacts. Then the convective power spectrum is computed. A simulated horizontal velocity field is then produced based on that observed spectrum using a series of vector spherical harmonics with randomized complex coefficients.

Though Hathaway's original implementation is time-evolving, with correlation times chosen to match observations, we consider here a static horizontal velocity field with a resolution of $N_\theta = 512$ and $N_\phi = 1024$. A sample Dopplergram computed from the simulated horizontal

flow field is shown in Fig. 7.2b and the horizontal power spectrum is shown in Fig. 7.2c. The peak at $\ell \approx 130$ represents supergranulation. This data set does not resolve the broad peak in power beyond $\ell \sim 1000$ due to granulation, as discussed by Hathaway et al. (2000). We will refer to this empirical surface velocity field as $\mathbf{V}_s(\theta, \phi, t)$. Though we consider only static flows fields in this study, we will retain the explicit time dependence in this section in order to illustrate how our approach can be readily generalized to evolving convective flows.

Our aim is to incorporate the empirical surface velocity field $\mathbf{V}_s(\theta, \phi, t)$ into STABLE. Since this velocities are non-axisymmetric, this exploits the 3D capabilities of our dynamo model. In particular, this implies that the transport and amplification of the non-axisymmetric magnetic field components can influence the time evolution of the mean fields. This is not the case for axisymmetric, kinematic flows fields in which the $m = 0$ component of the magnetic induction equation decouples from the $m > 0$ components, where m is the azimuthal wavenumber.

In order to incorporate the 2D empirical surface flow field of Fig. 7.2 into our 3D model, we must specify some radial structure. In specifying this radial structure we have made several assumptions and approximations. The first assumption is that the small-scale convection in the solar surface layers is much more vigorous than the convection in the deeper convection zone. This is justified by our theoretical understanding of solar convection, which attributes it to the relatively low density, steep density stratification, and steep superadiabatic entropy gradient in the solar surface layers (Miesch, 2005; Nordlund et al., 2009). It is also justified by recent attempts to estimate the convective velocity amplitudes in the deep solar interior by means of helioseismic inversions, photospheric observations, and numerical modeling (Cossette & Rast, 2016; Greer et al., 2015; Hanasoge et al., 2010, 2016; Lord et al., 2014; Miesch et al., 2012c; O'Mara et al., 2016). And, it is consistent with previous FTD models that often use an enhanced turbulent diffusivity in the solar surface layers as illustrated in Fig. 7.1. Thus, we wish to extrapolate the surface velocity field downward but no deeper than $r \sim 0.9$, so that it effectively replaces the enhanced turbulent diffusion near the surface as shown by the dashed line in Fig. 7.1.

The second assumption is that the mass flux is divergenceless: $\nabla \cdot (\bar{\rho} \mathbf{V}) = 0$. Here $\bar{\rho} = \bar{\rho}(r)$ is the background density stratification, neglecting density fluctuations associated with the convection. Thus, this is essentially an anelastic approximation, valid for low Mach numbers. This means that the mass flux can be decomposed into poloidal (W) and toroidal (Z) components defined by:

$$\bar{\rho} \mathbf{V} = \nabla \times \nabla \times (W \hat{r}) + \nabla \times (Z \hat{r}) \quad . \quad (7.4)$$

Our third assumption is that the convective velocities are purely poloidal, so $Z = 0$. This implies that the vertical component of the fluid vorticity is zero. This is justified mainly by

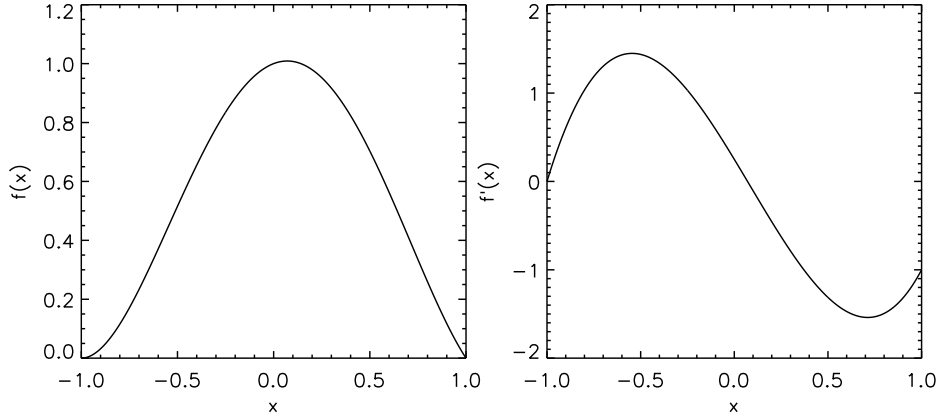


Fig. 7.3 Radial polynomial used for extrapolation of the surface flow to the deeper convection zone. Shown are (a) $f_\ell(x)$ and (b) $f'_\ell(x)$, where $x = (r - r_w)/(R - r_w)$. The plots extend from $r = r_p$ ($x = -1$) to $r = R$ ($x = 1$).

the steep density stratification in the solar surface layers, which imparts a strong horizontal divergence to vertical motions, and the clear signature of supergranulation in the horizontal divergence of surface flows (Gizon et al., 2010). There is also clear evidence that the action of the Coriolis force imparts a systematic vertical vorticity to supergranular-scale convective motions (Gizon et al., 2010) but this is a relatively weak effect and it is justified to neglect it as a first approximation. In future work we will include a vortical (toroidal) component to the flow field and we will investigate its influence both on the turbulent transport and on the potential amplification of magnetic flux.

This in effect means that we only assimilate the divergent component of the surface flow field into STABLE. Thus, we define $D(\theta, \phi, t)$ as the horizontal divergence of the imposed surface flow field: $D(\theta, \phi, t) = \nabla_h \cdot \mathbf{V}_s$. Recall that \mathbf{V}_s has only horizontal components so D is also equal to the full divergence of the surface flow field. Now we relate the horizontal divergence of the full 3D convective flow field to the poloidal stream function W as follows:

$$\rho \nabla_h \cdot \mathbf{V}_h = -\frac{1}{r^2} \frac{\partial}{\partial r} (r^2 \rho V_r) = -\nabla_h^2 \left(\frac{\partial W}{\partial r} \right) \quad (7.5)$$

Where ∇_h^2 and $\mathbf{V}_h = V_\theta \hat{\theta} + V_\phi \hat{\phi}$ are the horizontal Laplacian and the horizontal velocity respectively.

Now we expand W in a spherical harmonic series as follows

$$W(r, \theta, \phi, t) = \sum_{\ell=0}^{\ell_{\max}} \sum_{m=-\ell}^{\ell} \tilde{g}_{\ell m}(t) f_\ell(r) Y_{\ell m}(\theta, \phi) \quad (7.6)$$

Here $\tilde{g}_{\ell m}(t)$ describes the horizontal structure of the convective pattern at the surface and $f_\ell(r)$ describes its downward extrapolation. We have included an explicit ℓ dependence for $f_\ell(r)$ to allow for the possibility that different horizontal scales of convection may have different radial profiles; see Sec. 7.3.2. Note also that

$$-\nabla_h^2 W = \sum_{\ell=0}^{\ell_{\max}} \sum_{m=-\ell}^{\ell} \frac{\ell(\ell+1)}{r^2} \tilde{g}_{\ell m} f_\ell Y_{\ell m} \quad . \quad (7.7)$$

An expression for $\tilde{g}_{\ell m}$ can be obtained by applying a spherical harmonic transform to eq. (7.5) and evaluating it at the surface, $r = R$, with the help of eq. (7.7). This yields:

$$\tilde{g}_{\ell m}(t) = \frac{R^2 \bar{\rho}(R)}{\ell(\ell+1)} \tilde{D}_{\ell m}(t) [f'_\ell(R)]^{-1} \quad , \quad (7.8)$$

where $\tilde{D}_{\ell m}(t)$ are the spherical harmonic coefficients for the surface divergence $D(\theta, \phi, t)$ and $f'_\ell(r) = df_\ell(r)/dr$. All that remains is to define the vertical profile $f_\ell(r)$, which we discuss in Section 7.3.2.

Once we define $\tilde{g}_{\ell m}(t)$, $f_\ell(r)$, and $\bar{\rho}(r)$, then we can obtain all three components of the convective flow field throughout the entire 3D computational domain by means of equations (7.6) and (7.4):

$$V_r(r, \theta, \phi, t) = -\frac{1}{\bar{\rho}} \nabla_h^2 W(r, \theta, \phi, t) \quad (7.9)$$

$$V_\theta(r, \theta, \phi, t) = \frac{1}{\bar{\rho} r} \frac{\partial}{\partial \theta} \left(\frac{\partial W}{\partial r} \right) \quad (7.10)$$

$$V_\phi(r, \theta, \phi, t) = \frac{1}{\bar{\rho} r \sin \theta} \frac{\partial}{\partial \phi} \left(\frac{\partial W}{\partial r} \right) \quad (7.11)$$

Again, in this study we consider a time-independent convective flow field but this is easily generalizable to evolving flows in which the time evolution is governed by the imposed, empirical surface flow field $\mathbf{V}_s(\theta, \phi, t)$. This is in turn reflected in $\tilde{g}_{\ell m}(t)$ through eq. (7.8).

Equation (7.8) is the means by which Hathaway's simulated surface flow field, \mathbf{V}_s , is assimilated into STABLE. As noted above, only the horizontal divergence is used so any non-divergent components of \mathbf{V}_s will be omitted from our flow field. Hathaway's horizontal flow field is also constructed on the assumption that the flow is strictly poloidal ($\nabla \times \mathbf{V}_s = 0$) so this procedure should in principle ensure that V_θ and V_ϕ reproduce \mathbf{V}_s exactly at $r = R$. However, in practice there are numerical errors associated with the discretization of \mathbf{V}_s , the interpolation onto a Legendre grid for incorporation into STABLE, and the numerical computation of the derivatives (though the latter computation is spectrally accurate). So, the resulting horizontal

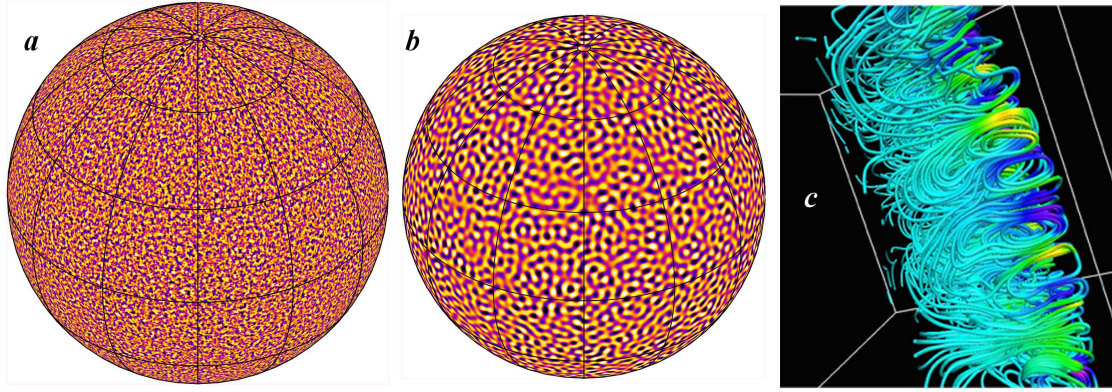


Fig. 7.4 Visualization of the imposed convective flow field. (a) The horizontal divergence at the surface $r = R$ is set equal to the divergence of the empirical flow field $\mathbf{V}_S(\theta, \phi)$. Here it is shown in an orthographic projection with yellow and blue representing divergence and convergence respectively. (b) As in (a) but for $r = 0.952$. (c) 3D rendering of a zoomed-in portion of the flow field showing streamlines of the mass flux colored by the vertical velocity (yellow upward, blue downward). Velocity amplitudes decrease with depth due to the increasing density.

power spectrum lies slightly below Hathaway's spectrum at high wavenumbers, as shown in Fig. 7.2c.

For the background density we use a polytropic, hydrostatic, adiabatic stratification (Jones et al., 2011):

$$\bar{\rho} = \rho_i \left(\frac{\zeta(r)}{\zeta(r_1)} \right)^n \quad (7.12)$$

where

$$\zeta(r) = c_0 + c_1 \frac{r_2 - r_1}{r} \quad (7.13)$$

$$c_0 = \frac{2\zeta_0 - \beta - 1}{1 - \beta} \quad (7.14)$$

$$c_1 = \frac{(1 + \beta)(1 - \zeta_0)}{(1 - \beta)^2} \quad (7.15)$$

and

$$\zeta_0 = \frac{\beta + 1}{\beta \exp(N_\rho/n) + 1} \quad (7.16)$$

Here $\rho_i = \rho(r_1) = 0.1788 \text{ g cm}^{-3}$, $\beta = r_1/r_2 = 0.69$ is the aspect ratio, $n = 1.5$ is the polytropic index, and $N_\rho = 5$ is the number of density scale heights across the computational domain, which extends from $r_1 = 0.69R$ to $r_2 = R$.

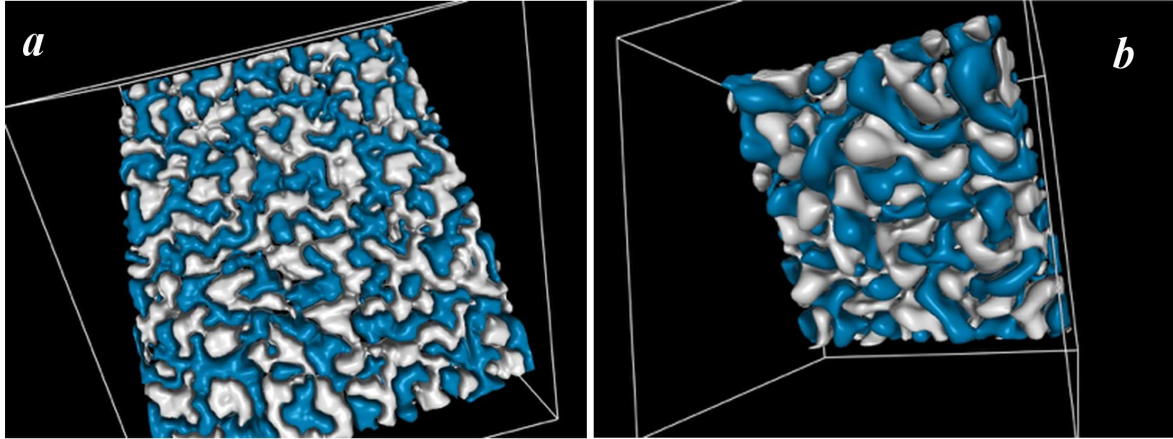


Fig. 7.5 Isosurfaces of the convective radial velocity V_r for a zoomed-in patch spanning 20° in latitude and longitude. Silver and blue denote upflow and downflow respectively. Shown are vantage points from (a) above and (b) below.

7.3.2 Subsurface Extrapolation of the Convective Flow

In order to extrapolate the empirical convective flow field at the surface downward, a suitable radial function is necessary which confines the convective motions to the upper convection zone, as discussed in Sec. 7.3.1. To achieve this, choose a function which satisfies the following boundary conditions:

$$f_\ell(r) = 0 \quad \& \quad f'_\ell(r) = -1, \quad r = R \quad (7.17)$$

$$f_\ell(r) = 1 \quad \& \quad r = r_w \quad (7.18)$$

$$f_\ell(r) = 0 \quad \& \quad f'_\ell(r) = 0, \quad r = r_p \quad (7.19)$$

$$f_\ell(r) = 0 \quad r \leq r_p \quad (7.20)$$

Here r_p is the penetration depth and $r_w = (r_p + R)/2$ is the middle of the convective layer, near the point where $f_\ell(r)$ peaks and $f'_\ell(r)$ changes sign. It can thus be regarded approximately as the convective turnover depth (see Fig. 7.3). The conditions (7.17)–(7.20) ensure that there is no convective mass flux through the surface or through the penetration radius r_p . Furthermore, the normalization ensures that the amplitudes of W and $\tilde{g}_{\ell m}$ are on the order of $\rho(R)U$ where U is a characteristic convective velocity amplitude at the surface.

These conditions can be satisfied with a fourth-order polynomial:

$$f(x) = a + bx + cx^2 + dx^3 + ex^4$$

where $x = (r - r_w)/(R - r_w)$, $a = 1$, $b = 0.25$, $c = -1.75$, $d = -0.25$, and $e = 0.75$. The function $f_\ell(x)$ and its first derivative $f'_\ell(x)$ are shown in Fig. 7.3. Note that $x = -1$, $x = 0$ and $x = 1$ correspond to r_p , r_w and R respectively.

We have yet to specify the penetration depth r_p . In doing so, it is reasonable to assume that larger-scale motions will penetrate more deeply than smaller-scale motions. The horizontal length scale L_h of a spectral mode at the surface with total wavenumber ℓ is approximately given by

$$\left(\frac{2\pi}{L_h}\right)^2 \sim \frac{\ell(\ell+1)}{R^2} . \quad (7.21)$$

If we assume that the vertical length scale L_v of a convective mode is comparable to its horizontal length scale, and if we assume that $\ell \gg 1$ as it is for most of the convective power (Fig. 7.2), then this gives

$$L_v \approx L_h \approx \frac{2\pi}{\ell} R . \quad (7.22)$$

Thus, we set $r_p = R - L_v = R(1 - 2\pi/\ell)$. However, we set a minimum value of $r_p = 0.9$ so even the largest motions do not penetrate below this.

The resulting convective flow fields are illustrated in Figures 7.4 and 7.5. The increase of the horizontal length scale of the convection with depth is clear by comparing Fig. 7.4a and Fig. 7.4b and by comparing the two frames in Fig. 7.5. Fig. 7.4c highlights the overturning nature of the motions. Note that at this resolution, the asymmetry between upflows and downflows is not apparent. In all calculations reported here we have used radial grid $N_r = 340$, latitudinal grid $N_\theta = 512$ and longitudinal grid $N_\phi = 1024$.

Once this 3D convective flow, \mathbf{v}_c , is defined, we add it to the axisymmetric flows \mathbf{v}_a such that $\mathbf{v} = \mathbf{v}_a + \mathbf{v}_c$. Here \mathbf{v}_a includes the differential rotation and the meridional flow described in Section 7.2. As mentioned in Section 7.1, we restrict our attention in this study to the case in which $\mathbf{v}_c(r, \theta, \phi)$ is independent of time. In future work we will implement an evolving flow field as in the AFT model of Upton & Hathaway (2014b,c).

7.4 Axisymmetric Flows

In this section, we present some results for the case in which \mathbf{v} is axisymmetric, consisting only of differential rotation and meridional circulation. These will be compared to the results presented in Section 7.5 that include 3D convective motions. All of the simulations presented in this chapter are summarized in Table 7.1. B_{pol} and B_{tor} refer to the amplitude of the mean poloidal and toroidal fields and B_{nax} refers to the amplitude of the non-axisymmetric field components. In each case we list the mean and standard deviation σ of the time series. The

Table 7.1 Simulation Summary

Cases ¹	α_{spot}	η_{top} (cm ² s ⁻¹)	Cycle Period (years)	Migration Speed ² (m s ⁻¹)	B_{pol} (G)		B_{tor} (kG)		B_{max} (kG)		$\frac{B_{tor}}{B_{pol}}$
					Mean	σ	Mean	σ	Mean	σ	
A1	15.0	3.0×10^{12}	13.3	11.6	596.6	118.3	33.54	1.91	1.76	0.51	56.45
A2	25.0	1.0×10^{13}	13.8	8.8	67.0	13.6	4.04	0.61	0.21	0.07	60.31
A3	25.0	3.5×10^{13}	sub-critical	–	–	–	–	–	–	–	–
A4	15.0	8.0×10^{11}	14.0	16.6	1523.2	292.8	71.18	4.47	4.64	0.93	46.73
A5	15.0	3.0×10^{11}	14.7	18.4	2075.5	435.2	84.72	9.88	6.97	1.10	40.94
A6	15.0	1.0×10^{11}	15.1	19.4	2431.4	430.1	89.24	9.58	9.37	1.15	36.68
A7	15.0	5.0×10^{10}	15.1	20.1	2546.7	455.2	85.73	8.37	11.13	1.60	33.64
A8	15.0	1.0×10^{10}	15.9	20.5	2531.7	388.2	89.74	12.33	12.08	1.35	35.56
C1	15.0	5.0×10^{11}	13.3	20.1	1541.2	226.0	77.70	7.40	2.29	0.27	50.42
C2	1.0	5.0×10^{11}	sub-critical	–	–	–	–	–	–	–	–
C3	15.0	5.0×10^{10}	14.0	22.7	1515.72	195.3	83.5	11.0	2.48	0.40	55.08

¹Cases A1-A8 include only axisymmetric flows (DR and MC). Cases C1-C3 also incorporate explicit convection.

²See Section 7.6.2.

cycle period is calculated by reversals of the mean toroidal field in the lower CZ (e.g. Figs. 7.6d and 7.12d). The primary motivation for the range of diffusive simulations A1-A8 is to assess what value of η_{top} most closely corresponds to explicit convective transport, as discussed in Sections 7.5 and 7.6.

The initial conditions for all cases is a weak dipole field. This gets stretched out by the differential rotation and when the toroidal field strength exceeds the threshold value of 1 kG, BMRs begin to appear. Soon the field strengths become strong enough to saturation the dynamo by means of eq. (7.3). Case A1 has been run for over 260 years, which corresponds to about 10-15 cycles after the dynamo saturates and settles down to a steady cycle. Cases A2-A8 have each been run for about 120 years, around 6-7 cycles after saturation. Cases C1 and C3 have also been run for nearly 190 years each (7-8 cycles after saturation, see Sec. 7.5).

As discussed in Sec. 7.1, SFT models rely on flux injection through artificial or observed BMR databases and solve only the radial component of the induction equation. Meanwhile, previous 2D FTD models were not able to reproduce the evolution of the non-axisymmetric components of the surface field. STABLE unifies these two models by spontaneously producing BMRs based on the dynamo-generated toroidal field and by capturing their subsequent evolution after emergence.

One of the main aims of STABLE is to reproduce the observed butterfly diagram (radial field) of the solar photosphere. Though producing solar-like butterfly diagrams is a valuable test of any solar dynamo model, most rely on the mean toroidal field near the base of the convection zone as a proxy for the surface field. Since STABLE produces explicit BMRs, there is no need for such a proxy. Both quantities are shown in Fig. 7.6. Notable solar-like features include equatorward propagation of active bands at low latitudes and poleward migration of

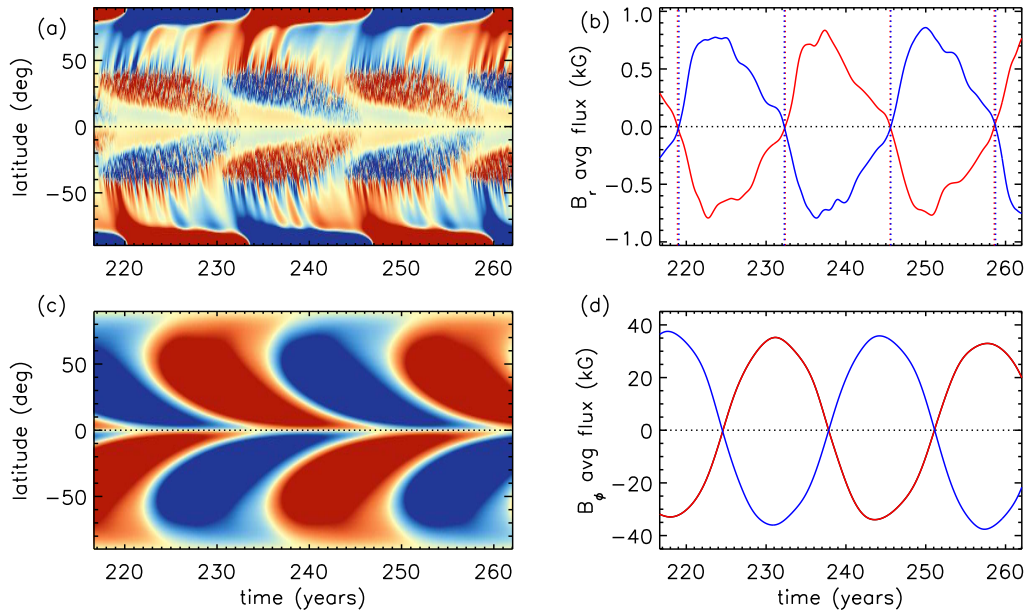


Fig. 7.6 (a) Time-latitude plot of the mean radial magnetic field on the solar surface, $\langle B_r \rangle$, for Case A1. The color scale is set from -200G (blue) to $+200\text{G}$ (red). (b) Mean polar field calculated by averaging the radial field in (a) over latitudes poleward of $\pm 88^\circ$. Blue and red curves correspond to the northern and southern hemispheres respectively and dotted lines of each color indicate polar field reversals. (c) Time-latitude plot of the mean toroidal field $\langle B_\phi \rangle$ at the bottom of the convection zone $r = 0.71R$. The color scale saturates at $\pm 50\text{ kG}$, with red and blue denoting eastward and westward field respectively. (d) Mean toroidal flux at low latitudes near the base of the CZ, obtained by averaging the plots in (c) over the northern (blue) and southern (red) hemispheres.

trailing BMR flux at high latitudes, which eventually reverses the polar fields. The equatorward propagation of active bands at the surface (Fig. 7.6a) is a consequence of the subsurface toroidal field propagation (Fig. 7.6c). Note that polar field reversals occur a few years after the peak toroidal field, comparable to solar observations (Fig. 7.6 c,d).

Figure 7.7 highlights the surface flux transport in Case A1. Compare this with Fig. 7.8, which shows the same thing but for a case with a lower surface diffusion (Case A4). The structures in the former case tend to be wider and spread out, commensurate with the higher diffusion. This is reflected in lower average field strengths for the non-axisymmetric field components: 1.76 kG in Case A1 versus 4.64 kG in Case A4 (Table 7.1). Higher diffusion always make a dynamo less efficient. The mean fields in Case A5-A8 are about 3-4 times stronger than in Case A1 even though the quenching field strength B_q is the same in both Cases (see eq. 7.3). The evolution of the mean fields for Case A1 is shown in Fig. 7.9, which highlights the general FTD aspects of these simulations. The basic operation of the dynamo

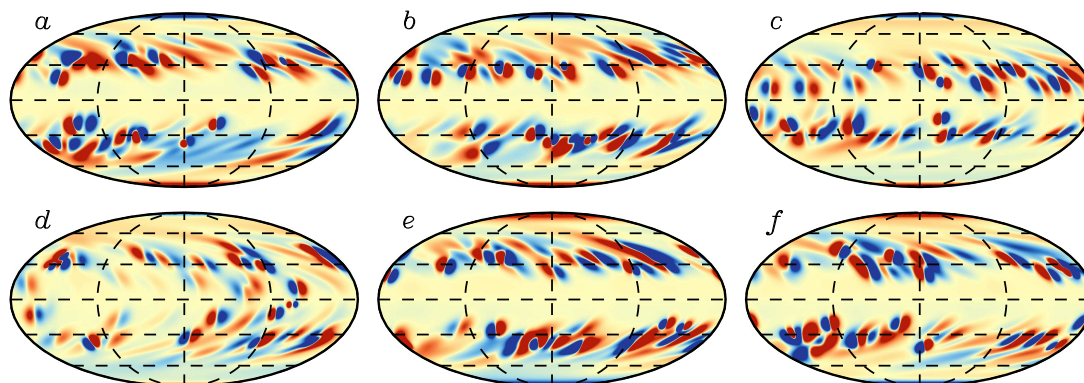


Fig. 7.7 Mollweide projection of B_r at $r = R$ in Case A1 at six different times that span a full magnetic cycle: (a) 223.9 yr, (b) 226.0 yr, (c) 229.0 yr, (d) 232.0 yr, (e) 234.0 yr and (f) 237.0 yr. Red and blue denote outward and inward field respectively and the saturation level on the color table is ± 1 kG. Dashed lines denote latitudes of 0° , $\pm 30^\circ$, and $\pm 60^\circ$.

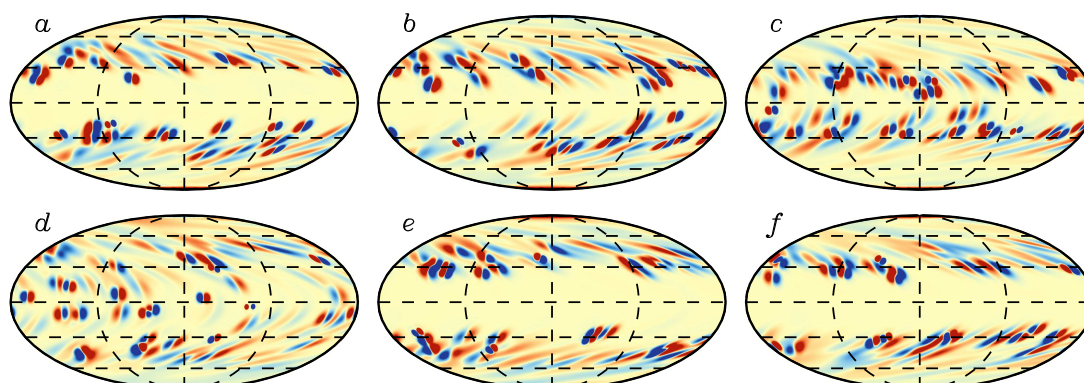


Fig. 7.8 Similar to Fig. 7.7 but for Case A4, with a color saturation level of ± 3 kG. The times again span a full magnetic cycle: (a) 124.0yr, (b) 127.0 yr, (c) 130.0 yr, (d) 133.0 yr, (e) 136.0 yr and (f) 139.0 yr.

is similar to that described in [Miesch & Dikpati \(2014\)](#) and [Miesch & Teweldebirhan \(2016\)](#). Differences between those previous results and the results shown here are mainly due to modified meridional circulation profile described in [Hazra et al. \(2017\)](#) and the varying values of η_{top} .

The cycle period increases somewhat as η_{top} is decreased (Table 7.1). We attribute this to a “short-circuiting” of the flux-transport dynamo by diffusive mixing. Even though all cases have the same value of η in the mid and lower CZ, a greater value of η_{top} promotes a more efficient downward transport of poloidal flux from the surface to the base of the CZ. The difference is significant, but not substantial. A decrease in η_{top} by a factor of 300 (from A1 to A8) lengthens the cycle period by about 20%.

Note that this result is in contrast to other FTD dynamo parameter studies that report a slight increase in the cycle period as the diffusion is increased ([Dikpati & Charbonneau, 1999](#); [Yeates et al., 2008](#)). However, these studies mainly focus on increasing the diffusivity in the bulk of the convection zone, not in the surface layers. For example, in terms of our notation, [Yeates et al. \(2008\)](#) vary η_{mid} while keeping η_{top} fixed, whereas we do the opposite. This accounts for the difference in our results, as we now explain.

There are at least three ways in which an increase in the turbulent diffusion can influence the cycle period in a Flux-Transport dynamo model: (A) The “short-circuit” effect noted above, by which diffusion enhances the efficiency of poloidal flux transport across the CZ, (B) a decrease in the efficiency of equatorward transport of toroidal flux at the base of the CZ, and (C) a decrease in the efficiency of toroidal flux generation at the base of the CZ. Effect (A) tends to decrease the cycle period, as described above. Meanwhile, effects (B) and (C) tend to increase the cycle period.

Effect (B) arises because of a decrease in the magnetic Reynolds number associated with the MC near the base of the CZ, $Rm = U_{mc}L_{mc}/\eta_{mid}$, where U_{mc} and L_{mc} are the relevant velocity and length scales. Lower Rm inhibits transport, as the magnetic field slips through the plasma. This slows down the equatorward advection of both toroidal and poloidal flux. It also tends to smooth out the structure of the field, which decreases the field amplitudes and inhibits toroidal field generation by the Ω -effect. This is effect (C) referred to in the previous paragraph. In a purely kinematic model, the toroidal field generation time scale would be independent of the field strength. However, many parameter studies such as [Dikpati & Charbonneau \(1999\)](#) and [Yeates et al. \(2008\)](#) include a quenching field strength for the toroidal field which limits the amplitude of the dynamo. At high values of η_{mid} , it takes the dynamo longer to reach this quenching field strength.

The simulations by [Dikpati & Charbonneau \(1999\)](#) and [Yeates et al. \(2008\)](#) include all three effects, but the latter two dominate. For example, a comparison of Figs. 8*d* and 8*i* in

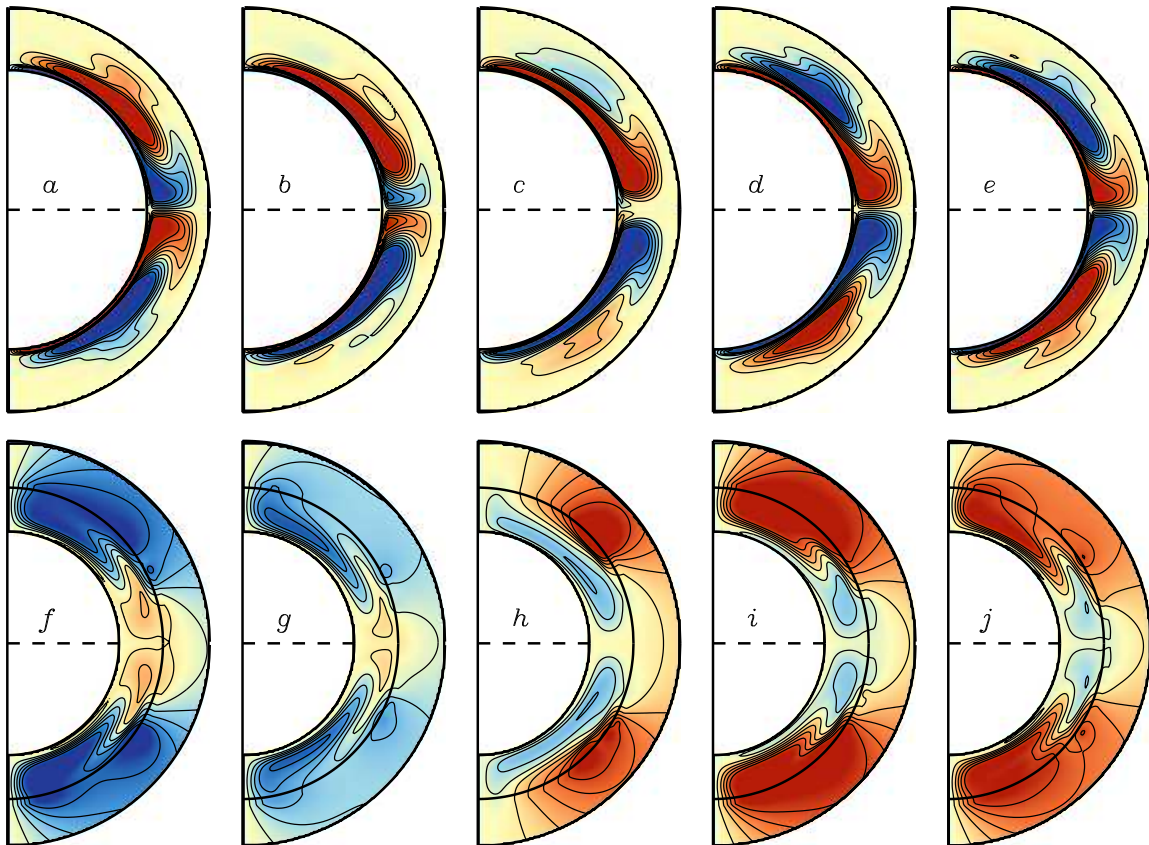


Fig. 7.9 Evolution of mean ($a-e$) toroidal and ($f-j$) poloidal fields in Case A1, spanning one magnetic cycle. Snapshots are shown for the same magnetic cycle as in Fig 7.7: $t = (a,f)$ 226.0 yr, (b,g) 229.2 yr, (c,h) 233.0 yr, (d,i) 237.1 yr and (e,j) 239.9 yr. Frames ($a-e$) show $\langle B_\phi \rangle$ with red and blue indicating eastward and westward field respectively. Frames ($f-j$) show the poloidal magnetic potential with a potential field extrapolation above $r = R$ to $r = 1.25R$. Colors indicate (red) clockwise and (blue) counter-clockwise field orientations. Average toroidal and poloidal field strengths are about 33 kG and 596 G respectively, as listed in Table 7.1, though peak toroidal fields can exceed 100 kG (the color table for $\langle B_\phi \rangle$ is clipped at ± 50 kG).

Yeates et al. (2008) clearly shows effect (A). By contrast, our simulations only include effect (A) because we keep the value of η_{mid} (and thus the value of R_m in the lower CZ) fixed in all of our simulations. We are aware of one previous study that investigated the influence of η_{top} on the operation of an FTD dynamo with fixed η_{mid} , namely (Hotta & Yokoyama, 2010). They find, as do we, that the cycle period decreases with increasing η_{top} (see their Fig. 5).

7.5 Convective Flows

In this section we describe dynamo simulations that include 3D convective flow fields as described in Section 7.3. We remind the reader that these are not full MHD simulations. Rather, the convective velocity field is prescribed in a kinematic sense based on observations of the photospheric power spectrum. We also remind the reader that the imposed convection does not occupy the entire convection zone. Rather, it is intended to mimic the relatively vigorous, small-scale convective motions in the solar surface layers ($r > 0.9R$) that are well understood both observationally and theoretically. But as described in the section 7.5.1, we eventually keep the convective flow confined near the surface layer only ($r \sim R$). This imposed convective flow is in lieu of the turbulent diffusion that is used to represent surface convection in most SFT and FTD models (Jiang et al., 2014a). Thus, we correspondingly reduce the turbulent diffusion coefficient near the surface, η_{top} , as shown in Fig. 7.1. This follows the approach used by Upton & Hathaway (2014b,c) in their AFT model. In the deeper CZ we continue to represent convective transport as a turbulent diffusion. For further details on the implementation, see Section 7.3.

7.5.1 Amplification of fields by convective flows

Babcock-Leighton (BL) dynamo models rely on the dispersal and migration of magnetic field by near-surface convection but they typically neglect the fact that these same convective motions can operate as a small-scale dynamo (e.g. Cattaneo, 1999). In our model, when we include 3D convective motions as described in Sec. 7.3, we find that this flow does indeed operate as a small-scale dynamo.

A characteristic length scale of the convection can be estimated as $L \sim 2\pi R/\ell_0 \sim 34$ Mm, where $\ell_0 \sim 130$ is the spherical harmonic degree at which the spectrum peaks (Fig. 7.2c). For a velocity scale, we can use the rms value of $U \sim 250$ m s⁻¹. Together with $\eta_{top} = 5 \times 10^{10}$ cm² s⁻¹, this implies a magnetic Reynolds number of $R_m = UL/\eta_{top} \sim 1700$. So, it is not surprising that this flow is supercritical to small-scale dynamo action. We find that it is even

supercritical for $\eta_{top} = 5 \times 10^{11}$ ($R_m \sim 170$). Though this behavior is reasonable, it is not conducive to establishing magnetic cycles.

We find that small scale dynamo action disrupts the operation of the BL dynamo. BMRs are quickly overwhelmed by random small-scale fields that grow exponentially. This inhibits poloidal field generation by the BL mechanism and thus suppresses the magnetic cycles. This problem is not found in the AFT model (Upton & Hathaway, 2014b,c), which uses the same surface flows, because AFT is 2D and therefore cannot exhibit sustained dynamo action.

We have considered several approaches to suppressing this small-scale dynamo action in order to get a functioning BL dynamo. First, we enhanced the dissipation on small (convective) scales by imposing a horizontal hyperdiffusion ∇_h^4 or ∇_h^8 . But we were unable to find appropriate hyperdiffusion coefficients to yield a cyclic dynamo solution. Then, we attempted to saturate the small-scale fields by introducing a threshold field strength B_s , applied to the non-axisymmetric field components. However, it was not possible to apply this selectively to suppress dynamo-generated fields but not the remnant fields from emerging BMRs. We also tried nonlinear quenching of the non-axisymmetric field, with similar results.

We were able to achieve some degree of BL activity by using a drag term of the form

$$\frac{\partial \mathbf{B}'}{\partial t} = -\frac{\mathbf{B}'}{\tau} + \dots \quad (7.23)$$

where \mathbf{B}' is the non-axisymmetric field and $\tau \sim 24$ hrs is a suppression time scale that is comparable to the small-scale dynamo growth rate. This is effectively a scale-independent variation of the hyperviscosity approach. However, the solutions were not solar-like, exhibiting a large asymmetry about the equator, with BMRs in one hemisphere and not the other.

The only effective way we found to suppress small-scale dynamo action is to essentially make the convective flow 2D, as in AFT. Thus, for Cases C1, C2, and C3 presented in this chapter, we have only applied the convective flow to the radial field B_r at the radial grid point that is adjacent to the top boundary. Thus, the upper boundary condition (radial field) is applied at radial grid point 1 and the convective flow is included by adding it to the radial component of the induction equation (7.2) at grid point 2. And, even in this case, we still found it beneficial to use a higher value of the hyperdiffusion ($\eta_h = 3 \times 10^{10} \text{ cm}^2 \text{ s}^{-1}$) relative to the diffusive Cases A1-A8 ($\eta_h = 2 \times 10^8 \text{ cm}^2 \text{ s}^{-1}$) in order to suppress small-scale fields (see Sec. 7.2). In this way we were able to achieve a viable BL dynamo model as described in section 7.5.2.

We appreciate that this solution is not ideal, but it is required by the kinematic nature of our model. In the Sun, small-scale dynamo action surely occurs but it is saturated by Lorentz-force feedbacks. The only way to self-consistently capture this in our model is to solve the full set of

anelastic MHD equations. We do intend to implement this, but it would require a substantial increase in the sophistication of the model so we defer it to a future publication.

7.5.2 Results with convective flows

In this section, we present results with explicit convective motions as the effective transport mechanism of large scale magnetic field on the surface of the Sun, in addition to meridional circulation and differential rotation. This convective transport is limited to the horizontal advection of vertical field near the upper boundary as described in Sec. 7.5.1, though we still decrease the explicit diffusion η_{top} as illustrated in Fig. 7.1. Thus, when we refer to including *convective flows* in our models we really mean explicit horizontal flow fields chosen to mimic the observed properties of convection on the solar surface. Convective transport in the mid convection zone is still modeled with a turbulent diffusivity.

It is worth noting that the introduction of the convective flow field \mathbf{v}_c increases the computational expense substantially. This is because of the Courant-Friedrichs-Lewy (CFL) constraint on the time step. At the horizontal resolution used here ($N_\theta = 512$, $N_\phi = 1024$), the peak convective velocity is on the order of 900 m s^{-1} . This is a factor of 6.7 larger than the peak axisymmetric flow speed of 135 m s^{-1} , requiring a commensurate decrease in the time step. If vertical convective motions are included this requires a further decrease of the time step since the vertical grid spacing is about a factor of 7 smaller than the horizontal grid spacing. Turbulent diffusion is not subject to a CFL constraint because it is handled by a semi-implicit Crank-Nicolson scheme.

We have performed three simulations with convection, as summarized in Table 7.1. Case C1 is a fiducial solar-like dynamo solution that we will discuss further below. Case C2 is similar to Case C1 but with $\alpha_{spot} = 1$. This is found to be sub-critical for sustained dynamo action, as found in many diffusive cases (MT16). Case C3 is similar to Case C1 but with a lower value of η_{top} ; $5 \times 10^{10} \text{ cm}^2 \text{ s}^{-1}$ instead of η_{top} ; $5 \times 10^{11} \text{ cm}^2 \text{ s}^{-1}$. The rationale for choosing a low value is because η_{top} is intended to parameterize the convective transport that we are now capturing explicitly, as emphasized in Sec. 7.3. However, we find that if we make η_{top} too low the dynamo flips into a quadrupolar parity ($\langle B_r \rangle$ and $\langle B_\phi \rangle$ symmetric about the equator). We believe that Case C3 is in that quadrupolar regime. Though it's parity is still largely negative (dipolar) after 190 years of evolution, it is tending toward quadrupolar. Furthermore, a longer simulation with lower resolution (otherwise the same parameters) shifts to quadrupolar after about 300 years.

This is a known feature of BL dynamo models. Efficient diffusive coupling between the two hemispheres is known to promote dipolar parity ($\langle B_r \rangle$ and $\langle B_\phi \rangle$ antisymmetric about the equator), as demonstrated by Chatterjee et al. (2004) and Hotta & Yokoyama (2010). Evidently,

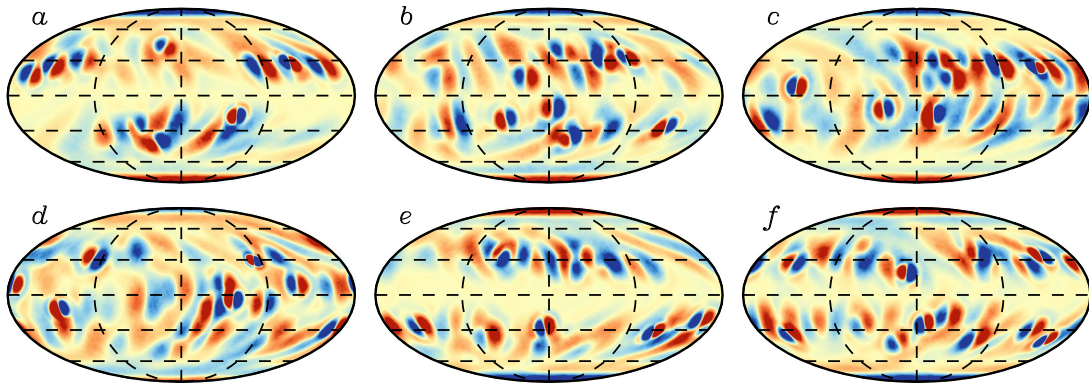


Fig. 7.10 Similar to Figures 7.7 and 7.8 but for the convective Case C1, with a color saturation level of ± 3 kG. Snapshots are shown for $t =$ (a) 165.0 yr, (b) 168.1 yr, (c) 171.0 yr, (d) 173.9 yr, (e) 176.0 yr and (f) 180.0 yr.

the convective transport alone is not sufficient to establish dipolar parity in our models. This may be because the explicit convective flows are limited to the surface whereas the 3D structure of the BMRs upon emergence extends down to $0.9R$. In short, the net turbulent transport (advection plus diffusion) in Case C3 appears to be insufficient to yield dipolar parity but in Case C1 it is. The value of η_{top} in Case C1 is high enough to enhance the subsurface diffusive coupling between hemispheres but low enough that the explicit convective flows dominate the surface flux transport (as will be demonstrated below). Since the Sun exhibits dipolar parity, we will hereafter focus on Case C1.

Fig. 7.10 shows the evolution of the surface flux in Case C1. Qualitatively it looks more like Case A1 (Figs. 7.7) than A4 (Figs. 7.8), with more diffuse bipolar structures at low latitudes, though Case C1 has stronger fields (Table 7.1). The evolution of the mean fields in Case C1 is also similar to Case A1, as shown in Fig. 7.11. This suggests that the efficiency of convective flux transport is comparable to that of the turbulent diffusion in Case A1. We will see below that this first impression is borne out by a more thorough analysis.

The poloidal and toroidal butterfly diagrams for Case C1 are shown in Fig. 7.12. The most apparent differences in the surface flux transport (Fig. 7.12a) relative to Case A1 (Fig. 7.6a) are less pronounced bipolar structures in the low latitudes and mix polarity polar caps. In Case C1, active regions are shredded by convective flows which results a less concentrated active regions compared to Case A1. A more subtle difference is that the poleward migration rate of the streams is somewhat more rapid (see Section 7.6.2). Though the broader polar regions in Case C1 possess mixed polarities, the polar fields are stronger than the unipolar polar regions of Case A1; compare Figs. 7.6b and 7.12b. Such behavior may be attributed to the tendency for the convective motions to disperse and transport BMR fields without dissipating them (see Sec.

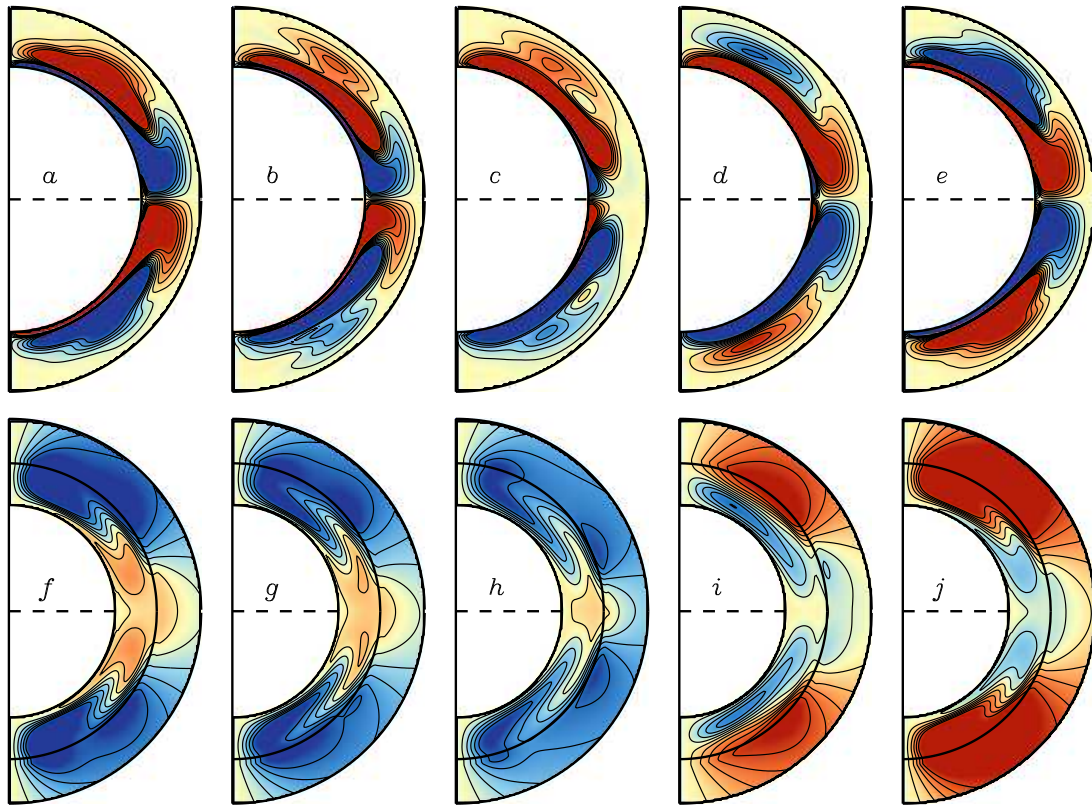


Fig. 7.11 As in Fig. 7.9 but for Case C1. This spans the same magnetic cycle as in Fig. 7.10, at times of $t = (a,f)$ 166.0 yr, (b,g) 169.0 yr, (c,h) 172.0 yr, (d,i) 175.0 yr and (e,j) 179.0 yr.

7.6.3). In the case of A1, BMRs emerge and the opposite polarities partially cancel each other as they disperse. By contrast, in Case C1, the fields disperse but cancellation is less efficient as a result of the smaller ohmic diffusion. Thus, both polarities are transported poleward and concentrated into strong, alternating bands.

The shape of the polar flux plot for Case C1 (7.12b) is similar to Case A1 (Fig. 7.6b) but with somewhat more variation and a sharper decay at the end of each cycle. This variability reflects the mixed polarity fields that cross into the polar regions before they cancel one another. The slower decay phase for Case C1 implies a longer interval of polar flux generation by poleward migrating streams which persists for almost the entire cycle, as seen in Fig. 7.12a. By contrast, poleward migrating streams are less prominent late in the cycle for Case A1 (Fig. 7.6a). As BMRs emerge at progressively lower latitudes, most of the emerging flux in this more diffusive case cancels locally before it can migrate to higher latitudes. This sustained flux emergence at mid latitudes is not supported by solar observations, which show few mid-latitude BMRs in the declining phase of the cycle. This discrepancy may be due in part to our simple

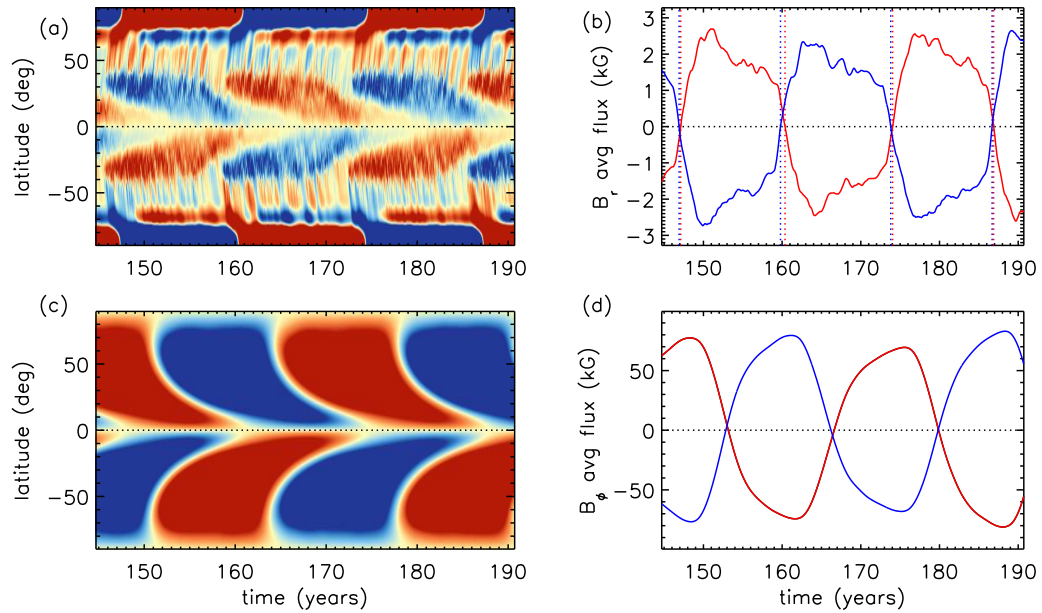


Fig. 7.12 As in Fig. 7.6 but for Case C1. Here the color tables saturate at (a) ± 500 G and (c) ± 100 kG.

flux emergence algorithm. Resolving it will likely require a better understanding of the flux emergence process.

The sustained supply of poloidal flux to the poles throughout most of the cycle in Case C1 also has consequences for the toroidal field generation. As this flux is transported to the base of the CZ by meridional circulation and turbulent diffusion, it promotes sustained toroidal flux generation through the Ω -effect, particularly at mid-latitudes where the latitudinal shear is strongest. This is evident in Fig. 7.12c which shows strong toroidal fields persist near $\pm 50 - 60^\circ$ throughout most of the cycle. Compare this to Case A1, (Fig. 7.6(c)), where the mid-latitude toroidal flux diminishes late in the cycle as the bands propagate equatorward. This excess of mid-latitude flux in Case C1 also accounts for the distortion of the integrated toroidal flux curve (Fig. 7.12d), which peaks later in the cycle than Case A1 (Fig. Fig. 7.6d).

Figure 7.13 compares the surface butterfly diagram in Case C1 to several diffusive cases with relatively high and low values of η_{top} , ranging from $1 \times 10^{13} \text{ cm}^2 \text{ s}^{-1}$ to $8 \times 10^{11} \text{ cm}^2 \text{ s}^{-1}$. Qualitatively, it bears the greatest resemblance to Case A1. This conclusion is based on the width of the poleward-migrating streams (though note the different ranges for the time axes), the structure and width of the polar flux concentrations, the relative strength of the polar and low-latitude fields, and the location of the active latitudes. In Section 7.6.2 we take a more quantitative approach to comparing the poleward migration speeds.

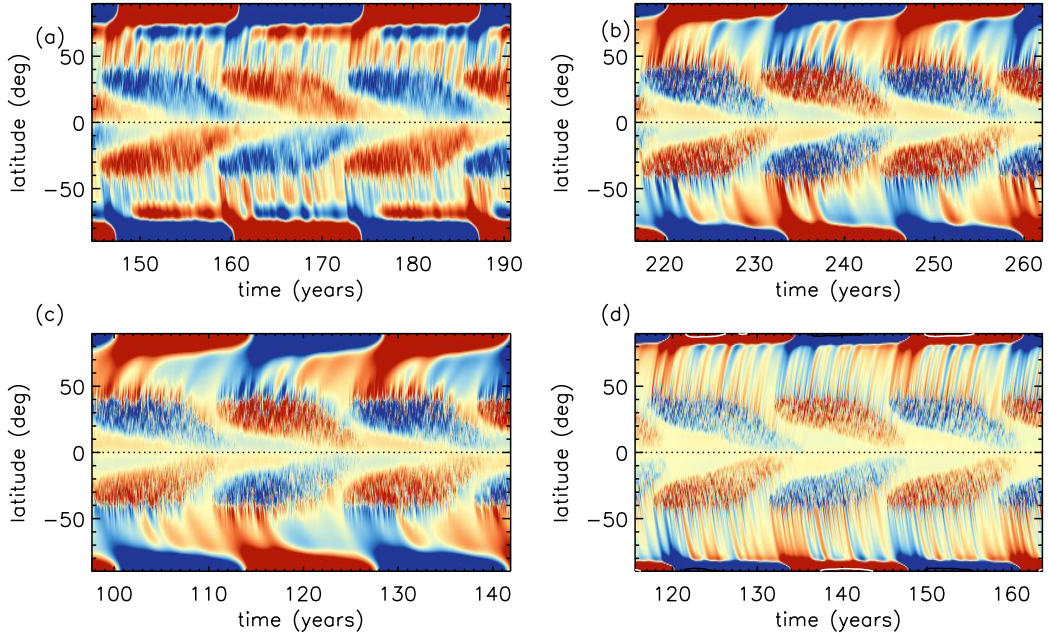


Fig. 7.13 Time latitude plot of $\langle B_r \rangle$ at $r = R$ for: (a) Case C1 (B_r scale = ± 500 G). (b) Case A1 with $\eta_{top} = 3 \times 10^{12}$ (B_r scale = ± 200 G) (c) Case A2 with $\eta_{top} = 10^{13}$ (B_r scale = ± 30 G) and (d) Case A4 with $\eta_{top} = 8 \times 10^{11}$ (B_r scale = ± 2000 G).

It is worth noting that the polar field strength of ~ 1.5 kG in Case C1 is significantly higher than typical measurements of the polar fields in the solar photosphere, which are on the order of 1-3 G (Muñoz-Jaramillo et al., 2012, e.g.). In our model, we calculate the polar field by averaging the radial magnetic field over the region 88° to pole. However, observational measurements usually quote the line-of-sight field strength averaged over a large region, often down to latitudes of 70° or even 55° . Projection and averaging effects therefore diminish the observed field strengths. After correcting for these effects, the observed value of the polar field strength is on the order of 10 G, which is consistent with the backwards extrapolation of coronal and heliospheric measurements and models (Gibson et al., 1999). Also, it must be remembered that the BMR fluxes that we use here are artificially large. As discussed in Section 7.2, we enhance the photospheric flux budget by setting $\alpha_{spot} > 1$ in order to ensure that the dynamo solution is super-critical. For Case C1 $\alpha_{spot} = 15$. We have confirmed that setting $\alpha_{spot} = 1$ leads to decaying solutions (Case C2 in Table 7.1). Still, the high polar field strengths are a concern and are a known issue with BL/FT models. A possible remedy might be to take into account the connectivity of emerging BMRs with their deep-seated roots. Yeates & Muñoz-Jaramillo (2013) show that this can shift the region of poloidal field generation more to the interior, producing weaker poloidal fields at the surface and particularly at the poles.

In summary, the convective Case C1 behaves in many ways like the diffusive Case A1, which has $\eta_{top} \sim 3 \times 10^{12} \text{ cm}^2 \text{ s}^{-1}$. However, the mean fields in Case C1 are much stronger. In the next section we investigate why this is and we take a closer look at the similarities and differences between Case C1 and the cases in which convective transport is approximated by turbulent diffusion.

7.6 Discussion: Does Convection Operate as a Turbulent Diffusion?

The main objective of our study is to improve the fidelity of the surface flux transport in our 3D Babcock-Leighton dynamo model by replacing turbulent diffusion with a more realistic depiction of photospheric convection. However, as mentioned in Section 7.5, this introduces challenges, including small-scale dynamo action and reduced computational efficiency. For this reason, and also for understanding the nature of convective transport, it is important to ask how much we gain from the explicit convective flows. Is convective transport accurately parameterized by a turbulent diffusion or is it fundamentally non-diffusive? If the former, what value of η_{top} is optimal? These are the questions we address in this section.

In Section 7.5 we argued that, at least qualitatively, the convective Case C1 resembles Case A1, which has $\eta_{top} = 3 \times 10^{12} \text{ cm}^2 \text{ s}^{-1}$. This is comparable to estimates of the turbulent diffusion from photospheric observations of magnetic flux elements, which suggest $\eta_{top} \sim 2\text{--}6 \times 10^{12} \text{ cm}^2 \text{ s}^{-1}$ (Abramenko et al., 2011; Mosher, 1977; Schrijver et al., 1996b; Topka et al., 1982). In mean-field theory, the value of η_t is linked to the kinetic energy of the turbulence. In particular, if U and L are characteristic velocity and length scales of \mathbf{v}' , then $\eta_t \sim UL/3$ (e.g. Ossendrijver, 2003). Here we have $U \sim 250 \text{ m s}^{-1}$ and $L \sim 34 \text{ Mm}$ (Sec. 7.5.1), which suggests a value of $\eta_{MFT} \sim 10^{13} \text{ cm}^2 \text{ s}^{-1}$ - somewhat higher than the observational estimate.

In the remainder of this section, we take a closer look at these estimates.

7.6.1 The turbulent electromotive force (emf)

In kinematic mean-field dynamo theory, turbulent diffusion is only one component to the turbulent electromotive force (emf), \mathcal{E} . Though more general averaging procedures are sometimes used, here we define the turbulent emf as

$$\mathcal{E} = \langle \mathbf{v}' \times \mathbf{B}' \rangle \quad (7.24)$$

where the angular brackets indicate averages over longitude and primes indicate non-axisymmetric components, e.g. $\mathbf{v}' = \mathbf{v} - \langle \mathbf{v} \rangle$.

The ansatz of turbulent diffusion as expressed in eq. (7.1) assumes that

$$\mathcal{D} \approx -\eta_t \nabla \times \langle \mathbf{B} \rangle \quad . \quad (7.25)$$

This is the hypothesis we wish to test. In particular, we can compute \mathcal{E} explicitly in Case C1 from the non-axisymmetric components of \mathbf{v} and \mathbf{B} and then see if it is essentially diffusive in nature as expressed in eq. (7.25).

If we focus on the longitudinally-averaged radial field $\langle B_r \rangle$ at the surface ($r = R$), then the relevant component of the emf in eq. (7.24) is $\mathcal{E}_\phi = -\langle V'_\theta B'_r \rangle$. When comparing this to the diffusive parameterization in eq. 7.25, we wish to focus on the component of \mathcal{D} that captures the horizontal diffusion of vertical field at the surface, which is

$$\mathcal{D}_\phi \approx \frac{\eta_t}{R} \left(\frac{\partial \langle B_r \rangle}{\partial \theta} \right)_{r=R} \quad . \quad (7.26)$$

We find that a value of $\eta_t \sim 10^{12} \text{ cm}^2 \text{ s}^{-1}$ gives similar amplitudes for \mathcal{E}_ϕ and \mathcal{D}_ϕ . This is an order of magnitude smaller than the mean-field estimate of $10^{13} \text{ cm}^2 \text{ s}^{-1}$ given at the beginning of Section 7.6 but comparable to Case A1 and to observational estimates.

However, we found little correlation between \mathcal{E}_ϕ and \mathcal{D}_ϕ . In fact, there is a weak anti-correlation. Averaging each over a one-month interval in the early and late phases of a typical cycle yields correlation coefficients of about -0.06 and -0.08 respectively. This result was somewhat of a surprise but it arises because this measure highlights the non-diffusive aspects of the convective transport.

To appreciate this, consider that \mathcal{E}_ϕ is largest where B'_r is largest, namely regions of unipolar field within BMRs and in the polar caps. Here the convective flow tends to advect vertical magnetic field into regions of horizontal convergence—the equivalent of downflow lanes, though v'_r is effectively zero in Case C1 (see Sec. 7.5.1). Thus, B'_r is squeezed before it is dispersed. This squeezing action is anti-diffusive and opposes the background diffusion, which is weak but non-negligible on the scale of the convergence lanes ($\eta_{top} = 5 \times 10^{11} \text{ cm}^2 \text{ s}^{-1}$).

This mimics the evolution of vertical magnetic flux in the solar photosphere, which is non-diffusive at early times, as the flux is advected toward supergranular boundaries to form the magnetic network, and diffusive at spatial and temporal scales much larger than those of the convective motions (Cadavid et al., 1999). This long-term diffusive behavior is difficult to capture by means of the pointwise comparison of \mathcal{E}_ϕ and \mathcal{D}_ϕ . More sophisticated techniques are needed to quantify the effective diffusion coefficient, such as correlation tracking of magnetic

flux elements. In the next Section (Sec. 7.6.2) we consider an alternative approach, which is to quantify the speed at which residual BMR flux is transported to the poles.

7.6.2 Poleward Migration

One way to quantify the efficiency of surface flux transport is by estimating the rate at which trailing flux migrates from mid-latitudes to the poles. In particular, we see that the butterfly diagrams in Figures 7.6a, 7.12a and 7.13 are dominated by successive streams of mixed polarities that reflect the propagation of radial field from latitudes below about $\pm 40^\circ$ to latitudes above $\pm 70^\circ$. How do these propagation/migration rates vary among the different cases? In this section we address that question quantitatively by means of a correlation function.

We proceed by first constructing a 2D map of the mean, radial, surface magnetic field $\langle B_r \rangle (r = R, \theta, t)$ for each case as in Fig. 7.13 but now limited to the latitude range between 40° and 70° . For shorthand, we will refer to this 2D map as $B(\theta_k, t)$ where k is the discrete colatitudinal index. Then we compute a revised map, $B(\theta_k, t')$ by shifting each row in time such that $t' = t - (\lambda - 40^\circ)/V_p$ where $\lambda = 90^\circ - \theta$ is the latitude in degrees and V_p is a specified tracking speed.

We then compute a correlation function between different rows of the shifted map as

$$c(i, k; V_p) = \frac{\int B(\theta_i, t') B(\theta_k, t') dt'}{\sqrt{\int B^2(\theta_i, t') dt' \int B^2(\theta_k, t') dt'}} \quad (7.27)$$

Here indices i and k span all latitudes between 40° and 70° . The time integration extends over three cycles, as shown in Fig. 7.13.

Then we sum the result of eq. (7.27) over all i, k pairs to obtain a single correlation coefficient for each value of V_p :

$$C(V_p) = \frac{1}{N} \sum_i \sum_{k>i} c(i, k; V_p) \quad (7.28)$$

where N is the total number of pairs in the summation ($k > i$). The final step is to plot $C(V_p)$ and choose the value of V_p that maximizes the correlation as the characteristic flux migration speed for each case. The results are listed in Table 7.1 and the correlation plots for several cases are compared in Fig. 7.14.

The meridional circulation is mainly responsible for the poleward transport of magnetic flux but convective transport can also play an important role. For those cases in which the convective transport is represented by a turbulent diffusion (A1-A8), one might expect that an increase in the diffusion coefficient η_{top} might enhance the transport of flux toward the poles

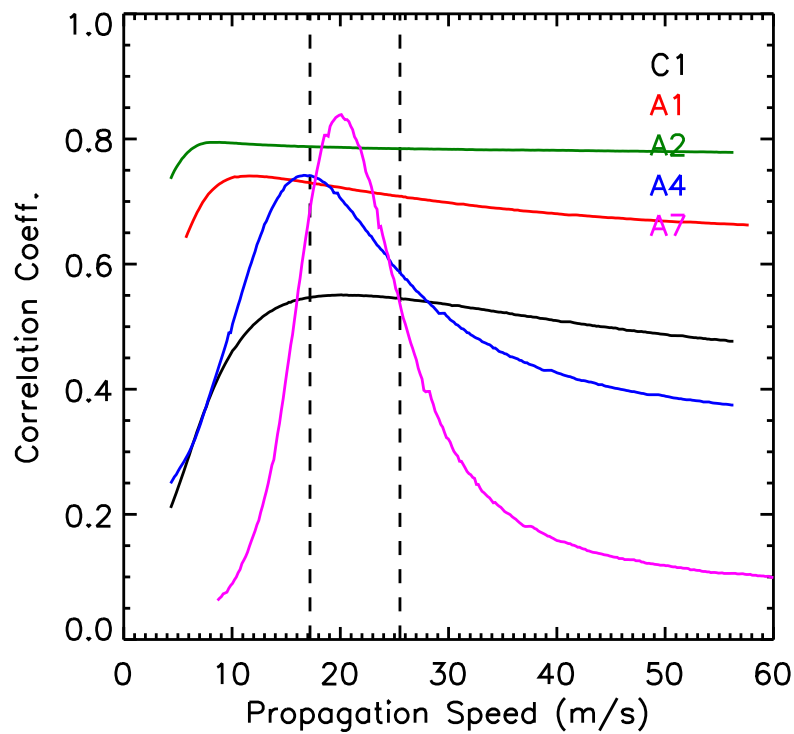


Fig. 7.14 The correlation coefficient C versus migration speed V_p is plotted for five different cases. The black solid line represents Case C1. Red, green, blue and magenta lines represent Cases A1, A2, A4, and A7, as indicated. The two dotted vertical lines show the minimum and maximum speed of the meridional circulation in the chosen latitude range of 40° – 70° .

because both transport mechanisms (diffusion and MC) will work in concert. However, we find the opposite; cases with higher diffusion have slower poleward migration speed (Table 7.1).

The broad shape of the curve in Fig. 7.14 for Case A1 reflects the general tendency for high levels of diffusion to smooth out the field. The width of the streams is broad, so a range of V_p values will give similar correlation coefficients. However, there is a clear peak at about 11.6 m s^{-1} that is substantially slower than the corresponding values of 19 – 20 m s^{-1} for the less diffusive Cases A5, A7 and A8. Furthermore, this migration speed is substantially slower than the meridional circulation speed (dashed lines), indicating that the presence of strong diffusion inhibits the poleward transport.

This result is akin to that discussed at the end of Section 7.4 with regard to the cycle period. The higher value of diffusion implies a lower effective magnetic Reynolds number for flux transport near the surface. For a velocity scale $U_{mc} \sim 20 \text{ m s}^{-1}$ at the surface and $L \sim \pi R/2$, a value of $\eta_{top} = 3 \times 10^{12}$ yields $Rm \sim 73$. At this value of Rm , the magnetic field can slip

through the plasma, violating Alfvén's theorem and rendering the poleward advection by the meridional flow less effective.

The suppression of poleward transport by downward turbulent diffusion is an effect that is not seen in 2D SFT models. In 2D SFT models, once the dipole has started building up, there is a pole-to-equator downgradient in B_r at high latitude with which is associated an equatorward diffusive flux, which clearly opposes poleward transport by the meridional flow. But the suppression of poleward transport by the downward turbulent diffusion depends on the radial structure of the radial field, so the radial dimension is needed to capture it. While the surface meridional flow acts to advect flux poleward, the subsurface field lags behind, resisting this advection. As the diffusion is decreased, the migration rate approaches the rate associated with advection by the meridional flow.

This result was previously demonstrated for axisymmetric fields by [Guerrero et al. \(2012\)](#) using 1D (latitude) and 2D (latitude, radius) advection-diffusion models for $\langle B_r \rangle$. They showed that the 1D surface transport model produced poleward flux migration at the rate of the meridional flow, regardless of the value of η_{top} . However, in the 2D model, the poleward migration rate was systematically slower than the meridional flow of the plasma and the discrepancy increased with increasing η_{top} . This is consistent with the parameter study of [Baumann et al. \(2004\)](#) who considered the effects of varying diffusion on 2D SFT models. Close scrutiny of their Figure 6 reveals that the trailing polarity flux from mid-latitude BMRs begins to erode the pre-existing polar fields earlier in the cycle when the diffusion is large. However, the timing of the polar field reversal is insensitive to η_{top} . This is consistent with the idea that flux migrates poleward at a mean rate determined by the meridional flow but it also spreads, so that the leading edge of the flux migration reaches the poles sooner when the diffusion is large.

In some ways, solar observations appear to favor relatively high diffusion, as in Case A1. The observed poleward migration speed of magnetic flux is about 10 m s^{-1} ([Hathaway & Rightmire, 2010](#); [Howard & LaBonte, 1981](#); [Topka et al., 1982](#)), which is only about 60-70% of the meridional flow speed ([Ulrich, 2010](#)). Furthermore, many 2D SFT models report optimal results when η_{top} is on the order of $2-6 \times 10^{12} \text{ cm}^2 \text{ s}^{-1}$ ([Jiang et al., 2010](#); [Jiang et al., 2014a](#); [Lemerle et al., 2015](#); [Wang et al., 1989b](#)). This latter value is justified by estimates of the diffusion rate from solar observations ([Abramenko et al., 2011](#); [Mosher, 1977](#); [Schrijver et al., 1996b](#); [Topka et al., 1982](#)).

The correlation curve in Figure 7.14 for our convective Case C1 is suggestive of a high-diffusion case. It is widely spread out and the peak value of 20.1 m s^{-1} is slower than low-diffusive cases such as A7. However, the correlation coefficient is significantly lower than in any of the diffusive cases and the characteristic migration speed is notably faster than

comparable cases such as Case A1 (11.6 m s^{-1}). Furthermore, despite the higher migration speed, Case C1 has the same period as Case A1. How can these features be explained?

The higher poleward migration speed in Case C1 relative to Case A1 can be attributed to the lower value of the diffusion coefficient, η_{top} . Though the convection enhances the horizontal transport of B_r , we have neglected the vertical convective flow component (Sec. 7.5.1) so the vertical flux transport occurs only through the parameterized turbulent diffusion. As described earlier in this section, inefficient vertical transport allows the surface flux to be advected poleward at a speed comparable to the meridional flow speed. This is also consistent with Case C3, which has a lower value of η_{top} than Case C1 and a slightly higher migration speed (Table 7.1).

The broad profile of the correlation curve for Case C1 in Fig. 7.14 reflects the efficient horizontal transport. As in Cases A1 and A2, the poleward streams are broad and diffuse, giving similar correlation coefficients for a range of tracking speeds. The low value of the correlation coefficient (< 0.55) reflects the presence of residual mixed polarity from both leading and trailing spots, as we will discuss further in Section 7.6.3. We also address the cycle period of Case C1 in Section 7.6.3, which is linked to the issue of mixed polarity and dynamo efficiency.

7.6.3 Dynamo Efficiency

As in any hydromagnetic dynamo, the field strengths achieved in our simulations are determined by a balance between magnetic field generation, nonlinear saturation, and ohmic diffusion. In our model, the ohmic diffusion operates through the turbulent diffusivity η which is varied by altering its value in the upper CZ, η_{top} . All simulations have the same nonlinear saturation mechanism, as expressed in eq. (7.3), the same mean flows, and the same parameters for the flux emergence algorithm, SpotMaker, as discussed in Section 7.2. So, one would expect simulations with lower diffusion to achieve higher field strengths. And, this is indeed the trend seen for Cases A1-A8 in Table 7.1.

Case C1 also falls within this general picture. The mean field strengths achieved here are similar to Case A4 (Table 7.1), which has a comparable value of η_{top} . Thus, convection can transport fields, as demonstrated by the diffuse appearance of Fig. 7.13a compared to Fig. 7.13d and the broad profile of the correlation curve in Fig. 7.14, but it does not greatly enhance the ohmic dissipation. Although Case C1 resembles Case A1 in other respects (see Sections 7.5 and 7.6.2), its efficiency (as measured by the strength of the mean fields) is more comparable to Case A4.

The tendency for the convection to disperse fields without dissipating them is also reflected in the lower magnetic energy in the non-axisymmetric field component in Case C1 (2.29 kG) relative to Case A4 (4.47 kG). This aspect of turbulent diffusion was emphasized in a series

of papers by [Piddington \(1975a,b, 1981\)](#). He argued that turbulent diffusion may not be good representation of merging and cancellation of fields, possibly over-estimating the cancellation rate by as much as $0.3 R_m$ ([Piddington, 1981](#)).

In the context of our simulations, this implies that both polarities present in a particular BMR will be dispersed by convective motions, with little cancellation. The mixed polarity in Case C1 is particularly apparent at the poles. As mentioned in Section 7.5.2, the polar regions are surrounded by a region of opposite polarity formed from leading flux that has been advected poleward along with the trailing flux. The low value of η_{top} implies a small ohmic dissipation scale; flux elements must come into close proximity in order to cancel. So, the polar field strength in Case C1 (Fig. 7.12b) is about a factor of three higher than in Case A1 (Fig. 7.6b; as is the mean poloidal field—see Table 7.1), and this in turn promotes the generation of strong toroidal fields.

However, when the flux in Case C1 is concentrated at the poles, it does eventually cancel. This may explain why the cycle period in Case C1 (13.3 yrs) is less than in Case A4 (15.1 yrs) even though they have similar values of η_{top} . In particular, the enhanced transport of mixed polarity flux to the poles by the convective motions leads to faster polar field reversals. Thus, the similarity between the cycle periods in Cases C1 and A1 may be fortuitous. The former may be shorter than in Case A4 because of the enhanced horizontal transport by convective motions while the latter may be shorter than in Case A4 because of higher vertical diffusion (see Section 7.6.2).

In summary, a turbulent diffusion coefficient of $\sim 3 \times 10^{12} \text{ cm}^2 \text{ s}^{-1}$ as in Case A1 adequately captures the surface flux transport in Case C1 but it does not adequately capture the dissipation of magnetic energy. Approximating convective transport with a turbulent diffusion will likely have an adverse effect on the dynamo efficiency, producing artificially weak mean fields.

7.7 Summary and Conclusion

Turbulent transport of vertical magnetic flux by near-surface convective motions is an essential component of BL dynamo models. In particular, it plays an important role in generating the polar fields that are the seed for the next cycle ([Choudhuri et al., 2007](#)). This process is captured with high fidelity by the AFT Surface Flux Transport (SFT) model, which simulates the advection of vertical magnetic flux by a horizontal flow field that is based on the observed convective power spectrum in the solar photosphere ([Ugarte-Urra et al., 2015](#); [Upton & Hathaway, 2014b,c](#)). In this study we have taken a substantial step forward in the unification of BL dynamo models and SFT models by presenting the first BL dynamo model that incorporates a realistic photospheric convection spectrum.

Our 3D BL dynamo model, STABLE, uses the same surface flow field as AFT, though unlike AFT, ours is independent of time. The generalization to an evolving field as used by AFT is straightforward and will be implemented in future work. In our initial implementation, we extrapolated this surface flow field downward based on mass conservation, producing a vigorous 3D convective flow that permeated the upper portion of the convection zone (Sec. 7.3.2). However, we quickly found that this caused problems for our kinematic framework. In particular, we found that this 3D convective flow field is an efficient small-scale dynamo, producing a chaotic field component that grew exponentially, overwhelming the cyclic field component (Sec. 7.5.1). Note that our implemented convective flow is non-helical, so there is no turbulent α effect, but it is capable of generating small scale fields by stretching and shearing of the vertical fields on the surface. One could in principle suppress this by increasing η_{top} until the effective value of the magnetic Reynolds number is subcritical to dynamo action. However, achieving $R_m \sim 50$ would require a value of η_{top} of about $1.7 \times 10^{12} \text{ cm}^2 \text{ s}^{-1}$, which is comparable to the estimate of convective transport from photospheric observations (see Sec. 7.1). Since our objective is to *replace* turbulent diffusion with a more realistic depiction of convective transport, such a large value of η_{top} is undesirable.

Instead we chose to suppress small-scale dynamo action by only implementing the horizontal convective flow field at the surface, abandoning our subsurface extrapolation. So, the link to AFT is even stronger than in our initial implementation. Since this horizontal flow does not capture vertical transport, we did keep a background value of the turbulent diffusion of $\eta_{top} = 5 \times 10^{11} \text{ cm}^2 \text{ s}^{-1}$ in the upper layers of the convection zone ($r > 0.9R$), in addition to the explicit convective motions. Without this, we found that the horizontal transport by the 2D surface convection was insufficient to establish dipolar parity.

Through this approach we were able to achieve viable, cyclic, solar-like dynamo models. The general appearance and behavior of these models is similar to non-convective cases with a surface diffusion $\eta_{top} \sim 3 \times 10^{12} \text{ cm}^2 \text{ s}^{-1}$ (Case A1; Secs. 7.5.2, 7.6.2). This is demonstrated in particular by the flat profile of the correlation function for Case C1 shown in Figure 7.14. This value of η_{top} is comparable to the range of $2\text{--}6 \times 10^{12} \text{ cm}^2 \text{ s}^{-1}$ that is estimated from solar observations and that is often used in SFT models (Abramenko et al., 2011; Jiang et al., 2010; Jiang et al., 2014a; Lemerle et al., 2015; Mosher, 1977; Schrijver et al., 1996b; Topka et al., 1982; Wang et al., 1989b).

Treating the BL mechanism with explicit convective transport (Case C1) gives us more realistic surface flux transport in comparison to the case with an equivalent surface diffusion (Case A1). The BMRs that emerge at active latitudes are fragmented and dispersed by the convective flows, with less flux cancellation. However, Case C1 does exhibit a band of opposite polarity surrounding the polar cap that is not seen in solar observations, at least not to this

extent (Fig. 7.12a). This mixed polarity in the polar region is not seen in the case with turbulent diffusion. We attribute its existence to residual leading flux that is advected poleward along with the trailing flux.

In our models, the speed at which residual poloidal flux from BMRs migrates to the poles is determined mainly by the vertical diffusion, η_{top} . For small values of the η_{top} ($\lesssim 8 \times 10^{11}$ cm s⁻¹), this poleward migration speed approaches the meridional flow speed. However, for high vertical diffusion (efficient mixing), the migration speed is slower, as surface flux transport is impeded by the subsurface field that is being “dragged along”.

Several aspects of Case C1 highlight the limitations of parameterizing convective transport as a turbulent diffusion. First, the spatial structure of the turbulent emf does not in general take the form of a downgradient diffusive flux (Sec. 7.6.1). We attribute this to the tendency of convective flows to advect vertical flux into “downflow lanes”, or more precisely, regions of horizontal convergence, before dispersing it. The diffusive character of the convective transport only manifests itself on scales larger than that of the convection ($\gtrsim 34$ Mm), which is almost an order of magnitude larger than the horizontal grid spacing (~ 4.3 Mm).

A second limitation of the turbulent diffusion parameterization is an over-estimate of the ohmic dissipation (Sec. 7.6.3). The mean fields in the convective Case C1 are about a factor of three stronger than in Case A1, which has $\eta_{top} = 3 \times 10^{12}$ cm² s⁻¹ and the same cycle period. This is particularly true for the peak polar fields, which are an important factor in determining the strength of the following cycle. This over-estimate of the ohmic dissipation, or alternatively, an under-estimate of the dynamo efficiency, cannot be addressed with traditional SFT models; since these are not dynamo models, the field strengths are not regulated by the same interplay between field generation, nonlinear saturation, and ohmic dissipation. Thus, it is a new result that has not been identified in previous studies.

In conclusion, the use of explicit convective motions is a promising way to improve the fidelity of BL dynamo models that have the capability to model 3D flows. However, the main challenge to producing viable models of the solar cycle with this approach is to properly handle the small-scale dynamo action that will likely ensue. This may ultimately require a more consistent MHD formulation that takes into account flow suppression by Lorentz force feedbacks.

*“Let me not pray to be sheltered from dangers, but to be fearless in facing them.
Let me not beg for the stilling of my pain, but for the heart to conquer it.”*

–Rabindranath Tagore, Geetabitan

8

Concluding Remarks

The results presented in this thesis are broadly classified into two parts. In the first part of the thesis, we explain various important issues regarding the treatment of magnetic buoyancy, irregularities of the solar cycle, the effect of the different spatial structure of meridional flow on the dynamo and how dynamo generated fields would affect the meridional flow using 2D axisymmetric Flux Transport Dynamo model. In the second part, the build up of polar fields from the decay of sunspots and a proper treatment of the Babcock-Leighton process by invoking realistic convective flows are presented using 3D Flux Transport Dynamo model.

In 2D axisymmetric Flux Transport Dynamo models, magnetic buoyancy has been treated mainly in two ways—a non-local method and a local method. In **Chapter 2**, we have analyzed the advantages and disadvantages of both the methods. We find that none of them are satisfactory to depict the correct picture of magnetic buoyancy because magnetic buoyancy is an inherently 3D process. Unless we go to the 3D framework of Flux Transport Dynamo models, we have to treat the magnetic buoyancy in such simplistic way. We find that the non-local treatment of magnetic buoyancy is very robust for a large span of parameter space but it does not take into account the depletion of flux from the bottom of the convection zone which has a significant importance in irregularity study of the solar cycle. The local treatment of magnetic buoyancy includes the flux depletion from the bottom of the convection zone and treats the magnetic

buoyancy much realistically than the non-local treatment. But this local treatment of magnetic buoyancy is not so robust. We also pointed out that the long-standing issue about the appearance of sunspots in the low-latitudes needs to be studied carefully.

In **Chapter 3**, we have studied various irregularities of the solar cycle during its decaying phase. We have reported that the decay rate of the cycle is strongly correlated with the amplitude of the same cycle as well as the amplitude of the next cycle from different sunspot proxies like sunspot number, sunspot area, and 10.7 cm radio flux data. We explain these correlations from flux transport dynamo models. We find that the correlations can only be reproduced if we introduce stochastic fluctuations in the meridional circulations. We have also reproduced most of the correlations found in ascending and descending phase of the solar cycle from century long sunspot area data (Mandal et al., 2017a) from Kodaikanal Observatory, India which are in great agreement with the correlations found earlier from Greenwich sunspots data.

With the recent development in Helioseismology, plenty of results have come out about the spatial structure of meridional circulation (Jackiewicz et al., 2015a; Rajaguru & Antia, 2015; Schad et al., 2013; Zhao et al., 2013). Some helioseismology groups (Zhao et al., 2013) reported that the meridional circulation have a double cell structure in solar convection zone and some groups (Jackiewicz et al., 2015a; Schad et al., 2013) reported a multi-cellular structure of meridional circulation in the convection zone. By probing the supergranular motion Hathaway (2012b) estimated that the meridional flow has an equatorward return flow in the upper convection zone 70 Mm below the surface. In view of the above observed results, we have discussed in **Chapter 4** what will happen to Flux Transport Dynamo model if we consider other structure of meridional circulation instead of a single cell meridional circulation encompassing whole convection zone. We find that our dynamo model works perfectly fine as long as there is an equatorward propagation in the bottom of the convection zone. Our model also works with shallow meridional circulation as found by Hathaway (2012b), if we consider the latitudinal pumping in our model (Section 4.6).

The temporal variation of meridional circulation on the surface is also observed from various measurement techniques. Chou & Dai (2001) first observed a variation with the solar cycle from their helioseismic measurements. By measuring the magnetic elements on the surface of the Sun Hathaway & Rightmire (2010) found a variation up to 5 m s^{-1} for the solar cycle 23. Recently Komm et al. (2015) have analyzed MDI and HMI dopplergram data and reported a solar cyclic variation with detail latitudinal dependence. In **Chapter 5** we have developed a theoretical model coupled with the equations of the dynamo model to explain this variation of the meridional circulation with the solar cycle. In this prescribed model, we have considered the Lorentz force feedback on the meridional flow as a perturbation over the steady flows. Considering the magnetic fields have a small effect on the thermodynamics of the

Sun, we have decoupled the equation of the perturbed vorticity corresponding to the perturbed meridional flow, from the unperturbed vorticity and solve it simultaneously along with the dynamo equations. We obtained a good match with the observation with a magnetic Prandtl number $P_m = 1$. Since it is difficult to drive a flow below the bottom of the convection zone, we take perturbed vorticity $w_1 = 0$ at $r = 0.70R$.

In the second part of the thesis which includes **Chapter 6** and **Chapter 7**, we have studied some of the aspects of solar magnetic field generation process using 3D dynamo model that were not possible to study earlier using axisymmetric 2D Flux Transport dynamo models. We have used the 3D dynamo model developed by Mark Miesch ([Miesch & Dikpati, 2014](#); [Miesch & Teweldebirhan, 2016](#)) and study how polar fields build up from the decay of sunspots more realistically in **Chapter 6**. We first reproduce the observed butterfly diagram and periodic solution considering higher diffusivity value than reported in earlier studies ([Miesch & Dikpati, 2014](#); [Miesch & Teweldebirhan, 2016](#)) to consider it as a reference model. Then we study the build up of the polar fields by putting a single sunspot pair in one hemisphere and two sunspot pairs in both the hemispheres using this reference model. The build up of the polar field from the decay of sunspots is studied earlier using Surface Flux Transport model ([Baumann et al., 2004, 2006](#); [Cameron et al., 2010](#); [Schrijver et al., 2002](#); [Wang et al., 1989d](#); [van Ballegoijen et al., 1998](#)) which solve only radial component of the induction equation on the surface of the Sun (θ — ϕ plane). But these 2D SFT models have some inherent limitation for not considering the 3D vectorial nature of the magnetic fields and subsurface processes. We have shown that not considering the vectorial nature and subsurface process has an important effect on the development of the polar fields. We have also studied the effect of a few large sunspot pairs violating Hale's law on the strength of the polar field in this Chapter. We find that such anti-Hale sunspot pairs do produce some effect on the polar field, if they appear at higher latitudes during the mid-phase of the solar cycle—but the effect is not dramatic.

In **Chapter 7**, we have incorporated observed surface convective flows directly in our 3D dynamo model. As we know that the dispersal and migration of the sunspots fields in Babcock-Leighton process are mostly done by the convective flows i.e. by supergranulation and granulation. In most of the SFT and FTD models, dispersal and migration of sunspot fields are modeled as a random walk process with an effective diffusion coefficient ([DeVore et al., 1984](#); [Leighton, 1964](#)). We have directly incorporated the observed convective flows on the surface of the Sun in our model to capture the B-L process much realistically than before instead of modeling them as a turbulent diffusion. While incorporating them in our 3D model, we make the convective flows to be non-helical in order to avoid the generation of the fields by helical turbulent α effect and extrapolated them radially inwards from the surface guided by convective simulations. Though our incorporated convective flows are non-helical, we find

that they are capable of generating small scale fields by stretching the sunspot fields. Unless we apply a higher hyperdiffusion and confine the convective motion on the surface layers only, the exponential growth of small scale fields can disrupt the operation of large scale dynamo. The results obtained by confining the convective flows on the surface only are generally in good agreement with the observed surface flux evolution and with non-convective models that have a turbulent diffusivity on the order of $3 \times 10^{12} \text{ cm}^2 \text{ s}^{-1}$ ($300 \text{ km}^2 \text{ s}^{-1}$). However, we find that the use of a turbulent diffusivity underestimates the dynamo efficiency, producing weaker mean fields than in the convective models. Also, the convective models exhibit mixed polarity bands in the polar regions that have no counterpart in solar observations. Also, the explicitly computed turbulent electromotive force (emf) bears little resemblance to a diffusive flux. We also find that the poleward migration speed of poloidal flux is determined mainly by the meridional flow and the vertical diffusion.

Future work

The works that we have performed in this thesis, have initiated many interesting possibilities for doing further investigations.

The various works presented throughout the thesis starting from Chapter 2 are performed at different times and the turbulent diffusivity profiles used in those studies are not identical. Since the nature of turbulent diffusivity is not known from the first principle, we have this freedom to choose various profile of the turbulent diffusivity. But what we have learned from the different studies in this thesis is various results (e.g., parity, irregular properties of the solar cycle) are sensitive to the chosen value of turbulent diffusivity in the convection zone. Therefore, our aim would be to **study the turbulent transport co-efficients in the solar convection zone from 3D magnetoconvection simulations** that help to understand transport coefficient much better than what mixing length theory estimates, and combine them with the mean-field dynamo simulations to better understand the origin of solar magnetic field and its cycle.

We would like to **develop a good predictive model for solar cycle 25** using flux transport dynamo model. As we know that the main source of irregularities of the solar cycle is the fluctuation in the poloidal field and fluctuation in the meridional circulation. The measurement of the polar field during the solar minimum gives us an estimate of the value of the polar field which is going to determine the strength of the next cycle. But we don't have any idea about the behavior of the meridional circulation in the next cycle which is also an important parameter to determine the strength of the cycle (Yeates et al., 2008). As discussed in Chapter 3, we find an idea to model the meridional circulation of the next cycle using the information available in the present cycle. Based on that we want to develop a model which would take the information of

polar field as well as the meridional circulation to predict the amplitude of the next cycle with more accuracy.

As discussed in Chapter 5, we find that the perturbed amplitude of the meridional circulation due to Lorentz force feedback near the bottom of the convection zone is not negligible in comparison to the unperturbed meridional flow there. Hence, the back-reaction due to the Lorentz force on the velocity fields is really important which was not considered in the most of the Flux Transport Dynamo models. Therefore, **a non-kinematic Flux Transport Dynamo models are necessary to develop** which would include the back-reaction due to the Lorentz force on the velocity fields.

The development of the 3D Flux Transport Dynamo models opens up many opportunities to study the solar magnetic fields with much more detail. As we know that sunspots appear mostly on the higher latitudes during the beginning of the solar cycle and eventually migrate towards equator with time as cycle progresses. Similar to these active latitudes, sunspots mostly appear in two longitudes of the Sun separated by 180° which is known as the active longitudes of the Sun (Mandal et al., 2017b; Usoskin et al., 2005). It is believed that the non-axisymmetric component of the solar magnetic field is responsible for the persistence of the active longitudes. Studying active longitudes of the Sun was not possible by the previous 2D axisymmetric models. But now, we can study their existence by non-axisymmetric 3D flux transport dynamo models. So our next aim would be to **study the persistence of the active longitudes of the Sun using 3D dynamo models**.

As we have explained in the Chapter 7, the Babcock-Leighton Mechanism of the Sun can be modeled much more realistically by invoking direct observed convective flows. But we have used a time independent flow for the results shown in the Chapter 7. Next **a time dependent convective flows can be invoked** in our 3D model to reproduce the solar photospheric magnetic fields that would be much closer to observations. Reproducing the solar photosphere magnetic field is important because it sets the boundary condition for the coronal and heliospheric magnetic fields. So if we can reproduce the solar photospheric magnetic fields, then we can extrapolate it to get some estimate about the coronal magnetic fields structures. Hence, theoretically, we can couple the coronal magnetic fields with dynamo generated fields in the interior of the Sun. In view of current Indian mission *Aditya-L1* for the Sun, which is planning to measure the coronal magnetic fields, the 3D model of dynamo would be very relevant to couple the interior of the Sun with the corona.

References

- Abramenko V. I., et al., 2011, *ApJ*, 743, 133 (9pp)
- Antia H. M., 2005, *Journal of Astrophysics and Astronomy*, 26, 161
- Antia H. M., Basu S., 2000, *ApJ*, 541, 442
- Augustson K., Brun A. S., Miesch M., Toomre J., 2015, *ApJ*, 809, 149
- Babcock H. W., 1953, *ApJ*, 118, 387
- Babcock H. W., 1961, *ApJ*, 133, 572
- Babcock H. W., Babcock H. D., 1955, *ApJ*, 121, 349
- Basu S., Antia H. M., 2000, *Sol. Phys.*, 192, 469
- Basu S., Antia H. M., 2010, *ApJ*, 717, 488
- Baumann I., Schmitt D., Schüssler M., Solanki S. K., 2004, *A & A*, 426, 1075
- Baumann I., Schmitt D., Schüssler M., 2006, *A & A*, 446, 307
- Beaudoin P., Charbonneau P., Racine E., Smolarkiewicz P. K., 2013, *Sol. Phys.*, 282, 335
- Beck J. G., Gizon L., Duvall Jr. T. L., 2002, *ApJL*, 575, L47
- Bekki Y., Yokoyama T., 2017, *ApJ*, 835, 9
- Belvedere G., Kuzanyan K. M., Sokoloff D., 2000, *MNRAS*, 315, 778
- Bonanno A., Elstner D., Belvedere G., Rüdiger G., 2006, *Memorie della Societa Astronomica Italiana Supplementi*, 9, 71
- Brandenburg A., 2001, *ApJ*, 550, 824

- Brandenburg A., Jennings R. L., Nordlund Å., Rieutord M., Stein R. F., Tuominen I., 1996, [Journal of Fluid Mechanics](#), 306, 325
- Braun D. C., Fan Y., 1998a, [ApJL](#), 508, L105
- Braun D. C., Fan Y., 1998b, [ApJL](#), 508, L105
- Brown G. M., 1976, [MNRAS](#), 174, 185
- Brown B. P., Browning M. K., Brun A. S., Miesch M. S., Toomre J., 2010, [ApJ](#), 711, 424
- Brown B. P., Miesch M. S., Browning M. K., Brun A. S., Toomre J., 2011, [ApJ](#), 731, 69 (19pp)
- Brun A. S., Miesch M. S., Toomre J., 2004, [ApJ](#), 614, 1073
- Bushby P. J., 2006, [MNRAS](#), 371, 772
- Cadavid A. C., Lawrence J. K., Ruzmaikin A. A., 1999, [ApJ](#), 521, 844
- Caligari P., Moreno-Insertis F., Schüssler M., 1995, [ApJ](#), 441, 886
- Cameron R., Schüssler M., 2007, [ApJ](#), 659, 801
- Cameron R., Schüssler M., 2008, [ApJ](#), 685, 1291
- Cameron R. H., Schüssler M., 2010, [ApJ](#), 720, 1030
- Cameron R., Schüssler M., 2015, [Science](#), 347, 1333
- Cameron R. H., Jiang J., Schmitt D., Schüssler M., 2010, [ApJ](#), 719, 264
- Cameron R. H., Schmitt D., Jiang J., Işık E., 2012, [A & A](#), 542, A127
- Cameron R. H., Dasi-Espuig M., Jiang J., Işık E., Schmitt D., Schüssler M., 2013, [A & A](#), 557, A141
- Cattaneo F., 1999, [ApJL](#), 515, L39
- Cattaneo F., Brummell N. H., Cline K. S., 2006, [MNRAS](#), 365, 727
- Chae J., Litvinenko Y. E., Sakurai T., 2008, [ApJ](#), 683, 1153
- Chakraborty S., Choudhuri A. R., Chatterjee P., 2009, [Physical Review Letters](#), 102, 041102
- Chandrasekhar S., 1952, [The London, Edinburgh, and Dublin Philosophical Magazine and Journal of Science](#), 43, 501

- Charbonneau P., 2010, *Living Rev. Solar Phys.*, 7, 3
- Charbonneau P., 2013, *Solar and Stellar Dynamos: Saas-Fee Advanced Course 39 Swiss Society for Astrophysics and Astronomy, Saas-Fee Advanced Courses, Volume 39.*~ISBN 978-3-642-32092-7.~Springer-Verlag Berlin Heidelberg, 2013, 39
- Charbonneau P., 2014, *Anu Rev. in Astronomy and Astrophysics.*, 52, 251
- Charbonneau P., Dikpati M., 2000, *ApJ*, 543, 1027
- Charbonneau P., St-Jean C., Zacharias P., 2005, *ApJ*, 619, 613
- Chatterjee P., Choudhuri A. R., 2006, *Sol. Phys.*, 239, 29
- Chatterjee P., Nandy D., Choudhuri A. R., 2004, *A & A*, 427, 1019
- Chou D.-Y., Dai D.-C., 2001, *ApJL*, 559, L175
- Choudhuri A. R., 1989, *Sol. Phys.*, 123, 217
- Choudhuri A. R., 1990, *A & A*, 239, 335
- Choudhuri A. R., 1992, *A & A*, 253, 277
- Choudhuri A. R., 1998, *The physics of fluids and plasmas : an introduction for astrophysicists* (Cambridge: Cambridge University Press)
- Choudhuri A. R., 2003, *Sol. Phys.*, 215, 31
- Choudhuri A. R., 2008, *Advances in Space Research*, 41, 868
- Choudhuri A. R., 2011a, in *Astronomical Society of India Conference series.* ([arXiv:1111.2443](https://arxiv.org/abs/1111.2443))
- Choudhuri A. R., 2011b, *Pramana*, 77, 77
- Choudhuri A. R., 2014a, *Indian Journal of Physics*, 88, 877
- Choudhuri A. R., 2014b, *Indian Journal of Physics*, 88, 877
- Choudhuri A. R., 2015, *Journal of Astrophysics and Astronomy*, 36, 5
- Choudhuri A. R., 2017, *Science China Physics, Mechanics, and Astronomy*, 60, 413
- Choudhuri A. R., D'Silva S., 1990, *A & A*, 239, 326

- Choudhuri A. R., Dikpati M., 1999, *Sol. Phys.*, 184, 61
- Choudhuri A. R., Gilman P. A., 1987, *ApJ*, 316, 788
- Choudhuri A. R., Hazra G., 2016, *Advances in Space Research*
- Choudhuri A. R., Karak B. B., 2009, *Research in Astronomy and Astrophysics*, 9, 953
- Choudhuri A. R., Karak B. B., 2012, *Physical Review Letters*, 109, 171103
- Choudhuri A. R., Schüssler M., Dikpati M., 1995, *A & A*, 303, L29
- Choudhuri A. R., Chatterjee P., Nandy D., 2004, *ApJL*, 615, L57
- Choudhuri A. R., Nandy D., Chatterjee P., 2005, *A & A*, 437, 703
- Choudhuri A. R., Chatterjee P., Jiang J., 2007, *Physical Review Letters*, 98, 131103
- Christensen-Dalsgaard J., 2002, *Reviews of Modern Physics*, 74, 1073
- Christensen-Dalsgaard J., et al., 1996, *Science*, 272, 1286
- Clette F., Svalgaard L., Vaquero J. M., Cliver E. W., 2014, *Space Sci. Rev.*, 186, 35
- Corbard T., Thompson M. J., 2002, *Sol. Phys.*, 205, 211
- Cossette J.-F., Rast M. P., 2016, *ApJL*, 829, L17 (5pp)
- Covas E., Tavakol R., Moss D., Tworkowski A., 2000, *A & A*, 360, L21
- Cowling T. G., 1933, *MNRAS*, 94, 39
- D'Silva S. Z., Choudhuri A. R., 1991, *Sol. Phys.*, 136, 201
- D'Silva S., Choudhuri A. R., 1993, *A & A*, 272, 621
- Dasi-Espuig M., Solanki S. K., Krivova N. A., Cameron R., Peñuela T., 2010a, *A & A*, 518, A7
- Dasi-Espuig M., Solanki S. K., Krivova N. A., Cameron R., Peñuela T., 2010b, *A&A*, 518, A7 (10pp)
- DeVore C. R., Boris J. P., Sheeley N. R., 1984, *Solar Phys.*, 92, 1
- Dikpati M., 2014, *Geophysical and Astrophysical Fluid Dynamics*, 108, 222
- Dikpati M., Charbonneau P., 1999, *ApJ*, 518, 508

- Dikpati M., Choudhuri A. R., 1994, *A & A*, [291, 975](#)
- Dikpati M., Choudhuri A. R., 1995, *Sol. Phys.*, [161, 9](#)
- Dikpati M., Gilman P. A., 2006, *ApJ*, [649, 498](#)
- Dikpati M., Gilman P. A., 2009, *Space Sci. Rev.*, [144, 67](#)
- Dikpati M., Corbard T., Thompson M. J., Gilman P. A., 2002, *ApJL*, [575, L41](#)
- Dikpati M., de Toma G., Gilman P. A., Arge C. N., White O. R., 2004, *ApJ*, [601, 1136](#)
- Dikpati M., Gilman P. A., de Toma G., 2008, *ApJL*, [673, L99](#)
- Durney B. R., 1995, *Sol. Phys.*, [160, 213](#)
- Durney B. R., 1996, *Sol. Phys.*, [169, 1](#)
- Durney B. R., 1997, *ApJ*, [486, 1065](#)
- Durney B. R., 2000, *Sol. Phys.*, [196, 1](#)
- Eddy J. A., 1976, *Science*, [192, 1189](#)
- Fan Y., 2009, *Living Reviews in Solar Physics*, [6, 4](#)
- Fan Y., Fang F., 2014, *ApJ*, [789, 35 \(13pp\)](#)
- Fan Y., Fisher G. H., Deluca E. E., 1993, *ApJ*, [405, 390](#)
- Featherstone N. A., Miesch M. S., 2015, *ApJ*, [804, 67](#)
- Garaud P., Brummell N. H., 2008, *ApJ*, [674, 498](#)
- Ghizaru M., Charbonneau P., Smolarkiewicz P. K., 2010, *ApJL*, [715, L133](#)
- Gibson S. E., et al., 1999, *ApJ*, [520, 871](#)
- Giles P. M., Duvall T. L., Scherrer P. H., Bogart R. S., 1997, *Nature*, [390, 52](#)
- Gilman P. A., 1983, *ApJ Suppl.*, [53, 243](#)
- Gilman P. A., Miesch M. S., 2004, *ApJ*, [611, 568](#)
- Gilman P. A., Miller J., 1981, *ApJ Suppl.*, [46, 211](#)
- Gizon L., Rempel M., 2008, *Sol. Phys.*, [251, 241](#)

- Gizon L., Birch A. C., Spruit H. C., 2010, *Ann. Rev. Astron. Astrophys.*, 48, 289
- Glatzmaier G. A., 1984, *J. Comp. Phys.*, 55, 461
- Glatzmaier G. A., 1985, *ApJ*, 291, 300
- Goel A., Choudhuri A. R., 2009, [Research in Astronomy and Astrophysics](#), 9, 115
- Greer B. J., Hindman B. W., Featherstone N. A., Toomre J., 2015, *ApJ*, 803, L17 (5pp)
- Gruzinov A. V., Diamond P. H., 1994, *Phys. Rev. Lett.*, 72, 1651
- Guerrero G. A., Muñoz J. D., 2004, [MNRAS](#), 350, 317
- Guerrero G., de Gouveia Dal Pino E. M., 2007, [A & A](#), 464, 341
- Guerrero G., de Gouveia Dal Pino E. M., 2008, [A & A](#), 485, 267
- Guerrero G., Rheinhardt M., Brandenburg A., Dikpati M., 2012, *MNRAS*, 420, L1
- Gupta S. S., Sivaraman K. R., Howard R. F., 1999, [Sol. Phys.](#), 188, 225
- Hale G. E., 1909, [Pub. Astron. Soc. Pac.](#), 21, 205
- Hale G. E., Ellerman F., Nicholson S. B., Joy A. H., 1919, *ApJ*, 49, 153
- Hanasoge S. M., Duvall T., DeRosa M. L., 2010, *ApJL*, 712, L98
- Hanasoge S. M., Gizon L., Sreenivasan K. R., 2016, *Ann. Rev. Fluid Mech.*, 48, 191
- Hasan S. S., Mallik D. C. V., Bagare S. P., Rajaguru S. P., 2010, [Astrophysics and Space Science Proceedings](#), 19, 12
- Hathaway D. H., 2010, [Living Reviews in Solar Physics](#), 7
- Hathaway D. H., 2012a, *ApJL*, 749, L13
- Hathaway D. H., 2012b, *ApJ*, 760, 84
- Hathaway D. H., Rightmire L., 2010, *Science*, 327, 1350
- Hathaway D. H., Beck J. G., Bogart R. S., Bachmann K. T., Khatri G., Petitto J. M., Han S., Raymond J., 2000, *Solar Physics*, 193, 299
- Hathaway D. H., Wilson R. M., Reichmann E. J., 2002, [Sol. Phys.](#), 211, 357

- Hathaway D. H., Nandy D., Wilson R. M., Reichmann E. J., 2003, *ApJ*, 589, 665
- Hazra G., Choudhuri A. R., 2017, *MNRAS*, 472, 2728
- Hazra G., Miesch M. S., 2017, *ApJ*
- Hazra S., Nandy D., 2016, *ApJ*, 832, 9
- Hazra G., Karak B. B., Choudhuri A. R., 2014, *ApJ*, 782, 93
- Hazra G., Karak B. B., Banerjee D., Choudhuri A. R., 2015, *Sol. Phys.*, 290, 1851
- Hazra G., Choudhuri A. R., Miesch M. S., 2017, *ApJ*, 835, 39
- Hotta H., Yokoyama T., 2010, *ApJL*, 714, L308
- Hotta H., Rempel M., Yokoyama T., 2016, *Science*, 351, 1427
- Howard R., LaBonte B. J., 1981, *Solar Phys.*, 74, 131
- Howard R., Labonte B. J., 1981, *Sol. Phys.*, 74, 131
- Howard R. F., Gupta S. S., Sivaraman K. R., 1999, *Sol. Phys.*, 186, 25
- Howard R. F., Sivaraman K. R., Gupta S. S., 2000, *Sol. Phys.*, 196, 333
- Jackiewicz J., Serebryanskiy A., Kholikov S., 2015a, *ApJ*, 805, 133
- Jackiewicz J., Serebryanskiy A., Kholikov S., 2015b, *ApJ*, 805, 133 (9pp)
- Jiang J., Chatterjee P., Choudhuri A. R., 2007, *MNRAS*, 381, 1527
- Jiang J., Cameron R., Schmitt D., Schüssler M., 2010, *ApJ*, 709, 301
- Jiang J., Cameron R. H., Schmitt D., Işık E., 2013, *A & A*, 553, A128
- Jiang J., Hathaway D. H., Cameron R. H., Solanki S. K., Gizon L., Upton L., 2014a, *Space Sci. Rev.*, 186, 491
- Jiang J., Cameron R. H., Schüssler M., 2014b, *ApJ*, 791, 5
- Jiang J., Cameron R. H., Schüssler M., 2015, *ApJL*, 808, L28
- Jones C. A., Boronski P., Brun A. S., Glatzmaier G. A., Gastine T., Miesch M. S., Wicht J., 2011, *Icarus*, 216, 120

- Jouve L., Brun A. S., 2007, *A & A*, 474, 239
- Kane R. P., 2008, *J. Atmos. Solar-Terr. Phys.*, 70, 1533
- Käpylä P. J., Korpi M. J., Ossendrijver M., Stix M., 2006, *A & A*, 455, 401
- Käpylä P., Mantere M., Brandenburg A., 2012, *ApJ*, 755, L22 (5pp)
- Käpylä P. J., Mantere M. J., Cole E., Warnecke J., Brandenburg A., 2013a, *ApJ*, 778, 41
- Käpylä P. J., Mantere M. J., Cole E., Warnecke J., Brandenburg A., 2013b, *ApJ*, 778, 41 (18pp)
- Käpylä M. J., Käpylä P. J., Olsper N., Brandenburg A., Warnecke J., Karak B. B., Pelt J., 2016, *A&A*, 589, A56 (24pp)
- Karak B. B., 2010, *ApJ*, 724, 1021
- Karak B. B., Cameron R., 2016, *ApJ*
- Karak B. B., Choudhuri A. R., 2011, *MNRAS*, 410, 1503
- Karak B. B., Choudhuri A. R., 2012, *Sol. Phys.*, 278, 137
- Karak B. B., Choudhuri A. R., 2013, *Research in Astronomy and Astrophysics*, 13, 1339
- Karak B. B., Nandy D., 2012, *ApJL*, 761, L13
- Karak B. B., Jiang J., Miesch M. S., Charbonneau P., Choudhuri A. R., 2014a, *Space Sci. Rev.*, 186, 561
- Karak B. B., Kitchatinov L. L., Choudhuri A. R., 2014b, *ApJ*, 791, 59
- Karak B. B., Rheinhardt M., Brandenburg A., Käpylä P. J., Käpylä M. J., 2014c, *ApJ*, 795, 16
- Karak B. B., Käpylä P. J., Käpylä M. J., Brandenburg A., Olsper N., Pelt J., 2015, *A & A*, 576, A26
- Kippenhahn R., 1963, *ApJ*, 137, 664
- Kitchatinov L. L., 2011, in *Astronomical Society of India Conference Series*. ([arXiv:1108.1604](https://arxiv.org/abs/1108.1604))
- Kitchatinov L. L., 2013, in *Kosovichev A. G., de Gouveia Dal Pino E., Yan Y., eds, IAU Symposium Vol. 294, Solar and Astrophysical Dynamos and Magnetic Activity*. pp 399–410 ([arXiv:1210.7041](https://arxiv.org/abs/1210.7041)), [doi:10.1017/S1743921313002834](https://doi.org/10.1017/S1743921313002834)

- Kitchatinov L. L., Olemskoy S. V., 2011a, *Astron. Lett.*, **37**, 656
- Kitchatinov L. L., Olemskoy S. V., 2011b, *MNRAS*, **411**, 1059
- Kitchatinov L. L., Olemskoy S. V., 2012, *Sol. Phys.*, **276**, 3
- Kitchatinov L. L., Ruediger G., 1995, *A & A*, **299**, 446
- Komm R., González Hernández I., Howe R., Hill F., 2015, *Sol. Phys.*, **290**, 3113
- Kosovichev A. G., 2011, in Rozelot J.-P., Neiner C., eds, *Lecture Notes in Physics*, Berlin Springer Verlag Vol. 832, *Lecture Notes in Physics*, Berlin Springer Verlag. p. 3 ([arXiv:1103.1707](https://arxiv.org/abs/1103.1707)), [doi:10.1007/978-3-642-19928-8_1](https://doi.org/10.1007/978-3-642-19928-8_1)
- Küker M., Rüdiger G., Schultz M., 2001, *A & A*, **374**, 301
- Labonte B. J., Howard R., 1982, *Sol. Phys.*, **80**, 361
- Lantos P., 2000, *Sol. Phys.*, **196**, 221
- Leighton R. B., 1964, *ApJ*, **140**, 1547
- Leighton R. B., 1969, *ApJ*, **156**, 1
- Leighton R. B., Noyes R. W., Simon G. W., 1962, *ApJ*, **135**, 474
- Lemerle A., Charbonneau P., Carignan-Dugas A., 2015, *ApJ*, **810**, 78 (18 pp)
- Longcope D., Choudhuri A. R., 2002, *Sol. Phys.*, **205**, 63
- Lopes I., Passos D., 2009, *MNRAS*, **397**, 320
- Lord J., Cameron R., Rast M., Rempel M., Roudier T., 2014, *ApJ*, **793**, 24 (11pp)
- Makarov V. I., Sivaraman K. R., 1989, *Sol. Phys.*, **119**, 35
- Makarov V. I., Tlatov A. G., 2000, *Astronomy Reports*, **44**, 759
- Makarov V. I., Fatianov M. P., Sivaraman K. R., 1983, *Sol. Phys.*, **85**, 215
- Mandal S., Hegde M., Samanta T., Hazra G., Banerjee D., Ravindra B., 2017a, *A & A*, **601**, [A106](#)
- Mandal S., Chatterjee S., Banerjee D., 2017b, *ApJ*, **835**, 62
- McClintock B. H., Norton A. A., 2013, *Solar Phys.*, **287**, 215

- Miesch M. S., 2005, Living Reviews in Solar Physics, 2
- Miesch M. S., Dikpati M., 2014, *ApJL*, 785, L8
- Miesch M. S., Teweldebirhan K., 2016, Advances in Space Research
- Miesch M. S., Toomre J., 2009, *Annual Review of Fluid Mechanics*, 41, 317
- Miesch M. S., Elliott J. R., Toomre J., Clune T. L., Glatzmaier G. A., Gilman P. A., 2000, *ApJ*, 532, 593
- Miesch M. S., Featherstone N. A., Rempel M., Trampedach R., 2012a, *ApJ*, 757, 128
- Miesch M. S., Featherstone N. A., Rempel M., Trampedach R., 2012b, *ApJ*, 757, 128 (14pp)
- Miesch M. S., Featherstone N. A., Rempel M., Trampedach R., 2012c, *ApJ*, 757, 128 (14pp)
- Moffatt H. K., 1978, Magnetic field generation in electrically conducting fluids
- Moreno-Insertis F., 1983, *A & A*, 122, 241
- Moreno-Insertis F., Schuessler M., Ferriz-Mas A., 1992, *A & A*, 264, 686
- Mosher J. M., 1977, PhD thesis, Cal. Inst. Tech.
- Muñoz-Jaramillo A., Nandy D., Martens P. C. H., Yeates A. R., 2010, *ApJL*, 720, L20
- Muñoz-Jaramillo A., Nandy D., Martens P. C. H., 2011, *ApJL*, 727, L23
- Muñoz-Jaramillo A., Sheeley N. R., Zhang J., DeLuca E. E., 2012, *ApJ*, 753, 146
- Muñoz-Jaramillo A., Dasi-Espuig M., Balmaceda L. A., DeLuca E. E., 2013, *ApJL*, 767, L25
- Nandy D., Choudhuri A. R., 2001, *ApJ*, 551, 576
- Nandy D., Choudhuri A. R., 2002, *Science*, 296, 1671
- Nelson N. J., Brown B. P., Brun A. S., Miesch M. S., Toomre J., 2013a, *Solar Phys.*, 289, 441
- Nelson N. J., Brown B. P., Brun A. S., Miesch M. S., Toomre J., 2013b, *ApJ*, 762, 73 (20pp)
- Nordlund A., Stein R. F., Asplund M., 2009, Living Reviews in Solar Physics, 6
- Noyes R. W., Hartmann L. W., Baliunas S. L., Duncan D. K., Vaughan A. H., 1984, *ApJ*, 279, 763

- O'Mara B., Miesch M. S., Featherstone N. A., Augustson K. C., 2016, *Adv. Space Res.*, 58, in press
- Odenwald S. F., Green J. L., Taylor W., 2005, *Advances in Space Research*, 38, 280
- Ogurtsov M., Lindholm M., 2011, *ISRN Astron. Astrophys.*, 2011, 3
- Ossendrijver M., 2003, *Astron. Astrophys. Rev.*, 11, 287
- Ossendrijver M., Stix M., Brandenburg A., Rüdiger G., 2002, *A & A*, 394, 735
- Owens M. J., Lockwood M., Hawkins E., Usoskin I., Jones G. S., Barnard L., Schurer A., Fasullo J., 2017, *J. Space Weather Space Clim.*, 7, A33
- Parfrey K. P., Menou K., 2007, *ApJL*, 667, L207
- Parker E. N., 1955a, *ApJ*, 121, 491
- Parker E. N., 1955b, *ApJ*, 122, 293
- Parker E. N., 1975, *ApJ*, 198, 205
- Parker E. N., 1979, *Cosmical magnetic fields: Their origin and their activity* (Oxford University Press)
- Passos D., 2012, *ApJ*, 744, 172
- Passos D., Charbonneau P., 2014, *A&A*, 568, A113 (16pp)
- Passos D., Lopes I., 2012, *MNRAS*, 422, 1709
- Passos D., Charbonneau P., Beaudoin P., 2012, *Sol. Phys.*, 279, 1
- Passos D., Charbonneau P., Miesch M., 2015, *ApJL*, 800, L18
- Passos D., Miesch M., Guerrero G., Charbonneau P., 2017, preprint, ([arXiv:1702.02421](https://arxiv.org/abs/1702.02421))
- Petrovay K., 2010, *Living Reviews in Solar Physics*, 7, 6
- Piddington J. H., 1975a, *Astrophys. Space Sci.*, 34, 347
- Piddington J. H., 1975b, *Astrophys. Space Sci.*, 35, 269
- Piddington J. H., 1981, *ApJ*, 247, 293
- Pipin V. V., Kosovichev A. G., 2013, *ApJ*, 776, 36

- Priyal M., Banerjee D., Karak B. B., Muñoz-Jaramillo A., Ravindra B., Choudhuri A. R., Singh J., 2014, *ApJL*, 793, L4
- Racine É., Charbonneau P., Ghizaru M., Bouchat A., Smolarkiewicz P. K., 2011, *ApJ*, 735, 46
- Rajaguru S. P., Antia H. M., 2015, *ApJ*, 813, 114
- Rempel M., 2005, *ApJ*, 622, 1320
- Rempel M., 2006, *ApJ*, 647, 662
- Rempel M., Schlichenmaier R., 2011, *Living Reviews in Solar Physics*, 8, 3
- Rempel M., Schüssler M., 2001, *ApJL*, 552, L171
- Roberts P. H., Stix M., 1972, *A & A*, 18, 453
- Sabine E., 1852, *Phil. Trans. R. Soc. Lond.*, 142, 103
- Schad A., Timmer J., Roth M., 2013, *ApJL*, 778, L38
- Schou J., et al., 1998, *ApJ*, 505, 390
- Schrijver C. J., Harvey K., 1994b, *Solar Phys.*, 150, 1
- Schrijver C. J., Harvey K. L., 1994a, *Sol. Phys.*, 150, 1
- Schrijver C. J., Siscoe G. L., 2010, *Heliophysics: Space Storms and Radiation: Causes and Effects*. Cambridge University Press
- Schrijver C. J., et al., 1996a, *ApJ*, 468, 921
- Schrijver C. J., et al., 1996b, *ApJ*, 468, 921
- Schrijver C. J., De Rosa M. L., Title A. M., 2002, *ApJ*, 577, 1006
- Schüssler M., Rempel M., 2002, in Wilson A., ed., *ESA Special Publication Vol. 508, From Solar Min to Max: Half a Solar Cycle with SOHO*. pp 499–506
- Schüssler M., Rempel M., 2005, *A & A*, 441, 337
- Schüssler M., Caligari P., Ferriz-Mas A., Moreno-Insertis F., 1994, *A & A*, 281, L69
- Shindell D., Rind D., Balachandran N., Lean J., Lonergan P., 1999, *Science*, 284, 305
- Sivaraman K. R., Gupta S. S., Howard R. F., 1993, *Sol. Phys.*, 146, 27

- Sivaraman K. R., Gupta S. S., Howard R. F., 1999, *Sol. Phys.*, 189, 69
- Sivaraman K. R., Sivaraman H., Gupta S. S., Howard R. F., 2003, *Sol. Phys.*, 214, 65
- Solanki S. K., 2002, *Astronomische Nachrichten*, 323, 165
- Solanki S. K., Schüssler M., Fligge M., 2002a, *A & A*, 383, 706
- Solanki S. K., Krivova N. A., Schüssler M., Fligge M., 2002b, *A & A*, 396, 1029
- Spiegel E. A., Zahn J.-P., 1992, *A & A*, 265, 106
- Spruit H. C., 1981, *A & A*, 102, 129
- Spruit H. C., 2003, *Sol. Phys.*, 213, 1
- Steenbeck M., Krause F., 1969, *Astronomische Nachrichten*, 291, 49
- Steenbeck M., Krause F., Rädler K.-H., 1966, *Zeitschrift Naturforschung Teil A*, 21, 369
- Stenflo J. O., Kosovichev A. G., 2012, *ApJ*, 745, 129
- Stephenson F. R., 1990, *Phil. Trans. R. Soc. London.*, A330, 499
- Stix M., 1976, *A & A*, 47, 243
- Svalgaard L., Cliver E. W., Kamide Y., 2005, *Geophys. Res. Lett.*, 32, 1104
- Thompson W., 1951, *The London, Edinburgh, and Dublin Philosophical Magazine and Journal of Science*, 42, 1417
- Thompson M. J., 2004, *Astronomy & Geophysics*, 45, 4.21
- Thompson M. J., et al., 1996, *Science*, 272, 1300
- Thompson M. J., Christensen-Dalsgaard J., Miesch M. S., Toomre J., 2003, *Ann. Rev. Astron. Astrophys.*, 41, 599
- Thornton L. M., Parnell C., 2011, *Solar Phys.*, 269, 13
- Tobias S. M., Brummell N. H., Clune T. L., Toomre J., 1998, *ApJL*, 502, L177
- Topka K., Moore R., LaBonte B. J., Howard R., 1982, *Solar Phys.*, 79, 231
- Ugarte-Urra I., Upton L., Warren H. P., Hathaway D., 2015, *ApJ*, 815, 90 (9 pp.)

- Ulrich R. K., 2010, *ApJ*, 725, 658
- Ulrich R. K., Boyden J. E., Webster L., Padilla S. P., Snodgrass H. B., 1988, *Sol. Phys.*, 117, 291
- Upton L., Hathaway D. H., 2014a, *ApJ*, 780, 5
- Upton L., Hathaway D., 2014b, *ApJ*, 780, 5 (8 pp.)
- Upton L., Hathaway D., 2014c, *ApJ*, 792, 142 (7 pp.)
- Usoskin I. G., Berdyugina S. V., Poutanen J., 2005, *A & A*, 441, 347
- Vainshtein S. I., Cattaneo F., 1992, *ApJ*, 393, 165
- Wang Y.-M., Sheeley Jr. N. R., 1989, *Sol. Phys.*, 124, 81
- Wang Y. M., Sheeley N. R., 1991, *ApJ*, 375, 761
- Wang Y.-M., Nash A. G., Sheeley Jr. N. R., 1989a, *Science*, 245, 712
- Wang Y. M., Nash A. G., Sheeley N. R., 1989b, *Science*, 245, 712
- Wang Y.-M., Nash A. G., Sheeley Jr. N. R., 1989c, *ApJ*, 347, 529
- Wang Y.-M., Nash A. G., Sheeley Jr. N. R., 1989d, *ApJ*, 347, 529
- Wang Y.-M., Sheeley Jr. N. R., Nash A. G., 1991, *ApJ*, 383, 431
- Warnecke J., Käpylä P. J., Mantere M. J., Brandenburg A., 2013, *ApJ*, 778, 141
- Warnecke J., Käpylä P. J., Käpylä M. J., Brandenburg A., 2014, *ApJ*, 796, L12 (6pp.)
- Warnecke J., Rheinhardt M., Tuomisto S., Käpylä P. J., Käpylä M. J., Brandenburg A., 2016, preprint, ([arXiv:1601.03730](https://arxiv.org/abs/1601.03730))
- Watari S., 2008, *Space Weather*, 6, 12003
- Weber M. A., Fan Y., Miesch M. S., 2011, *ApJ*, 741, 11 (14pp)
- Wolf R., Brunner W., 1935, *Astronomische Mitteilungen der Eidgenössischen Sternwarte Zurich*, 14, 105
- Yeates A. R., Muñoz-Jaramillo A., 2013, *MNRAS*, 436, 3366
- Yeates A. R., Nandy D., Mackay D. H., 2008, *ApJ*, 673, 544

-
- Yokoi N., Schmitt D., Pipin V., Hamba F., 2016, *ApJ*, 824, 67
- Yoshida A., Yamagishi H., 2010, *Ann. Geophysicae*, 28, 417
- Yoshimura H., 1975, *ApJ*, 201, 740
- Zhao J., Kosovichev A. G., 2004, *ApJ*, 603, 776
- Zhao J., Bogart R. S., Kosovichev A. G., Duvall Jr. T. L., Hartlep T., 2013, *ApJL*, 774, L29
- van Ballegoijen A. A., Choudhuri A. R., 1988, *ApJ*, 333, 965
- van Ballegoijen A. A., Cartledge N. P., Priest E. R., 1998, *ApJ*, 501, 866

